Three-Dimensional Entanglement: Knots, Knits and Nets

Myfanwy Ella Evans

January 2011

A thesis submitted for the degree of Doctor of Philosophy
of The Australian National University

Department of Applied Mathematics
Australian National University

Preface

I declare that the research presented in this thesis is my original work. Parts of this research however, are done in collaboration with others. Firstly, some of the research in Ch. 2, titled "Free Tilings of the Hyperbolic Plane", was undertaken in collaboration with Dr Vanessa Robins, Mr Stuart Ramsden and Prof. Stephen T. Hyde. Specifically, § 2.1 which covers the extension of Delaney-Dress tiling theory to free tilings was done in collaboration and the remainder of the Chapter is my original work. Secondly, the development of the ideas presented in Ch. 5, "Dilatancy of Woven Filament Arrays", was undertaken in collaboration with Hyde. I also declare that the length of this thesis is under 100,000 words. Further, I have rendered all images in this thesis, except where otherwise referenced.

Myfanwy E. Evans

Acknowledgements

"We must not forget that when radium was discovered no one knew that it would prove useful in hospitals. The work was one of pure science. And this is a proof that scientific work must not be considered from the point of view of the direct usefulness of it. It must be done for itself, for the beauty of science, and then there is always the chance that a scientific discovery may become, like the radium, a benefit for humanity."

– Marie Curie (1867 - 1934), Lecture at Vassar College, 1921.

To my supervisors and mentors, Stephen Hyde and Vanessa Robins, I certainly owe you both a beer. Your contributions to my work so far and to my future work is unprecedented. You have taught me the "beauty of science" that our old friend Marie talks about above, through countless days of discussion, feedback and occasional disagreements, and that will stay with me forever. I hope that you both enjoy reading this final version! Significant contributions to this thesis have also come from both Toen Castle and Stuart Ramsden: thanks to comrade Toen for a wonderful collaborative environment, and to Stu for his help and encouragement with 3D animation. I hope you both enjoy this 'colouring-in book' thesis!

Parts of this thesis benefited greatly from my research stays in Milano: *grazie mille* to Davide, you were a wonderful host. The gratitude is also extended to all others who hosted me on international stays. A small collaboration was also undertaken with Peter Harrowell: many thanks for these helpful discussions.

The Applied Mathematics department has always been a delightful environment in which to work, thanks to you all for help, seminars, questions and feedback, many afternoons at the pub and great excursions to Kioloa. Further, a big thanks to all of my friends and foes... I know you will never read this thesis, but maybe you will make it far enough to get to this page. And to my family... this thesis is for you all, I would not be here without you (both literally and metaphorically)!

Abstract

Three-dimensional entanglement, including knots, periodic arrays of woven filaments (weavings) and periodic arrays of interpenetrating networks (nets), forms an integral part of the analysis of structure within the natural sciences. This thesis constructs a catalogue of 3-periodic entanglements via a scaffold of Triply-Periodic Minimal Surfaces (TPMS). The two-dimensional Hyperbolic plane can be wrapped over a TPMS in much the same way as the two-dimensional Euclidean plane can be wrapped over a cylinder. Thus vertices and edges of free tilings of the Hyperbolic plane, which are tilings by tiles of infinite size, can be wrapped over a TPMS to represent vertices and edges of an array in three-dimensional Euclidean space. In doing this, we harness the simplicity of a two-dimensional surface as compared with 3D space to build our catalogue.

We numerically tighten these entangled flexible knits and nets to an ideal conformation that minimises the ratio of edge (or filament) length to diameter. To enable the tightening of periodic entanglements which may contain vertices, we extend the Shrink-On-No-Overlaps algorithm, a simple and fast algorithm for tightening finite knots and links. The ideal geometry of 3-periodic weavings found through the tightening process exposes an interesting physical property: *Dilatancy*. The cooperative straightening of the filaments with a fixed diameter induces an expansion of the material accompanied with an increase in the free volume of the material. Further, we predict a dilatant rod packing as the structure of the keratin matrix in the corneocytes of mammalian skin, where the dilatant property of the matrix allows the skin to maintain structural integrity while experiencing a large expansion during the uptake of water.

Contents

Chapter 1

Introduction

Three-dimensional entanglement, including knots, periodic arrays of woven filaments (knits or weavings) and periodic arrays of interpenetrating networks (nets), forms an integral part of the analysis of structure within the natural science. This thesis constructs novel, 3-periodic knits and nets, then tightens them to an 'ideal' shape in order to give geometric inspiration to the many disciplines of science influenced by structure.

A 3-periodic net in three-dimensional Euclidean space ($\mathbb{E}^3$) is a simple[1] 3-connected[2] graph, which is invariant under three independent translations of $\mathbb{E}^3$ [Klee 04]. A 3-periodic weaving in $\mathbb{E}^3$ is an arrangement of infinite one-dimensional space curves, also invariant under three independent translations of $\mathbb{E}^3$. Fig. 1.1 shows a portion of both a net and a weaving: the infinite structure extends infinitely in three directions.

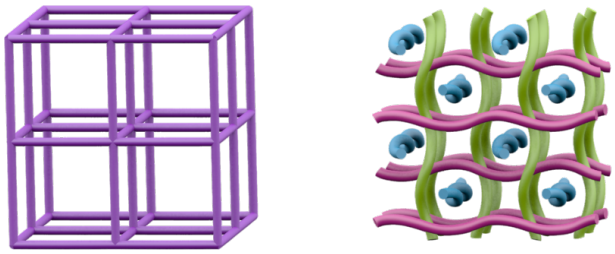

(a) **(b)**

Figure 1.1: A 3-periodic net and a 3-periodic weaving. The net (a) consists of vertices joined by edges and the weaving (b) of filaments that are infinite in length.

The scaffold we use for the construction of 3-periodic knits and nets are Triply-Periodic Minimal Surfaces (TPMS). A minimal surface is a surface with mean curvature of zero: it is equally concave and convex at every point. Every point on the surface is a saddle point,

[1] A simple graph is a set of vertices and edges, where each edge connects a distinct pair of vertices.

[2] A 3-connected graph can have no fewer than 3 vertices (and attendant edges) removed before it forms two or more disconnected components [Gros 92]

except at isolated flat points of zero gaussian curvature, hence the surface is hyperbolic. The term 'minimal' refers to the fact that many of these surfaces minimise the surface area given a set of conditions (boundary constraints, volume constraints, *et cetera*). A soap film on a wire loop is a minimal surface given the constraints of the wire [Dier 92]. TPMS are minimal surfaces that are periodic in three directions: they are invariant under three independent translation vectors.

The genus of an orientable surface (one which has two distinct sides) is a topological invariant defined as the largest number of non-intersecting simple closed curves that can decorate the surface without separating the surface into two distinct components [Stil 87]. Equivalently, the genus of an orientable surface is the number of torus-like handles it forms: the surface of a sphere has genus 0, the surface of a torus has genus 1. The genus of a TPMS is defined by taking a translational unit cell (of the oriented surface) and identifying opposite faces by gluing it modulo translations to obtain a compact surface [Hyde 10]. There are most likely only five highest symmetry TPMS for which this compact surface is genus 3 (a donut with three holes)[3]. These are Schwarz' *Primitive* surface (*P* surface), Schwarz' *Diamond* surface (*D* surface), Schoen's *Gyroid* Surface (*G* surface), Schwarz' *Hexagonal* Surface (*H* surface) and Schwarz' *Cross Layer Parallel* Surface (*CLP* surface) [Fogd 92]. In this thesis, we utilise each of the *P* surface, *D* surface, *G* surface and *H* surface.

To define the *cover* of a surface, we consider a cylinder of infinite length. Any infinite strip of the two-dimensional Euclidean plane ($\mathbb{E}^2$) can be wrapped over the cylinder such that it covers the surface. Thus any infinite strip of $\mathbb{E}^2$ is a *cover* of the infinite cylinder. The *universal cover* of a surface is the cover of all possible covers of that surface, for example the universal cover of the infinite cylinder is $\mathbb{E}^2$. More technically, the *universal cover* of a topological space Y (such as a TPMS), is a *simply connected*[4] space X, along with a *covering map*[5] $f : X \to Y$. The universal cover of a TPMS is the two-dimensional hyperbolic plane ($\mathbb{H}^2$), which can be wrapped over the TPMS, in much the same way as $\mathbb{E}^2$ can be wrapped over a cylinder. To harness the simplicity of a two-dimensional surface as compared with 3D space, tilings of the TPMS are initially constructed as tilings of the

[3]The completeness of these five genus-3 TPMS is still an open question due to the possibility of 'gyroid-like' intermediate surfaces within other families of TPMS.

[4]A domain is *simply connected* if any loop within the domain can be shrunk to a point continuously, *i.e.* the area enclosed by a circle is simply connected, the area between two concentric circles is not [Stil 87].

[5]A *covering map*, from a topological space (X) to another (Y), is a surjective map that is locally a homeomorphism, each point in X has a neighborhood whose image under the covering map in Y is equivalent [Stil 87].

universal cover of the TPMS: $\mathbb{H}^2$. These vertices and edges in $\mathbb{H}^2$ are wrapped over the TPMS, and in turn represent vertices and edges of an array in $\mathbb{E}^3$. For example, Fig. 1.2 shows the vertices and edges of a tiling in $\mathbb{H}^2$, an equivalent tiling wrapped over the *D* minimal surface and the vertices and edges of the tiling that results in $\mathbb{E}^3$.

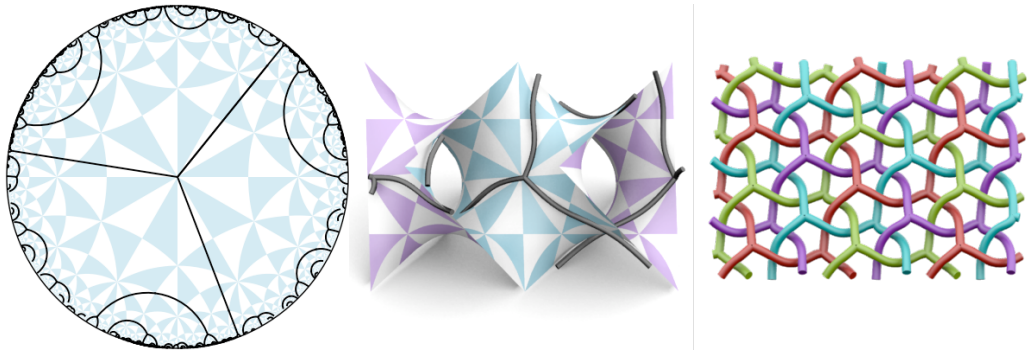

(a) **(b)** **(c)**

Figure 1.2: The vertices and edges of a tiling shown (a) in $\mathbb{H}^2$, (b) wrapped over the *D* minimal surface, and (c) as an entangled structure in $\mathbb{E}^3$.

Furthermore, we numerically tighten the entangled flexible structures to an ideal conformation that minimises the ratio of edge (or filament) length to diameter, which builds on a wide body of work containing the numerical tightening of finite knots and links [Katr 96, Stas 98]. To enable the tightening of periodic entanglements and structures containing vertices, we extend the Shrink-On-No-Overlaps (**SONO**) algorithm [Pier 98], a simple and fast algorithm for tightening finite knots and links.

The ideal geometry of weavings exposes an interesting physical property: *Dilatancy*. The cooperative straightening of the component filaments of a 3-periodic weaving with a fixed diameter induces an expansion of the material in conjunction with an increase in the free volume. We catalogue weavings with varying dilatancy, and predict a dilatant weaving as the alignment of keratin in the corneocytes of the outer 'horny' layer of mammalian skin. The dilatant property of the matrix allows the skin to maintain structural integrity while expanding during the uptake of water.

1.1 Historical Context

Soft condensed matter, including gels, foams, polymers, colloids and liquid crystals display behaviour not necessarily determined by their molecular or atomic structure alone. Interactions of structure assembled at the mesoscale, an intermediate length scale larger

than molecules but smaller than the bulk material, can influence macroscopic behaviour of the material: that which is visible to the naked eye ($> 1mm$). Particularly influential are the geometry and topology of mesoscale structures that self assemble from amphiphilic molecules [Char 85, Hyde 97, Sado 90]. These structures are clearly related to smaller scale patterns found in molecular and atomic crystals.

To understand the structure of chemical frameworks, we may consider their abstraction to geometric objects. A simple approach is the use of homogeneous sphere packings, where atoms are located at sphere centres and bonds at contacts between spheres. Enumeration of periodic structures by homogeneous sphere packings, which catalogues periodic nets of edge length 1, is still incomplete, but leads to a relatively manageable set of physically relevant frameworks [Koch 99, OKee 08]. An extension to this approach is to pack infinite cylinders, where cylinders represent rods of strongly bonded atoms within a chemical framework [OKee 01, OKee 05]. These so-called rod packings have structural stability yet low packing fractions, and are widely identified throughout structural chemistry [OKee 96]. An example of such a rod packing, the cubic Γ rod packing, is shown in Fig. 1.3.

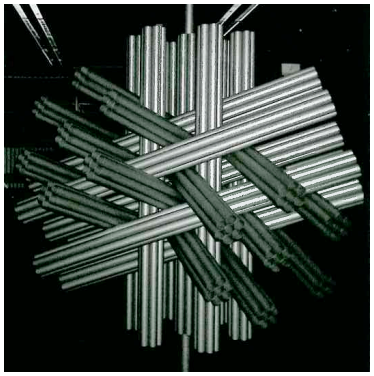

Figure 1.3: Sculpture of the Γ rod packing, located at the Max-Plank-Institut Für Metallforschung, Stuttgart. Photo courtesy of Vanessa Robins.

As another approach, a periodic structure may be considered as a packing of convex, closed, finite cells (polyhedra), where the vertices and edges of the cells within the packing define the net. A simple description of nets constructed in such a way comes from the component polyhedra: this description is known as a *polyhedral* description [OKee 96]. This may also be generalised to polyhedra with curved faces, as well as infinite polyhedra. Details of the use of these packings in new materials can be found in [Lord 06].

Despite these extensive collections of structures, there are still structures that may not

be described by these methods, particularly those that contain multiple interpenetrating nets or weavings of infinite filaments. The TPMS reticulation method presented in this thesis intends to fill these unexplored regions of structure that are not covered by current enumerative techniques.

The energetically favourable assembly of atoms (and molecules) in crystalline arrangements involves (intrinsic) curvature [Hyde 84]. Hanging structures from a TPMS scaffold mimics these conditions in crystalline solids such as Zeolites (microporous aluminosilicate minerals commonly referred to as molecular sieves) and Metal-Organic Frameworks (crystalline compounds consisting of metal ions or clusters coordinated to organic molecules to form porous structures). This curved geometry stems from the diffusion and confinement of interstitial charges within a charged lattice, or alternatively from templating molecules. Supporting this hypothesis, the theoretical framework of some (real) Zeolites were found to reticulate TPMS [Hyde 91, Hyde 93]. Fig. 1.4 shows how the graph of Sodalite, an aluminosilicate, can be considered as a reticulation of the *P* minimal surface. We note that this Sodalite graph also arises as a reticulation of the *D* minimal surface. Frameworks derived from TPMS reticulations may consist of multiple interwoven components, as well as large pore spaces [Chen 01].

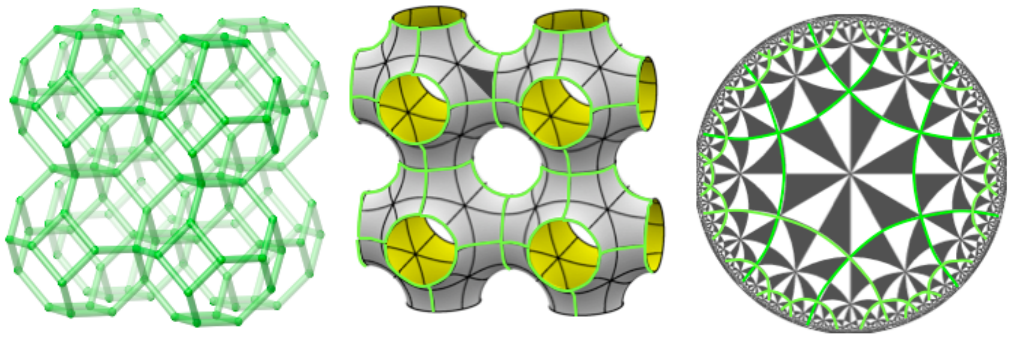

(a) **(b)** **(c)**

Figure 1.4: The Sodalite structure shown (a) in $\mathbb{E}^3$, (b) as a reticulation of the *P* minimal surface, and (c) as a tiling commensurate with the $*246$ tiling in the covering space of the surface, $\mathbb{H}^2$. Image courtesy of [Hyde 10].

If we map decorations in the universal covering space of the TPMS ($\mathbb{H}^2$) to $\mathbb{E}^3$, we allow complex (3D) euclidean geometry to be reduced to simpler (2D) hyperbolic geometry. Tiling the universal cover of a TPMS, discretised by the in-surface symmetries of the surface (rather than $\mathbb{E}^3$ symmetries), dates back to the ideas of Sadoc and Char-

volin [Sado 89]. As candidates for reticulation, decorations of $\mathbb{H}^2$ are restricted based on sub-symmetries and translational symmetries of the TPMS, where the latter restriction guarantees the periodicity of the resulting structures in $\mathbb{E}^3$ [Fogd 92]. Each family of TPMS has a set of in-surface symmetries that dictate allowed symmetry groups in $\mathbb{H}^2$ [Robi 04a, Robi 04b, Robi 05].

The systematic enumeration of commensurate tilings of $\mathbb{H}^2$, those with symmetry that is a subgroup of the maximal 2D symmetry group of the desired TPMS, calls upon the use of Delaney-Dress tiling theory. In the 1980's, Andreas Dress developed a finite symbol to encode both the topology and symmetry of an infinite periodic tiling (on 2D surfaces with positive, zero or negative curvature) using the earlier work of Matthew Delaney: the Delaney-Dress symbol [Dres 87]. The encoding is unique for finite disk-like tiles that fill any simply connected space. Delgado-Friedrichs and Huson harnessed the uniqueness of the Delaney-Dress symbol in developing an algorithmic enumeration of periodic tilings of each of the sphere, plane and hyperbolic plane [Huso 93, Delg 03a].

To obtain an enumeration of such tilings commensurate with the *P*, *D* and *G* surfaces and their corresponding TPMS reticulations is a complex process. The map from $\mathbb{H}^2$ tilings to TPMS tilings is many-to-many due to complications with group automorphisms and the multiply-connected nature of the TPMS. An online enumeration of these tilings (in $\mathbb{H}^2$ and on the TPMS) is located at [Hyde 10], and details of the process given in [Hyde 06]. A complete description of the reticulation of tilings with Kaleidoscopic symmetry is given in [Rams 09]. This work considers tilings of $\mathbb{H}^2$ that are composed entirely of tiles topologically equivalent to a compact disk: this constraint means that all resulting structures in $\mathbb{E}^3$ will be single component, 3-periodic nets. In this thesis, we extend to tilings of $\mathbb{H}^2$ by tiles that are topologically equivalent to infinite ribbons or infinite branched ribbons, *free tilings*, which gives two more classes of structures in $\mathbb{E}^3$: multiple component nets and filament weavings.

Examples of the reticulation of some high symmetry free tilings on TPMS have been published [Hyde 99, Hyde 00a, Hyde 00b, Hyde 00c, Hyde 03a, Hyde 03b, Hyde 03c]. Topology of the vertices and edges remaining in $\mathbb{E}^3$ once the surface is dissolved are examined in these publications, but no approach is detailed as to the analysis of the resulting structure. This thesis will examine a larger set of examples through the extension of the Delaney-Dress tiling theory to include free tilings. This enables easy description of free tilings as well as the scope for an enumeration. We also examine a particular class of these free tilings where the tile boundaries are infinite and vertex-free, which result in TPMS

reticulations that are weavings of curvilinear one-dimensional filaments.

Current techniques for analysis of nets in $\mathbb{E}^3$ that contain either a single component or multiple components include three main approaches: quotient graphs, SyStRe analysis and TOPOS analysis. A few simple methods are also available for the analysis of weavings of one-dimensional filaments: crossing number, minimal crossing number, average crossing number among others. We detail these methods here.

Note that a structure is comprised of three elements: the first is its *topology*, which refers to the abstract graph connectivity of the structure, the second is *ambient isotopy* class, which refers to all structures related to each other by an ambient isotopy[6] and the third is the geometry of the edges of the structure in $\mathbb{E}^3$. We consider each of the current methods in relation to these three elements of structure.

The *quotient graph* of a periodic network is built from a single representative of each translationally equivalent vertex and each translationally equivalent edge. A *labelled quotient graph* labels the edges by their lattice translation vectors in the periodic net [Chun 84]. For example, Fig. 1.5 shows the labelled quotient graph of a periodic graph which follows the edges of stacked cubes (the **pcu** net). Quotient graphs encapsulate the topology of periodic structures. In general however, there is no algorithm for determining when two quotient graphs represent the same periodic net. Further, the labelled quotient graph gives no information about the ambient isotopy class or edge geometry of the structure.

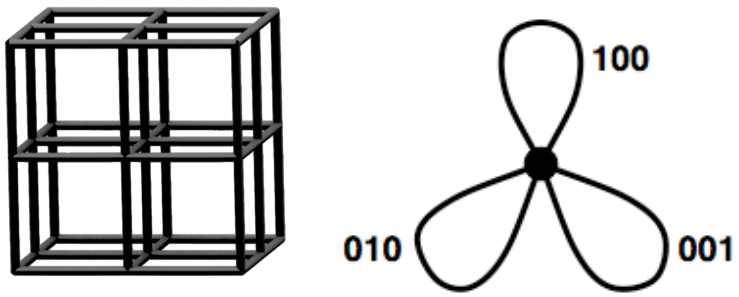

Figure 1.5: (a) The 3-periodic **pcu** net. (b) The labelled quotient graph of **pcu**.

The SyStRe algorithm [Delg] provides an equilibrium (barycentric) placement of vertices (crystalline form) within a labelled crystallographic quotient graph. This placement

[6] An *ambient isotopy* is a continuous deformation of an embedding space. Two nets are equivalent if there is an ambient isotopy from one to the other i.e. one net can be deformed into the other without allowing edges to cross through each other [Crom 04].

gives a system for comparing the topology of periodic nets [Delg 03b]. This canonical form for periodic nets, however, does not prescribe the equivalence of nets within an ambient isotopy class. Furthermore, the SyStRe algorithm is unable to find an equilibrium placement for nets where distinct vertices occupy the same location in an equilibrium placement (vertex collisions) and where distinct edges intersect in the equilibrium placement (edge collisions), and is also unable to relax non-crystallographic nets. Additionally, the algorithm is only able to find a canonical form for single-component nets.

TOPOS analysis of a net [Blat 06] collates the knots formed by single cycles, and links found by disjoint pairs of cycles, in the net. This approach is unique in that fact that it is sensitive to the equivalence of nets by ambient isotopy. An algorithm such as this, based on analysis of interpenetration of rings, is excellent at identifying when two nets belong to distinct ambient isotopy classes, but fails to prove two nets belong to equivalent ambient isotopy classes when their linking signature is equivalent. A further challenge to analysis methods such as this are entanglements that occur on a scale beyond cycles, such as the ravel [Cast 08]. These entanglements have no knotted or linked cycles, yet are still entangled, and hence will be overlooked by the TOPOS analysis. Such an entanglement has been recently synthesised: a finite molecule that forms a ravel is described in [Li 11].

To encompass more general spatial patterns, in particular those of one-dimensional (1D) filaments, we delve into an area examined by polymer physicists and mathematicians alike. The *Crossing Number* of a material is a simple intuitive measure counting the number of times a filament crosses over itself or another. This measure is also used in knot theory to analyse knots and links. A related quantity is the *Minimal Crossing Number*, where an object is manipulated (within an ambient isotopy class) so as to have the minimal number of crossing over itself or other objects [Buck].

To obtain a quantity that is independent of the viewing direction, one may consider an average of the crossing number across all 2D projections of the material (as the crossing number may vary with the chosen perspective). This value is known as the *Average Crossing Number* (ACN). Analysis of materials by the ACN is a geometric problem, involving a specific embedding of a topological object. A quantity associated with the ACN for entangled infinite filaments is how this ACN changes with the increase of the material sample size [Buck]. Another concept related to the ACN is the *temperature* of a tangle [Buck 08]. This considers what portion of a filamentous array is visible from a particular view point: those arrays that are more tangled will have a larger portion of filaments obscured, and thus a higher temperature.

We may also consider the shape of individual filaments within an array: restrictions on the curvature of a filament influences how filaments can tangle together [Buck 07]. This entanglement measure requires some physical thickness to the filament, and a minimisation of an energy associated with the curvature of the filament [Buck 98, Simo 09].

These available methods are far from comprehensive in the analysis of 3-periodic structure, and this is the gap in the literature that we will partially fill with the work in this thesis. To do this, we extend a technique that has been insightful when analysing finite knots and links. The idea is intuitive: take a knot, give it thickness and pull it tight, forming an *Ideal Knot*. To quantify the entanglement of an ideal knot, one must first choose a physical quantity associated with this conformation. There are many energy measures to consider[7], which include the *minimum distance* energy [Simo 94], the *symmetric* energy [Buck 93], [Buck 95], and the *conformal* energy [OHa 91, Dioa 98]. A simple quantity of the ideal conformation is the ratio of length to radius. This quantifies the entanglement of a knot, which is useful in identifying distinct conformation which belong to the same equivalence class by ambient isotopy. Much intuition has been gained in knot theory by considering this energy function of ideal knots [Stas 98].

Figure 1.6: The ideal conformation of a trefoil knot.

A different conformation energy is a compactness energy. The minimisation of this energy in turn minimises the occupied space of the filaments, which represents the structure in a most compact form. This has been considered elsewhere for a single untangled filament, where the result is a helical form [Przy 01]. Interestingly, the pitch given by the compact helix is the same as that of a collagen helix [Mari 00].

For each of these energy quantities, it is difficult to identify the conformation of a knot

[7] A comprehensive summary of energy measures for finite entanglements pre-1998 can be found in [Scha 98]

or link which minimises the energy. A fruitful approach is to computationally tighten any given configuration of the entanglement to a minimal energy state. One such algorithm is simulated annealing [Kirk 84, Laur 98]. Initially, the knot is discretised to a series of vertices and edges, and an energy functional is defined. A random move is applied to any node of the knot trajectory, the energy recalculated and the move either accepted if the energy is less or rejected if the energy is greater. Through the continued application of this process, a local energy minimum is achieved. A similar recipe is given in [Simo 94], which uses random perturbations to decrease the minimum distance energy. Further to this, another process of simulated annealing with some additional measures in place to remove trapping of the structure in local minima is given in [Grze 97]. Finally, an algorithm to relax the energy of a knot is given in [Kusn 97, Dioa 98]. There is no proof, however, that any of these simulated annealing algorithms find a global minimum.

The **SONO** algorithm (*Shrink-On-No-Overlaps* [Pier 98]) is one approach to the computational tightening of knots and links, which minimises the ratio of length to radius as the energy function. It uses a repulsion mechanism to push nearby segments of the knot away, coupled with a shrinking mechanism to tighten the knot. This algorithm is simple and efficient. Mechanisms are in place within the algorithm to shake the knot out of local minimum energy conformations (that are not global energy minima), but a proof that these mechanisms will always ensure the global minimum is reached is still elusive and likely untrue. In this thesis, we will extend the **SONO** algorithm to tighten both 3-periodic knits and nets to optimal forms by minimising the ratio of length to diameter.

We predict that the ideal forms of many of these branched and 3-periodic structures will realise all possible symmetries of the structures, however we see that previous results of the **SONO** algorithm may indicate otherwise. The **SONO** algorithm shows a symmetry breaking effect when tightening torus knots with a high crossing number, and also for the tightening of a periodic double helix [Pier 98], where the ideal form sees one strand of the helix pull straight and the other wind around the outside. We also note that an optimal conformation for the double helix while preventing a symmetry breaking event has also been studied [Olse 10].

1.2 Significant Results

A key body of work to come from this thesis is the construction of an array of structures with a specific embedding, rather than simply a prescribed topology, which are relevant to

the natural sciences. The nets that we construct in this thesis are, in most cases, multiple component interpenetrating nets. Such nets arise frequently in synthetic chemical frameworks, as seen in Ch. 3, and we generate more complex examples of such nets as possible targets for synthesis. In the construction process presented in this thesis, all three elements of the structure are prescribed, including topology, ambient isotopy class and edge geometry, which is in contrast to previous enumeration techniques. We obtain two such edge geometries for a net, one is the geometry of the tile edges as they sit on the TPMS, and the other is the ideal geometry found through simulation. These specific geometries, that are often distinct from SyStRe barycentric embeddings, may yield important material properties.

The 3-periodic entanglements of infinite filaments constructed in this thesis are, in the simplest cases, well recognised rod packings. Through the TPMS reticulation method, we are able to generalise the notion of a rod packing to contain curvilinear as well as rectilinear components, and build a more complete taxonomy of 3-periodic weavings. A catalogue of entanglements of infinite filaments is certainly missing from the current literature, and these new structures may provide insight into weavings of polymers, proteins and DNA.

An interesting consequence of the idealisation of weavings to optimal configurations is the geometry of the filaments is often helical. In many cases, the geometry prescribed by the idealisation is equivalent to that of the weaving as it sits on the TPMS, which implies relevance for the exact filament geometry obtained from the TPMS. The helical geometry of some weavings in their optimal configuration leads to an exotic physical property: *Dilatancy*. In addition to this, it is possible that these ideal weavings may display other interesting physical regimes, such as auxetic behaviour, which is a likely consequence of dilatancy.

These dilatant weavings are attractive design targets for new synthetic materials, stemming from the potent increases in the free volume of the material on straightening of the filaments, while maintaining structural stability of the material. As a bio-material, this beautiful property of the ideal Σ^+ rod packing gives an explanation for the keratin organisation in the corneocytes of the stratum corneum layer of the skin. The dilatancy of the keratin matrix allows us to explain the remarkable structural rigidity of the skin during the uptake of water and subsequent swelling of the skin. The ramifications of knowledge of the keratin organisation are immense: the barrier properties of the skin are important in many areas of the medical and therapeutic sciences, and surely relate to the structural forms of the skin.

1.3 Overview of the thesis

We begin in Ch. 2, titled "Free Tilings of the Hyperbolic Plane", where we extend the Delaney-Dress encoding of conventional tilings of $\mathbb{H}^2$ to include free tilings of $\mathbb{H}^2$, which are tilings by tiles of infinite size. The chapter includes a brief catalogue of such free tilings, that are regular (1-transitive edges, vertices and tiles) and are composed of infinite ribbon tiles with high symmetry. We embed these selected, high symmetry free tilings into either the $*246$ or $*2226$ chart of $\mathbb{H}^2$, so as to be commensurate for projection to the *P*, *D* and *G* surfaces in the former case, and the *H* surface in the latter. Complications arise in the embedding of free tilings with Stellate symmetry (to be defined later), for which there are an infinite number of embeddings commensurate with the TPMS, and we establish rules to systematically enumerate such embeddings.

Of the free tilings we consider, some have tile boundaries consisting of vertices and edges and others have tile boundaries that are vertex-free infinite geodesics. In Ch. 3, titled "Reticulations of Triply-Periodic Minimal Surfaces", the free tilings containing vertices and edges along the tile boundaries are reticulated over the TPMS to give a catalogue of multiple component interpenetrating nets in $\mathbb{E}^3$. We analyse these resulting structures using the standard SyStRe algorithm and TOPOS program to ascertain information about the structure. Additionally, this chapter contains the reticulation of examples of the other genre of free tilings, composed of infinite geodesic tile boundaries. These free tilings give 3-periodic knits composed of infinite tangled filaments when reticulated over the TPMS. We catalogue these structures, and give details about their geometry and entanglement.

Ch. 4, titled "Ideal geometry of branched and periodic structures", extends the SONO algorithm to computationally tighten 3-periodic structures and is capable of tightening entanglements that contain vertices. We lay the foundations of this algorithm by considering tight finite knots, where the tight configuration is previously established in the literature. Finite knotted graphs are tightened to show the reliability of the algorithm at vertices, and further obtain measurements of the $\frac{L}{D}$ energy for a variety of graph embeddings. Various 3-periodic entanglements of infinite filaments, constructed in Ch. 3, are computationally tightened to reveal the geometry of their tight configurations. Finally, we tighten a few selected single component nets to compare the tight configuration with the SyStRe canonical embedding, and include nets where the SyStRe embedding contains vertex collisions. We then consider the multiple component nets constructed on the TPMS to ascertain their ideal geometry.

The physical property of dilatancy for 3-periodic weavings, where the straightening of filaments leads to an unprecedented increase in the free volume of the material, is described in Ch. 5: "Dilatancy of Woven Filament Arrays" . We show examples of several genres: zero dilatancy, finite dilatancy and infinite dilatancy. We finally explore the dilatant weaving Σ^{+}, which we propose as the scheme for keratin organisation within the corneocytes of the outer layer of mammalian skin. The dilatant property of this matrix allows the swelling of the skin in the presence of water without loss of inter-keratin contacts with the corneocyte, which preserves structural stability.

Chapter 2

Free Tilings of the Hyperbolic Plane

A *tiling* is the faces, edges and vertices of a 2D tessellation of a surface, where tiles only intersect along their boundaries and the tiles cover the whole of the surface. A *reticulation* of a Triply-Periodic Minimal Surface (TPMS) is the edges and vertices (not faces) of a tessellation on the surface: these vertices and edges in three-dimensional Euclidean space ($\mathbb{E}^3$), define a structure. Tilings of the covering space of these intrinsically hyperbolic TPMS, *i.e.* tilings of the two-dimensional Hyperbolic plane ($\mathbb{H}^2$), mimic direct tilings of the TPMS when they adhere to a compatible set of isometries of the chosen surface: in-surface symmetries of the TPMS are represented by symmetries of $\mathbb{H}^2$. Tilings that consist of finite tiles with *Coxeter* symmetry, corresponding to Coxeter discrete groups which contain only mirror symmetries, have been previously explored in detail [Rams 09].

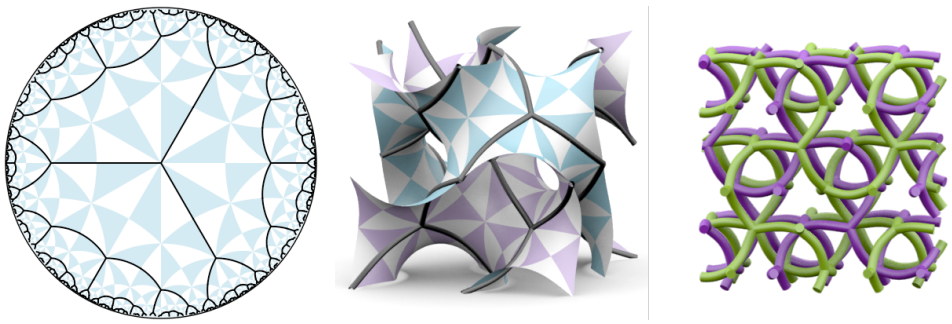

(a) **(b)** **(c)**

Figure 2.1: (a) A free tiling with symmetry $*2223$ in $\mathbb{H}^2$. (b) The tiling shown on one unit cell of the Gyroid surface. (c) The structure remaining in $\mathbb{E}^3$ is two interpenetrating **srs** networks.

This chapter explores tilings of $\mathbb{H}^2$ by tiles of infinite size with an infinite translation as an internal symmetry (*free tilings*). Free tilings are of interest for their form as tilings of TPMS: regular tilings give a single component net in $\mathbb{E}^3$, whereas free tilings give multiple disconnected components in $\mathbb{E}^3$ that are interpenetrating [Hyde 03a, Hyde 00a, Hyde 00c]. For example, Fig. 2.1 shows a free tiling with symmetry $*2223$ in $\mathbb{H}^2$, as a surface tiling of

the Gyroid minimal surface, and as a structure in $\mathbb{E}^3$: two interwoven **srs** nets of equivalent chirality. Further, this chapter extends beyond Coxeter tilings to those with rotational symmetry elements.

This is done by an extension to the Delaney-Dress method for encoding the abstract topology of tilings, which represents the abstract topology of free tilings. In addition, we embed these free tilings firstly into $\mathbb{H}^2$, where an ordering is borrowed from the Euclidean plane, and further into tilings commensurate with the TPMS. To begin, we introduce both orbifolds and the Poincaré Disc model of $\mathbb{H}^2$.

2.0.1 Conceptual Detour: Orbifolds and The Poincaré Disc model

An *orbifold* is the quotient of a manifold by a discrete group of isometries of the manifold [Thur 80]. An orbifold represents a single asymmetric domain of an infinitely repeating pattern along with its symmetry information. More specifically, it is a topological structure where all copies of the repeating pattern are "glued" under appropriate symmetries, such that "unrolling" the orbifold into any covering space results in a repeating pattern. The corner and cone points of this single unit combined with its topology (details of the symmetries of the pattern) gives the orbifold [Conw 92, Conw 02].

A two–dimensional orbifold encodes an infinite pattern on any two–dimensional surface, be it intrinsically Spherical ($\mathbb{S}^2$), Euclidean ($\mathbb{E}^2$) or Hyperbolic ($\mathbb{H}^2$). The isometries of two–dimensional space encoded by such orbifolds are [Conw 92]:

1. Reflections in a line, represented by the orbifold boundary and corner points. A vertex may have n mirror lines incident, denoted by Conway symbol $*\mathtt{n}$. Simply-connected orbifolds containing only reflections are denoted $*\mathtt{ab...c}$ and are called *Coxeter* orbifolds.

2. Rotations, represented by a cone point, denoted by Conway symbol $\mathtt{N}$ denoting a $2\pi/N$ rotation.

3. Translations: the identification of two pair of edges is denoted by $\circ$ (handle), two directions of translational copies symmetry. Topologically, $\circ$ adds a handle to the orbifold, adding to the genus.

4. Glide reflections, involving a reflection and a translation of the motif along the mirror line, denoted by Conway symbol $\times$. Topologically, a $\times$ adds a non–orientable cross–cap structure to the orbifold [Fran 99].

The terminology of orbifolds is combined to form a string of the relevant symmetries of the form $\mathsf{AB...C} * \mathsf{ab...c} \times ... \circ ....$ An arbitrary Conway symbol encodes a realisable orbifold and discrete group, except for the cases $*mn$ and mn where $(m \neq n)$, and also the specific case of $*\mathsf{m}$ and M, $(m, M > 1)$. These are the only orbifold symbols that do not represent groups [Conw 02].

The combinations of topological features within an orbifold give rise to eight distinct categories, classified by the orientability of simply – or multiply – connected orbifolds, with or without boundaries [Hyde 11]. We describe three of these categories, to be considered later in this chapter. The first is the *Coxeter* orbifolds, which contain only mirror symmetries and correspond to Coxeter groups (Fig. 2.2(a)). This orbifold is a polygonal section of the plane (be it Spherical, Euclidean or Hyperbolic) bounded by mirror boundaries. The second category is the *Hat* orbifolds, which consist of rotational symmetries with a single mirror boundary. The rotational symmetries define the cone points and the mirrors define the boundary (Fig. 2.2(b)). Finally, the *Stellate* orbifolds contain only rotational symmetries, and resemble a pillow punctuated by distinct cone points (Fig. 2.2(c)).

(a) $*\mathsf{abcd}$ **(b)** $\mathsf{A} * \mathsf{ab}$ **(c)** ABCD

Figure 2.2: (a) A *Coxeter* orbifold: it is bounded by mirror boundaries and corner points. (b) A *Hat* orbifold, it has a single mirror boundary and rotational symmetry. This consists of a cone point bounded by the mirror lines. (c) A *Stellate* orbifold: it has purely rotational symmetry. The orbifold is a pillow punctuated by each of the distinct cone points.

The neat orbifold notation of Conway described above allows us to find directly the *cost* (C) of the orbifold, which is identical to both its Euler–Poincaré characteristic and the area of the orbifold [Conw 92]. The global Gauss–Bonnet formula gives a relationship between the Gaussian curvature of a surface (K) and the Euler–Poincaré Characteristic (χ) [Spiv 79]. More precisely, where A is the given area:

$$2\pi\chi = \iint K \, dA$$

Thus where the Gaussian curvature of the surface is constant, or the area is taken in the universal cover of the surface, the sign of the Euler–Poincaré characteristic gives the sign of the Gaussian curvature of the surface by:

$$K = \frac{2\pi\chi}{A}$$

The cost, C, of the orbifold (and in turn the mean Gaussian curvature) is calculated by:

$$C = 2 - \sum_i d_i$$

The following table shows the value of each d_i.

Symmetry Element	Symbol	d_i
Mirror	$*$	1
Glide Reflection	$\times$	1
n–fold rotation centre	N	$\frac{N-1}{N}$
Mirror Intersection (angle $\frac{\pi}{n}$)	n	$\frac{n-1}{2n}$
Translation (handle)	$\circ$	2

The hyperbolic plane, $\mathbb{H}^2$, has constant negative Gaussian curvature, denying it the luxury of embedding in $\mathbb{E}^3$ without singularities. These singularities manifest as obstructions in the visual representation of $\mathbb{H}^2$in our Euclidean world: immersing $\mathbb{H}^2$ in $\mathbb{E}^3$ with singularities may result in the singularities acting as obstructions to the paths of geodesics [Hilb 52]. This is not ideal for our purposes, and in turn we are led to the Poincaré Disc model of the $\mathbb{H}^2$ [Hilb 52, Coxe 47a, Bear 95].

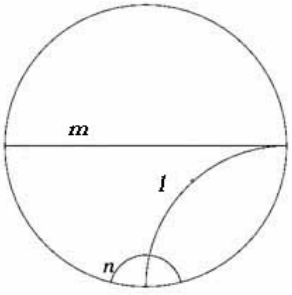

Figure 2.3: The Poincaré Disc: a conformal representation of the $\mathbb{H}^2$. Geodesic paths passing through the centre of the circle, such as m, are represented by straight lines. All other geodesic paths, such as l and n, are represented by circular arcs that intersect the boundary at right angles.

The Poincaré Disc model represents $\mathbb{H}^2$ as the interior of a circle, where $\mathbb{H}^2$ approaches infinity at the boundary of the circle. A geodesic is an arc of the circle that is incident at right angles to the boundary of the circle, as shown in Figure 2.3. Defining the interior of the Poincaré Disc by $\{z \in \mathbb{C} : |z| < 1\}$, the metric for this model is given by

$$ds = \frac{2|dz|}{1-|z|^2}$$

The Poincaré Disc model is a conformal model: Euclidean angles on the disc correspond to angles in $\mathbb{H}^2$. Parallel lines, or "equidistant" lines, in the hyperbolic plane are signified by lines that meet at the disc boundary, *e.g* lines 'l' and 'm' in Fig. 2.3 [Coxe 47a]. "Hyperparallel" lines are represented by non–intersecting lines, *e.g* lines 'm' and 'n' in Fig. 2.3. Fig. 2.4 shows a regular hexagon in both the two–dimensional Euclidean plane ($\mathbb{E}^2$) and $\mathbb{H}^2$, where the Poincaré Disc model is used to represent $\mathbb{H}^2$.

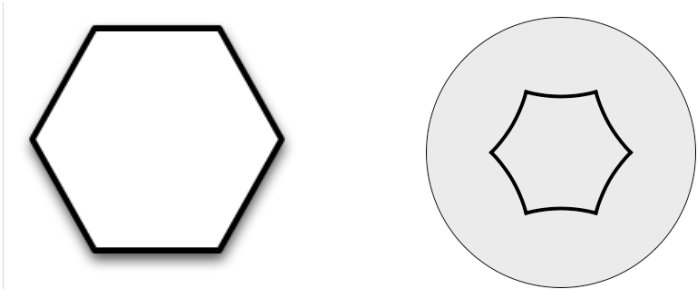

(a) **(b)**

Figure 2.4: (a) A regular hexagon in $\mathbb{E}^2$. (b) A regular hexagon in $\mathbb{H}^2$, shown on the Poincaré Disc model of $\mathbb{H}^2$. It has angles less that 120°.

2.1 Abstract topology of tilings: Delaney–Dress

Conventional tilings

To encode conventional tilings of $\mathbb{H}^2$ (those which are topologically equivalent to a disk), we consider the Schläfli symbol. The Schläfli symbol is of the form $\{p,q,r,...\}$, and encodes regular polytopes and tessellations [Coxe 47b]: a symbol $\{p\}$ encodes a regular ('Platonic') polygon with p sides, a symbol $\{p,q\}$ encodes the tessellation of q regular p–sided polygons around each vertex. Where this tessellation may be embedded in $\mathbb{S}^2$, the symbol defines the polyhedron enclosed by the tiling.

Where the Schläfli symbol encodes only the topology of the tiling, the so–called

Delaney–Dress symbol encodes more information: for any periodic tiling of a two–dimensional plane by tiles of finite size it gives a canonical and finite encoding of the topology and symmetry of the tiling [Dres 87]. Conversely, the Delaney–Dress symbols can be used to build tilings of a given symmetry and topology. The symbol triangulates each tile of the periodic tiling into a series of *chambers*, where the three vertices of the chamber lie at a vertex, edge and face of the tiling respectively. Tilings with the following properties have canonical encodings [Dres 87, Rams 09]:

1. Each tile is topologically equivalent to a disk (they are closed).
2. Tiles only intersect along their boundaries.
3. The size of the tiles is uniformly bounded.
4. Tiles cover the whole of the plane (be it $\mathbb{S}^2$, $\mathbb{E}^2$ or $\mathbb{H}^2$).

Given a tiling of any two–dimensional plane, the construction of the triangulation for the purposes of encoding the topology of the tiling follows a specific recipe:

1. At the barycentre of each tile (the geometric centroid of masses placed at each vertex of the tile), place a vertex denoted '2'.
2. At the midpoint of each edge, place a vertex denoted '1'.
3. At each vertex of the tiling, place a vertex denoted '0'.
4. The domain is triangulated by connecting vertices as shown to the right.
5. 'Colour' the chambers such that those related by isometries of the tiling are the same colour.

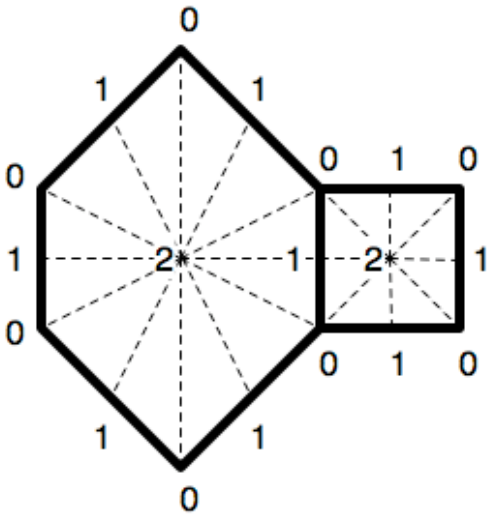

For example, the triangulation of a portion of a tiling of $\mathbb{H}^2$ is constructed using this prescription in Fig. 2.5. A smallest asymmetric unit of the tiling contains two triangular

regions, one shown in red and the other in blue, these two regions represent the two distinct tiles of the tiling. When encoding the tiling, we consider only the chambers within an asymmetric domain: all copies of these chambers are encoded through the adjacency relation information.

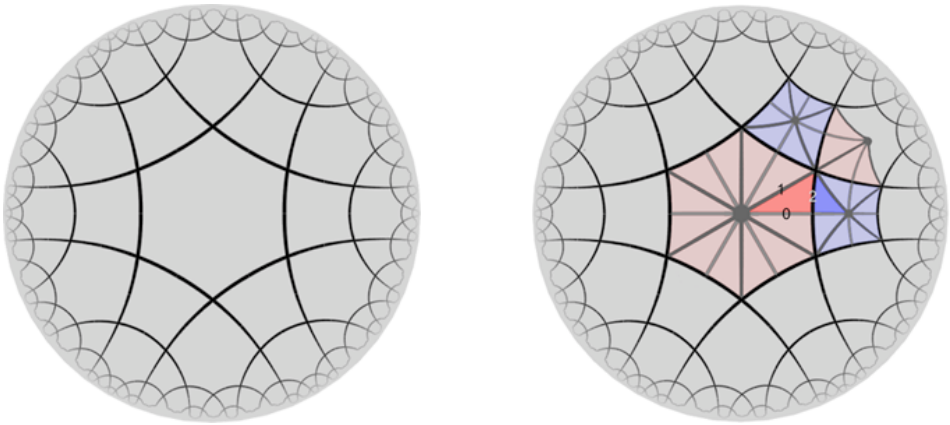

(a) **(b)**

Figure 2.5: (a) A tiling of $\mathbb{H}^2$ by two distinct tiles. (b) A triangulation of an area of the tiling. The triangulation is composed of vertices placed at each of the tile faces, tile vertices and tile edges. This example has two distinct chambers within a asymmetric domain, one shown in red and one shown in blue [Hyde 10].

The 'adjacency map' of each chamber encodes which chambers are adjacent to a selected chamber on each of its boundaries. The term $s0$ denotes the neighbouring chamber across the 0–edge, $s1$ across the 1–edge, and $s2$ across the 2–edge. To encode the topology, we consider the orbits around each of the vertices for each distinct chamber. Around the 2–vertex (the vertex in the centre of the face), we consider how many sets of 0–edges (the edge opposite the 0–vertex) and 1–edges (the edge opposite the 1–vertex) are incident to that 2–vertex. The order of this orbit is denoted $m01$. In general, $m01$ corresponds to the number of edges of a tile. For example, in Fig. 2.5, $m01$ for the red chamber is 6, and $m01$ for the blue chamber is 4. Similarly, we require the order of the 0–vertex orbit, $m12$. For each distinct chambers in Fig. 2.5, $m12$ is of order four. The 1–vertex orbit ($m02$) is always two, by the prescribed construction of triangulation. The full encoding of the tiling shown in Fig. 2.5 is given by the following table:

Chamber Class	$s0$	$s1$	$s2$	$m01$	$m12$
Red	Red	Red	Blue	6	4
Blue	Blue	Blue	Red	4	4

A unique ordering of complexity may be obtained from Delaney–Dress encodings, and in turn these tilings are enumerable up to a given complexity [Delg 03a]. Another approach to encoding the equivalent information is the Generalised Schläfli Symbol [Conw 08]. This is an extension of the Schläfli symbol as it defines a tessellation together with its symmetries, as opposed to an abstract polyhedron. This encoding gives a good visual representation of the tiling. Within this section, however, we use only the Delaney–Dress encoding for tilings of $\mathbb{H}^2$.

Free tilings

To construct and encode tilings of $\mathbb{H}^2$ by tiles of infinite size, termed *free tilings*, we delete edges from a conventional tiling while preserving the original Delaney–Dress triangulation. The term *free tiling* (Vanessa Robins, private communication) is due to the internal symmetry elements of the resulting infinite tile being a free group. These free tilings are denoted by the original Delaney–Dress encoding with an additional signifier, namely a $\bar{1}$–vertex rather than the standard 1–vertex, on the chambers that now contain a 'ghosted' edge. By associating each free tiling with a conventional tiling, free tilings inherit the enumerable structure of Delaney–Dress symbols.

This encoding is complicated by the fact that most free tilings may be constructed from multiple distinct conventional tilings: if two conventional tilings differ only by a single edge (and have different Delaney–Dress encodings), and this particular edge is ghosted, the same free tiling will result and will be classified by two distinct encodings. For example, Fig. 2.6 shows the ghosting of two conventional tilings, where the result is equivalent free tilings.

The unique encoding of a free tiling is chosen to be the simplest among all possible encodings, as defined by the number of chambers within the triangulation of a single orbifold domain. Where there exist multiple simplest encodings of a single free tiling, the unique encoding is chosen to be that which has come from the least complexity Delaney–Dress encoding (Delaney–Dress encodings may be uniquely ordered [Delg 03a]). For example, the encoding of the free tiling shown in Fig. 2.6 part (b) is simpler than that which is shown in part (d).

Two issues arise in finding a unique encoding of a free tiling. Given two distinct encodings, how do we determine if they represent the same free tiling? To find the unique encoding of a free tiling, how do I first enumerate all possible encodings from which to

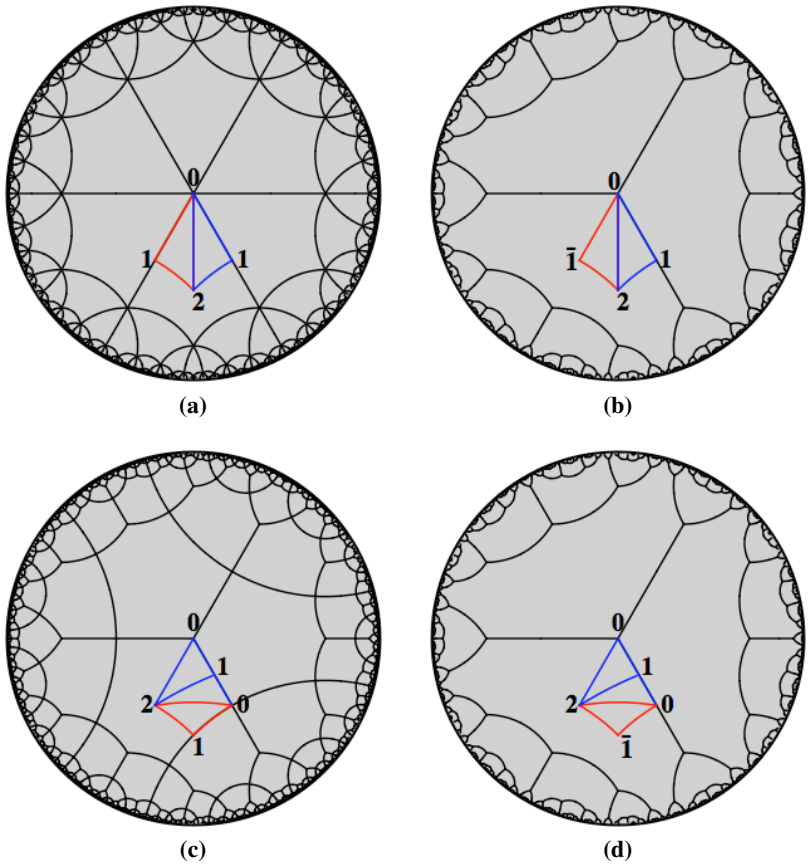

Figure 2.6: (a) A conventional tiling of $\mathbb{H}^2$ shown with its Delaney–Dress encoding. (b) By ghosting a single edge of the conventional tiling shown in part (a), a free tiling of $\mathbb{H}^2$ results, which inherits the Delaney–Dress encoding. (c) A conventional tiling of $\mathbb{H}^2$, which is different from that shown in part (a), shown with its encoding. (d) The ghosting of an edge gives a free tiling which is equivalent to that shown in part (b), yet it inherits a distinct encoding.

choose the simplest? We address these issues through a set of rules that construct the unique encoding of a free tiling from the tile vertices and edges of the free tiling, without information about the conventional tiling from which it originated.

A necessary restriction for the uniqueness of the encoding obtained from this construction process is that we only remove edges from a conventional tiling that leave at least two edges incident at each of its vertices (i.e. the removal of an edge does not remove all edges incident at a vertex), and only remove edges which begin and end at symmetry sites of the orbifold. The completeness of the set of free tilings enumerated with these restrictions is not yet proven, nevertheless this lies outside the scope of this thesis.

We proceed with the construction algorithm. The notation $\bar{1}$ is added to the encoding to represent edges that are present in the conventional tiling but not in the free tiling (ghosted).

We begin with a *parent symbol*, constructed as follows:

1. Identify an asymmetric orbifold domain of the free tiling; this is the domain for triangulation.

2. All symmetry 'corners' of the tile boundary (intersection points of mirror lines or rotation centres) are occupied by 0–vertices. These locations are the only locations where vertices may have been present in the conventional tiling, given the restrictions placed on where edges may be removed from conventional tilings.

3. A 1–vertex is placed at the mid–point of all tile edge segments which connect 0–vertices.

4. All symmetry 'corners' in the interior of the tile with order > 2 are occupied by 2–vertices.

5. All other symmetry 'corners' in the interior of the tile (those with order ≤ 2) are occupied by $\bar{1}$–vertices. This defines all locations where edges may have been removed.

6. A 2–vertex is placed at the mid–point of all orbifold boundary segments in the interior of the tile which connect two $\bar{1}$–vertices.

7. The domain is triangulated where each triangle has a 0–vertex, a 2–vertex and either a 1–vertex or a $\bar{1}$–vertex.

For example, Fig. 2.7 part (a) shows a free tiling of $\mathbb{H}^2$ and part (b) shows the parent symbol of one asymmetric orbifold domain: this triangulation has two 0–vertices at the $*3$ and $*2$ mirror intersections on the tile boundary with a 1–vertex between, and two $\bar{1}$–vertices at each of the $*2$ mirror intersections in the interior of the tile and a 2–vertex between. The triangulation in the example exactly covers a single orbifold domain.

A further process must now take place to find the unique encoding, which is the simplest symbol related to the parent symbol. A simplification may be performed by removing chambers of the encoding (where possible). We then permute through all possible simplifications to find the simplest (and unique) encoding. As simplifications, we wish to remove chambers of the symbol such that we no longer have 0–vertices which are of degree–2 (those which do not lie at actual vertices of the free tiling), and also delete chambers such that we remove as many $\bar{1}$–vertices as possible.

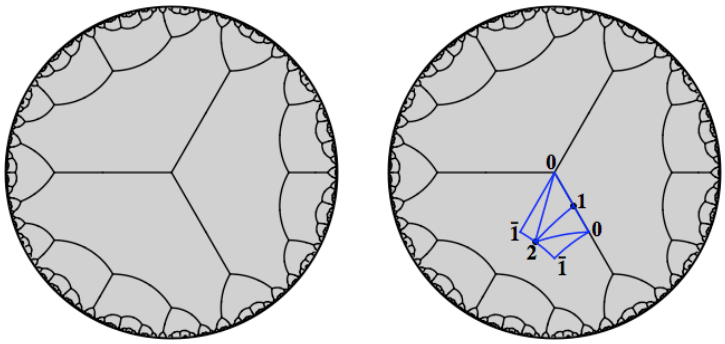

Figure 2.7: (a) A free tiling of $\mathbb{H}^2$. (b) The construction recipe dictates the placement of the vertices and chambers of the parent triangulation, where both $\bar{1}$–vertices are superfluous.

A $\bar{1}$–vertex is a candidate for removal when it is of degree–4 in the full triangulation of $\mathbb{H}^2$ or equivalently of degree-2 in the triangulation of a single orbifold domain, and it is neighboured by a 2–vertex that is not at a symmetry corner. For example, each of the $\bar{1}$–vertices in the parent symbol shown in Fig. 2.7 are candidates for removal. After the removal of a $\bar{1}$–vertex (and its associated edges), the neighbouring 2–vertex slides to the location of the past $\bar{1}$–vertex, and maintains all other connections. This decreases the number of chambers within the symbol by 1, yet the topology and symmetry of the free tiling which it describes is equivalent.

In a similar process, a 0–vertex that lies on an edge of the tiling and is not at a vertex of the tiling is a candidate for removal when it is neighboured by a 1–vertex not at a symmetry corner, and it is also of degree–4 in the full triangulation of $\mathbb{H}^2$ or equivalently of degree–2 in the triangulation of a single orbifold domain. The 0–vertex in the parent symbol shown in Fig. 2.7 is not a candidate for removal as it is of degree–3 in one orbifold domain of the triangulation. After the removal of a 0–vertex (and its associated edges), the neighbouring 1–vertex slides to the location of the past 0–vertex, and maintains all other connections. This process also decreases the number of chambers within the symbol by 1, yet the topology and symmetry of free tiling which it describes is equivalent.

These chamber removals are performed until there are no longer any candidate chambers for removal. It is at this stage that a unique simplest encoding is found. For example, consider the parent symbol shown in Fig. 2.7. Each of the $\bar{1}$–vertices of the encoding are candidates for removal: we note however, that once one is removed, the other is no longer suitable for removal, as its neighbouring 2–vertex will now be on a symmetry corner. We remove each of the $\bar{1}$–vertices, and examine the resulting encodings, as shown in Fig. 2.8.

After the initial chamber removal, the upper encoding in Fig. 2.8 has no further chambers which are suitable for removal. In the lower encoding, however, the 0–vertex of degree–2 is now a candidate for removal. The removal of this chamber, and the subsequent sliding of the 1–vertex gives a simpler encoding of the free tiling. This is the unique encoding of the free tiling.

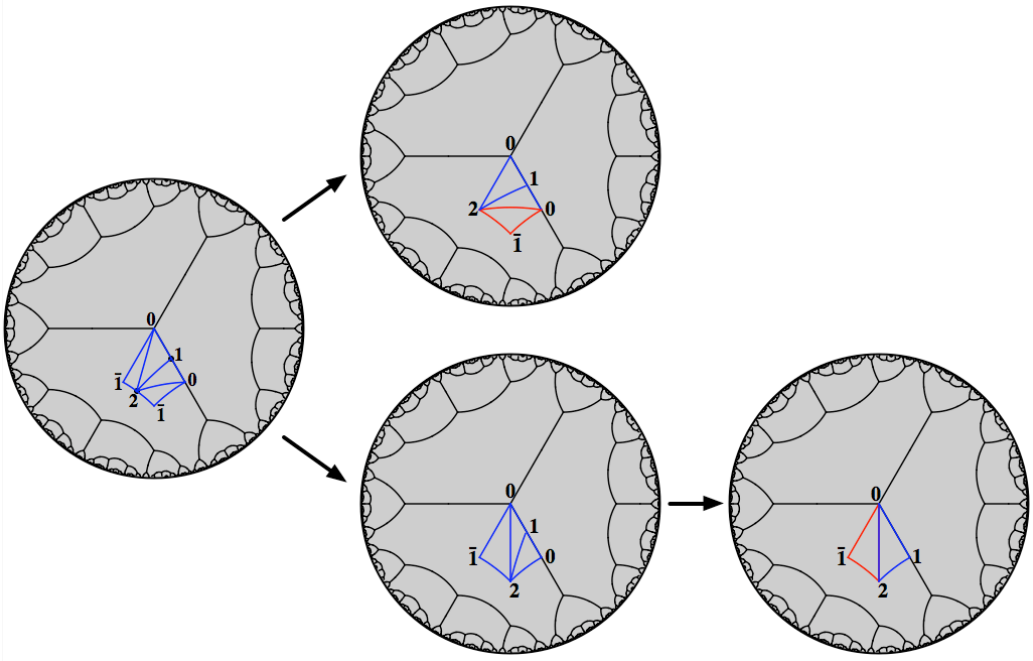

Figure 2.8: The parent symbol of a free tiling in $\mathbb{H}^2$ may be simplified in two ways, which give two distinct encodings. The upper encoding may not be simplified any further, yet the lower encoding may be further simplified by the removal of the 0–vertex of degree 2. This simplification leads to the unique encoding of the free tiling.

We document the encoding from the neighbour maps, as well as the orbits of the 0–vertices and 2–vertices of the chambers. To encode the missing edge, we must note the chamber with the 'ghost' edge. We do this by denoting all chambers with a real (not ghosted) edge in bold and the ghosted edge $\bar{1}$. Denote the chamber shown in blue '*A*' and that shown in red '*B*' to obtain the following tabular representation of the simplest encoding of the free tiling shown in Fig. 2.8:

Chamber Class	s0	s1	s2	m01	m12
A	**A**	B	**A**	4	6
B	B	**A**	B	4	6

2.2 Embedding orbifolds in the universal cover space

The Delaney–Dress symbol is an encoding of the topology and symmetry of a tiling, but not the geometry, for both conventional tilings and free tilings. This encoding is a decoration of an orbifold. An embedding of an orbifold assigns a presentation of the symmetry group encompassed by the orbifold in its universal cover, where a *presentation* is a way to define a group by listing a specific set of elements which generate the group plus a set of relations between the generators. It is trivial to interchange between orbifolds and symmetry groups by choosing a set of generators.

We explore the embedding of orbifolds of the form $*222k$, $2*2k$ and $222k$ in their universal cover. For Coxeter orbifolds, the orbifold is (by definition) bounded by mirrors. When embedded in the covering plane, the positions of the generators (the distinct mirrors) are set uniquely relative to each other as bounding an asymmetric patch. For "hat" orbifolds (with the form $2*2k$), the relative positions of the generators are uniquely set, which gives a unique embedding into the covering space. The uniqueness of this embedding is obvious if you consider the domain of two orbifolds doubled around the 2–fold rotation: this is a $*2k2k$ (Coxeter) domain, which we know uniquely embeds.

Stellate orbifolds have infinite freedom in the relative positions of the generators (rotations) in the covering plane (i.e. infinite scope in the presentation of the group). We wish to systematically generate all distinct presentations of the $222k$ group, so as to specify all distinct embeddings of the orbifold into the covering plane. We begin with the 2222 orbifold, which embeds in $\mathbb{E}^2$ by the orbifold cost formula: $C = 2 - \sum_i d_i = 2 - \left(\frac{1}{2} + \frac{1}{2} + \frac{1}{2} + \frac{1}{2}\right) = 0$.

Embedding the 2222 orbifold into $\mathbb{E}^2$ requires nominating four generating 2–fold rotation sites. Fig. 2.9(a) shows an embedding, where the generators are at the positions $\{0,0\}$, $\{1,0\}$, $\{1,1\}$ and $\{0,1\}$ of $\mathbb{E}^2$. This results in the set of all elements (not just the generators) of the infinite group being grid points in $\mathbb{Z} \times \mathbb{Z}$ (the two–dimensional integer grid: elements are represented by a couple $\{x,y\}$ where x and y are integers).

Given the reference frame established by the embedding in Fig. 2.9(a), distinct presentations of the same group may be obtained by expressing the generators as other elements of the group (i.e. other points in the plane) [Coxe 72]. Labelling the 2–fold rotations located at $\{0,0\}$, $\{1,0\}$, $\{1,1\}$ and $\{0,1\}$ as Q_T, Q_A, Q_B and Q_C respectively, presentation of the group given by the reference frame is

$$< \{Q_T, Q_A, Q_B, Q_C\} : (Q_A)^2 = (Q_B)^2 = (Q_C)^2 = (Q_T)^2 = I, Q_T = Q_A Q_B Q_C >$$

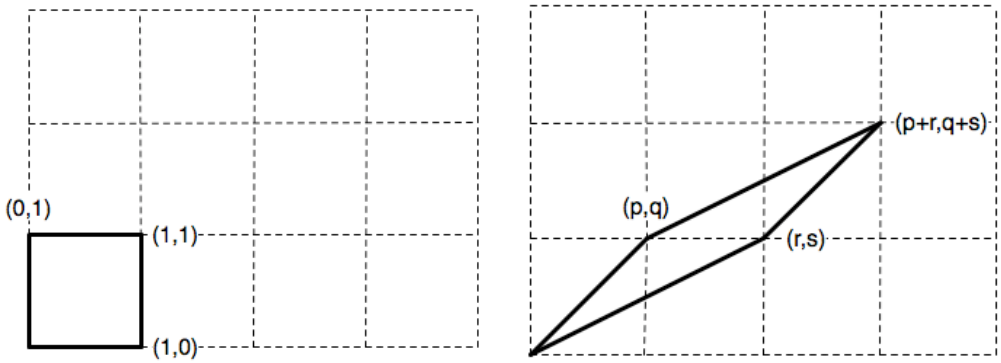

Figure 2.9: (a) An embedding of the 2222 orbifold in $\mathbb{E}^2$. The corners of the square coincide with the points $\{0,0\}$, $\{1,0\}$, $\{1,1\}$ and $\{0,1\}$, establishing a reference frame of $\mathbb{Z}\times\mathbb{Z}$ for subsequent embeddings (b) Another embedding of 2222 relative to the established reference frame.

A new presentation of the same symmetry group specifies generators Q'_T, Q'_A, Q'_B and Q'_C with respect to the reference frame such that the group relations are preserved. Thus we express the generators in terms of the original Q_T, Q_A, Q_B and Q_C.

The set of possible presentations may be represented through parallelograms on $\mathbb{Z}\times\mathbb{Z}$. To reduce duplication of embeddings, we begin by considering only one quadrant of $\mathbb{E}^2$ and we pin the 2–fold rotation Q_T in place, so as to eliminate the possibility of constructing a domain of equivalent shape translated by some vector. We require that the only isometries of the parallelograms are the 2–fold rotations at the corners and that the enclosed area must be 1 (area equivalent to the square in the reference frame embedding), as all cuttings of the orbifold must span the same area. These restrictions are equivalent to satisfying the group relations for a presentation. Note also that this domain is the area enclosed by the four distinct 2–fold rotations, and that a full 2222 symmetry group is double this quadrilateral over any of its edges, where this full domain has area exactly 2 units.

As an example, Fig. 2.9(b) shows a unit area parallelogram on $\mathbb{Z}\times\mathbb{Z}$ with corners $\{0,0\}$, $\{r,s\}$, $\{p+r,q+s\}$ and $\{p,q\}$. Each grid point in the plane represents elements of the infinite group, hence we may express the corner points of the parallelogram (with respect to the reference frame) as:

$$Q'_A = Q_B Q_C Q_B \qquad Q'_C = Q_B$$
$$Q'_B = Q_B Q_C Q_B Q_A Q_B Q_C Q_B \qquad Q'_T = Q_T$$

It is simple to show that the group relations $(Q'_A)^2 = (Q'_B)^2 = (Q'_C)^2 = (Q'_T)^2 = I$ are

satisfied for these new generators. The other group relation, where $Q'_A Q'_B Q'_C$ must be equal to Q'_T, is also satisfied by these elements (working shown below), hence the generators Q'_T, Q'_A, Q'_B and Q'_C are a presentation of the symmetry group of the 2222 orbifold.

$$\begin{aligned}
Q'_A Q'_B Q'_C &= Q_B Q_C (Q_B Q_B) Q_C Q_B Q_A Q_B Q_C (Q_B Q_B) \\
&= Q_B (Q_C Q_C) Q_B Q_A Q_B Q_C && \textit{using } (Q_B)^2 = I \\
&= (Q_B Q_B) Q_A Q_B Q_C && \textit{using } (Q_C)^2 = I \\
&= Q_A Q_B Q_C && \textit{using } (Q_B)^2 = I \\
&= Q_T \\
&= Q'_T
\end{aligned}$$

Enumeration of all such embeddings of parallelograms of unit area in $\mathbb{Z} \times \mathbb{Z}$ may be thought of as a 3–parameter family: the 5 parameters $\{p,q\}$, $\{r',s'\}$ and k, reduce to 3 when the area of the parallelogram is expressed as $ps' - r'q = 1$. To ensure that no additional symmetry points are located on the boundary of the parallelogram, the $\{p,q\}$ (or Q'_C) corner of the parallelogram is chosen such that $\{p,q\}$ are coprime. One solution of the other corner of the parallelogram, $\{r',s'\}$ (or Q'_A) is chosen such that the parallelogram has unit area. For a given $\{p,q\}$, the full set of solutions for the other corner is $\{r,s\} = \{r',s'\} + k\{p,q\}$. This 3–parameter family describes all embeddings of 2222 into a discretised $\mathbb{E}^2$.

The orbifold 2223 has $\mathbb{H}^2$ as the universal cover, as given by the cost formula:

$$C = 2 - \sum_i d_i = 2 - \left(\frac{1}{2} + \frac{1}{2} + \frac{1}{2} + \frac{2}{3}\right) = -\frac{1}{6}$$

Begin by choosing an embedding of the orbifold to be a reference frame in $\mathbb{H}^2$, nominating four generators to present the symmetry group: Q_T, Q_A, Q_B and Q_C. Consider the quadrilateral formed by connecting the four generating elements of the group (Fig. 2.10(a)), establishing a reference frame and discrete infinite grid.

The group relations for the 2223 symmetry group are given by

$$< \{Q_T, Q_A, Q_B, Q_C\} : (Q_A)^2 = (Q_B)^2 = (Q_C)^2 = (Q_T)^3 = I, Q_T = Q_A Q_B Q_C >$$

Fig. 2.10(b) shows a quadrilateral whose four corner points are elements of the infinite group 2223. To establish if the corner points represent generators of the group, and hence

if the quadrilateral is a valid presentation of the group, we consider the group relations. The corner points of the quadrilateral may be expressed as:

$$\begin{aligned} Q'_T &= Q_T \\ Q'_A &= Q_B Q_C Q_B \\ Q'_B &= Q_B Q_C Q_B Q_A Q_B Q_C Q_B \\ Q'_C &= Q_B \end{aligned}$$

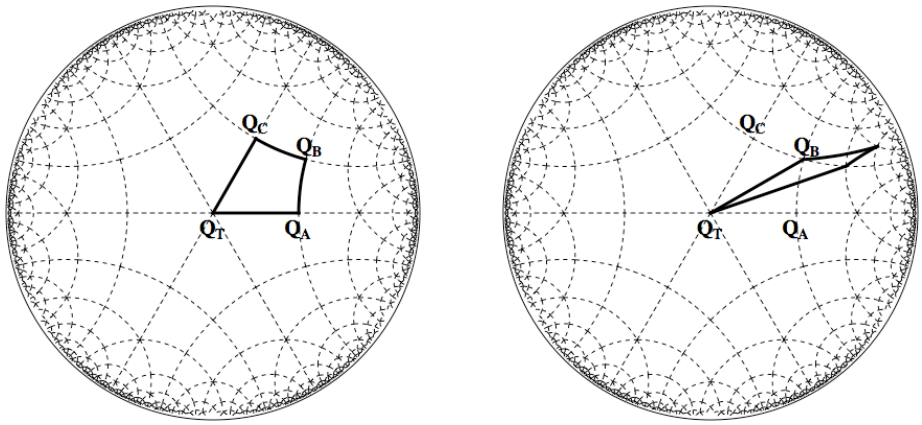

Figure 2.10: (a) An embedding of the 2223 orbifold into $\mathbb{H}^2$. The corners of the quadrilateral are a reference frame grid for other embeddings. (b) A subsequent embedding of the 2223 orbifold into $\mathbb{H}^2$ relative to the reference frame established previously.

It is straightforward to see that the group relations $(Q'_A)^2 = (Q'_B)^2 = (Q'_C)^2 = (Q'_T)^3 = I$ are satisfied for these elements. The other group relation, where $Q'_A Q'_B Q'_C$ must be equal to Q'_T, is also satisfied, with working shown below, and hence the quadrilateral shown is a valid embedding of the 2223 orbifold in $\mathbb{H}^2$ given the reference frame.

$$\begin{aligned} Q'_A Q'_B Q'_C &= Q_B Q_C (Q_B Q_B) Q_C Q_B Q_A Q_B Q_C (Q_B Q_B) \\ &= Q_B (Q_C Q_C) Q_B Q_A Q_B Q_C && \text{using } (Q_B)^2 = I \\ &= (Q_B Q_B) Q_A Q_B Q_C && \text{using } (Q_C)^2 = I \\ &= Q_A Q_B Q_C && \text{using } (Q_B)^2 = I \\ &= Q_T \\ &= Q'_T \end{aligned}$$

To enumerate possible embeddings, we determine possible locations of the Q'_C generator with respect to the reference frame: the analogue of finding the coprime $\{p,q\}$ vertex of the parallelogram. We fix the Q_T generator as an origin, and consider a $\frac{\pi}{3}$ sector of the plane, as all others will be equivalent by symmetry (as was the case for the $\frac{\pi}{2}$ sector of 2222 in $\mathbb{E}^2$). The edge from the origin to Q'_C must not intersect any image of itself.

Consider a 3–fold rotation site, ▲$_0$, in Fig. 2.11(a) to be at the origin, along with an image of the origin by a 2–fold operation, shown as the 3–fold rotation site ▲$_1$. Any geodesic ray from the origin (whose end will be the location of Q'_C) will have exactly three copies radiate from ▲$_1$, one in each of the sectors W_1, W_2 and W_3. If Q'_C (the end of the geodesic ray) is placed in the sector W_3, as shown by the blue geodesic in Fig. 2.11(b), it certainly intersects an image of itself radiating from ▲$_1$. This prohibits the placement of Q'_C in the sector W_3.

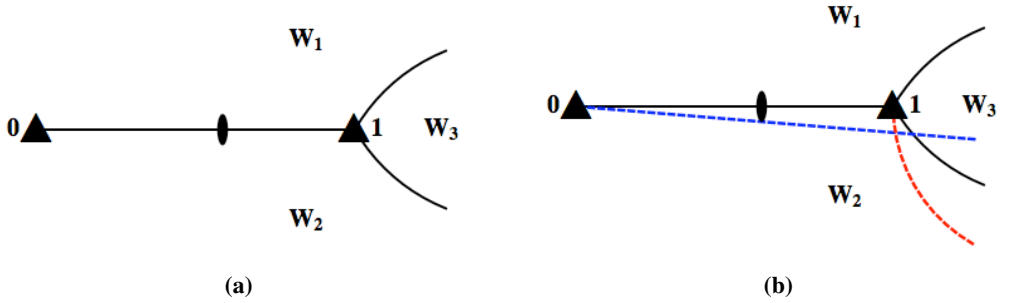

Figure 2.11: (a) The configuration of the 3–fold rotation at the origin (▲$_0$) and an image (▲$_1$), where ▲$_1$ divides $\mathbb{H}^2$into three sectors, W_1, W_2 and W_3. (b) If Q'_C (the end of the blue geodesic) is located in the W_3 sector, the edge from the origin to Q'_C (the blue geodesic) will certainly intersect an image of itself, as shown by the red geodesic.

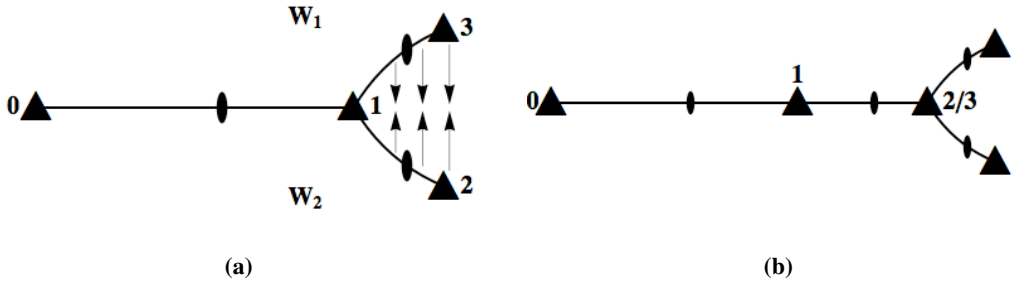

Figure 2.12: (a) The sector W_3 can be excised and the boundary sewn together to form a boundary free plane. (b) The result is a line of 2–fold rotations, terminating at a new 3–fold rotation. Repeating the cutting process further removes territory from where Q'_C is prohibited.

We then remove this prohibited sector (to infinity) from $\mathbb{H}^2$. Fig. 2.12(a) shows how

we may then sew up the remaining boundary to make the space boundary free once again. The result is shown in Fig. 2.12(b), the 3–fold rotation $\blacktriangle_1$ has now become a 2–fold rotation, and the 3–fold rotations $\blacktriangle_2$ and $\blacktriangle_3$ have been joined. By use of the same argument on this new configuration, further W_3 sectors of the plane can excised and the boundary sewn, resulting in an infinite line of 2–fold rotations on a boundary free plane. These prohibited sectors are shown on the 2223 discretisation of $\mathbb{H}^2$ in Fig. 2.13.

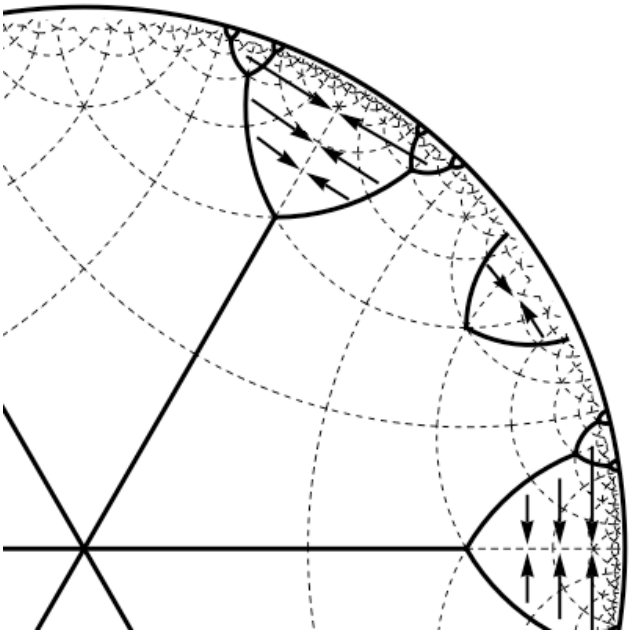

Figure 2.13: Prohibited sectors of the 2223 discretisation of $\mathbb{H}^2$ are shown. There are infinitely many prohibited sectors, located at every 3–fold rotation of the discretisation, where only three such sectors are shown here. The remaining 'allowed" section is a Euclidean subdomain of $\mathbb{H}^2$.

Reducing every 3–fold rotation of the discretisation of $\mathbb{H}^2$ to a 2–fold rotation transforms the discretisation to exactly the 2222 symmetry group, hence, by the orbifold cost formula, we are left with a discretisation of $\mathbb{E}^2$. The removal of sectors of the Hyperbolic plane and subsequent sewing of the boundaries has resulted in exactly a boundary free Euclidean plane.

By only removing territory in which the Q'_C location is prohibited, we have shown that the scope of possible locations of Q'_C are in a Euclidean subset of $\mathbb{H}^2$, discretised by exactly $\mathbb{Z} \times \mathbb{Z}$. The same geometric argument may be used to show that the edge from the origin to Q'_A is also limited to also lie within $\mathbb{E}^2$ discretised by $\mathbb{Z} \times \mathbb{Z}$. The location of Q'_B is then completely determined by Q'_A and Q'_C.

As a result of this ordered Euclidean subdomain of $\mathbb{H}^2$, we may index all possible

quadrilateral domains of the 2223 orbifold exactly by embeddings of parallelograms of unit area in $\mathbb{Z}\times\mathbb{Z}$. Fig. 2.14 shows the $\mathbb{Z}\times\mathbb{Z}$ grid within a $\frac{\pi}{3}$ sector of the discretisation of $\mathbb{H}^2$ by the 2223 reference frame embedding.

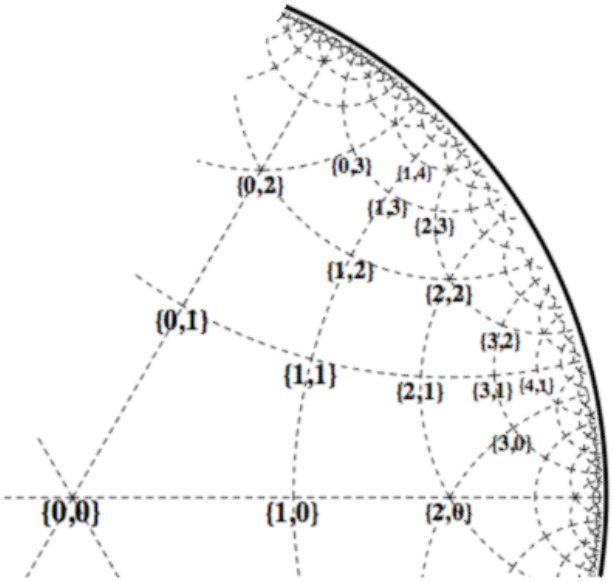

Figure 2.14: The positioning of the grid points of $\mathbb{Z}\times\mathbb{Z}$ in a $\frac{\pi}{3}$ sector of 2223 discretisation of $\mathbb{H}^2$.

An equivalent process may be applied to any 222k discretisation of $\mathbb{H}^2$. The rotational symmetry at each k–fold vertex always restricts the location of the Q'_C generator to be within the adjacent sector, and hence any 222k discretisation of $\mathbb{H}^2$ has an allowed sub-domain for the embedding of the orbifold that is equivalent to the 2222 discretisation of $\mathbb{E}^2$ within a $\frac{2\pi}{k}$ sector.

2.3 Embedded tilings commensurate with TPMS

Reticulation patterns of a TPMS must be commensurate with the sub–symmetries of the chosen surface. The 2D asymmetric patch of each of the P, D and G surfaces is a triangle bounded by in–surface mirrors meeting at angles of $\pi/2$, $\pi/4$ and $\pi/6$ at the corners of the patch. The asymmetric patch corresponds to a single $*246$ triangle uniquely embedded in $\mathbb{H}^2$, whose generators are mirrors R_1, R_2 and R_3: the reflection R_1 maps across the line passing from $*6$ though $*2$ vertices, R_2 from $*2$ through $*4$ vertices and R_3 from $*6$ through $*4$ vertices [Robi 04a, Moln 02]. The infinite $*246$ pattern is shown in Fig. 2.15(a). Similarly for the H surface, the smallest asymmetric patch of the surface is a quadrilateral bounded by in–surface mirrors meeting at angles of $\pi/6$, $\pi/2$, $\pi/2$ and $\pi/2$ at each of the

corners [Robi 04b]. This has hyperbolic orbifold $*2226$, and one example of this orbifold is shown in the universal cover of the H surface ($\mathbb{H}^2$) in Fig. 2.15(b).

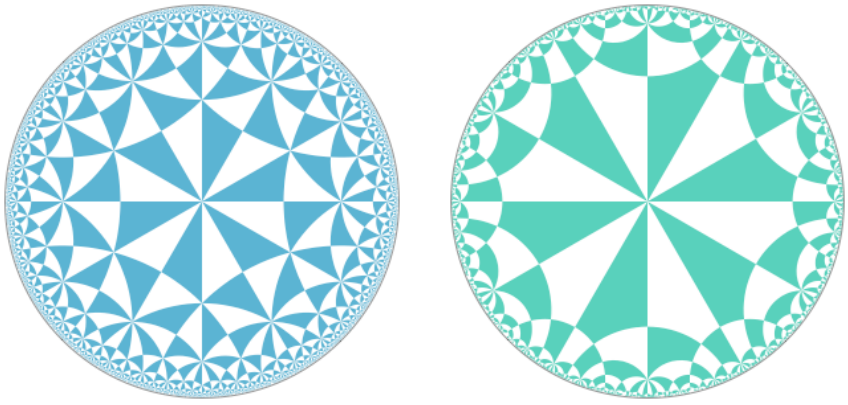

(a) **(b)**

Figure 2.15: $*246$ and $*2226$ tilings represented on the Poincaré Disc model of $\mathbb{H}^2$. The tilings are coloured by an orientation preserving subgroup.

The H surface has a degree of freedom corresponding to a deformation of the surface along the z–axis (variation of the ratio of a to c in the lattice parameters) [Hyde 03b]. This gives a degree of freedom in the asymmetric patch, and a degree of freedom in the $*2226$ tiling of $\mathbb{H}^2$. The $*2226$ tile in $\mathbb{H}^2$ can be divided into two triangles, with the first having angles $\pi/6$, α and β, and the second having angles $\pi/2-\alpha$, $\pi/2-\beta$ and $\pi/2$. The angles α and β are related using hyperbolic trigonometric identities to give:

$$\frac{cos(\alpha)cos(\beta)+cos(\pi/6)}{sin(\alpha)sin(\beta)} = \frac{sin(\alpha)sin(\beta)}{cos(\alpha)cos(\beta)}$$

This results in a one–parameter family of asymmetric domains for $*2226$ [Hyde 03b], given by the following association:

$$cos(\alpha) = \sqrt{1-\frac{13}{16}cos^2(\beta)} - \frac{\sqrt{3}}{4}cos(\beta)$$

Surface reticulations are also chosen adhere to the translational symmetries of the TPMS: "$\circ\circ\circ$" (in Conway's notation), as one primitive unit cell of the oriented (coloured) TPMS has integral curvature -8π, which corresponds to genus–3 with gluings. In doing so, we ensure that reticulations are continuous over the primitive unit cell boundaries, and also display all translations of the TPMS [Rams 09, Robi 04a, Robi 04b].

The combination of these symmetry requirements restricts possible reticulations of

the surfaces to come from particular decorated orbifolds. Specifically, reticulation of the *P*, *D* and *G* surfaces must have decorated orbifolds within the quotient group $*246/\circ\circ\circ$: the orbifold must be a subgroup of $*246$, yet always contain $\circ\circ\circ$ symmetries. The 131 possible orbifolds has been enumerated [Robi 04a], and this list of numbered groups are presented in Appendix A. Likewise, reticulations of the *H* surface must have decorated orbifolds within the quotient group $*2226/\circ\circ\circ$: the orbifold must be a subgroup of $*2226$, yet always contain $\circ\circ\circ$ symmetry. The 32 possible orbifolds commensurate with the *H* surface are also enumerated [Robi 04b], and this numbered list is also presented in Appendix A.

Before embedding with a commensurate symmetry, we must consider our final goal: structures in $\mathbb{E}^3$. Where two reticulations of a single TPMS are related by an intrinsic surface symmetry which lifts to a Euclidean isometry of 3D space, they are called conjugates, and we wish to consider only one representative within a conjugacy class. In hyperbolic terms, this indicates that tilings of $\mathbb{H}^2$ that are related by a symmetry of the underlying surface tiling ($*246$ or $*2226$) are considered within the same conjugacy class. An example of two tilings of $\mathbb{H}^2$ that are related by a symmetry of $*246$, and will give equivalent surface frameworks, is shown in Fig. 2.16.

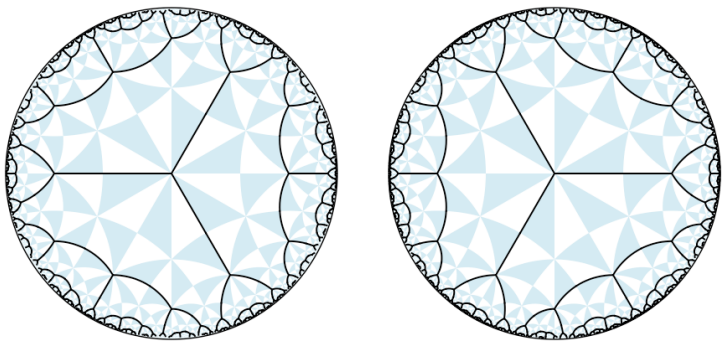

Figure 2.16: Two free tilings with symmetry $*2223$ (group 124 [Robi 04a]) that are related by a reflection of the $*246$ tiling shown behind the tiling. These tilings fall within the same conjugacy class, and they give equivalent frameworks on the TPMS.

The embedding into $*246$ or $*2226$ requires us to express the reference frame generators of the group in terms of the generators of the underlying tiling. For Coxeter and Hat orbifolds, we must take into account automorphic embeddings of the orbifold. An automorphism of an orbifold is an abstract symmetry of the orbifold. Where the automorphism of an embedded orbifold is not a symmetry within the underlying tiling, automorphic em-

beddings of a tiling, which are images of each other through the abstract symmetry, will give distinct surface patterns. An example of two automorphic embeddings of the ∗2224 orbifold, which gives two distinct tilings not related by a symmetry of ∗246, is shown in Fig. 2.17. For Stellates, enumeration of embedded parallelograms into the reference frame accounts for all automorphic embeddings.

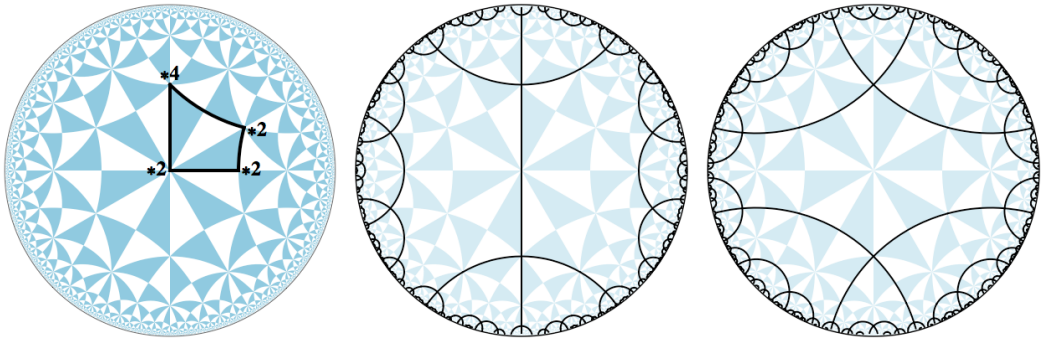

Figure 2.17: (a) Unique embedding of the ∗2224 (group 123 [Robi 04a]) orbifold into the ∗246 tiling, where the abstract symmetry of the orbifold is now asymmetrised. (b,c) Two regular ribbon tilings related by an automorphism of ∗2224.

Regular ribbon tilings and their complements

A *regular ribbon tiling* is a tiling by infinite ribbons that has 1–transitive edges (one type of tile edge), 1–transitive vertices (one type of tile vertex) and 1–transitive tiles (one type of tile face). A *complementary* tiling, related to a regular ribbon tiling, has tile vertices and faces interchanged, and edges interchanged with ghosted edges. Complementary tilings are equivalent to regular, dense forests in alternative nomenclature [Hyde 00a][1]. This terminology is compatible with that for standard tilings.

In a regular ribbon tiling, 1–transitive edges imply that the degree–3 vertex of the tile boundary must have either 3–fold symmetry or ∗3 symmetry. Further, 1–transitive vertices indicate that an edge must have a midpoint at either a 2–fold rotation or ∗2 site. The translation within a tile may be defined by some combination of ∗2 symmetries, 2–fold rotations, '○' or '×'. Of the groups within the ∗246/○○○ quotient group, 4 groups fit these criteria: ∗2223 (group 124), 2∗23 (group 129), 2223 (group 118), and 23× (group 121). We find that simple decorations, such as regular ribbon tilings, on the 23× orbifold

[1] Regularity is an equivalent term in the two schema: *i.e.* in a dense forest, the tile between neighbouring trees is a ribbon.

has increased symmetry of $2*23$ (a supergroup of $23\times$), thus we disregard decorations of this orbifold. We consider regular ribbon tilings and their complements on the three remaining orbifolds, and their embedding into the $*246$ chart of $\mathbb{H}^2$.

The abstract orbifold $*2223$ supports a regular ribbon tiling with a decorative edge passing from the $*3$ location along the mirror boundary to a $*2$ site. The decoration has boundary vertices at the $*3$ corner, edge midpoints at the $*2$ corner, and an infinite translation generated by the parallel mirrors of the remaining two $*2$ corners. This decoration is shown in Fig. 2.18 along with a table representing its Delaney–Dress encoding. We refer to this tiling by the name 124*R*: the **R**egular ribbon tiling of group 124.

Chamber Class	s0	s1	s2	m01	m12
A	**A**	B	**A**	4	6
B	B	**A**	B	4	6

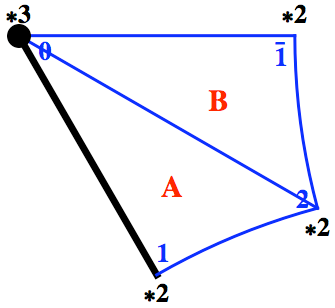

Figure 2.18: The Delaney–Dress representation of a regular ribbon tiling on the $*2223$ orbifold: 124*R*. The edge passes along the mirror boundary from the $*3$ site to the $*2$ site.

The complement of the regular ribbon tiling on $*2223$ interchanges the 0–vertex and 2–vertex sites of the triangulation as well as the 1–vertex and $\bar{1}$–vertex sites. This process swaps the boundaries of the tiles with the infinite translation axes of the tiles. The Delaney–Dress encoding of the complementary regular ribbon tiling of $*2223$ is shown in Fig. 2.19. We call this tiling 124*C*: the **C**omplementary tiling of group 124.

Chamber Class	s0	s1	s2	m01	m12
A	A	**B**	A	6	4
B	**B**	A	**B**	6	4

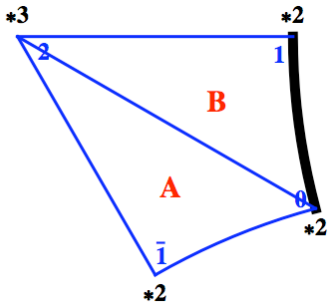

Figure 2.19: The Delaney–Dress coding of the complementary tiling on the $*2223$ orbifold: 124*C*. It is obtained by interchanging the 0–vertex and 2–vertex sites and the 1–vertex and $\bar{1}$–vertex sites of the regular ribbon tiling.

The $*2223$ orbifold has a unique embedding into the $*246$ chart of the *P*, *D* and *G* sur-

faces [Robi 04a], but is not commensurate with the ∗2226 chart of the *H* surface [Robi 04b]. This embedded orbifold is composed of exactly two ∗246 triangles, glued along R_3 (the mirror passing from ∗6 to ∗4). This amalgamated domain has two ∗2 vertices from the original two triangles, an additional ∗2 vertex from a gluing of two ∗4 vertices, and a ∗3 vertex from a gluing of two ∗6 vertices. One fundamental domain of the ∗2223 orbifold embedded in the ∗246 is shown in Fig. 2.20(a).

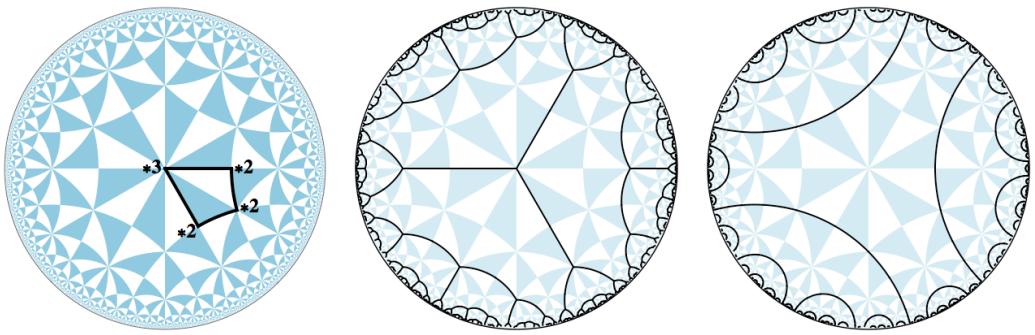

Figure 2.20: (a) The embedding of the ∗2223 orbifold in the ∗246 tiling of $\mathbb{H}^2$: two ∗246 triangles fused along an R_3 boundary. (b) $*246_{124R}$, the embedded regular ribbon tiling of ∗2223. (c) $*246_{124C}$, the embedding of the complementary regular ribbon tiling on ∗2223.

The ∗2223 orbifold has an abstract symmetry (automorphism) along the axis passing from the ∗3 vertex to the opposite ∗2 vertex. Once the orbifold is embedded, however, this abstract symmetry aligns with the R_3 reflection of the ∗246 chart: the automorphism of the orbifold corresponds to a conjugacy of the ∗246 map, so we need only consider one form. The embedded regular ribbon tiling from Fig. 2.18 and the embedding of the complementary tiling represented in Fig. 2.19 are shown in Fig. 2.20(b,c) respectively. The interchange of the tile boundary for the medial axis, the axis of points with more than one closest edge, is apparent. We refer to these embedded tilings by the names $*246_{124R}$ and $*246_{124C}$, symbolising the 124*R* and 124*C* tilings embedded in the ∗246 tiling of $\mathbb{H}^2$.

The orbifold $2*23$ (group 129) contains a 2–fold cone point (the peak of the hat, as shown in Fig. 2.2(b)), with the open brim consisting of two mirrors intersecting each other at two points, one intersection with an angle of $\frac{\pi}{2}$ and the other $\frac{\pi}{3}$. A regular ribbon tiling with a degree–3 vertex and symmetry $2*23$ has an edge passing from the ∗3 site along the mirror boundary to the ∗2 site. This decoration and information can be represented by a Delaney–Dress triangulation of the orbifold (Fig. 2.21), and is called 129*R*. Tiling 129*C* is the complement of this tiling, representing an interchanging of the tile boundaries for the

medial axes. The Delaney–Dress encoding of 129*C* is shown in Fig. 2.22.

Chamber Class	s0	s1	s2	m01	m12
A	**A**	B	**A**	3	9
B	C	**A**	C	3	9
C	B	C	B	3	9

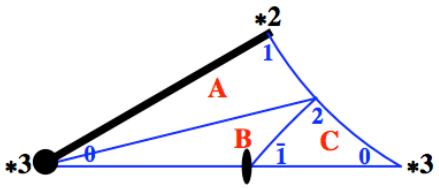

Figure 2.21: The regular ribbon tiling of the $2*23$ orbifold. The decoration passes from the $*3$ site, along the mirror boundary, to the $*2$ site. This tiling is referred to by the label 129*R*.

Chamber Class	s0	s1	s2	m01	m12
A	A	**B**	A	9	3
B	**C**	A	**C**	9	3
C	**B**	**C**	**B**	9	3

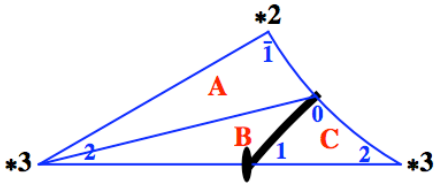

Figure 2.22: The complement of the regular ribbon tiling on $2*23$, 129*C*. The edge passes from the 2–fold rotation to the mirror boundary, incident at right angles. The edge would continue to a copy of the 2–fold rotation in the neighbouring domain.

The $2*23$ orbifold embeds uniquely in $*246$ (Fig. 2.23(a)). The automorphism of the $2*23$ orbifold (an abstract mirror symmetry on the axes passing from the$*3$vertex to the 2–fold rotation) is a conjugacy of the $*246$ tiling: we need only consider a single automorphic embedding of the orbifold. Fig. 2.23(b) and (c) show the embedding of the regular ribbon tiling with $2*23$ symmetry (Fig. 2.21) and the complementary tiling (Fig. 2.22) respectively. We call these two embedded tilings $*246_{129R}$ and $*246_{129C}$, as they are embedded in the $*246$ tiling of $\mathbb{H}^2$.

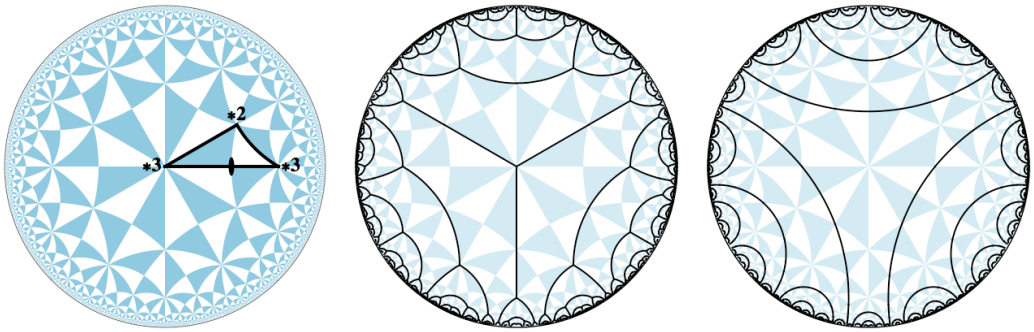

(a) **(b)** **(c)**

Figure 2.23: (a) The unique embedding of the $2*23$ orbifold into the $*246$ tiling of $\mathbb{H}^2$. (b) The embedded regular ribbon tiling with symmetry $2*23$ (Fig. 2.21). (c) The embedded complement of a regular ribbon tiling with symmetry $2*23$ (Fig. 2.22).

A regular ribbon tiling is also supported by the 2223 Stellate orbifold (group 118). The orbifold is decorated by an edge passing from the 3–fold rotation to a 2–fold rotation. Fig. 2.24 shows the regular ribbon tilings tabular representation along with an image of the decorated orbifold, cut open to lay (somewhat) flat. This tiling is referred to as 118*R*. Fig. 2.25 shows the Delaney–Dress representation of the complementary regular ribbon tiling with 2223 symmetry, known as 118*C*.

Chamber Class	s0	s1	s2	m01	m12
A	**D**	B	**D**	4	6
B	C	**A**	C	4	6
C	B	**D**	B	4	6
D	**A**	C	**A**	4	6

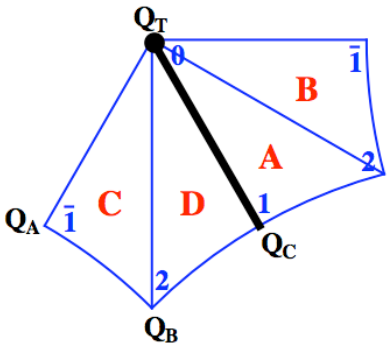

Figure 2.24: Representation of the regular ribbon tiling on the 2223 orbifold. The 2–folds are at Q_A, Q_B and Q_C, the 3–fold is at Q_T. The edge is from Q_T to Q_C.

Chamber Class	s0	s1	s2	m01	m12
A	D	**B**	D	6	4
B	**C**	A	**C**	6	4
C	**B**	D	**B**	6	4
D	A	**C**	A	6	4

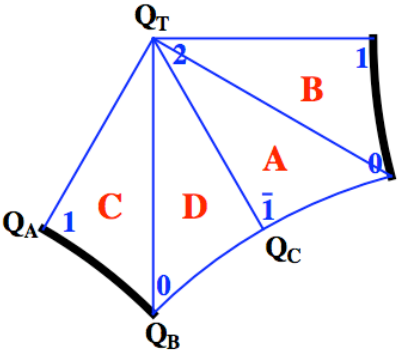

Figure 2.25: Encoding of the complementary regular ribbon tiling on 2223. The 2–folds are at Q_A, Q_B and Q_C, and the 3–fold is Q_T. The edge is from Q_A to Q_B.

The distinct embeddings of the 2223 Stellate orbifold into the $*246$ chart of $\mathbb{H}^2$ discussed in Section 2.2, decorated by the free tilings given in Fig. 2.24 and Fig. 2.25, produce distinct embedded decorations of $\mathbb{H}^2$. The positions of the reference frame generators Q_T, Q_A, Q_B and Q_C in the $*246$ chart are shown in Fig. 2.26. The full fundamental domain, as given in the Delaney–Dress representations of the abstract tilings, may be obtained by doubling the quadrilateral joining the generators across the line joining Q_T and Q_C.

Distinct embeddings of the decorated orbifold into $*246$ directly correspond to embedded parallelograms of unit area in the $\mathbb{Z} \times \mathbb{Z}$ discretisation of $\mathbb{E}^2$. Fig. 2.27 shows two

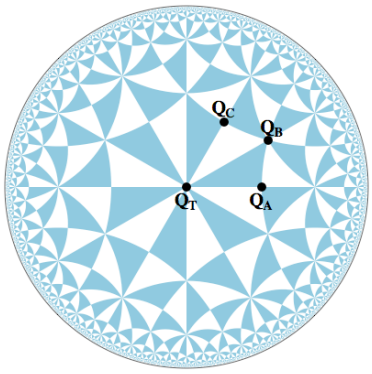

Figure 2.26: The locations of the reference frame generators of the 2223 symmetry group in the $*246$ tiling of $\mathbb{H}^2$.

decorations resulting from the embedding of the 2223 orbifold corresponding to the unit area parallelogram with vertex at the origin, $\{p,q\} = \{0,1\}$ and $\{r,s\} = \{1,0\}$. Additional symmetry is induced in the tiling by the embedding: these tilings have symmetry $*2223$, and are equivalent to those constructed on the $*2223$ orbifold (Fig. 2.20), namely embedded tilings $*246_{124R}$ and $*246_{124C}$.

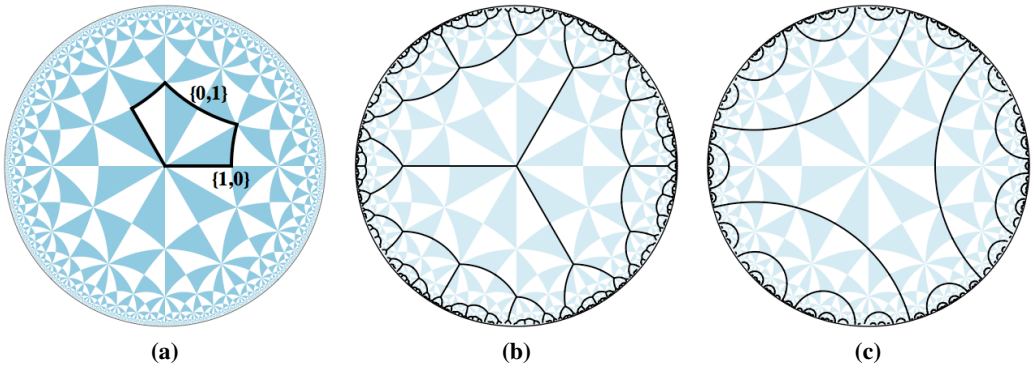

Figure 2.27: (a) An embedded 2223 fundamental domain into $*246$, where Q'_C and Q'_A are located at $\{0,1\}$ and $\{1,0\}$ respectively (see Fig. 2.14 for coordinate grid). This embedding in analogous to a parallelogram in $\mathbb{E}^2$with $\{p,q\}$=$\{0,1\}$ and $\{r,s\}$=$\{1,0\}$. (b) The embedded regular ribbon tiling. (c) The embedded complementary tiling. Both have increased symmetry of $*2223$, equivalent to the tilings shown in Fig. 2.20, namely embedded tilings $*246_{124R}$ and $*246_{124C}$.

Fig. 2.28 shows the decorations resulting from an embedding of the 2223 orbifold indexed by the $\mathbb{E}^2$ parallelogram $\{p,q\} = \{1,1\}$ and $\{r,s\} = \{1,0\}$. Additional symmetry is induced by the embedding, hence these tilings are equivalent to those constructed as decorations of the $2*23$ orbifold (Figs. 2.23), which are embedded tilings $*246_{129R}$ and $*246_{129C}$. Altering the values of r and s for embedded regular ribbon tilings and complements leaves both of the decorations unchanged.

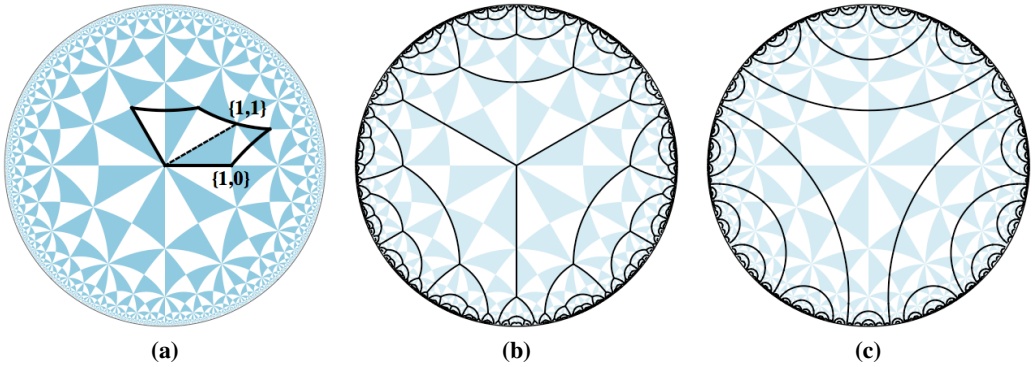

Figure 2.28: (a) An embedding of the 2223 domain into $*246$, where Q'_C and Q'_A are located at $\{1,1\}$ and $\{1,0\}$ respectively. (b) The embedded regular ribbon tiling. (c) The embedded complementary tiling. This embedding has additional symmetries, equivalent to those constructed on the orbifold $2*23$ (Fig. 2.23), namely $*246_{129R}$ and $*246_{129C}$.

For all other embeddings, 2223 will be the maximal symmetry group of the tiling. Where the maximal symmetry of the free tiling is 2223, the free tiling is given the name $*246_{118R}(n)$ or $*246_{118C}(n)$. The variable n ranges from 1 to ∞, and the free tiling is given a value of n based on its relative edge length in $\mathbb{H}^2$: the embedding which has 2223 maximal symmetry and the shortest possible tile edge length of all embeddings will have $n = 1$, the second shortest edge length $n = 2$, *et cetera*. Fig. 2.29 shows example decorations from several embeddings of 2223, indexed by distinct parallelograms of $\mathbb{E}^2$. The three parallelograms, as well as the embedded tiling names are:

1. $\{p,q\} = \{2,1\}$ and $\{r,s\} = \{1,0\}$: $*246_{118R}(1)$ and $*246_{118C}(1)$ (Fig. 2.29(b,c))
2. $\{p,q\} = \{3,1\}$ and $\{r,s\} = \{1,0\}$: $*246_{118R}(2)$ and $*246_{118C}(2)$ (Fig. 2.29(e,f))
3. $\{p,q\} = \{3,2\}$ and $\{r,s\} = \{1,1\}$: $*246_{118R}(3)$ and $*246_{118C}(3)$ (Fig. 2.29(h,i))

As the choice of parallelograms become increasingly oblique (i.e. the tiling approaches $*246_{118R}(\infty)$ and $*246_{118C}(\infty)$), the tilings approach a degenerate case of a set of star graphs with a vertex and three infinite edges in the ribbon tiling case, and a set of asymptotic triangles in the complementary tiling case. Some of these embedded free tilings were studied previously [Hyde 00a]. There are an infinite number of embeddings of the decorated 2223 orbifold into the $*246$ chart of $\mathbb{H}^2$, where these may be indexed by embedded parallelograms of $\mathbb{E}^2$. We have shown the three free tilings which result from the three embeddings with the shortest tile edge lengths in $\mathbb{H}^2$, and the methodology presented may be used to further enumerate all embeddings, if so desired.

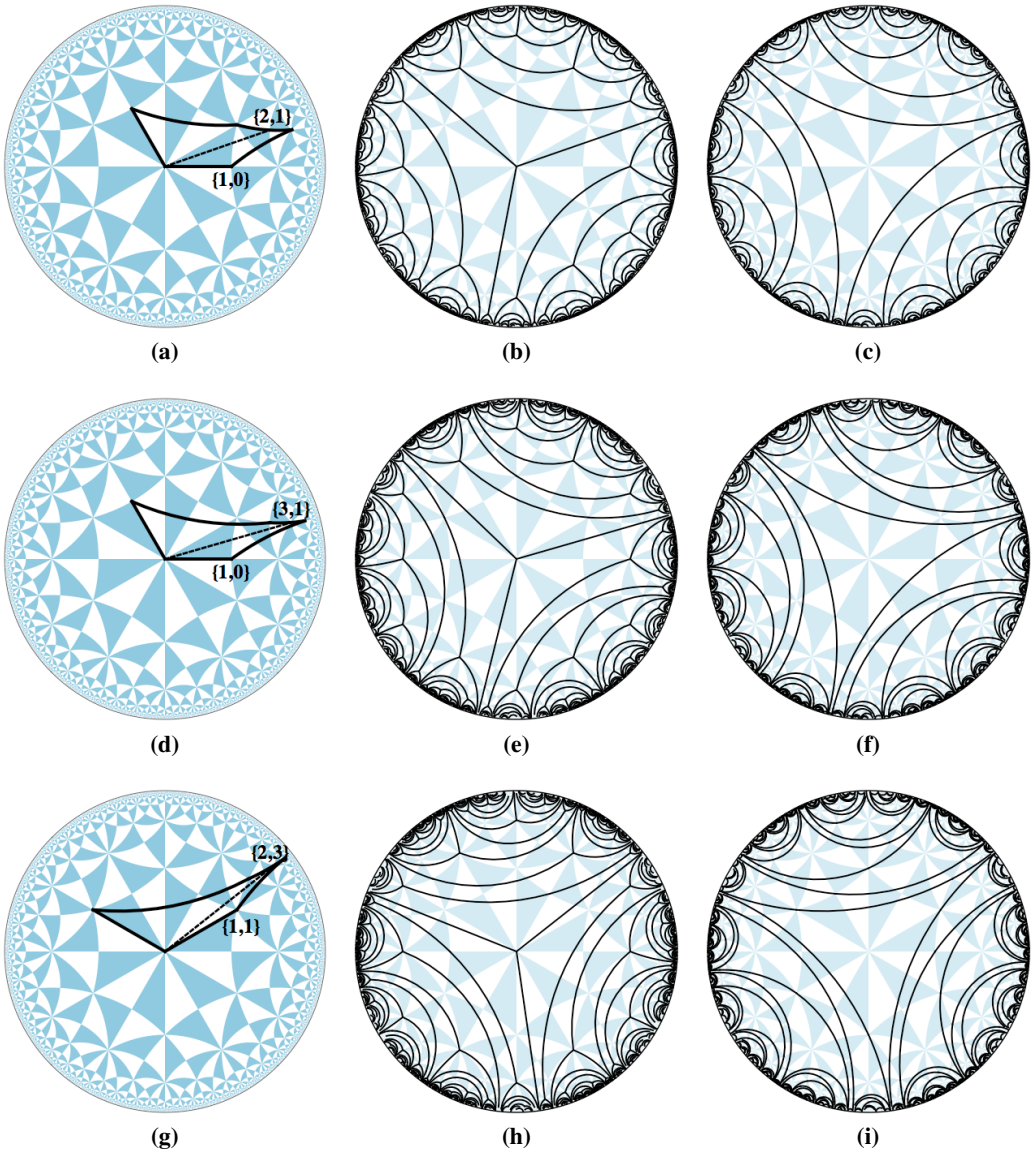

Figure 2.29: Example decorations from several embeddings of 2223. The embedded tiling names are (b) $*246_{118R}(1)$, (c) $*246_{118C}(1)$, (e) $*246_{118R}(2)$, (f) $*246_{118C}(2)$, (h) $*246_{118R}(3)$ and (i) $*246_{118C}(3)$.

The ∗2224 and 2224 symmetry groups permit regular ribbon tilings with degree–4 vertices by a similar construction to the degree–3 tiling case. Regularity and edge–1 transitivity are ensured by a ∗4 junction or 4–fold rotation at the tile vertex, and vertex–1 transitivity by a ∗2 junction or 2–fold rotation at the edge midpoint. The remaining two ∗2 junctions or 2–fold rotations define the translation symmetry of the infinite ribbon tile.

Consider first the ∗2224 orbifold, or group 123 [Robi 04a]. A regular ribbon tiling decorates the ∗2224 orbifold by an edge passing from the ∗4 site, along the mirror boundary, to a ∗2 site. These symmetry components are situated on the infinite boundary components of the tile. The two remaining ∗2 sites of the orbifold define the translation along the interior of the infinite tile. This decoration of the ∗2224 orbifold, known as 123*R*, is shown in Fig. 2.30 along with a table representing the Delaney–Dress encoding of the decorated orbifold.

Chamber Class	s0	s1	s2	m01	m12
A	**A**	B	**A**	4	8
B	B	**A**	B	4	8

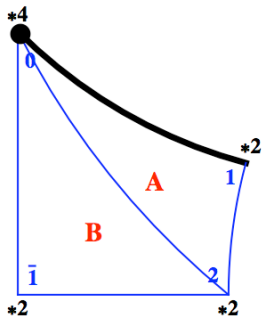

Figure 2.30: Encoding of a regular ribbon tiling on the ∗2224 orbifold, known as 123*R*. The decorations passes from the ∗4 site of the orbifold, along the mirror boundary, to a ∗2 site.

Chamber Class	s0	s1	s2	m01	m12
A	A	**B**	A	8	4
B	**B**	A	**B**	8	4

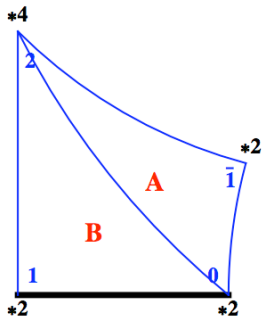

Figure 2.31: Encoding of the complement of a regular ribbon tiling on the ∗2224 orbifold, known as 123*C*. The 0–vertex and 2–vertex sites have been inverted, as well as the 1–vertex and $\bar{1}$–vertex sites. The decoration now passes from a ∗2 site along a mirror boundary to another ∗2 site.

The complement of a regular ribbon tiling on ∗2224 inverts the 0–vertex and 2–vertex sites of the Delaney–Dress triangulation, as well as inverting the 1–vertex and $\bar{1}$–vertex

sites. This exchange of vertices interchanges the boundary of the tile with the axis which is invariant under the internal symmetries of the tile, which is exactly the infinite translation axis of the tile. The Delaney–Dress encoding of the complementary regular ribbon tiling of $*2224$, known as the $123C$ tiling, is shown in Fig. 2.31.

The $*2224$ orbifold may be embedded into the $*246$ chart of the P, D and G surfaces [Robi 04a], but is not commensurate with the $*2226$ chart of the H surface [Robi 04b]. In the process of embedding the orbifold, an automorphism of $*2224$ (along the axis from the $*4$ vertex to the opposite $*2$ vertex) is asymmetrised with respect to the $*246$ tiling. The symmetry breaking induces two geometrically distinct automorphic free tilings for each abstract decoration of the orbifold. Fig. 2.32 shows the $*2224$ orbifold embedded in the $*246$ tiling of $\mathbb{H}^2$, as well as two automorphic regular ribbon tilings (represented in Fig. 2.30), and the two complementary tilings (represented in Fig. 2.31). We label these embedding $*246_{123R}(n)$ and $*246_{123C}(n)$, where n takes the value of 1 for the embedding with the shorter edge length, and 2 for the embedding with the longer edge length.

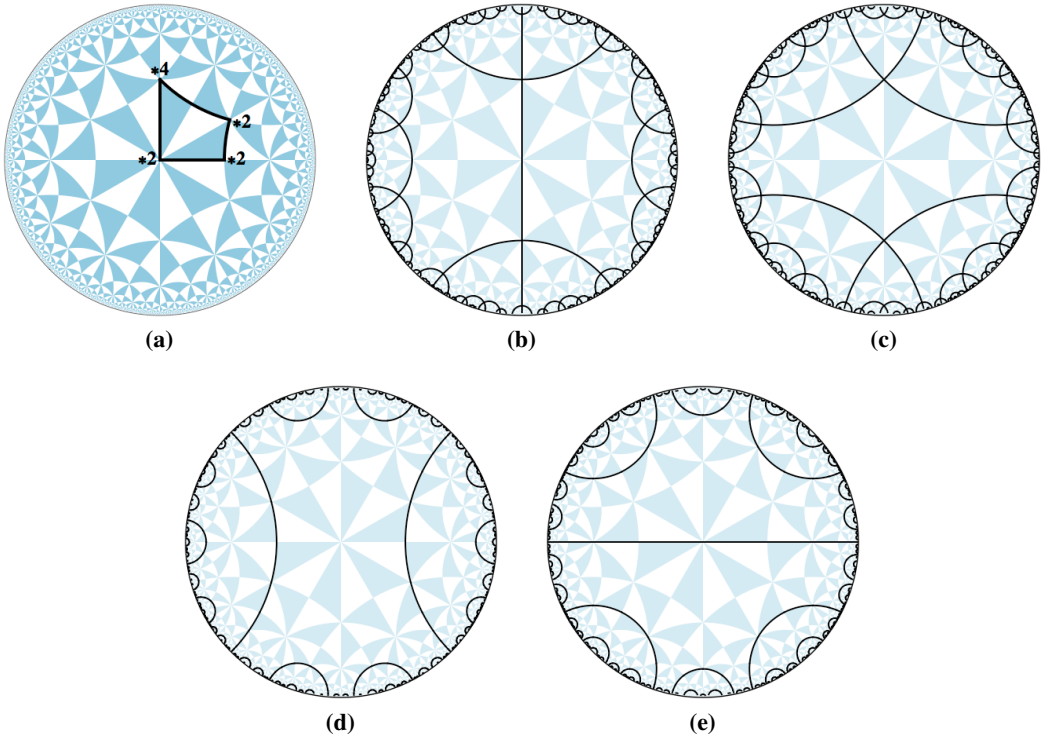

Figure 2.32: (a) Embedding of the $*2224$ orbifold into the $*246$ tiling, where the abstract symmetry of the orbifold is now asymmetrised. (b,c) Two automorphic regular ribbon tilings (Fig. 2.30), titled $*246_{123R}(1)$ and $*246_{123R}(2)$ respectively. (d,e) Two automorphic complementary tilings (Fig. 2.31), which are known as $*246_{123C}(1)$ and $*246_{123C}(2)$ respectively.

We note that the $2*24$ orbifold is not a member of the quotient group $*246/\circ\circ\circ$, and hence we do not consider regular ribbon tilings or their complements constructed on this symmetry group. In general, however, this orbifold will support such regular ribbon tilings, and may be constructed as per the $2*23$ regular ribbon tilings.

A regular ribbon tiling decorates the 2224 orbifold, group 114 [Robi 04a], by an edge passing from the 4–fold rotation to a 2–fold rotation. Fig. 2.33 shows the tabular representation of this decoration, along with a decorated image of the orbifold. This tiling is known as 114*R*, as it the regular ribbon tiling of group 114.

Chamber Class	s0	s1	s2	m01	m12
A	**D**	B	**D**	4	8
B	C	**A**	C	4	8
C	B	**D**	B	4	8
D	**A**	C	**A**	4	8

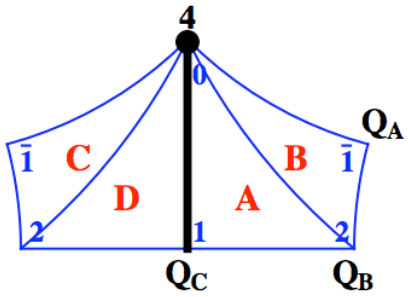

Figure 2.33: A regular ribbon tiling on the 2224 orbifold, known as 114*R*. The decoration passes from the 4–fold rotation to the 2–fold rotation labelled Q_C.

Exchanging the tile boundary with the infinite translation axis of the tile gives a complementary free tiling. Fig. 2.25 shows the encoding of this complementary regular ribbon tiling, the 114*C* tiling, which has the decorative edge passing between two distinct 2–fold rotations.

Chamber Class	s0	s1	s2	m01	m12
A	D	**B**	D	8	4
B	**C**	A	**C**	8	4
C	**B**	D	**B**	8	4
D	A	**C**	A	8	4

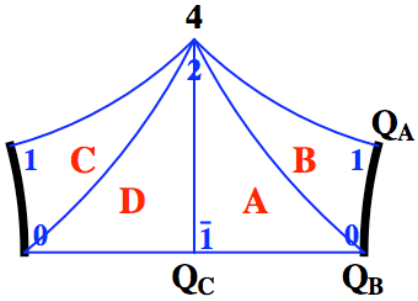

Figure 2.34: The complement to the regular ribbon tiling on the 2224 orbifold domain, also known as 114*C*. The decoration passes between the 2–fold rotations labelled Q_A and Q_B.

We index $\mathbb{H}^2$ embeddings of the 2224 orbifold by embedded parallelograms of $\mathbb{E}^2$, as is the case for all 222k orbifolds. A quadrant of $\mathbb{E}^2$ embeds in a $\frac{\pi}{4}$ sector of the 2224 discretisation of $\mathbb{H}^2$(Fig. 2.35(a)). The embedded quadrant has both coordinates positive, and

passing to adjacent $\frac{\pi}{4}$ sectors of the 2224 discretisation yields distinctly signed quadrants of $\mathbb{E}^2$.

The reference frame embedding of the generators of the 2224 orbifold into the $*246$ tiling of $\mathbb{H}^2$ is set (Fig. 2.35(b)). A fundamental domain (equivalent to that which is shown in the Delaney–Dress encoding) may be obtained by doubling the quadrilateral formed by the generating elements across the line joining Q_T and Q_C. Distinct free tilings result from the choice of embedded unit parallelograms in the $\mathbb{Z}\times\mathbb{Z}$ grid of $\mathbb{E}^2$.

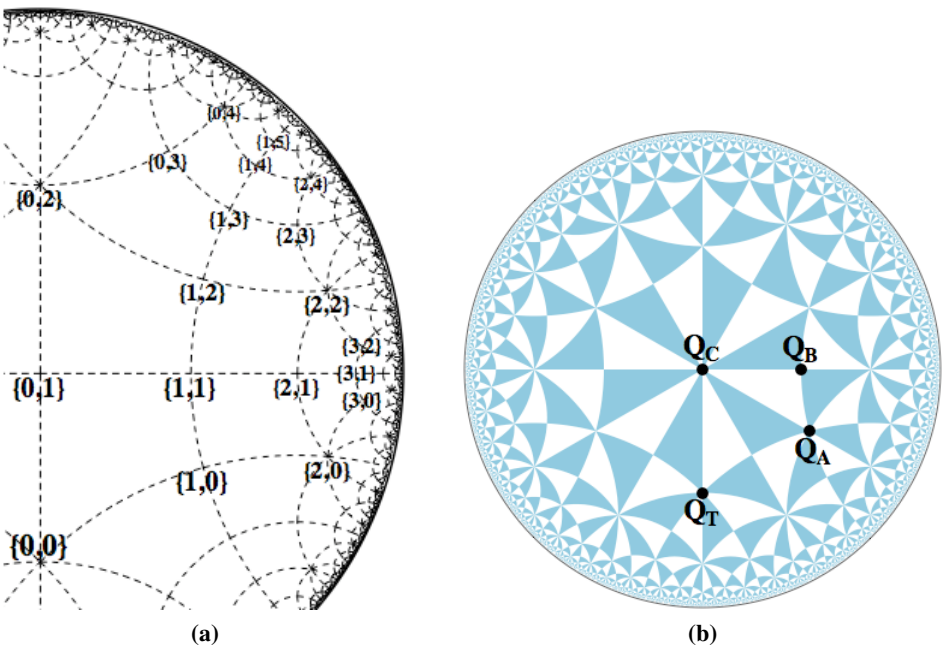

Figure 2.35: (a) Coordinates of the grid $\mathbb{Z}\times\mathbb{Z}$ within the 2224 discretisation of $\mathbb{H}^2$. (b) The reference frame generators within the $*246$ tiling of $\mathbb{H}^2$.

Mirrors are inherent in the geometry when embedding the parallelograms $\{p,q\}=\{0,1\}$, $\{r,s\}=\{1,0\}$ and $\{p,q\}=\{1,0\}$, $\{r,s\}=\{0,1\}$ into the 2224 discretisation of $\mathbb{H}^2$. This results in tilings with $*2224$ symmetry, equivalent to the $*246_{123R}(1)$, $*246_{123R}(2)$, $*246_{123C}(1)$ and $*246_{123C}(2)$ embedded tilings, as constructed on the $*2224$ orbifold (Fig. 2.32).

The regular ribbon tilings and complementary tilings that result from the embedding of some Euclidean parallelograms into the 2224 discretisation of $\mathbb{H}^2$ are given as examples (Fig. 2.36). We name these embedded tilings $*246_{114R}(n)$ for regular ribbon tilings and $*246_{114C}(n)$ for their complements, where n counts from smallest edge length (by hyperbolic length) within the embedded fundamental domain upwards through all possi-

ble embeddings. The Euclidean parallelograms defining the embeddings, as well as their embedded tiling names, are given by:

1. $\{p,q\} = \{1,1\}$ and $\{r,s\} = \{1,0\}$: $*246_{114R}(1)$ and $*246_{114C}(1)$ (Fig. 2.36(b,c))
2. $\{p,q\} = \{1,2\}$ and $\{r,s\} = \{1,1\}$: $*246_{114R}(2)$ and $*246_{114C}(2)$ (Fig. 2.36(e,f))
3. $\{p,q\} = \{2,1\}$ and $\{r,s\} = \{1,0\}$: $*246_{114R}(3)$ and $*246_{114C}(3)$ (Fig. 2.36(h,i))

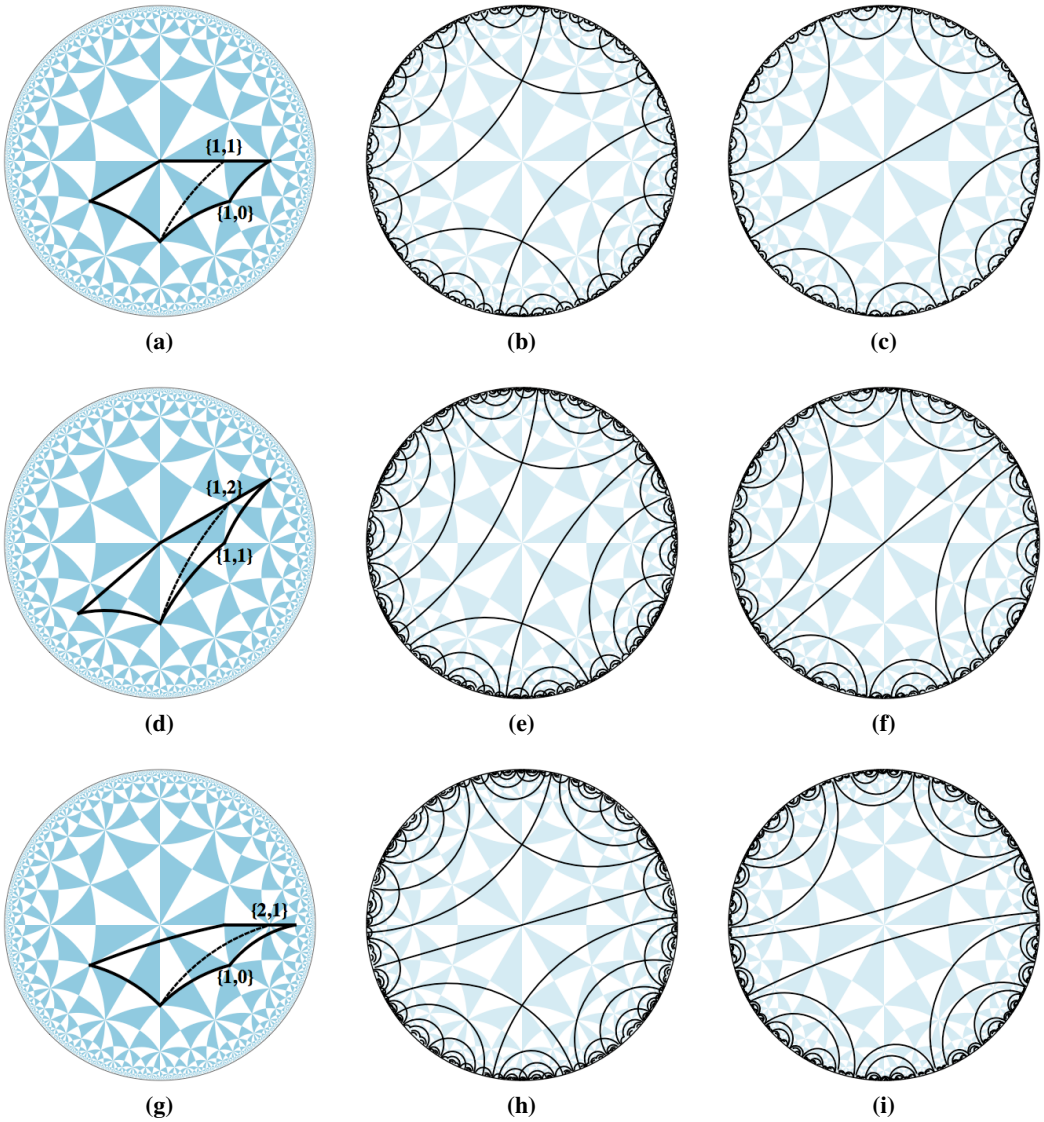

Figure 2.36: Example decorations from several embeddings of 2224. Their embedded tiling names are (b $*246_{114R}(1)$, (c) $*246_{114C}(1)$, (e) $*246_{114R}(2)$, (f) $*246_{114C}(2)$, (h) $*246_{114R}(3)$, (i) $*246_{114C}(3)$.

Tilings with 5–fold regular symmetry are not compatible with either the ∗246 or the ∗2226 tiling, hence we disregard these cases. Regular ribbon tilings with 6–fold symmetry at the tile vertex may have symmetry ∗2226, 2∗26, 2226 or 26×. Regular ribbon tilings on the 26× orbifold always have increased symmetry of 2∗26, hence we disregard decorations of this orbifold. The ∗2226 symmetry group is in the ∗2226/○○○ quotient group, the 2∗26 symmetry group is in the ∗246/○○○ quotient group, and the 2226 symmetry group is in both of the ∗246/○○○ and ∗2226/○○○ quotient groups.

A regular ribbon tiling reticulates the ∗2226 orbifold, which is group 32 of the ∗2226/○○○ quotient group [Robi 04b], by passing from the ∗6 site, along a mirror boundary, to a ∗2 site (Fig. 2.37). These symmetry elements, to which the decoration is incident, generate the boundary components of the infinite tile. The set of parallel mirrors contained within the two remaining ∗2 sites generate the single internal translation of the infinite ribbon tile. This tiling is known as 32*R*, as it is the regular ribbon tiling of group 32 in the ∗2226/○○○ quotient group.

Chamber Class	s0	s1	s2	m01	m12
A	**A**	B	**A**	4	12
B	B	**A**	B	4	12

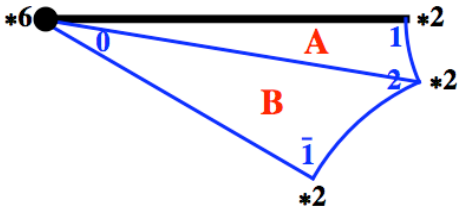

Figure 2.37: A regular ribbon tiling represented as a decoration on the ∗2226 orbifold, passing from the ∗6 site, along a mirror boundary, to a ∗2 site. This tiling is known as the 32*R* tiling.

The complement of the regular ribbon tiling exchanges the infinite translation axis of the infinite ribbon tile with the boundary components of the tile. On the ∗2226 orbifold, this complementary tiling can be represented by a decorative edge passing from a ∗2 site, along a mirror boundary, to another ∗2 site of the orbifold. This tiling, known as 32*C*, is encoded in Fig. 2.38.

Chamber Class	s0	s1	s2	m01	m12
A	A	**B**	A	12	4
B	**B**	A	**B**	12	4

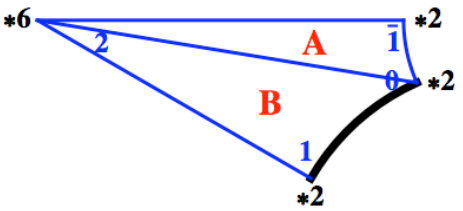

Figure 2.38: The complement to the regular ribbon tiling on the ∗2226 orbifold. The decoration passes from a ∗2 site, along a mirror boundary, to another ∗2 site. This tiling as known as the 32*C* tiling.

The $*2226$ orbifold is precisely the $*2226$ chart of $\mathbb{H}^2$ inherited from the H surface. The orbifold has an abstract symmetry (automorphism) that swaps the two $*2$ vertices adjacent to the $*6$ corner. This abstract symmetry is broken by the embedding of the $*2226$ domain into $\mathbb{H}^2$ (by the free parameter of the H surface discussed previously), and hence the automorphic tilings have distinct geometries in the $*2226$ chart. Fig. 2.39 shows the embedded fundamental domain of the $*2226$ orbifold, along with the four free tilings of this symmetry group (two automorphic versions of the regular ribbon tiling, and two of the complementary tiling, all with symmetry $*2226$). These embedded tilings are named to reflect their embedding into the $*2226$ tiling of $\mathbb{H}^2$: hence they are named $*2226_{32R}(1)$, $*2226_{32R}(2)$, $*2226_{32C}(1)$ and $*2226_{32C}(2)$, where the '1' refers to a shorter edge length in one asymmetric domain.

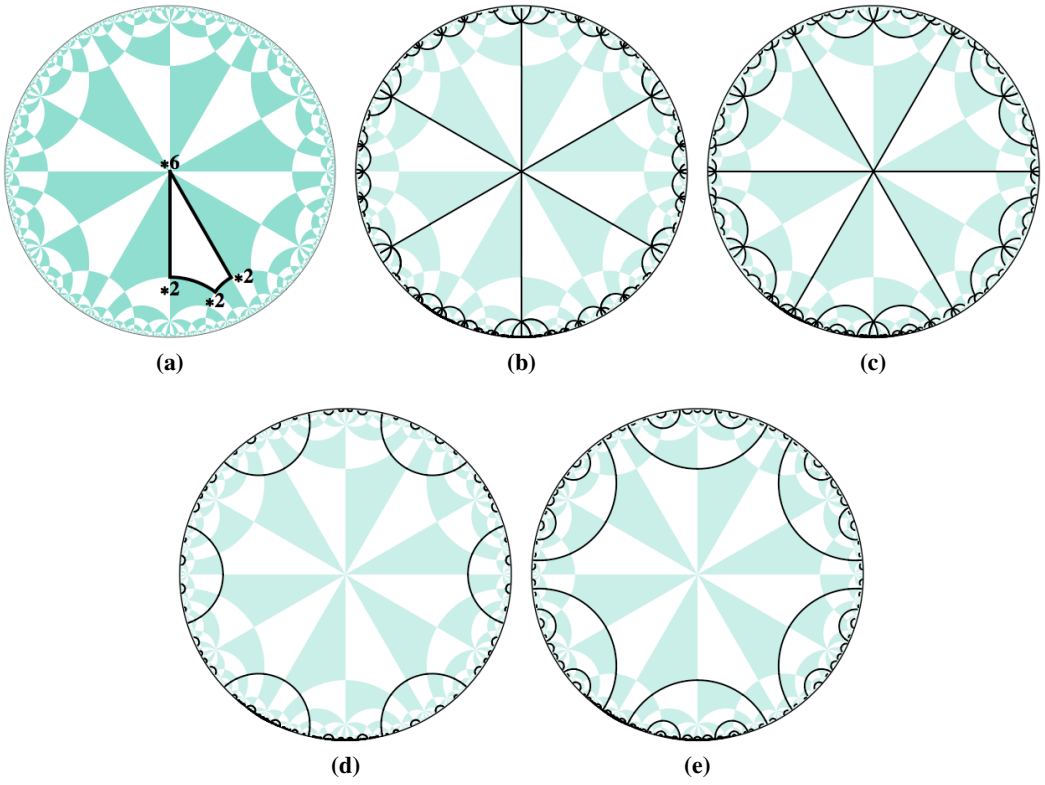

Figure 2.39: (a) A fundamental domain of the $*2226$ orbifold uniquely embedded into the $*2226$ tiling of $\mathbb{H}^2$. (b,c) Two automorphic regular ribbon tilings on the $*2226$ orbifold, known as $*2226_{32R}(1)$ and $*2226_{32R}(2)$. (d,e) Two automorphic versions of the complementary tiling on the $*2226$ orbifold, namely $*2226_{32C}(1)$ and $*2226_{32C}(2)$.

We treat the $2*26$ orbifold equivalently to the $2*23$ orbifold considered previously. We construct two simple orbifold decorations: an edge passing from the $*6$ vertex to the $*2$ vertex to give the regular ribbon tilings on this orbifold, and the complementary

tiling having an edge passing from the 2–fold rotation, through a mirror boundary at right angles, to an image of the same 2–fold rotation. The topology of these two tilings, named 122*R* and 122*C*, are abstractly represented by the two Delaney–Dress symbols given in Figs. 2.40 and 2.41.

Chamber Class	s0	s1	s2	m01	m12
A	**A**	B	**A**	3	18
B	C	**A**	C	3	18
C	B	C	B	3	18

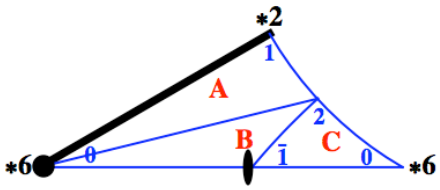

Figure 2.40: Encoding of the topology of a regular ribbon tiling on the $2*26$ orbifold: 122*R* The decoration consists of an edge passing from the $*6$ site, along the mirror boundary to the $*2$ site.

Chamber Class	s0	s1	s2	m01	m12
A	A	**B**	A	18	3
B	**C**	A	**C**	18	3
C	**B**	**C**	**B**	18	3

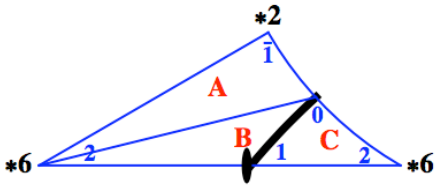

Figure 2.41: Encoding of the topology of a complementary regular ribbon tiling on the $2*26$ orbifold: 122*C*. The decoration consists of an edge passing from the 2–fold rotation to an image of itself through a mirror boundary.

Fig. 2.42(a) shows the unique embedding of the $2*26$ orbifold into the $*246$ chart of $\mathbb{H}^2$. The automorphism of the orbifold $2*26$ is a symmetry line passing from the $*2$ vertex to the 2–fold rotation, mapping the $*6$ site to the other $*6$ site in the embedding. This symmetry is broken with respect to the $*246$ chart when the orbifold is embedded, hence we consider both geometries that arise from automorphic embeddings. Fig. 2.42(b,c) show the two automorphic regular ribbon tilings with distinct geometry that arise from the embedding of the 122*R* tiling (Fig. 2.40) in the $*246$ chart of $\mathbb{H}^2$. These embedded tilings are symbolised by $*246_{122R}(1)$ and $*246_{122R}(2)$ respectively, where the former has a shorter edge length in the asymmetric domain. Fig. 2.42(d,e) also shows the two automorphic complementary tilings given by the embedding of the 122*C* tiling (Fig. 2.41). These tilings are called $*246_{122C}(1)$ and $*246_{122C}(2)$ respectively.

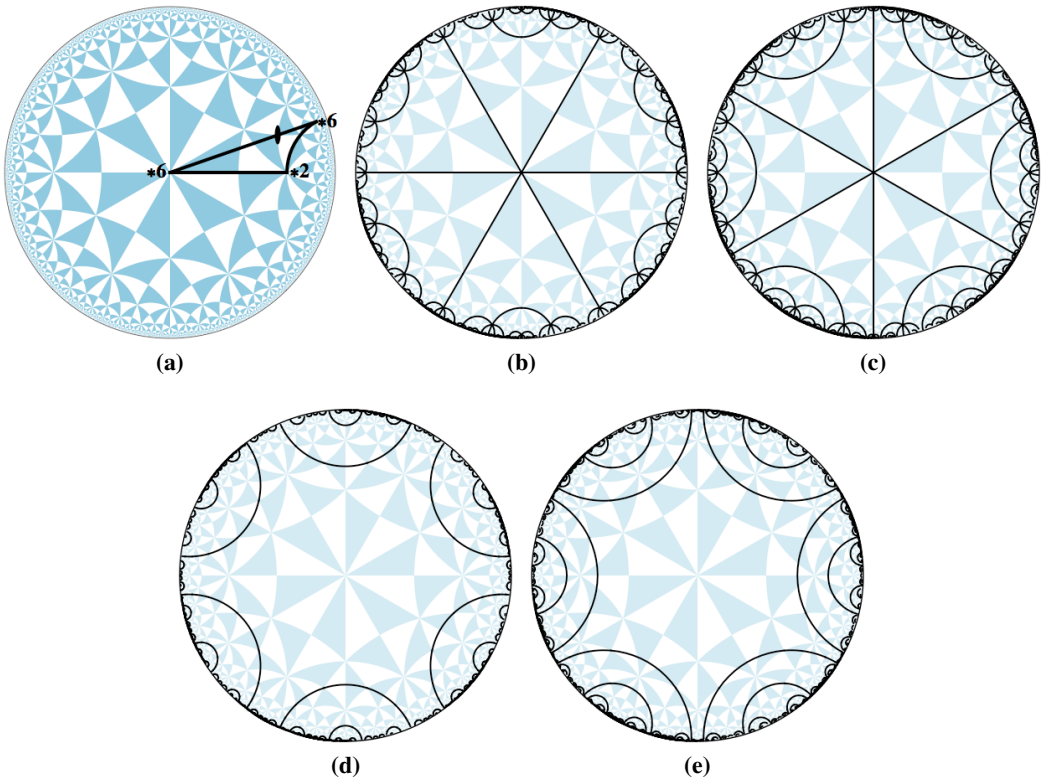

Figure 2.42: (a) Unique embedding of the $2*26$ orbifold into the $*246$ chart of $\mathbb{H}^2$. (b,c) The two automorphic regular ribbon tilings resulting embedding of the $2*26$ domain, namely $*246_{122R}(1)$ and $*246_{122R}(2)$. (d,e) The two automorphic complementary tilings called $*246_{122C}(1)$ and $*246_{122C}(2)$.

A regular ribbon tiling is constructed on the 2226 orbifold (group 31 in ∗2226/○○○ or group 93 in ∗246/○○○ [Robi 04b, Robi 04a]) by an edge passing from the 6–fold rotation to any 2–fold rotation. Fig. 2.43 shows the Delaney–Dress representation of this decoration, and an image of the decorated orbifold. We call this tiling either 31*R* where it may be embedded in the ∗2226 tiling, or 93*R* for embedding in ∗246. The exchange of the tile boundary with the medial axis gives the complementary tiling, whose Delaney–Dress encoding is sown in Fig. 2.44. This tiling is called 31*R* for ∗2226 embeddings or 93*R* for ∗246 embeddings.

Chamber Class	s0	s1	s2	m01	m12
A	**D**	B	**D**	4	12
B	C	**A**	C	4	12
C	B	**D**	B	4	12
D	**A**	C	**A**	4	12

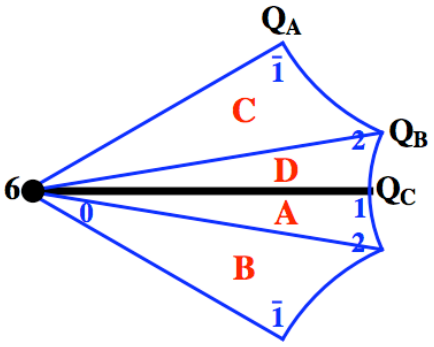

Figure 2.43: Encoding of the regular ribbon tiling on 2226, having the decoration passing from the 6–fold rotation to the 2–fold rotation marked Q_C. We call this tiling either 31*R* where it may be embedded in the ∗2226 tiling, or 93*R* for embedding in ∗246.

Chamber Class	s0	s1	s2	m01	m12
A	D	**B**	D	12	4
B	**C**	A	**C**	12	4
C	**B**	D	**B**	12	4
D	A	**C**	A	12	4

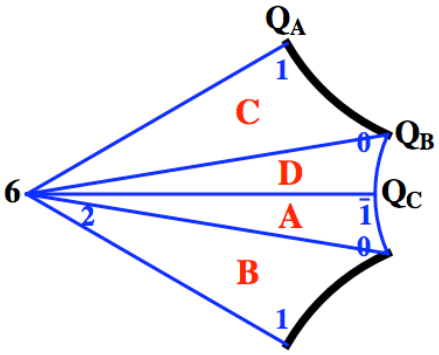

Figure 2.44: Encoding of the complement of the regular ribbon tiling on 2226. The decoration passes between the 2–fold rotations marked Q_A and Q_B. This tiling is called 31*R* for ∗2226 embeddings or 93*R* for ∗246 embeddings.

The 2226 orbifold is commensurate with both of the ∗246 and ∗2226 tilings, and can be mapped onto the *P*, *D*, *G* and *H* surfaces. To assign geometry commensurate with the surfaces, we utilise parallelograms embedded in $\mathbb{E}^2$ to embed the orbifold into $\mathbb{H}^2$ given a specific reference frame (Section 2.2). The positions of the reference frame generators for

the 2226 symmetry group in the ∗2226 and ∗246 tilings are shown in Fig. 2.45.

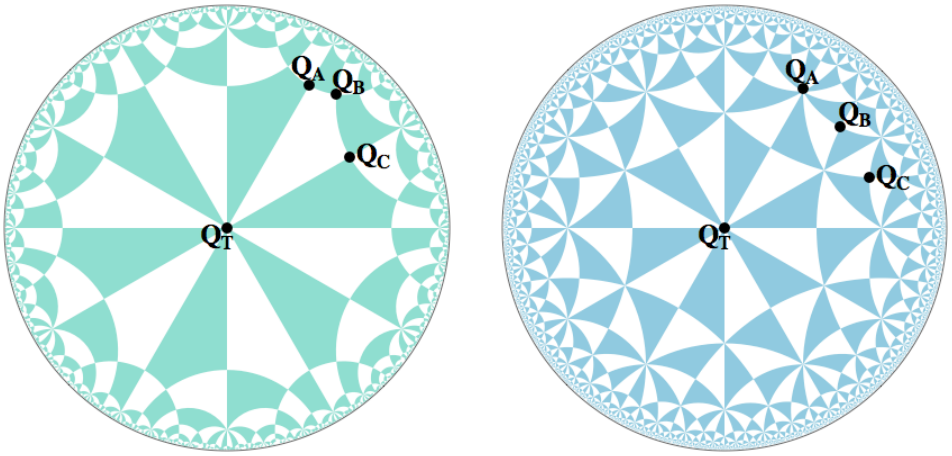

Figure 2.45: The reference frame generators for the 2226 symmetry group in the (a) ∗2226 and (b) ∗246 tilings. To establish an integer grid, Q_A, Q_B and Q_C are located at {0,1}, {1,1} and {1,0} respectively.

We embed the abstract decorations of 2226, tilings 31R and 31C, into the ∗2226 chart of $\mathbb{H}^2$. This process specifies three generators of the 2226 symmetry group relative to the reference frame embedding, and the full fundamental domain is found by doubling the quadrilateral formed across the line connecting Q_T–Q_C. To achieve this embedding, we specify a $\{p,q\}$ and $\{r,s\}$ value in $\mathbb{Z}\times\mathbb{Z}$, where $\{p,q\}$ designates the position of Q_C and $\{r,s\}$ designates the position of Q_A. The geometry inherited from embedding the parallelograms $\{p,q\}=\{0,1\}$ and $\{r,s\}=\{1,0\}$, as well as $\{p,q\}=\{1,0\}$ and $\{r,s\}=\{0,1\}$ have mirror symmetry present, giving a tiling with ∗2226 symmetry. These embedded tilings are equivalent to those constructed on the ∗2226 orbifold (Fig. 2.39), called $*2226_{32R}(1)$, $*2226_{32R}(2)$, $*2226_{32C}(1)$ and $*2226_{32C}(2)$.

Fig. 2.46 shows three examples of embedded regular ribbon tilings and complementary tilings, where the maximal symmetry is 2226. The embedding of the 2226 domain in the ∗2226 tiling of $\mathbb{H}^2$ is inherited from parallelograms in $\mathbb{E}^2$. We give their parallelogram coordinates and embedded tiling names:

1. $\{p,q\}=\{1,1\}$ and $\{r,s\}=\{0,1\}$: $*2226_{31R}(1)$ and $*2226_{31C}(1)$ (Fig. 2.46(b,c))
2. $\{p,q\}=\{2,1\}$ and $\{r,s\}=\{1,1\}$: $*2226_{31R}(2)$ and $*2226_{31C}(2)$ (Fig. 2.46(e,f))
3. $\{p,q\}=\{1,2\}$ and $\{r,s\}=\{0,1\}$: $*2226_{31R}(3)$ and $*2226_{31C}(3)$ (Fig. 2.46(h,i))

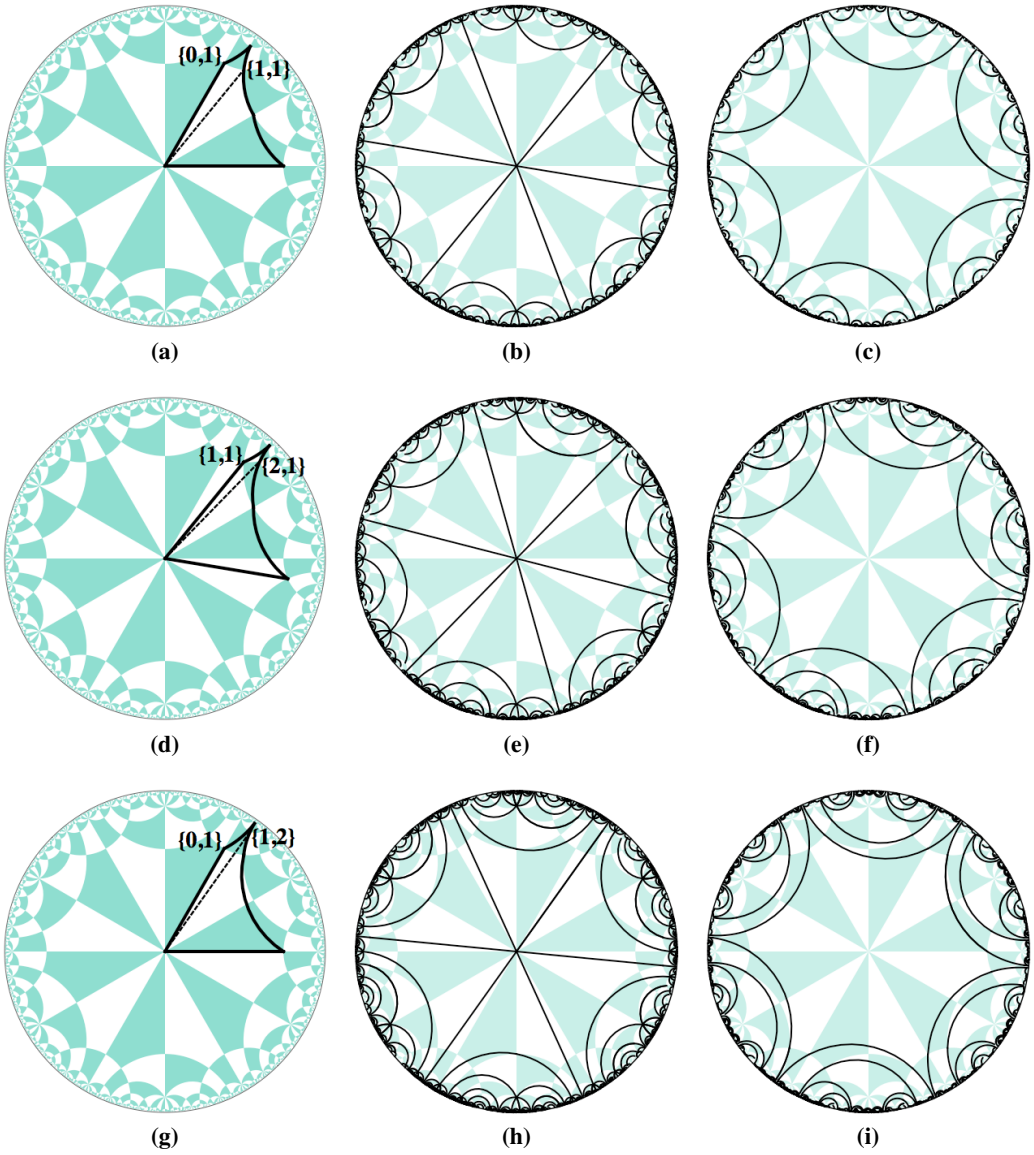

Figure 2.46: Example decorations from embedding 2226 into the $*2226$ chart of $\mathbb{H}^2$. (b) $*2226_{31R}(1)$, (c) $*2226_{31C}(1)$, (e) $*2226_{31R}(2)$, (f) $*2226_{31C}(2)$, (h) $*2226_{31R}(3)$, (i) $*2226_{31C}(3)$.

We now consider embeddings of the $93R$ and $93C$ into the $*246$ chart of $\mathbb{H}^2$. The embedding associated with $\{p,q\} = \{0,1\}$ and $\{r,s\} = \{1,0\}$ (recall that $\{p,q\}$ always specifies the Q_C value), as well as the embedding $\{p,q\} = \{2,1\}$ and $\{r,s\} = \{1,1\}$ will give an increase of symmetry of the pattern to $2*26$, which are the tilings $*246_{122R}(1)$, $*246_{122R}(2)$, $*246_{122C}(1)$ and $*246_{122C}(2)$, as seen in Fig. 2.42.

Fig. 2.47 shows two examples of embedded regular ribbon and complementary tilings into the $*246$ chart. The embeddings used for these tilings correspond to the parallelograms in $\mathbb{E}^2$ with coordinates, and embedded tiling names, as follows:

1. $\{p,q\} = \{1,1\}$ and $\{r,s\} = \{0,1\}$: $*246_{93R}(1)$ and $*246_{93C}(1)$ (Fig. 2.47(b,c))
2. $\{p,q\} = \{1,2\}$ and $\{r,s\} = \{0,1\}$: $*246_{93R}(2)$ and $*246_{93C}(2)$ (Fig. 2.47(e,f))

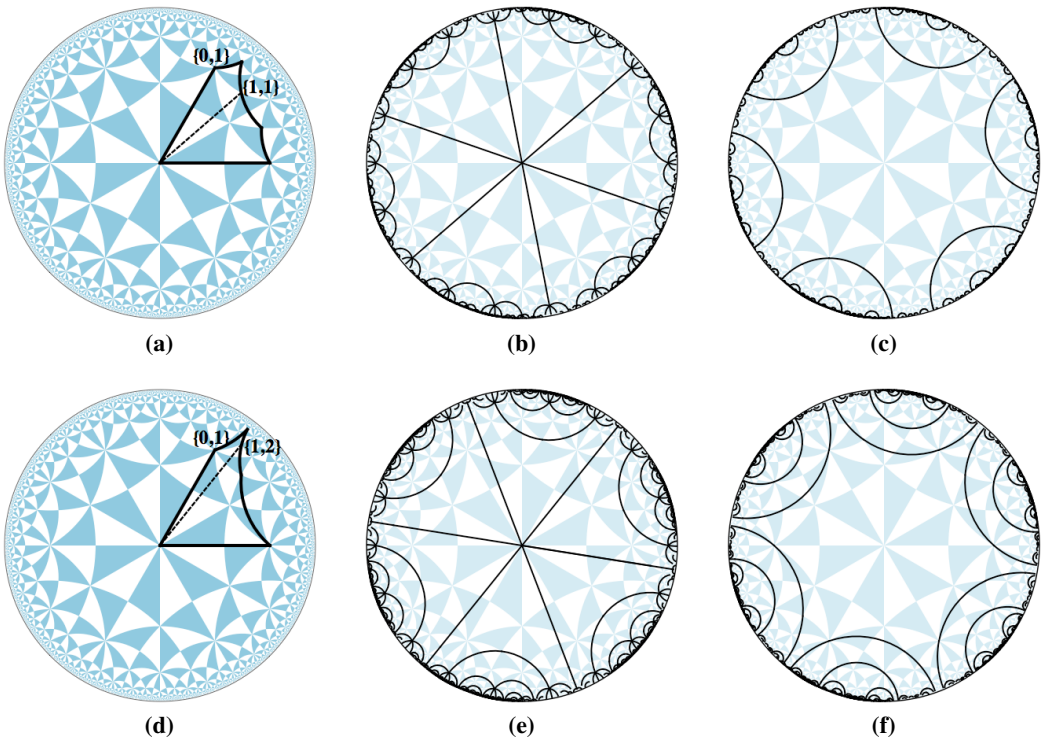

Figure 2.47: Example decorations from several embeddings of 2226 into the $*246$ chart of $\mathbb{H}^2$, indexed by distinct parallelograms (a–c) $\{p,q\} = \{1,1\}$ and $\{r,s\} = \{0,1\}$, known as $*246_{93R}(1)$ and $*246_{93C}(1)$, (d–f) $\{p,q\} = \{1,2\}$ and $\{r,s\} = \{0,1\}$, known as $*246_{93R}(2)$ and $*246_{93C}(2)$.

These cases cover some examples of the embedding of regular ribbon tilings commensurate with the genus–3 TPMS chosen, the regular ribbon tiling supported only by orbifolds of the form 222k. We have, however, provided a method for indexing of possible embeddings of orbifolds of this form (222k), regardless of the orbifold decoration.

2.4 Lower Order Symmetry Groups

An indexing by Euclidean parallelograms has been possible for all of the embedded orbifolds presented so far. A simple extension of this indexation includes a slightly broader set of orbifolds: those where we may index embeddings by gluing distinct Euclidean parallelograms across an edge. This surgery enables indexation of stellate orbifolds of the type 2222j. We explain this construction, and then present examples of embedded 22223 orbifolds with a specific decoration.

A 2222j orbifold is double the size of a 222k orbifold for $k = 2j$, by the orbifold 'cost' formula (Section 2.0.1): 22223 is twice the area of 2226. An embedded 2222j domain may be constructed by taking a 222k symmetry group and doubling across an edge, where the k–fold rotation halves (becoming a j–fold rotation), one 2–fold rotation is deleted, and two copies of the remaining two 2–fold rotations give the four 2–fold rotations of 2222j. These embedded 2222j domains form a subset of the possible embeddings of the domain, and we extend here to encompass all possible embedded domains.

To construct a 22222 domain using multiple 2224 domains ($j = 2$, $k = 2j = 4$), we begin with a $\frac{\pi}{4}$ sector of $\mathbb{H}^2$ discretised by 2224 and the $\mathbb{Z} \times \mathbb{Z}$ grid. We then:

1. Set an origin. This will be a 4–fold rotation of 2224, and will end up as a 2–fold rotation of the 22222 symmetry group.

2. Select Q'_C (or $\{p,q\}$) as a coprime in the $\mathbb{Z} \times \mathbb{Z}$ grid.

3. Select any Q'_A ($\{r_1,s_1\}$ in this case) such that $ps_1 - qr_1 = 1$. The result is a unit parallelogram that embeds as a 2224 quadrilateral, located on a specific side of Q'_C.

4. Select any Q''_A (called $\{r_2,s_2\}$) such that $ps_2 - qr_2 = -1$. This is a quadrilateral that sits on the opposite side of the Q'_C edge to the first constructed quadrilateral.

5. When the the symmetry element Q'_C is discarded and the symmetry of the 4–fold rotation is reduced to a 2–fold rotation, the remaining five 2–fold rotations define an embedded 22222 symmetry group. This process is shown in Fig. 2.48.

When embedding the 22222 domain into $*246$, we are embedding it into the 2224 reference frame. Hence there are three distinct infinite sets of 2–fold rotations, which correspond to the images of each of the three distinct 2–fold rotations of 2224. These three distinct sets are categorised by the 2–fold rotations which lie at $*6$ sites, $*4$ sites and $*2$

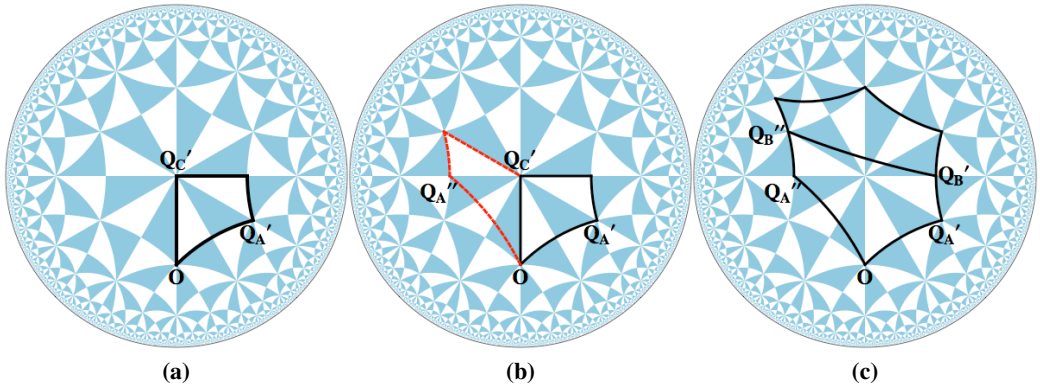

Figure 2.48: (a) Q'_C (or $\{p,q\}$) is the coprime pair $\{0,1\}$ in the $\mathbb{Z}\times\mathbb{Z}$ grid, and Q'_A ($\{r_1,s_1\}$) is the point $\{1,0\}$, where $ps_1 - qr_1 = (0) - (1) = -1$. This parallelogram embeds as a 2224 quadrilateral. (b) Q''_A ($\{r_2,s_2\} = \{-1,1\}$) is selected such that $ps_2 - qr_2 = (0) - (-1) = 1$. This gives a quadrilateral on the opposite side of Q'_C. (c) When Q'_C is discarded, the 4–fold reduced to a 2–fold, and the remaining 2–fold rotations define 22222.

sites respectively. By choosing Q'_C from a particular set of 2–fold rotations, we designate which set of 2–fold rotations will not be isometries of the 22222 embedding. Thus there are three embeddings of the 22222 orbifold with distinct generators, as described in [Robi 04a].

Chamber Class	s0	s1	s2	m01	m12
A	A	**B**	A	8	4
B	**C**	A	**B**	8	4
C	**B**	D	**C**	8	6
D	D	**C**	D	8	6

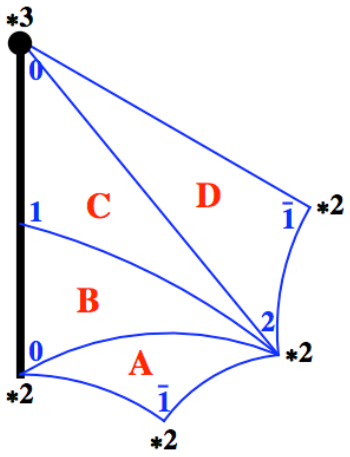

Figure 2.49: The Delaney–Dress symbol for the ∗22223 orbifold decoration having one edge pass from the ∗3 vertex along the mirror boundary to a ∗2 vertex, called 26*R* A visual representation of the decoration and chambers on the orbifold is also shown.

More generally, the 4–fold vertex in the example that has been constructed may be any even number of rotations, thus an equivalent construction will work for any 2222j orbifold. The examples we wish to analyse with this construction are the symmetry groups ∗22223 (group 26 in ∗2226/○○○) and 22223 (group 22 in ∗2226/○○○ and group 49 in

$*246/\circ\circ\circ$). Consider free tilings that are regular (1–transitive edges), and the infinite tiles are branched rather than ribbons. These branched tiles induce vertices in the complementary tiles, rather than infinite geodesic boundaries in the case of ribbon tilings, and we omit these complementary tilings. The Delaney–Dress representation of the decoration of the $*22223$ domain is given in Fig. 2.49: as a decoration of the orbifold, this tiling is called $26R$.

There is one embedding of this orbifold into the $*2226$ domain that is commensurate with the translational symmetries of the H surface ($\circ\circ\circ$) [Robi 04b]. This embedding and the resulting embedded free tiling is shown in Fig. 2.50. This embedded tiling is called $*2226_{26R}$.

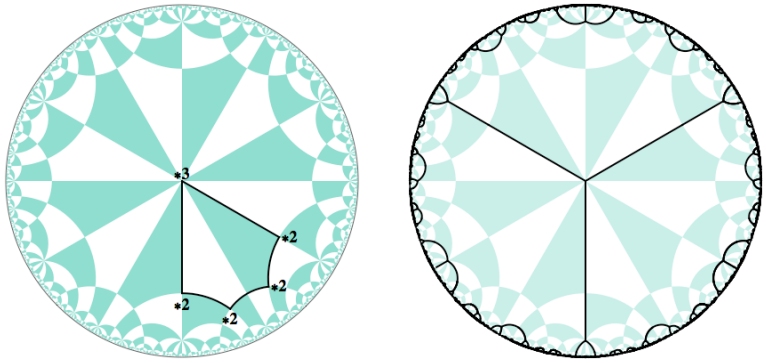

Figure 2.50: (a,b) One embedding of the $*22223$ domain into the $*2226$ tiling of $\mathbb{H}^2$, and the resulting free tiling: $*2226_{26R}$.

The only regular free tiling of the 22223 orbifold is shown in Fig. 2.51, having a single edge passing from the 3–fold rotation to the 2–fold rotation called Q_E. This abstract decoration of the orbifold is called $22R$ as a member of the $*2226/\circ\circ\circ$ quotient group, and $29R$ as a member of $*246/\circ\circ\circ$.

To embed this orbifold in the $*2226$ tiling of $\mathbb{H}^2$, we select parameters to form two euclidean parallelograms with a common edge. Set the $\mathbb{Z}\times\mathbb{Z}$ grid to be as located for the embedding of 2226, which we show again in Fig. 2.52: the point Q_A is located at the coordinate $\{0,1\}$, Q_B is at $\{1,1\}$ and Q_C is at $\{1,0\}$.

The vertex Q'_C (the 2–fold rotation that will not be a generator of 22223) must be chosen as an image of Q_C (not an image of Q_A or Q_B). This will ensure that the 22223 group constructed will have the correct generators to be a member of $*2226/\circ\circ\circ$. If Q'_C is chosen to be at an image of Q_A or Q_B, this will construct a 22223 group that is not a

Chamber Class	s0	s1	s2	m01	m12
A	E	**B**	E	8	4
B	**C**	A	**F**	8	4
C	**B**	D	**G**	8	6
D	**H**	**C**	**H**	8	6
E	A	**F**	A	8	4
F	**G**	E	**B**	8	4
G	**F**	**H**	**C**	8	6
H	D	**G**	D	8	6

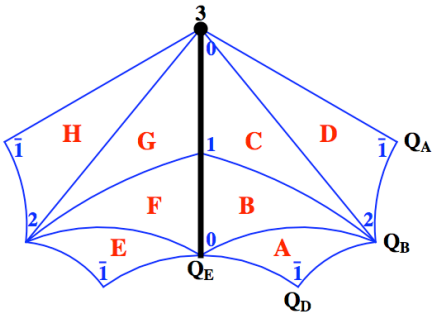

Figure 2.51: The encoding for the 22223 orbifold decoration having one edge pass from the 3–fold rotation to the 2–fold rotation marked Q_E. This tiling is called 22R as a member of the ∗2226/○○○ quotient group, or 29R as a member of ∗246/○○○.

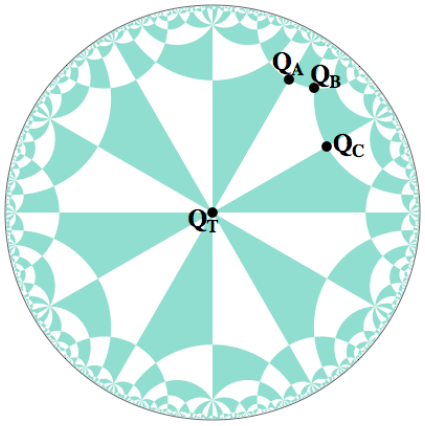

Figure 2.52: The reference frame generators for the 2226 symmetry group in the ∗2226 tiling. To establish an integer grid, Q_A, Q_B and Q_C are located at {0,1}, {1,1} and {1,0} respectively.

member of the ∗2226/○○○ quotient group. To ensure the correct group is obtained, we restrict the position of Q'_C to be a coprime integer pair $\{p,q\}$, where p is even (or 0) and q is odd (This restriction ensures that the deleted 2–fold rotation is an image of Q_C).

Fig. 2.53 shows the construction of a fundamental domain of the 22223 symmetry group by the parameters $Q'_C = \{0,1\}$ and $Q'_A = \{-1,0\}$, where the determinant of the parallelogram $ps_1 - qr_1 = (0) - (-1) = 1$ and $Q'_E = \{1,0\}$, where the determinant of the second parallelogram is $ps_2 - qr_2 = (0) - (1) = -1$. The geometry resulting from the embedding has additional symmetry of ∗22223, and the decoration is equivalent to one constructed on the ∗22223 orbifold, and shown in Fig. 2.50(b).

Consider the decoration of the orbifold shown in Fig. 2.51. The tiling boundary is composed of a single edge which passes from the 3–fold rotation to Q'_E. Thus the free tiling depends only on the position of Q'_E, and remains unchanged for distinct choices of Q'_A, Q'_B and Q'_D. We recall that the point Q'_E may be any coprime pair in the integer grid,

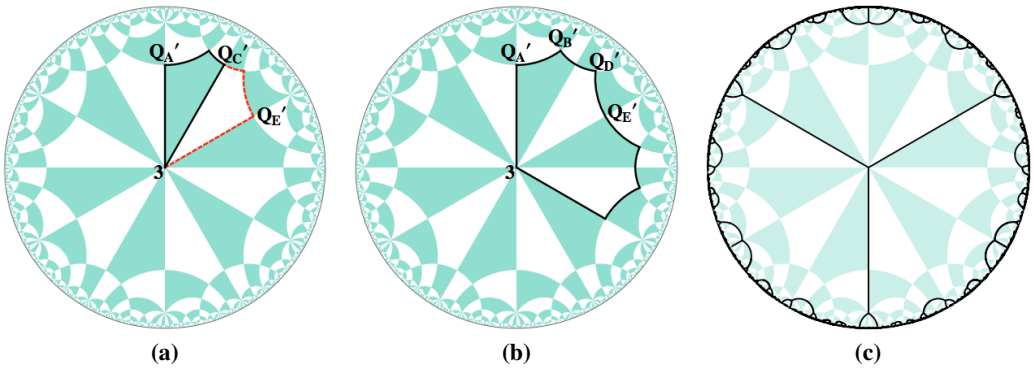

Figure 2.53: (a) Q'_C is the point $\{0,1\}$ in the $\mathbb{Z}\times\mathbb{Z}$ grid. Two quadrilaterals are constructed either side of this line, with $Q'_A=\{-1,0\}$ and $Q'_E=\{1,0\}$. (b) The resulting 22223 fundamental domain. (c) The free tiling resulting from the decorated and embedded orbifold, with increased symmetry of $*22223$.

$\{r_2,s_2\}$, where r_2 is odd, hence we need only select the position of Q'_E with this restriction to completely define the tiling. Further, by conjugacies of the $*2226$ grid, we need only consider coprime pairs in the positive–positive quadrant of $\mathbb{Z}\times\mathbb{Z}$.

Fig. 2.54 shows three examples of the decorated and embedded 22223 orbifold in the $*2226$ tiling of $\mathbb{H}^2$. The three embeddings are defined by the choice of Q'_E to be the following coordinates in $\mathbb{Z}\times\mathbb{Z}$: $Q'_E=\{1,1\}$ (namely $*2226_{22R}(1)$, shown in Fig. 2.54(a)), $Q'_E=\{1,2\}$ (namely $*2226_{22R}(2)$, shown in Fig. 2.54(b)), and $Q'_E=\{3,2\}$ (namely $*2226_{22R}(4)$, Fig. 2.54(c)).

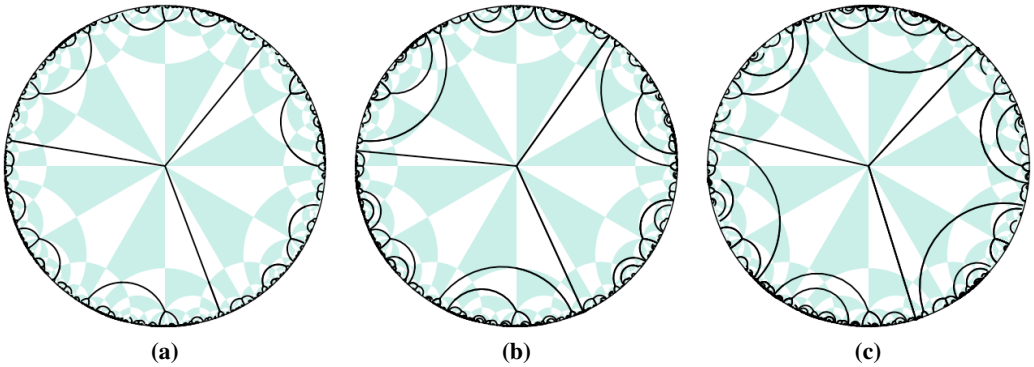

Figure 2.54: Three embeddings of the decorated 22223 orbifold in the $*2226$ tiling of $\mathbb{H}^2$to give three distinct free tilings. Q'_E is chosen to be (a) $\{1,1\}$: $*2226_{22R}(1)$, (b) $\{1,2\}$: $*2226_{22R}(2)$, (c) $\{3,2\}$: $*2226_{22R}(4)$.

The symmetry group 22223 is also a subgroup of the $*246$ symmetry group. Hence we can consider embedding the same decorated orbifold to be commensurate with the $*246$

tiling. This embedding follows the same process as for the $*2226$ embedding, however the location of the integer grid in $\mathbb{H}^2$ is slightly different (see examples in Fig. 2.47 for the location of the integer grid with respect to the $*246$ tiling). Fig. 2.55 shows a few examples, where the location of Q'_E is varied as follows:

1. $Q'_E = \{1,1\}$: $*246_{49R}(1)$ (Fig. 2.55(a))
2. $Q'_E = \{1,2\}$: $*246_{49R}(2)$ (Fig. 2.55(b))
3. $Q'_E = \{3,2\}$: $*246_{49R}(3)$ (Fig. 2.55(c))

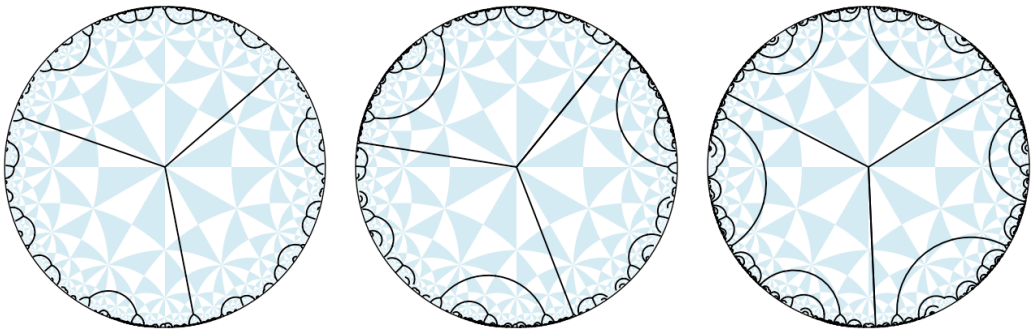

(a) **(b)** **(c)**

Figure 2.55: Three embeddings of the decorated 22223 orbifold in the $*246$ tiling of $\mathbb{H}^2$to give three distinct free tilings. Q'_E is chosen to be (a) $\{1,1\}$: $*246_{49R}(1)$, (b) $\{1,2\}$: $*246_{49R}(2)$, (c) $\{3,2\}$: $*246_{49R}(3)$.

This chapter presented a series of simply constructed free tilings. They were constructed to be commensurate with the symmetries of the genus–3 TPMS: the *P*, *D*, *G* and *H* surfaces. For a decoration of a Stellate orbifold, an infinite number of distinct embeddings into the surface charts exists, which all lead to distinct tilings of the surfaces. We presented the simplest embeddings of such tilings, along with the methodology to construct an infinite series of embedded tilings.

Free tilings are of interest because of the structures that result from their reticulation over the TPMS. In the case of regular ribbon tilings, the structures that result are the interpenetration of multiple net components. In the case of the complementary tilings, the vertex–free geodesic boundaries map to infinite 1–dimensional filaments, which are woven together in structures of varying complexity. This beautiful set of 3D structures will be presented in Ch. 3.

Chapter 3

Reticulations of Triply-Periodic Minimal Surfaces

The free tilings described in Ch. 2 may be reticulated over genus-3 Triply Periodic Minimal Surfaces (TPMS): Schwarz' Primitive (*P*) surface, Schwarz' Diamond (*D*) surface, Schoen's Gyroid (*G*) Surface and Schwarz' Hexagonal (*H*) Surface, all shown in Fig. 3.1. In this chapter, we project regular ribbon tilings of the two-dimensional Hyperbolic plane ($\mathbb{H}^2$) and their complements to each of these surfaces, and examine the structures that remain in three-dimensional Euclidean space ($\mathbb{E}^3$) when the surface scaffold is removed.

The 3D structures which arise from this construction fall into two main genres: if the free tiling in $\mathbb{H}^2$ contains vertices and edges on the tile boundaries, the structure will be the interpenetration of one or more nets, if the free tiling contains only vertex-free geodesic tile boundaries, the structure will be a weaving of infinite 1D filaments.

Structures within the first genre, which are composed of multiple nets, have interesting entanglement properties. The tile edges in the reticulation are restricted to be trajectories on the TPMS rather than the more traditional geodesic paths of $\mathbb{E}^3$ (straight edges). Through this extension, we enable edges to curve and tangle around each other, and allow the construction of structures which belong to a specific ambient isotopy class (as defined in Ch. 1.1), rather than simply a structure with a prescribed topology. Interesting entangled structures such as these are directly relevant to synthetic chemistry, where an increasing library of entangled molecules and structures are being synthesised to give varied material properties, for example see [Carl 03c].

Structures of the second genre are composed of entangled infinite 1D filaments, where a specific ambient isotopy class for each structure is inherited from the surface reticulation. Real structures composed of such filaments include polymer materials, felts, spindles in actin bundles and others, all of which readily allow bending and weaving of the filaments

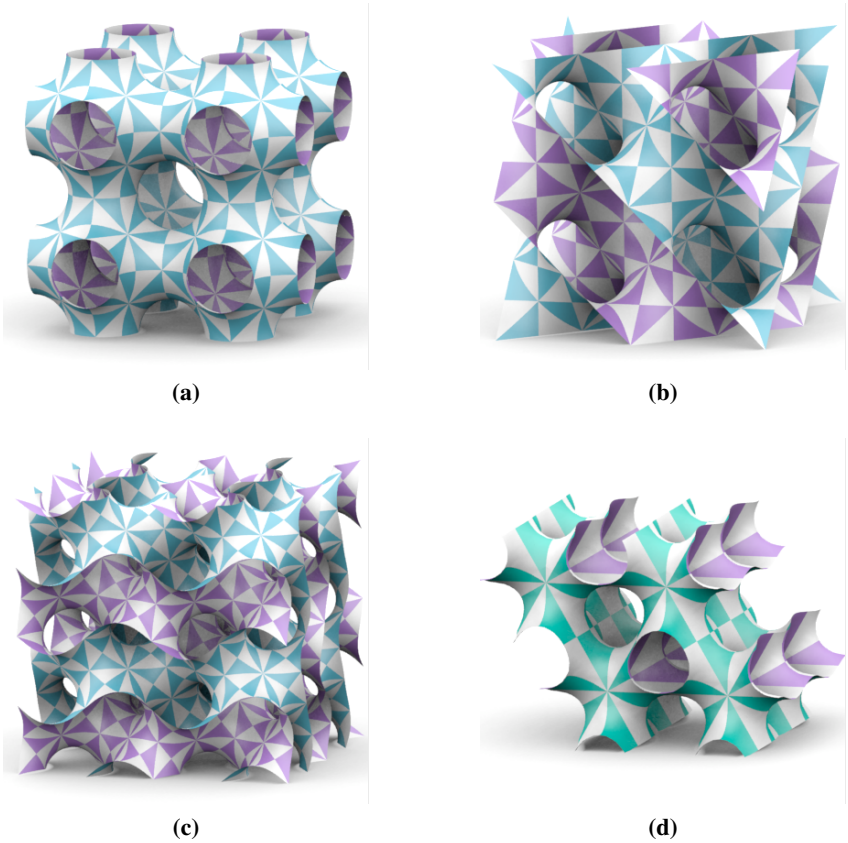

(a) **(b)**

(c) **(d)**

Figure 3.1: The cubic and hexagonal genus-3 TPMS, (a) *P* surface (b) *D* surface (c) *G* surface (d) *H* surface. The *P*, *D* and *G* surfaces are covered by an orientation preserving subgroup of $*246$, the *H* surface by an orientation preserving subgroup of $*2226$, see Ch. 2.0.1 for orbifold notation.

as they entangle, making entangled structures such as those constructed on the TPMS easily realisable.

To date, there is a complete lack of quantitative approaches to enumeration of entangled structures, whether they are composed of single or multiple nets, or infinite filaments. Here we present a broad range of entangled structures, which inherit their geometry (and ambient isotopy class) from TPMS.

3.1 From $\mathbb{H}^2$ to $\mathbb{E}^3$

An analytic construction allows us to go from an asymmetric domain of $\mathbb{H}^2$ to a unit cell of a TPMS, and in turn, the infinite surface. We begin with a domain in the two-dimensional Hyperbolic plane ($\mathbb{H}^2$) and obtain an embedded region of the surface in $\mathbb{E}^3$. In-surface symmetries of the TPMS are utilised to assemble the infinite surface from the asymmetric

region, *via* analytic continuation using the Schwarz reflection principle for extensions of complex functions to the entire complex plane ($\mathbb{C}^2$) [Bage 64]. In parallel with this process, we transfer decorations (tilings) in $\mathbb{H}^2$ to the embedded surfaces to obtain surface tilings in $\mathbb{E}^3$. This section analytically constructs each of the *P*, *D*, *G* and *H* surfaces.

3.1.1 Triply Periodic Minimal Surfaces

The *Gauss map* assigns to each point on a surface embedded in $\mathbb{E}^3$ a point on the unit two–dimensional sphere ($\mathbb{S}^2$), determined by the (oriented) surface normal orientation at that point on the surface [Dier 92]. Distinct families of TPMS arise from the relative orientations of the surface normal vectors at singular, isolated flat points where the Gaussian curvature vanishes. The relative orientations of the flat points manifest as the relative positions of branch points in the Gauss map [Fogd 92].

The *P*, *D* and *G* surfaces have a common Gauss map (they are isometric TPMS), and the *H* surface another. For both families, the Gauss map exhibits in-surface symmetries in $\mathbb{S}^2$ (and is a Coxeter group), where the complete Gauss map in $\mathbb{S}^2$ may be generated from values within a single asymmetric tile bounded by mirrors. Stereographic projections of the Gauss maps into the complex plane ($\mathbb{C}^2$) for these two families of TPMS are shown in Fig. 3.2 [Fogd 92].

The Gauss maps exhibit $*234$ symmetry in the *P*/*D*/*G* surface family, and $*223$ symmetry in the *H* surface family. The branch points of the Gauss map imply that the intrinsic surface symmetry of these TPMS in $\mathbb{E}^3$ will be $*246$ and $*2226$ respectively: a branch point of order one at a $*n$ symmetry site in the Gauss map gives a $*2n$ symmetry site on the TPMS [Hyde 03b]. More specifically, from the orbifold cost formula given in Ch. 2, these TPMS surface symmetries are hyperbolic!

The "Weierstrass parameterisation" from $\mathbb{C}^2$ into $\mathbb{E}^3$ gives an analytical representation of any minimal surface [Dier 92]. A set of equations specifies the Weierstrass parameterisation, where the Weierstrass-Enneper function $R(\omega)$ and the Bonnet angle (θ) are varied according to the specific TPMS desired [Fogd 92]:

$$x(\omega) = x_0 + Re\left(e^{i\theta}\int_{\omega_0}^{\omega}\left(1-\omega'^2\right)R\left(\omega'\right)\right) \tag{3.1}$$

$$y(\omega) = y_0 + Re\left(e^{i\theta}\int_{\omega_0}^{\omega} i\left(1+\omega'^2\right)R\left(\omega'\right)\right) \tag{3.2}$$

$$z(\omega) = z_0 + Re\left(e^{i\theta}\int_{\omega_0}^{\omega}\left(2\omega'\right)R\left(\omega'\right)\right) \tag{3.3}$$

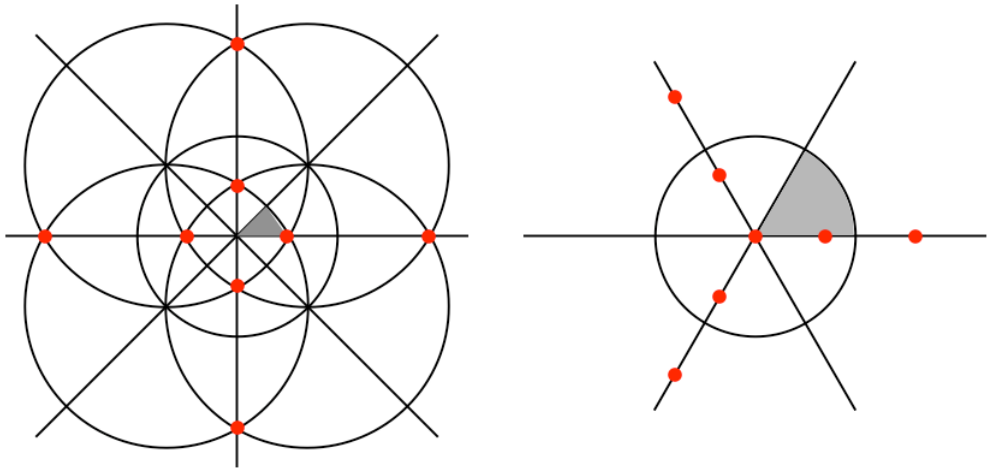

(a) **(b)**

Figure 3.2: Stereographic projection of the Gauss map from $\mathbb{S}^2$ to the complex plane, $\mathbb{C}^2$, of (a) the *P*/*D*/*G* surface family, and (b) the *H* surface family [Fogd 92]. The solid arcs represent mirror symmetries of the Gauss map in $\mathbb{S}^2$, the red circles represent order-1 branch points, and the shaded region a smallest asymmetric domain. Part (b) also has an order-1 branch point at infinity. The $\mathbb{S}^2$ symmetries of the Gauss maps are (a) $*234$ and (b) $*223$. The positioning of the branch points in the *H* surface family (excluding those at symmetry sites, the origin and points at infinity) can be sited anywhere within the edge of the asymmetric domain. The exact location sets the single free parameter of the *H* surface [Fogd 92].

We designate the family of TPMS through the choice of $R(\omega)$ in the Weierstrass parameterisation. Within a family of TPMS, we vary the Bonnet angle (θ) to obtain distinct embeddings of surfaces sharing the same intrinsic geometry (*via* their Gauss map). The *P*/*D*/*G* family of surfaces is constructed using $R(\omega)$ with a complex argument (ω) as follows, where Bonnet angles (θ) of 90°, 0° [Fogd 92] and approximately 38.0147740° [Scho 70] designate the *P*, *D* and *G* surfaces respectively:

$$\left[1-14\omega^4+\omega^8\right]^{-\frac{1}{2}}$$

The *H* surface family is constructed using $R(\omega)$ with a complex argument (ω) as follows, where '*A*' is the variable in the one parameter family, and $0<A<1$ [Fogd 92]:

$$\left[\omega-(A^3+A^{-3})\omega^4+\omega^7\right]^{-\frac{1}{2}}$$

The Bonnet angle for the *H* surface is 90°, the $\theta=0^\circ$ variant (the *H*' surface), however, is a self-intersecting surface [Fogd 92].

The complete construction of the TPMS from $\mathbb{H}^2$ involves morphing a smallest asym-

metric tile in $\mathbb{H}^2$ into a tile of $\mathbb{S}^2$, which is a conformal transformation everywhere except at special sites that correspond to flat points on the TPMS [Hyde 03b]. Using conformal stereographic projection, this spherical tile is mapped to a domain in $\mathbb{C}^2$. The Weierstrass parameterisation maps this tile from $\mathbb{C}^2$ to $\mathbb{E}^3$ to give a tile of the TPMS [Fogd 92]. In this thesis, we parameterise the TPMS using path integrals over the asymmetric domain avoiding the branch points to build the objects in $\mathbb{E}^3$.

Once an asymmetric tile of the surface is embedded in $\mathbb{E}^3$, the infinite surface may be assembled using the space group that encapsulates the in-surface symmetries of the TPMS. These space groups are $Im\bar{3}m$ or $Pm\bar{3}m$ for the unoriented or oriented P surface respectively, $Pn\bar{3}m$ or $Fd\bar{3}m$ (unoriented/oriented) for the D surface, $Ia\bar{3}d$ or $I4_132$ (unoriented/oriented) for the G surface and $P6_3/mmc$ or $P6m2$ (unoriented/oriented) for the H surface [Hyde 97]. The G surface is a special case: it has an asymmetric tile in $\mathbb{E}^3$ which consists of two asymmetric domains of the 2D surface (246 symmetry rather than $*246$) [Robi 05].

3.1.2 Structures in $\mathbb{E}^3$

We consider the vertices and edges of a free tiling contained within one fundamental domain in $\mathbb{H}^2$. These vertices and edges are transferred to the corresponding patch on the TPMS. The infinite TPMS tiling is then generated using a space group that encapsulates the required $\mathbb{H}^2$ symmetries on the TPMS in $\mathbb{E}^3$. The correspondence between the $\mathbb{H}^2$ orbifolds symmetry and their space group manifestations on each of the TPMS will be published elsewhere [Hyde 11]. The surface tiling consists of vertices, edges and faces, all embedded in $\mathbb{E}^3$. To obtain a structure in $\mathbb{E}^3$, we disregard the faces of these surface tilings, so as to leave only vertices and edges in $\mathbb{E}^3$. This is the final 3-periodic structure in $\mathbb{E}^3$.

To transfer tilings (with TPMS commensurate symmetry) from $\mathbb{H}^2$ to the TPMS, we initially select a fundamental domain of the tiling in $\mathbb{H}^2$. Regardless of the freedom for choosing such a domain, we select exactly one region for each symmetry group of $\mathbb{H}^2$, and identify this region on each of the commensurate TPMS. For example, Fig. 3.3 shows a 2223 fundamental domain in the $*246$ tiling as well as the same region on the P surface.

The exception to this is the G surface, where there are two distinct covering maps of the surface from $*246$ commensurate tilings in $\mathbb{H}^2$ [Robi 05], and hence two distinct conjugacy classes of structures arise. Tilings in $\mathbb{H}^2$ that are unchanged under any of the $*246$

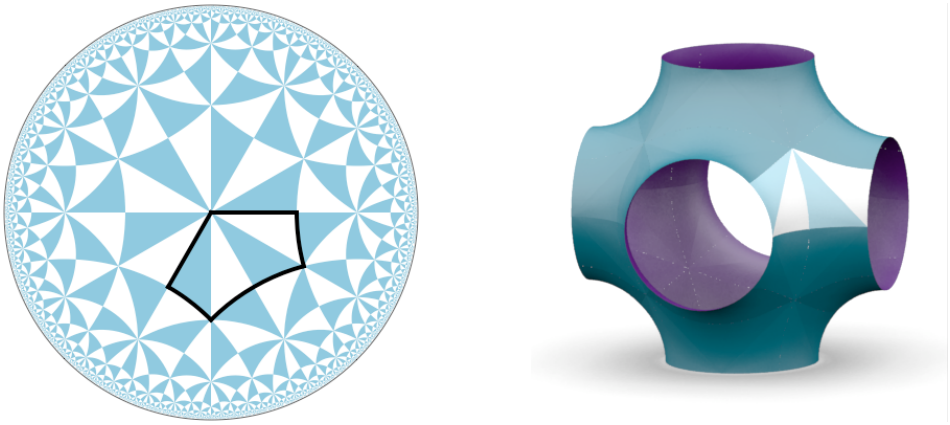

(a) (b)

Figure 3.3: A fundamental domain of the 2223 symmetry group (a) in $\mathbb{H}^2$, (b) on the *P* surface. The choice of domain in both cases has freedom, however, variation of the domain corresponds to conjugacies of $\mathbb{E}^3$. We transfer tilings from $\mathbb{H}^2$ to the TPMS on this domain, and assemble the infinite tiling using a space group corresponding to the symmetry of the tiling.

reflections will render the two conjugacy classes of structures equivalent, and tilings that do not have this inherent symmetry will have two distinct conjugacy classes of structures on the *G* surface. Reflection of a tiling in one set of mirrors of the $*246$ pattern will give these two distinct structures *via* the same map from $\mathbb{H}^2$ to the *G* surface.

Many of the structures fabricated in this chapter will contain multiple interpenetrating nets. There are five so called 'regular' Euclidean nets: if we consider a net as the vertices and edges of a packing of polyhedra, the packing which defines a regular net will have 1-transitive vertices, edges and faces *i.e.* all vertices, edges and faces are symmetrically equivalent, and the Delaney-Dress triangulation contains a single flag. The sole regular net of degree-3 is the **srs** net, also known as *SrSi*, Y^* or $3/10/c1$. There are two regular nets of degree-4, **nbo** (also known as *NbO*, J^* or $4/6/c2$) and **dia** (also known as *Diamond*, *D* or $4/6/c1$). Further, there are two regular nets of degree-6, **pcu** (also known as *Primitive Cubic Lattice*, $c-6$ or $6/4/c1$) and **bcu** (also known as *Body Centered Cubic*, *cI* or $8/4/c1$) [Delg 02].

Some structures also contain 2-periodic layers, catenated in a way that gives a 3-periodic structure. The layer graphs which have 1-transitive vertices and edges include **hcb** (also known as $(6,3)$, *honeycomb*, 6^3 or *OKH*03) in the case of degree-3 vertices, **sql** (also known as *Square Lattice*, $(4,4)$, 4^4 or *OKH*02) in the case of degree-4 vertices and **hxl** (also known as *Hexagonal Lattice*, $(3,6)$, 3^6 or *OKH*01) in the case of degree-6 vertices [OKee 08].

We analyse the structures built in this chapter *via* the following set of measures:

1. Number of connected components, obtained through TOPOS analysis [Blat 06].
2. Topology of connected components, obtained through TOPOS analysis [Blat 06] or GAVROG SyStRe analysis [Delg].
3. Symmetry relations between distinct components, as defined in [Carl 03c]. *Class I* has only translational relations between components: *Ia* has one translation and *Ib* has two independent translations. *Class II* has only rotational relations: *IIa* has one distinct rotation and *IIb* has two distinct rotations. *Class III* has both translational and rotational relations: *IIIa* has a single translation and single rotation, *IIIb* has multiple translations and a single rotation, *IIIc* has a single translation and multiple rotations, and *IIId* has multiple translation and rotations.
4. TOPOS analysis assesses the interpenetration of the structure through the entanglement of all cycles within the structure [Blat 06]. It considers each distinct type of ring and analyses the type of link formed with all distinct rings in the structure.
5. The *Density-of-Catenation* (DoC) is a measure of catenation in a structure: it collates the number of distinct cycles with which a single cycle is threaded [Carl 03c].
6. For nets composed of parallel, 2-periodic layers that catenate to form a 3-periodic structure, the *Index-of-Separation* (IoS) ascertains how many components must be removed for the structure to separate into two [Carl 03c].
7. Where a network is chiral (not superimposable on its mirror image), the *handedness* describes which enantiomer of the net is present. As these structures are surface reticulations, the other enantiomer of the structure may be obtained from a conjugacy of the surface, we consider the relative handedness of distinct components: are all of the components of the same chirality, or different?

There is another mode of entanglement that will occur in the structures in this chapter, namely Borromean entanglement. It is an entanglement analogous to the Borromean rings, Fig. 3.4, where no two rings are threaded, yet all three are entangled. The term *Brunnian*, which is a related phenomenon, refers to the property that the entanglement completely disintegrates on the removal of a single component. Structures containing nets entangled in such a way as to have no threaded cycles have been studied and synthesised [Carl 03a, Carl 03c]. There are two modes of entanglement that we call Borromean.

The first is *2D Borromean*, which is a 2-periodic layer composed of three 2-periodic nets, where there is no threading of cycles. This entanglement is also Brunnian, as no entanglement will remain on removal of a single component. The second is the *3D Borromean* structure, which is a 3-periodic structure composed of 2-periodic layers: there are no threaded cycles, and the removal of one layer of the structure will cause the structure to separate in two. This last entanglement is not strictly Brunnian, as some entanglement remains on the removal of a single component.

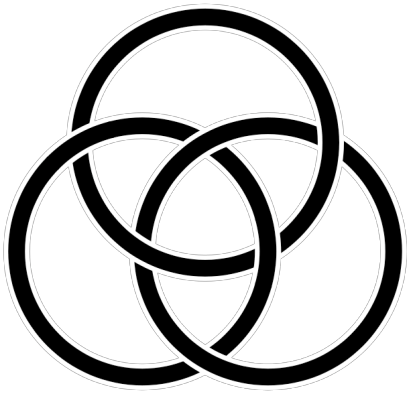

Figure 3.4: The Borromean rings, where no two rings are threaded, but all three are entangled.

Some of the free tilings considered are composed of infinite geodesic tile boundaries. When reticulated over the TPMS, the resulting structure is a crystalline array of one-dimensional (1D) filaments. Many of the methods employed in the analysis of interpenetrating nets are not applicable in the case of filament weavings. The only measure still applicable from the list above is the handedness measure, where the filaments are helical in shape. Measures of these crystalline filament arrays will be presented in Ch. 4.

3.2 Interpenetrating Nets

We consider the reticulation of the regular ribbon tilings over the TPMS, which give structures composed of interpenetrating nets in $\mathbb{E}^3$. Recall from Ch. 1 that a 3-periodic net in three-dimensional Euclidean space ($\mathbb{E}^3$) is a simple, 3-connected periodic graph, which is invariant under three independent translations of $\mathbb{E}^3$ [Klee 04]. We consider here structures the contain nets of degree-3, degree-4 and degree-6.

3.2.1 Degree-3 nets: srs, hcb and finite polyhedra

One fundamental domain of the $*2223$, $2*23$ and 2223 symmetry groups each contains two, two and four $*246$ triangles respectively. The cubic space groups whose isometries take a single patch of these orbifolds on each of the TPMS and construct the infinite surface are shown in the table in Fig. 3.5 for each of the *P*, *D* and *G* surfaces [Hyde 11]. The outline of the 2223 fundamental domain is shown in $\mathbb{H}^2$ and on the *P*, *D* and *G* surfaces in Fig. 3.5. Domains for the $*2223$ and $2*23$ symmetry groups may be inferred from this positioning.

	$*2223$	$2*23$	2223
P	$Pm\bar{3}m$	$I432$	$P432$
D	$P4_232$	$Fd\bar{3}m$	$F4_132$
G	-	-	$I4_132$

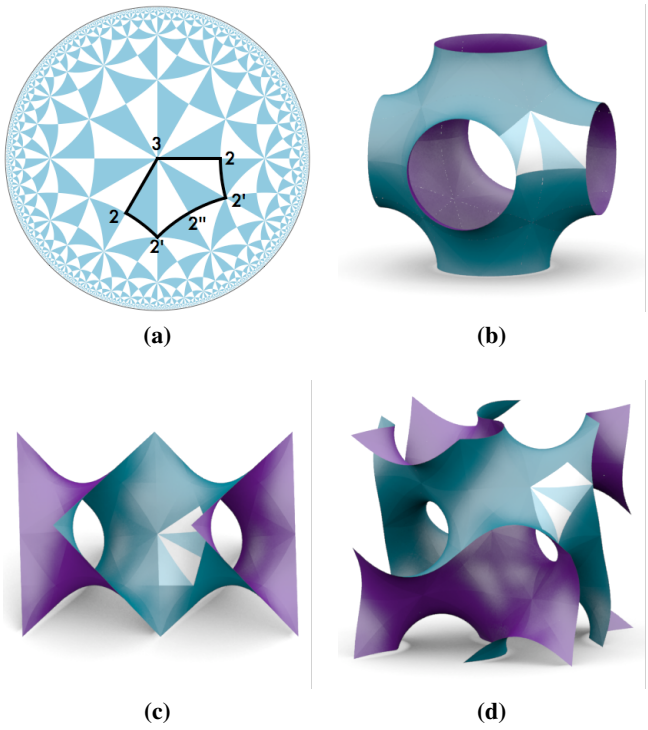

Figure 3.5: (Left) Space group and hyperbolic orbifold relations. (Right) The 2223 fundamental domain, shown (a) in $\mathbb{H}^2$, (b) on the *P* surface, (c) on the *D* surface, and (d) on the *G* surface.

Regular 2D ribbon tilings with symmetry $*2223$, $2*23$ and 2223, constructed in Ch. 2.3, have 8 vertices per translational TPMS unit cell (one such unit cell consists of 96 $*246$ tri-

angles, and the tilings have one vertex per 12 $*246$ triangles [Robi 04a]). These 8 vertices are equivalent by symmetry (1-transitive vertices), there are 3 edges incident at each vertex (degree-3) and all edges are related by symmetry (1-transitive edges). Thus the resulting structures on the TPMS must be embedded graphs of degree-3 with 1-transitive vertices and edges, which include **srs** in the 3-periodic case, **hcb** in the 2-periodic case, or arrays of finite cubes, tetrahedra, or theta-graphs (two vertices connected by three edges, reminiscent of the symbol θ). The structures that result have a range of connected components, and distinct threading between the components, which indicates that the structures are not equivalent by ambient isotopy (as defined in Ch. 1.1).

We summarise the results in Table 4.7. The structures are named to reflect the surface on which it is constructed and the embedded tiling name in $\mathbb{H}^2$ (see Ch. 2). For example, the structure that is the projection of the $*246_{118R}(1)$ tiling[1] to the P surface is called $P_{118R}(1)$. For G surface structures, a $+$ or $-$ signifies the two possible covering maps of the surface [Robi 05]: where this is absent, the two structures from the two covering maps are equivalent.

Structures $P_{118R}(1)$, $D_{118R}(1)$ and $G_{118R}(1)$ are constructed from equivalent tilings in $\mathbb{H}^2$ ($*246_{118R}(1)$), *via* each of the P, D and G surfaces respectively. Each structure consists of the inclined catenation of four directions of parallel trivial **hcb** nets, where the inclined layers normal vector orientations of $[1,1,1]$, $[-1,1,1]$, $[1,-1,1]$, and $[1,1,-1]$, giving angles of inclination of 70.5°. Topos analysis [Blat 06] of $P_{118R}(1)$ identifies 18 Hopf links: 6 cycles from each of the 3 other directions (4 directions in total) thread a single cycle. Each edge that threads this cycle will have two associated cycles, hence exactly 3 edges thread the cycle for each unique layer orientation, which gives a DoC of {9,9,9,9}. The structure $D_{118R}(1)$ has 12 Hopf links and hence has a DoC of {6,6,6,6}. The structure $G^{+}_{118}(1)$ G surface reticulation (Example 10) has 30 Hopf links: DoC is {15,15,15,15}.

Each of these structures is the inclined catenation of four directions of **hcb**. Of note is a synthesised case of a structure composed of the inclined catenation of four directions of **hcb** [Carl 03b]. This synthesised structure, however, has distinct normal vector orientations of the layers to the examples constructed on the TPMS: the synthesised case has normal vector orientations of $[1,0,4]$, $[-1,0,4]$, $[0,-1,4]$, and $[0,1,4]$, as opposed to $[1,1,1]$, $[-1,1,1]$, $[1,-1,1]$, and $[1,1,-1]$ in the constructed examples. TOPOS confirms that the synthesised structure is not equivalent by ambient isotopy to either $P_{118R}(1)$,

[1] Recall that group 124 is $*2223$, group 129 is $2*23$ and group 118 is 2223, see Appendix. A.

Table 3.1: Degree-3 structures. The column "# comp." refers to the number of connected components in the structure. Note that $n*$ designates infinitely many 2-periodic layers arranged in n distinct orientations. For some structures, we state the TOPOS linking signature (*e.g.* 92 Hopf links): this is the number of different linked cycles within the structure, all other linked cycles will be symmetric copies.

Structure	Figure	# comp.	Topology	Notes
P_{124R}	Fig. 3.6	∞	cubes	Array of isolated graphs
P_{129R}	Fig. 3.7(a-c)	8	**srs**	Equivalent handedness, 92 Hopf links
$P_{118R}(1)$	Fig. 3.7(d-f)	4*	**hcb**	Normal vector orientations of $[1,1,1]$, $[-1,1,1]$, $[1,-1,1]$, and $[1,1,-1]$, and DoC $\{9,9,9,9\}$
$P_{118R}(2)$	Fig. 3.7(g-i)	8	**srs**	Equivalent handedness, 168 Hopf links and 16 complex links
D_{124R}	Fig. 3.8(a-c)	4	**srs**	Equivalent handedness, 36 Hopf links
D_{129R}	Fig. 3.8(d-f)	∞	tetrahedra	Array of isolated graphs
$D_{118R}(1)$	Fig. 3.8(g-i)	4*	**hcb**	Normal vector orientations of $[1,1,1]$, $[-1,1,1]$, $[1,-1,1]$, and $[1,1,-1]$, and DoC $\{6,6,6,6\}$
G_{124R}	Fig. 3.9(a-c)	2	**srs**	Same handedness, 18 Hopf links and one complex link
G_{129R}	Fig. 3.9(d-f)	2	**srs**	Same handedness, 23 Hopf links and 3 complex links
$G^{+}_{118R}(1)$	Fig. 3.9(g-i)	4*	**hcb**	Normal vector orientations of $[1,1,1]$, $[-1,1,1]$, $[1,-1,1]$, and $[1,1,-1]$, and DoC $\{15,15,15,15\}$

$D_{118R}(1)$ or $G_{118R}(1)$.

Structures P_{129R} and $P_{118R}(2)$ each consist of 8 interpenetrating **srs** nets. In both cases, the interpenetration belongs to Class *IIIb*: the 8 nets are related by two independent translations and a single 2-fold rotation. We may infer that each of the **srs** components is of equivalent handedness, as there are no reflection symmetries. P_{129R} contains 92 hopf links in total. On the other hand, $P_{118R}(2)$ contains 168 Hopf links, and 16 links with higher crossing numbers. These distinct links are sufficient to demonstrate that these structures are not equivalent under ambient isotopy, despite their equivalent topology.

The interpenetration of multiple **srs** nets was first proposed in [Well 77], which describes the interpenetration of 4 **srs** nets of equivalent chirality. The structure D_{124R} also consists of 4 **srs** components, related by two independent translations, Class *Ib*, where all **srs** components are of the same chirality. The Topos output shows 36 Hopf links are

present in the structure. The interpenetration of 4 **srs** nets of equivalent chirality also exists as a synthetic structure [Kepe 98].

The structures G_{124R} and G_{129R} each contain two **srs** nets of equivalent handedness, related by a single translation (Class *Ia*) in the first case, and a single rotation (Class *IIa*) in second case. However, this does not demonstrate that these two structures are of distinct ambient isotopy classes, as this may be a symptom of the geometric embeddings of the structure. The G_{124R} structure consists of 18 Hopf links and a single higher order link and the G_{129R} structure 23 Hopf links and 3 higher order links, hence the two nets are not equivalent under ambient isotopy. Such a structure, composed of 2 **srs** nets of equivalent chirality, is synthesised in [Kepe 00].

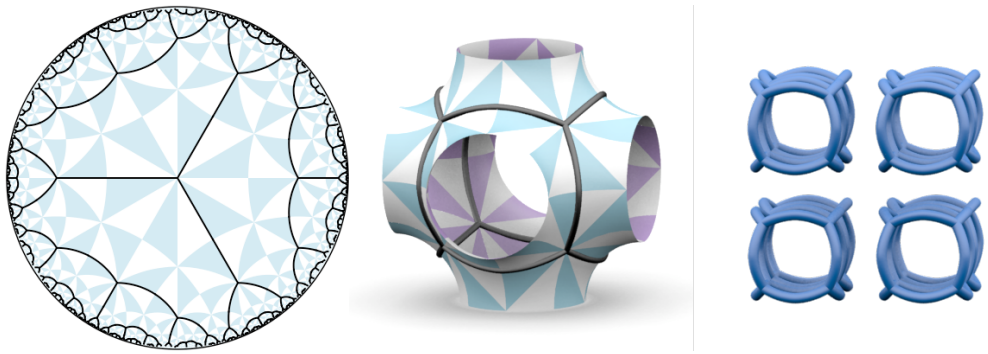

(a) **(b)** **(c)**

Figure 3.6: The P_{124R} structure is an array of isolated cube edge graphs, constructed via the reticulation of the *P* surface by the tiling $*246_{124R}$ of $\mathbb{H}^2$. The three images show the structure as a tiling of $\mathbb{H}^2$, on one unit cell of the *P* surface and in $\mathbb{E}^3$.

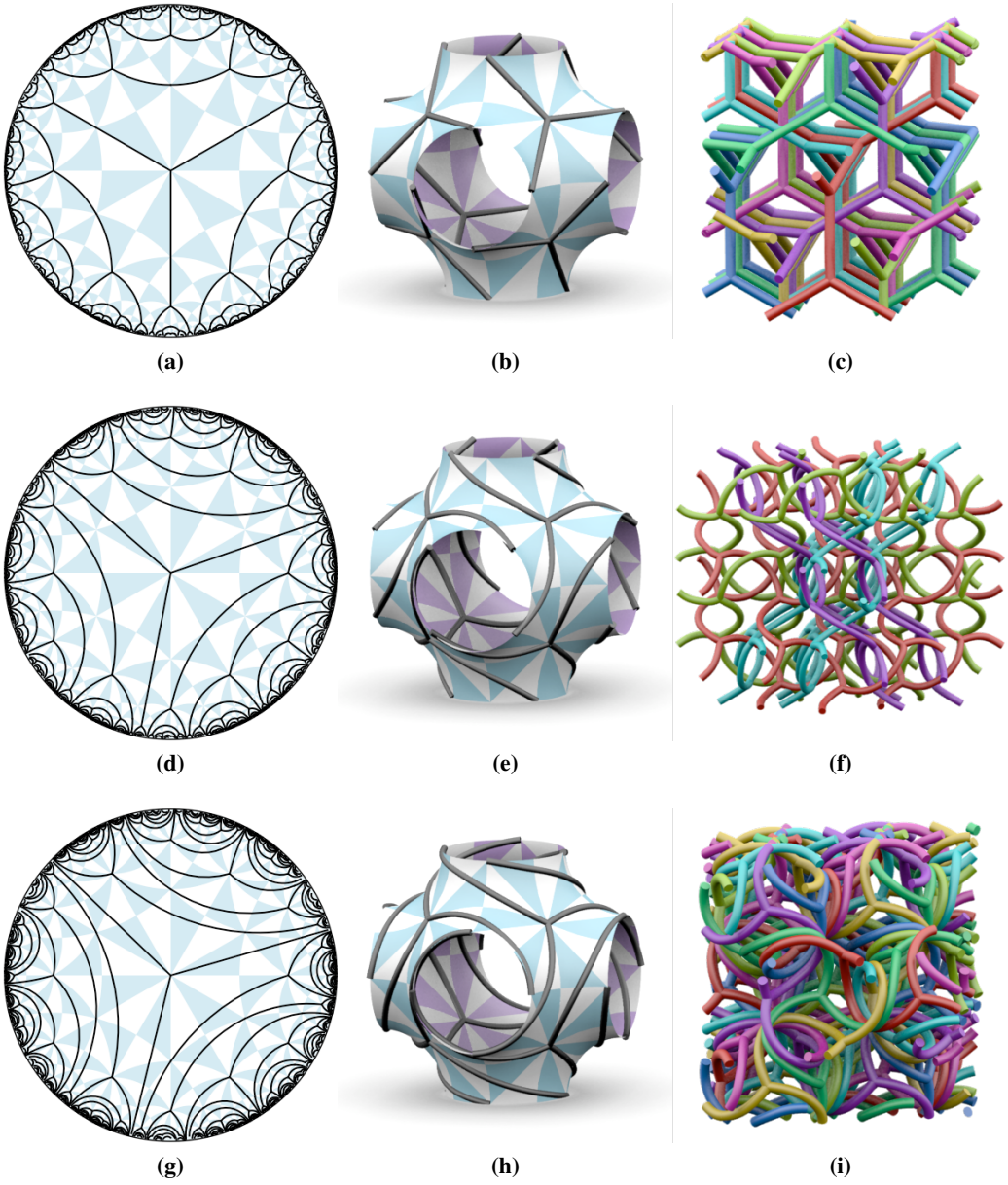

Figure 3.7: (a-c) The P_{129R} structure, built on the P surface from the $*246_{129R}$ tiling, is composed of 8 interpenetrating **srs** components. (d-f) The $P_{118R}(1)$ structure, constructed on the P surface from the tiling $*246_{118R}(1)$, consists of parallel **hcb** nets aligned in four directions with surface normal orientations of $[1,1,1]$, $[-1,1,1]$, $[1,-1,1]$, and $[1,1,-1]$, and a DoC of $\{9,9,9,9\}$. (g-i) The $P_{118R}(2)$ structure contains 8 **srs** components. A single cycle forms a Hopf link with 168 cycles, and a higher crossing link with 16 cycles. This structure is not equivalent to P_{129R} under ambient isotopy despite the equivalent topology.

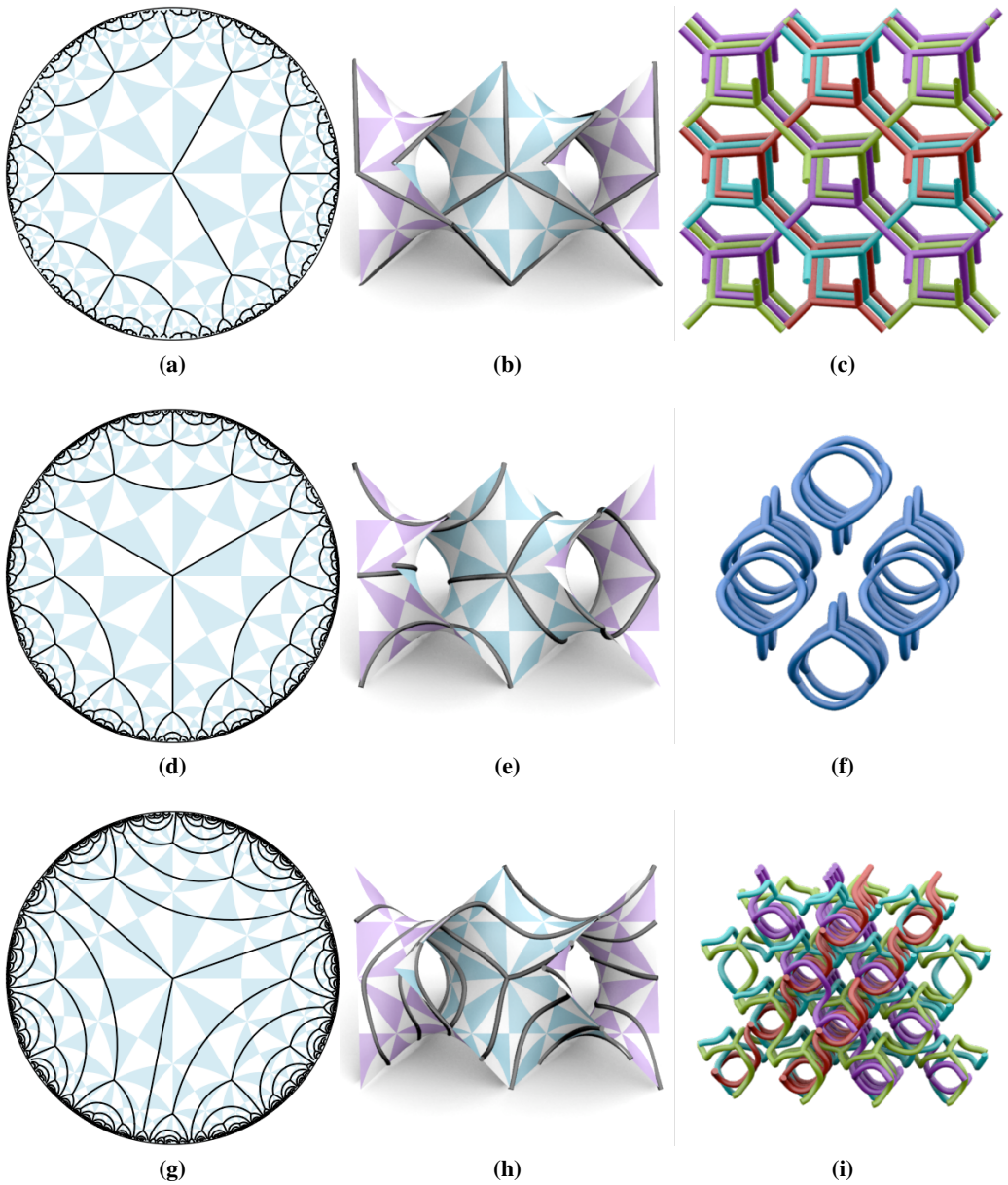

Figure 3.8: (a-c) The D_{124R} structure contains 4 interpenetrating **srs** nets, of equivalent handedness. The three images show the structure as a tiling of $\mathbb{H}^2$, on one unit cell of the D surface and in $\mathbb{E}^3$. (d-f) D_{129R} is an array of isolated tetrahedron graphs. (g-h) The $D_{118R}(1)$ structure contains four directions of **hcb** with normal vector orientations of $[1,1,1]$, $[-1,1,1]$, $[1,-1,1]$, and $[1,1,-1]$, and DoC of $\{6,6,6,6\}$.

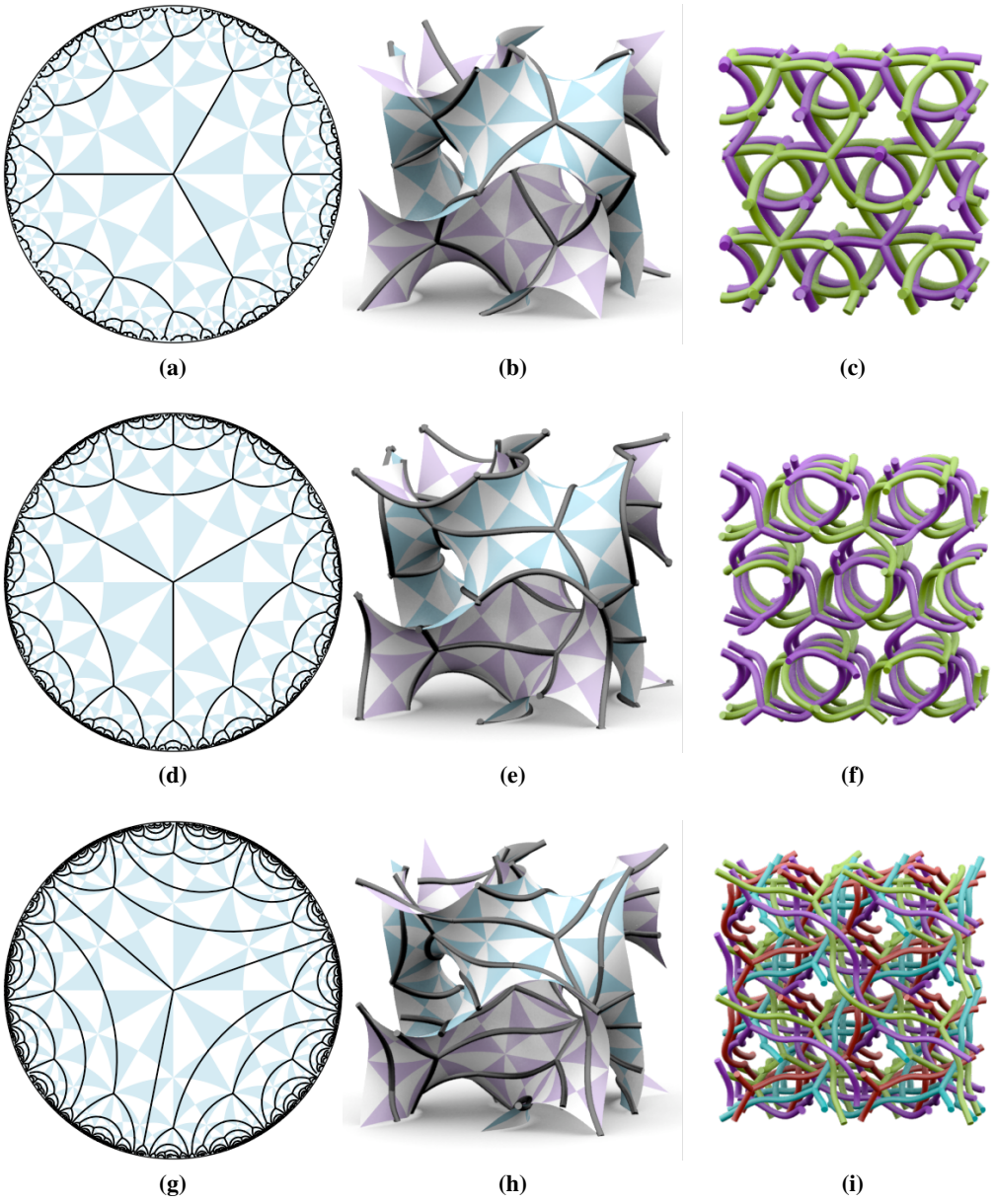

Figure 3.9: (a-c) The G_{124R} structure is 2 interpenetrating **srs** nets, of equivalent handedness. (d-f) The G_{129R} also consists of 2 interpenetrating **srs** nets, however this configuration is not equivalent under ambient isotopy to G_{124R}. (g-i) $G_{118R}(1)$ contains four orientations of $(6,3)$ nets with normal directions $[1,1,1]$, $[-1,1,1]$, $[1,-1,1]$, and $[1,1,-1]$.

3.2.2 Degree-4 nets: dia, sql and 4-chains

In $\mathbb{H}^2$, the $*2224$ and 2224 symmetry groups consist of 3 and 6 $*246$ triangles respectively, as may be ascertained by the orbifold cost formula (Ch. 2.0.1). We select a fundamental domain, which is not unique, for the 2224 symmetry group in the $*246$ tiling of $\mathbb{H}^2$, as outlined in Fig. 3.10. We then assign a corresponding domain on each of the *P*, *D* and *G* surfaces. The vertices and edges of an $\mathbb{H}^2$ tiling within this fundamental domain are transferred to the domain of each of the surfaces to give surface tilings. The in-surface symmetries of the 2224 symmetry group (or $*2224$) manifest as tetragonal space group symmetries in $\mathbb{E}^3$ [Hyde 11]: these space groups are shown in Fig. 3.10. The domain for the $*2224$ symmetry group may be inferred from the Figure (half of the 2224 domain).

	$*2224$	2224
P	$I4/mmm$	$P4/nnc$
D	$P4_2/nnm$	$I4_1/acd$
G	-	$I4_1/acd$

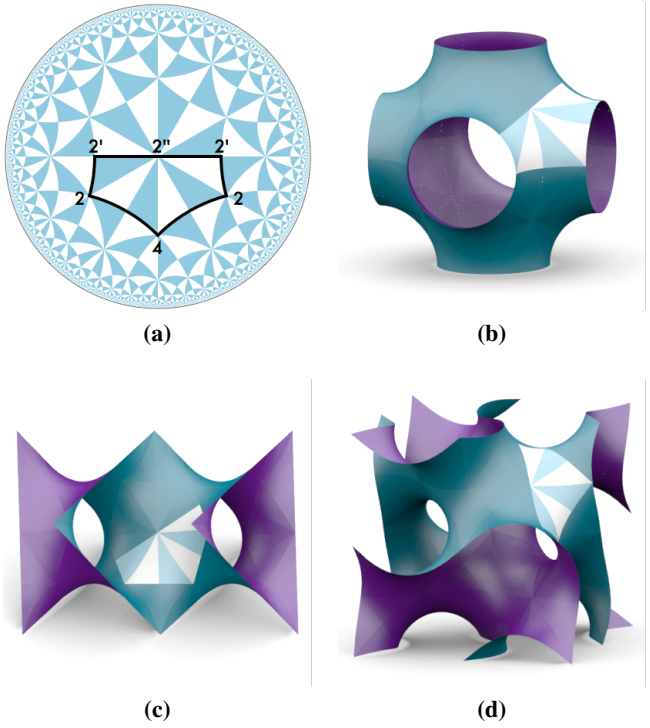

Figure 3.10: (Left) Space group and hyperbolic orbifold relations. (Right) The 2224 fundamental domain, shown (a) in $\mathbb{H}^2$, (b) on the *P* surface, (c) on the *D* surface, and (d) on the *G* surface.

Regular ribbon tilings with a degree-4 vertex (symmetry $*2224$ or 2224), which were constructed in Ch. 2.3, have 4 vertices per translational unit cell of the TPMS: one translational unit cell consists of 96 $*246$ triangles, and the tilings have one vertex per 24 $*246$ triangles. All vertices and edges are equivalent (1-transitive), hence we can infer possible resulting nets in $\mathbb{E}^3$ from known 1-transitive examples: these include 3-periodic **dia** components, 2-periodic **sql** components, or arrays of 1-periodic 4-chains (chains of degree-4

vertices, each connected by 2 edges).

A summary of the nets which result from the reticulation of regular ribbon tilings with symmetry $*2224$ (group 123) and 2224 (group 114) over the P, D, and G surfaces is shown in Table 4.8. The structures are named so as to reflect the surface over which the tiling is reticulated as well as the embedded tiling name in $\mathbb{H}^2$ (see Ch. 2). For example, the structure that comes from the projection of the $*246_{114R}(1)$ tiling, over the D surface will be called $D_{114R}(1)$.

Table 3.2: Degree-4 nets. The column "# comp." refers to the number of connected components in the structure. Note that $n*$ designates infinitely many 2-periodic layers arranged in n distinct orientations. For some structures, we state the TOPOS linking signature (*e.g.* 92 Hopf links): this is the number of different linked cycles within the structure, all other linked cycles will be symmetric copies.

Structure	Figure	# comp.	Topology	Notes
$P_{123R}(1)$	Fig. 3.11(a-c)	$1*$	**sql**	parallel array
$P_{123R}(2)$	Fig. 3.11(d-f)	∞	4-chains	array of parallel 1-periodic degree-4 chains
$P_{114R}(1)$	Fig. 3.12(a-c)	4	**dia**	18 Hopf links
$P_{114R}(4)$	Fig. 3.12(d-f)	4	**dia**	59 Hopf links and 3 links with higher crossing numbers
$D_{123R}(1)$	Fig. 3.13(a-c)	2	**dia**	6 Hopf links
$D_{114R}(1)$	Fig. 3.13(d-f)	2	**dia**	6 Hopf links
$G_{123R}(1)$	Fig. 3.14(a,c,e)	2	**dia**	6 Hopf links
$G_{123R}(2)$	Fig. 3.14(b,d,f)	2	**dia**	6 Hopf links

We analyse the examples that consist of multiple interpenetrating **dia** nets by the Topos program to detect distinct ambient isotopies where possible. The structures $P_{114R}(1)$ and $P_{114R}(4)$ each have 4 **dia** components. The relation between distinct components of the net is Class *IIIa* in both cases: components are related by both a translation and a 2-fold rotation. The $P_{114R}(1)$ structure has 18 Hopf links within a distinct cycle. In the $P_{114R}(4)$ structure, the interpenetration gives 59 Hopf links and 3 links of higher crossing numbers. This difference in interpenetration is sufficient to show that the two structures are not equivalent by ambient isotopy.

The structures $D_{123R}(1)$, $D_{114R}(1)$, $G_{123R}(1)$ and $G_{123R}(2)$ are each composed of 2

disjoint components of **dia**. To ascertain if the structures belong to an equivalent ambient isotopy class, we analyse by Topos. In all four cases, the relation between the constituent components is a single 2-fold rotation (Class *IIa*), and exactly 6 Hopf links are identified in the structure. It seems (by visual inspection) that these four structures are equivalent by ambient isotopy, however the current tools are insufficient to show this categorically. The tightening algorithm for periodic structures introduced in Ch. 4 may provide further evidence of equivalence in cases such as these.

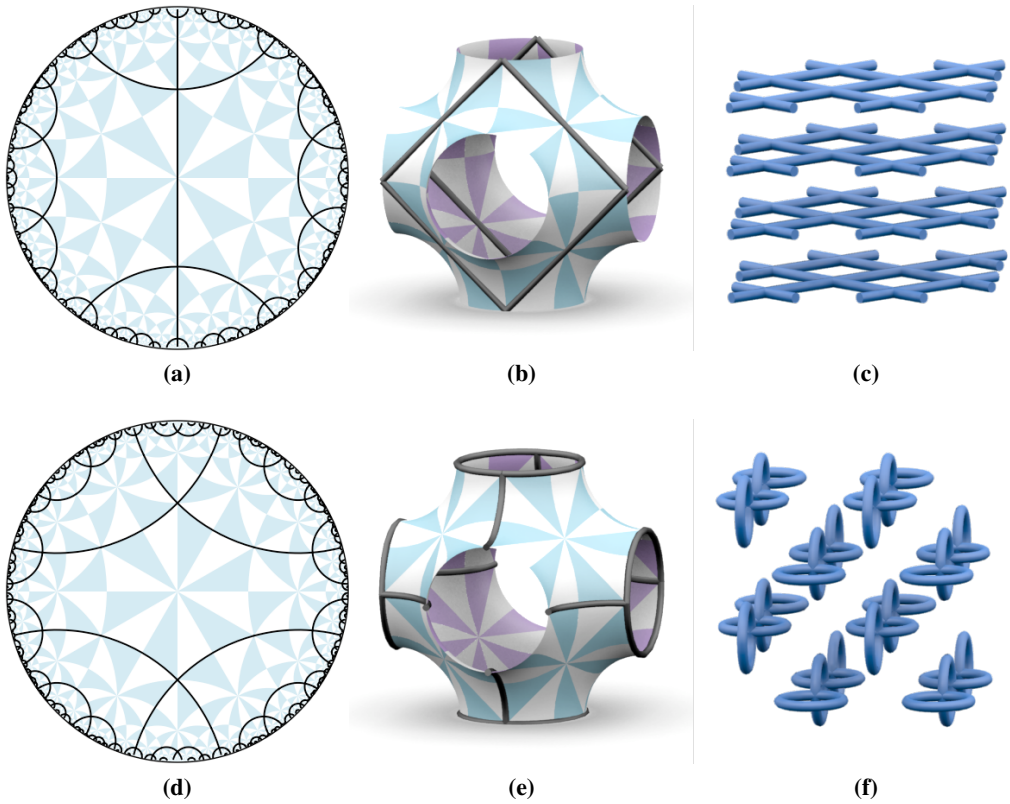

Figure 3.11: (a-c) The $P_{123R}(1)$ structure, constructed from the reticulation of the $*246_{123R}(1)$ tiling over the *P* surface, is composed of parallel 2-periodic **sql** nets. The three images show the structure as a tiling of $\mathbb{H}^2$, on one unit cell of the *P* surface and in $\mathbb{E}^3$. (d-f) The $P_{123R}(2)$ structure, built from the $*246_{123R}(2)$ tiling of $\mathbb{H}^2$, is an array of 1-periodic 4-chains.

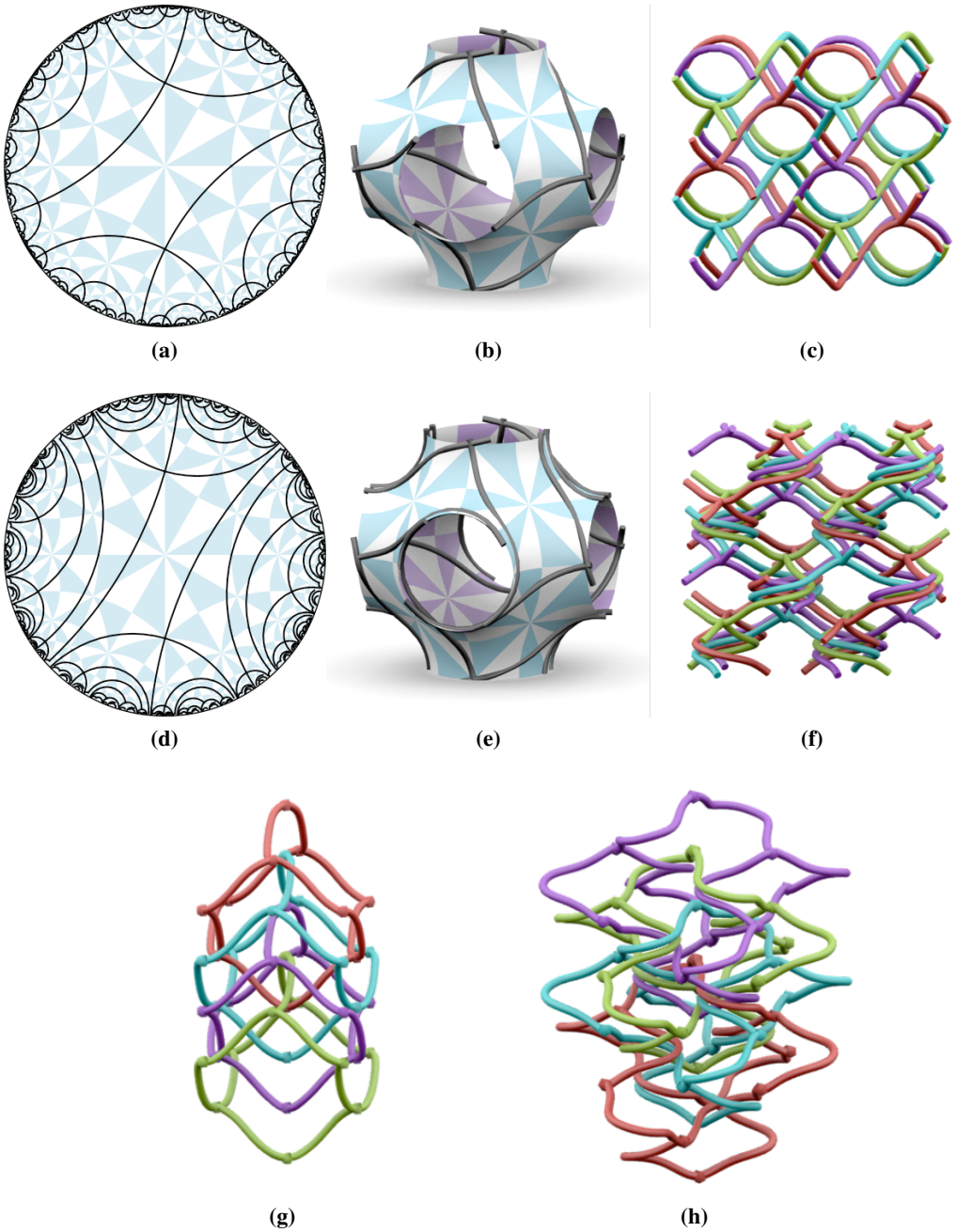

Figure 3.12: (a-c) The $P_{114R}(1)$ structure consists of the interpenetration of 4 components of **dia**. The three images show the structure as a tiling of $\mathbb{H}^2$, on one unit cell of the P surface and in $\mathbb{E}^3$. (d-f) The $P_{114R}(4)$ structure is also contains 4 interpenetrating components of **dia**. (g,h) A single adamantane cage of each disjoint component of **dia** for each of $P_{114R}(1)$ and $P_{114R}(4)$ respectively: subsequent analysis of these structures show that they are not equivalent under ambient isotopy.

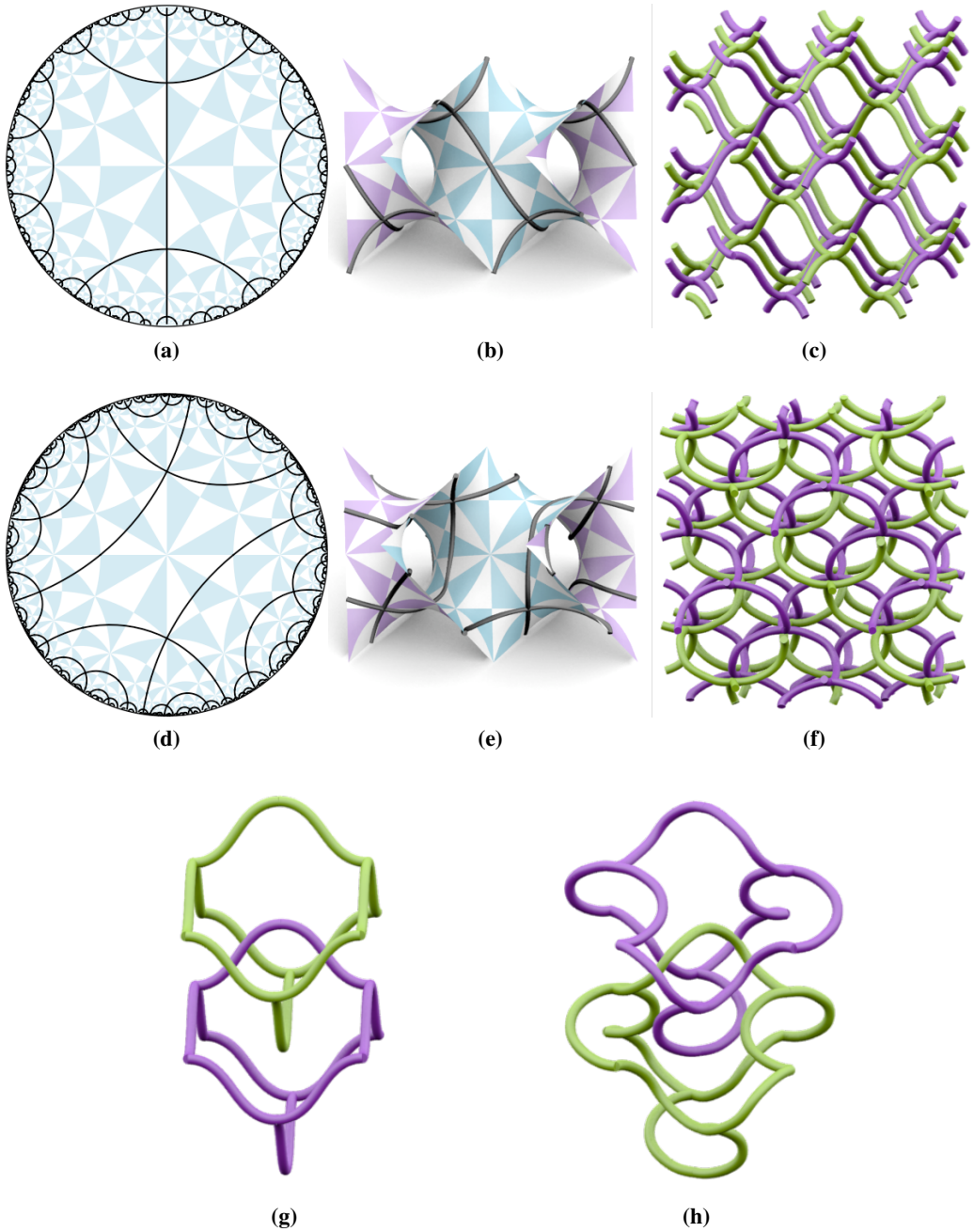

Figure 3.13: (a-c) The structure $D_{123R}(1)$, constructed on the D surface from the hyperbolic tiling $*246_{123R}(1)$, consists of 2 interpenetrating components of **dia**. The three images show the structure as a tiling of $\mathbb{H}^2$, on one unit cell of the D surface and in $\mathbb{E}^3$. (d-f) The structure $D_{114R}(1)$ as also composed of 2 interpenetrating components of **dia**. (g,h) A single adamantane cage of each disjoint component for the two structures. It is likely these structures are equivalent under ambient isotopy.

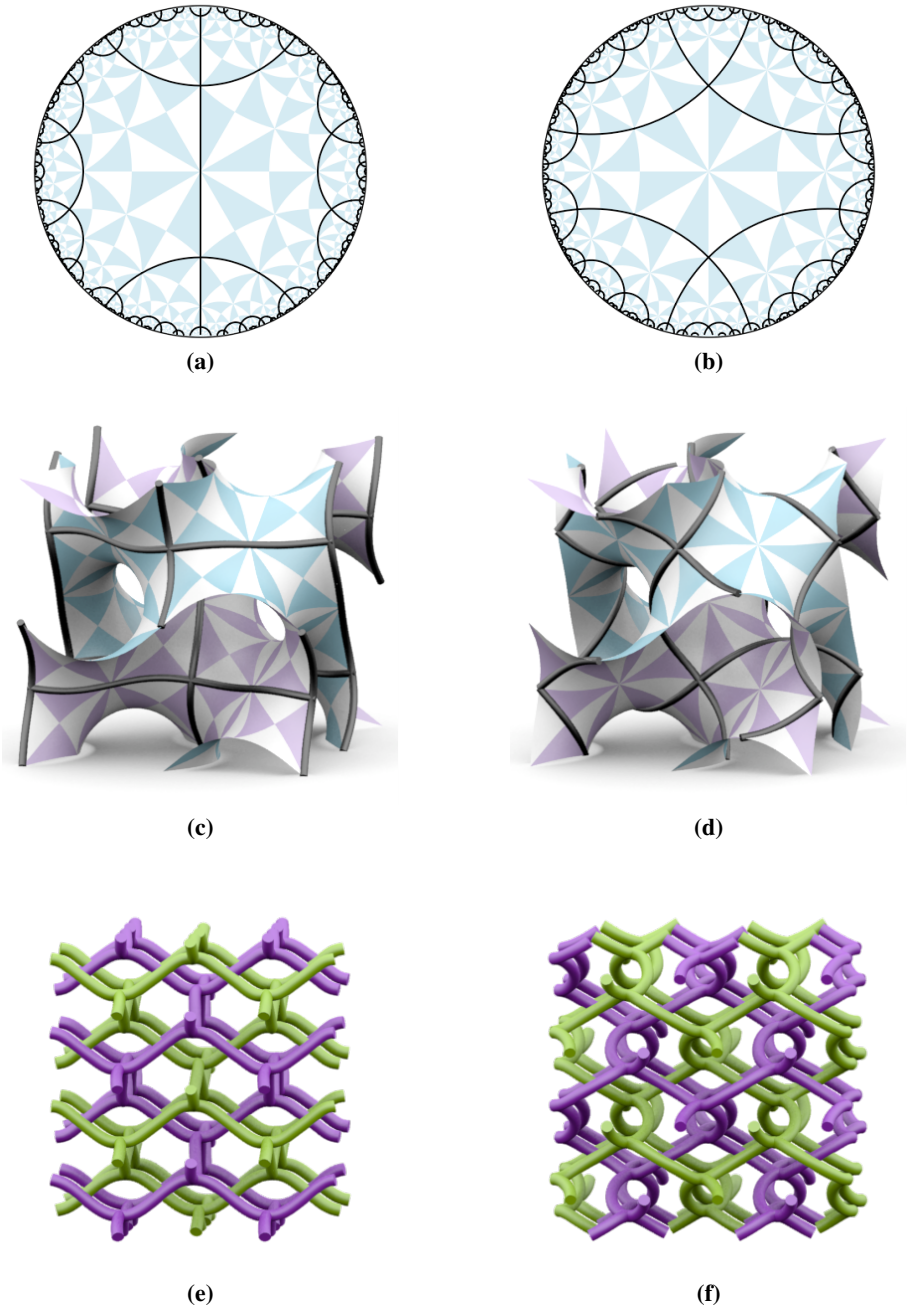

Figure 3.14: (a,c,e) The $G_{123R}(1)$ structure, constructed on the G surface, comprises 2 components of **dia**. The three images show the structure as a tiling of $\mathbb{H}^2$, on one unit cell of the G surface and in $\mathbb{E}^3$. (b,d,f) The $G_{123R}(2)$ structure also consists of 2 interpenetrating components of **dia**. By visual inspection, it seems that these two structures are equivalent by ambient isotopy, however the current tools are insufficient to show this categorically.

3.2.3 Degree-6 nets: pcu, hxl and 6-chains

Regular ribbon tilings with a degree-6 vertex are candidates for reticulation over each of the H, P, D, and G surfaces as these tilings have symmetry that belongs to both of the $*2226/ooo$ and $*246/ooo$ quotient groups. On the H surface, we consider those tilings with symmetry $*2226$ and 2226 embedded into the $*2226$ chart of $\mathbb{H}^2$. A 2226 fundamental domain is selected on the $*2226$ tiling of $\mathbb{H}^2$, as well as a corresponding domain on the H surface, as shown in Fig. 3.15(e,f). A $*2226$ fundamental domain on the H surface may be inferred from this image (half of the domain). On the P, D and G surfaces, we consider tilings with symmetry $2*26$ and 2226 embedded in the $*246$ chart of $\mathbb{H}^2$. Fig. 3.15(a-d) shows a fundamental domain of the 2226 symmetry group in the $*246$ tiling of $\mathbb{H}^2$, and the corresponding domain on each of the P, D and G surfaces. On all surfaces, this patch builds out to the full surface by the in-surface symmetries of 2226, or equivalently by the hexagonal and trigonal space groups listed below [Hyde 11]:

	H surface	P surface	D surface	G surface
$*2226$	$P6_3/mmc$	-	-	-
$2*26$	-	$R\bar{3}m$	$R\bar{3}m$	-
2226	$P\bar{3}1c$	$R\bar{3}c$	$R\bar{3}c$	$R\bar{3}c$

Regular ribbon tilings with symmetry $*2226$, $2*26$ or 2226, which were constructed in Ch. 2.3, have exactly 2 vertices per translational unit cell of each of the TPMS. These 2 vertices are equivalent, all of degree-6 with one kind of connecting edge. Possible topology of the structures in $\mathbb{E}^3$ when the surface is removed include 3-periodic **pcu** components, 2-periodic **hxl** components, or arrays of 1-periodic chains of degree-6 vertices (6-chains). A summary of the nets that arise from the reticulation of the regular ribbon tilings of degree-6 over the H, P, D and G surfaces is shown in Table 4.9, named by the standard naming scheme described above.

By inspection, it appears that each of the single component **pcu** structures ($P_{93R}(1)$, $D_{93R}(1)$ and $G^{+}_{93R}(1)$) are equivalent by ambient isotopy to a barycentric embedding of **pcu**, which we call the trivial embedding. Such a trivial embedding is only relevant to single component nets.

The $H_{31R}(1)$ and $H_{31R}(3)$ structures each contain 3 interpenetrating components of **pcu**, where the components are related by a single translation (Class *Ia*). If we consider only the rings of the **pcu** net containing 4 edges (it also has rings of length 6: we call these

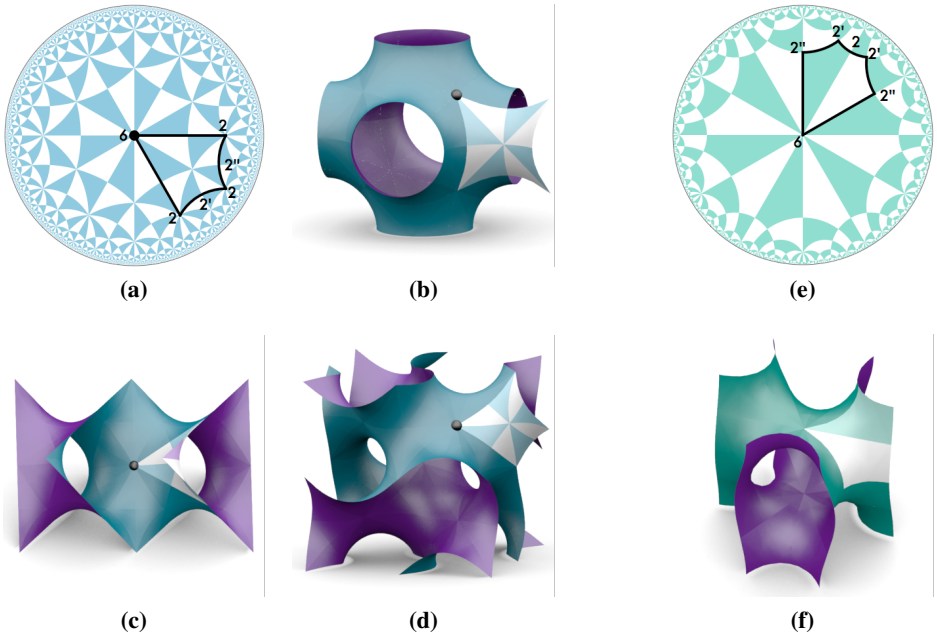

Figure 3.15: A fundamental domain outline of the 2226 symmetry group (a) in the $*246$ tiling in $\mathbb{H}^2$. This region is shown as a patch of the (b) *P* surface, (c) *D* surface, and (d) *G* surface, where the black circle indicates the location of the 6-fold rotation. (e) A 2226 fundamental domain shown in the $*2226$ tiling of $\mathbb{H}^2$, (f) this portion of $\mathbb{H}^2$ is shown as a patch of the *H* surface.

4-rings and 6-rings respectively), we find that one 4-ring in $H_{31R}(1)$ has Hopf link interactions with 8 other cycles, yet $H_{31R}(3)$ has Hopf link interactions with 20 other cycles. This information is sufficient to show that the structures do not belong to the same ambient isotopy class.

Structures $P_{122R}(1)$, $D_{122R}(2)$ and $G_{122R}(1)$ each contain 2 interpenetrating **pcu** components, where in all cases the 2 components are related by a single rotation (Class *IIa*). On examination of linked cycles of the structures, in all cases we find 4 Hopf links between the 4-rings of the structure, 24 Hopf links between rings of length 4 edges and rings of length 6 edges, and 40 Hopf links between 6-rings. It is highly likely that these three structures belong to the same ambient isotopy class, yet the links of the structures are not sufficient to prove this. Once again, the tight conformations of these structures, which can be found using the algorithm outlined in Ch. 4 might provide further evidence of equivalence.

The structures $D_{93R}(2)$ and $G_{122R}(2)$ each contain 4 **pcu** components, yet the structures have differing relations between the distinct components: $D_{93R}(2)$ is Class *Ib* (two independent translations map between components), and $G_{122R}(2)$ is Class *IIIa* (one rotation and one translation map between components). In both structures, the linking between

Table 3.3: Degree-6 nets. The column "# comp." refers to the number of components, $n*$ designates infinitely many 2-periodic layers arranged in n distinct orientations.

Structure	Figure	# comp.	Topology	Notes
$H_{32R}(1)$	Fig. 3.16(a,c,e)	∞	6-chains	array of parallel 1-periodic 6-chains
$H_{32R}(2)$	Fig. 3.16(b,d,f)	1*	**hxl**	parallel array
$H_{31R}(1)$	Fig. 3.17(a-c)	3	**pcu**	Interaction of 4-rings: 8 Hopf links
$H_{31R}(3)$	Fig. 3.17(d-f)	3	**pcu**	Interaction of 4-rings: 20 Hopf links
$P_{122R}(1)$	Fig. 3.18(a,c,e)	2	**pcu**	Interaction of 4-rings: 4 Hopf links. Interaction of 4-rings with 6-rings: 24 Hopf links. Interaction of 6-rings: 40 Hopf links
$P_{93R}(1)$	Fig. 3.18(b,d,f)	1	**pcu**	
$D_{122R}(2)$	Fig. 3.19(a-c)	2	**pcu**	Interaction of 4-rings: 4 Hopf links. Interaction of 4-rings with 6-rings: 24 Hopf links. Interaction of 6-rings: 40 Hopf links
$D_{93R}(1)$	Fig. 3.19(d-f)	1	**pcu**	
$D_{93R}(2)$	Fig. 3.19(g-i)	4	**pcu**	Interaction of 4-rings: 12 Hopf links. Interaction of 4-rings with 6-rings: 66 Hopf links. Interaction of 6-rings: 74 Hopf links and 1 higher link.
$G_{122R}(1)$	Fig. 3.20(a-c)	2	**pcu**	Interaction of 4-rings: 4 Hopf links. Interaction of 4-rings with 6-rings: 24 Hopf links. Interaction of 6-rings: 40 Hopf links
$G_{122R}(2)$	Fig. 3.20(d-f)	4	**pcu**	Interaction of 4-rings: 12 Hopf links. Interaction of 4-rings with 6-rings: 72 Hopf links. Interaction of 6-rings: 120 Hopf links
$G^{+}_{93R}(1)$	Fig. 3.20(g-i)	1	**pcu**	

4-rings yields 12 Hopf links, so we must look further afield to ascertain ambient isotopy classes. The linking between rings where one ring contains 4 edges and the other contains 6 edges gives 66 Hopf links for $D_{93R}(2)$ and 72 Hopf links for $G_{122R}(2)$, which shows that the structures are not equivalent under ambient isotopy. This is further supported by the links between 6-rings within the structures: $D_{93R}(2)$ has 74 Hopf links and a single higher crossing link, and $G_{122R}(2)$ has 120 Hopf links.

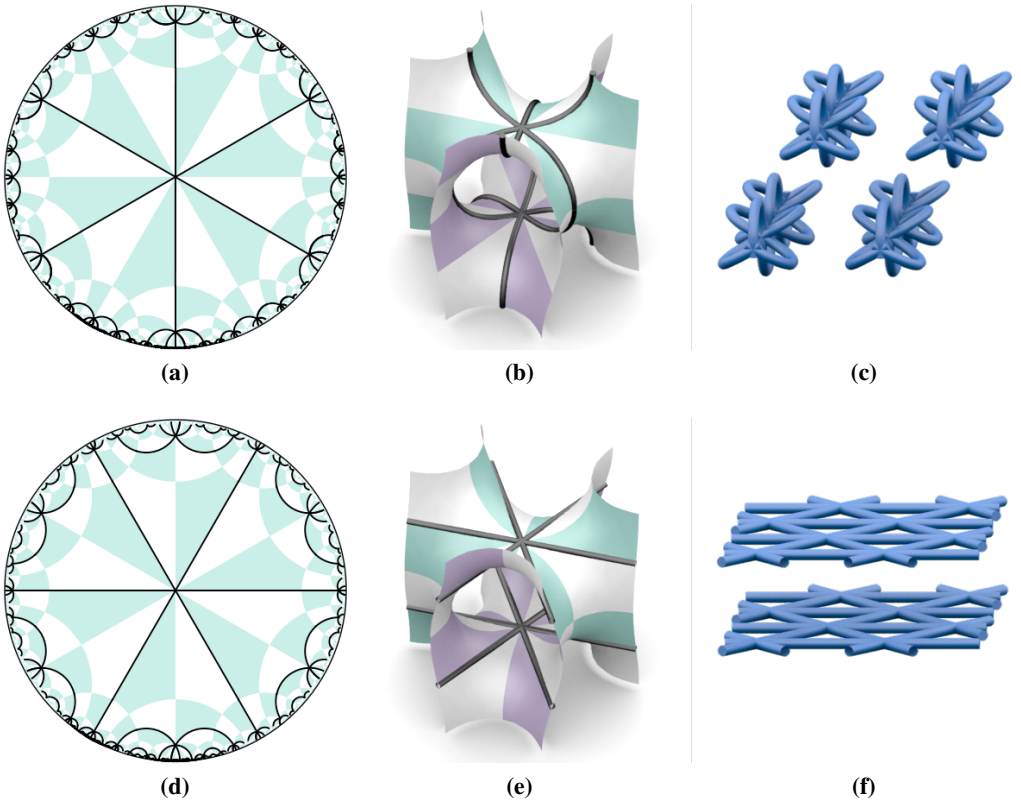

Figure 3.16: (a-c) The $H_{32R}(1)$ structure, built on the H surface from the $*2226_{32R}(1)$ tiling of $\mathbb{H}^2$, consists of parallel 1-periodic 6-chains. (d-f) The $H_{32R}(2)$ structure is comprised of parallel layers of 2-periodic **hxl**.

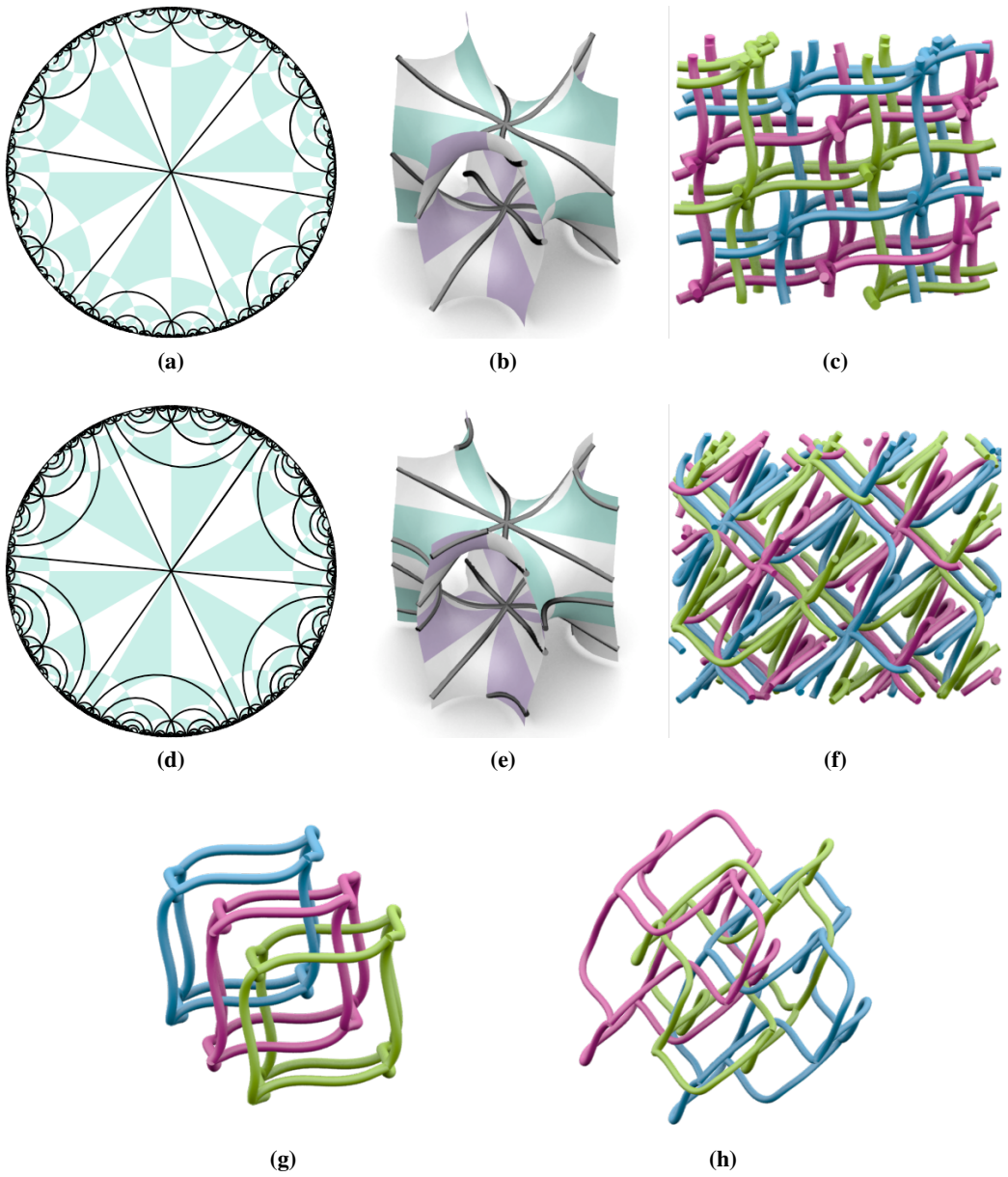

Figure 3.17: (a-c) The $H_{31R}(1)$ structure shown in $\mathbb{H}^2$, on one unit cell of the H surface and in $\mathbb{E}^3$. The structure consists of 3 interpenetrating **pcu** nets. (d-f) The $H_{31R}(3)$ structure shown in $\mathbb{H}^2$, on the H surface and in $\mathbb{E}^3$. This structure also consists of 3 interpenetrating components of **pcu**. (g,h) One cubic cage from each component is shown for $H_{31R}(1)$ and $H_{31R}(3)$ respectively: These structures are not equivalent by ambient isotopy, confirmed by the difference in the TOPOS output.

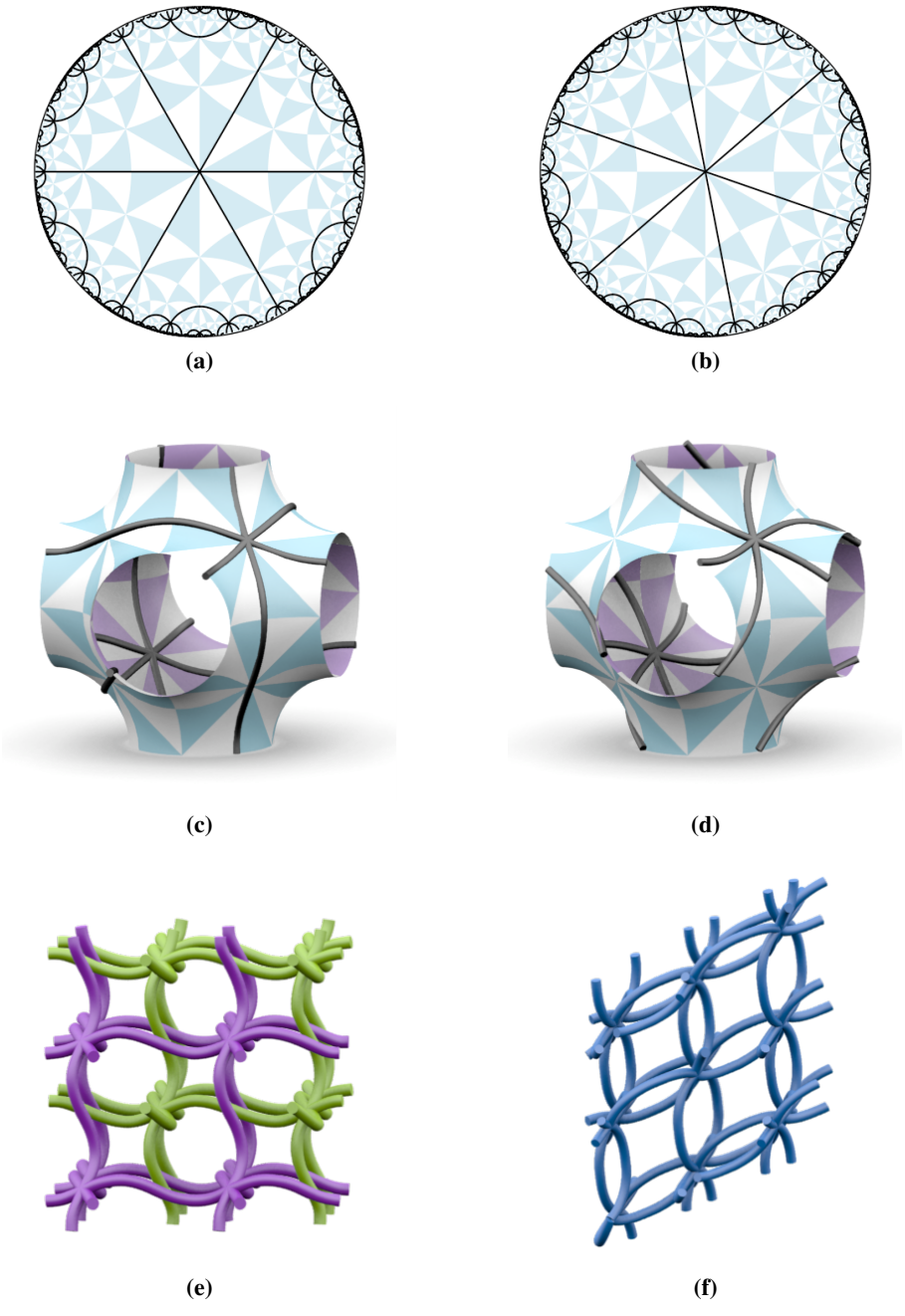

Figure 3.18: (a,c,e) The $P_{123R}(1)$ structure shown in $\mathbb{H}^2$, on one unit cell of the P surface and in $\mathbb{E}^3$. The structure consists of 2 interpenetrating components of **pcu**. (b,d,f) The $P_{93R}(1)$ structure contains a single trivial component of **pcu** in a deformed symmetry setting.

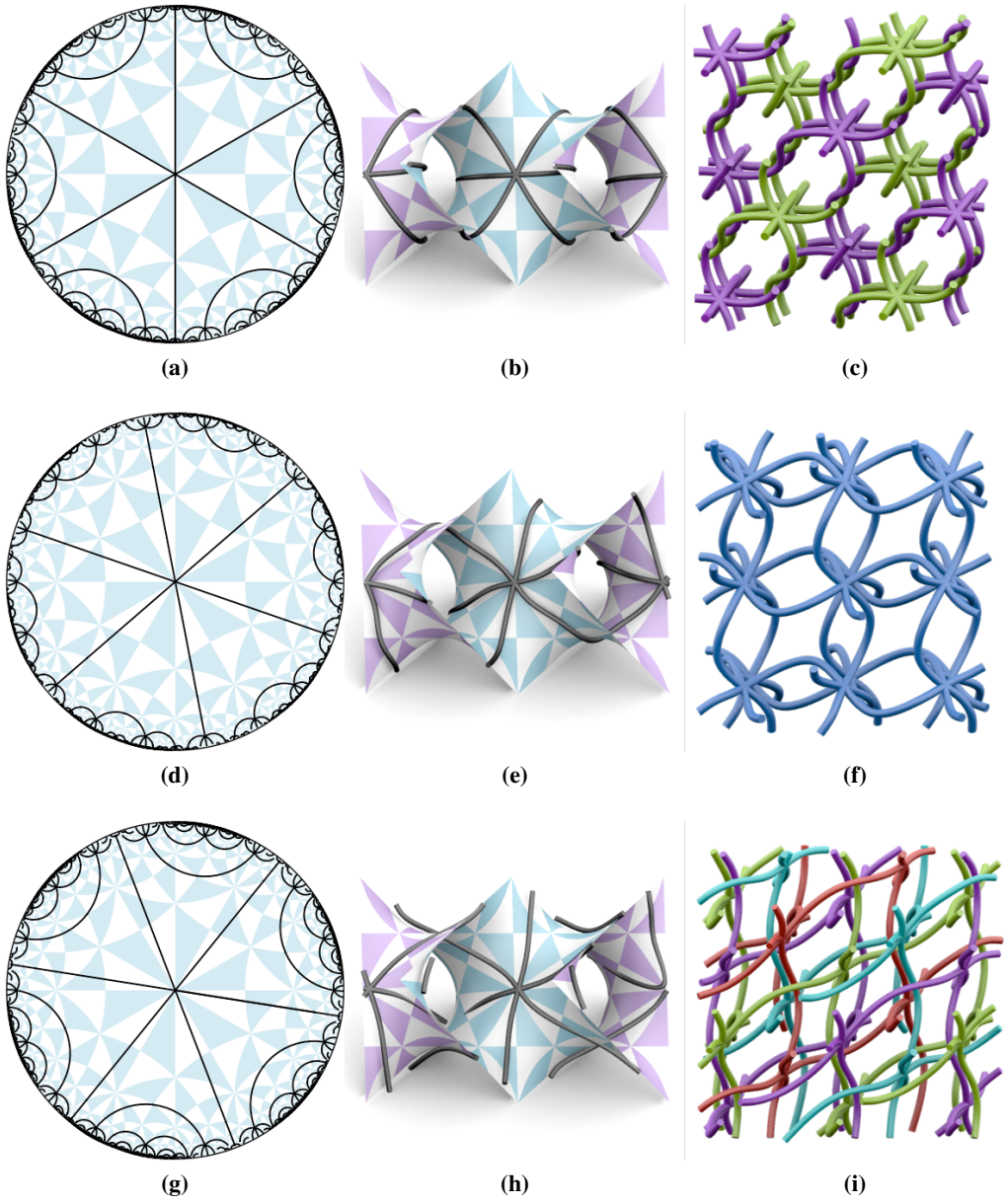

Figure 3.19: (a-c) The $D_{122R}(2)$ structure is shown in $\mathbb{H}^2$, on the D surface and in $\mathbb{E}^3$. The structure consists of 2 interpenetrating components of **pcu**. (d-f) The $D_{93R}(1)$ structure is also shown in $\mathbb{H}^2$, on the D surface and in $\mathbb{E}^3$. It is composed of a single **pcu** net. (g-i) The structure $D_{93R}(2)$ contains 4 interpenetrating components of **pcu**.

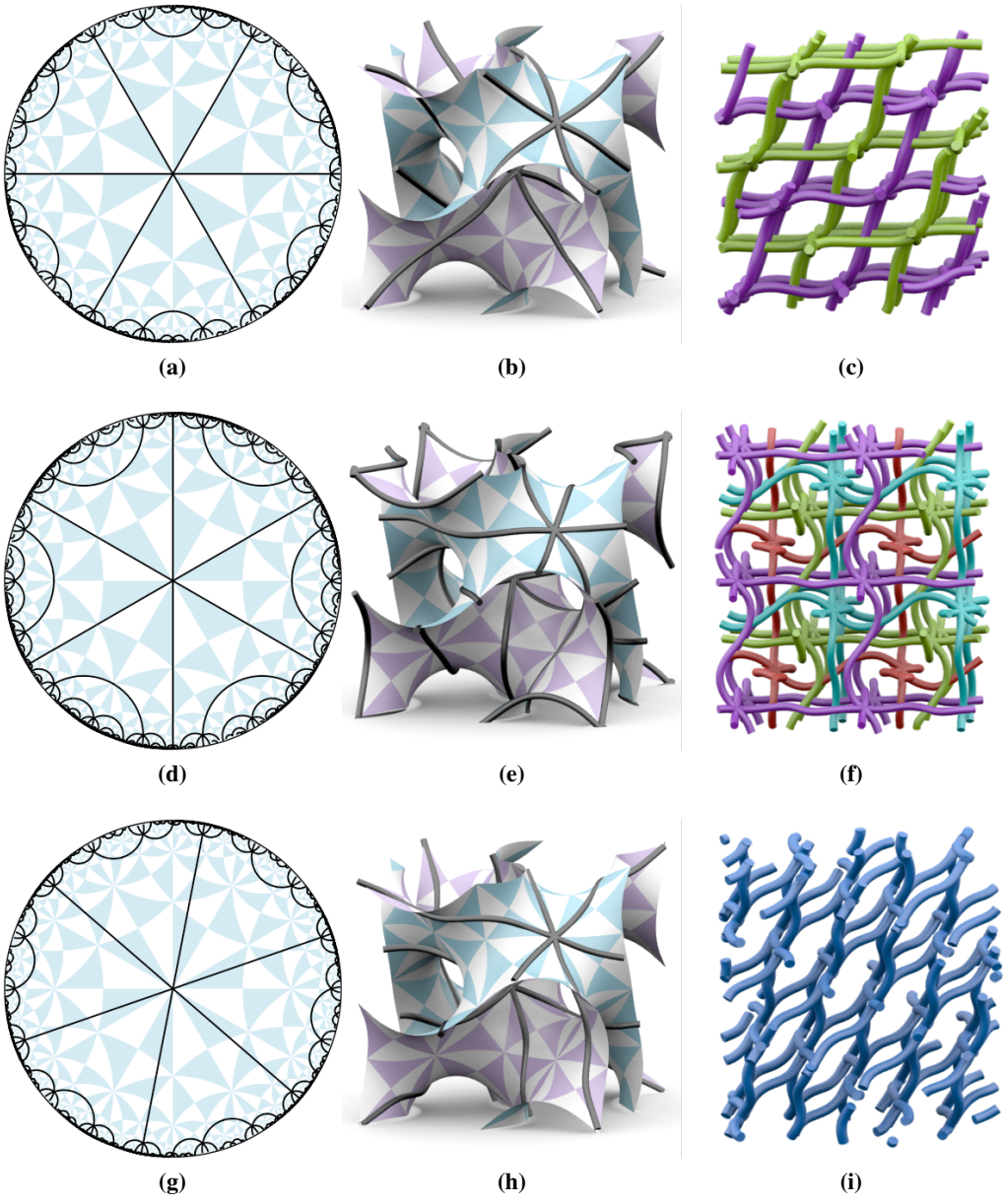

Figure 3.20: (a-c) The $G_{122R}(1)$ structure, shown in $\mathbb{H}^2$, on the G surface and in $\mathbb{E}^3$. The structure is the interpenetration of 2 **pcu** components. (d-f) The structure $G_{122R}(2)$ comprises 4 interpenetrating components of **pcu**. (g-i) The structure $G^{+}_{93R}(1)$ structure, constructed via one covering map of the G surface, contains a single **pcu** net.

3.2.4 Sparse degree-3 nets: hcb and finite θ-graphs

We consider sparse degree-3 nets that are constructed from regular tilings with symmetry ∗22223 or 22223, which were constructed in Ch. 2.3. The 22223 orbifold belongs to both the ∗246/∘∘∘ (group 49) and ∗2226/∘∘∘ (group 22) quotient groups, but ∗22223 is only a member of ∗2226/∘∘∘ (group 23). As a finite tile of the *P* surface, *D* surface and *G* surface, a fundamental domain of the orbifold 22223 builds out to the infinite surfaces by the 2D isometries of the 22223 symmetry group, or equivalently the space group operations of the trigonal group *R*32. Similarly, a fundamental domain of 22223 builds the infinite *H* surface by the space group operations of the hexagonal group *P*312, and ∗22223 by the hexagonal space group $P\bar{6}m2$. Corresponding fundamental domain outlines are shown in $\mathbb{H}^2$ and on each of the surfaces in Fig. 3.21.

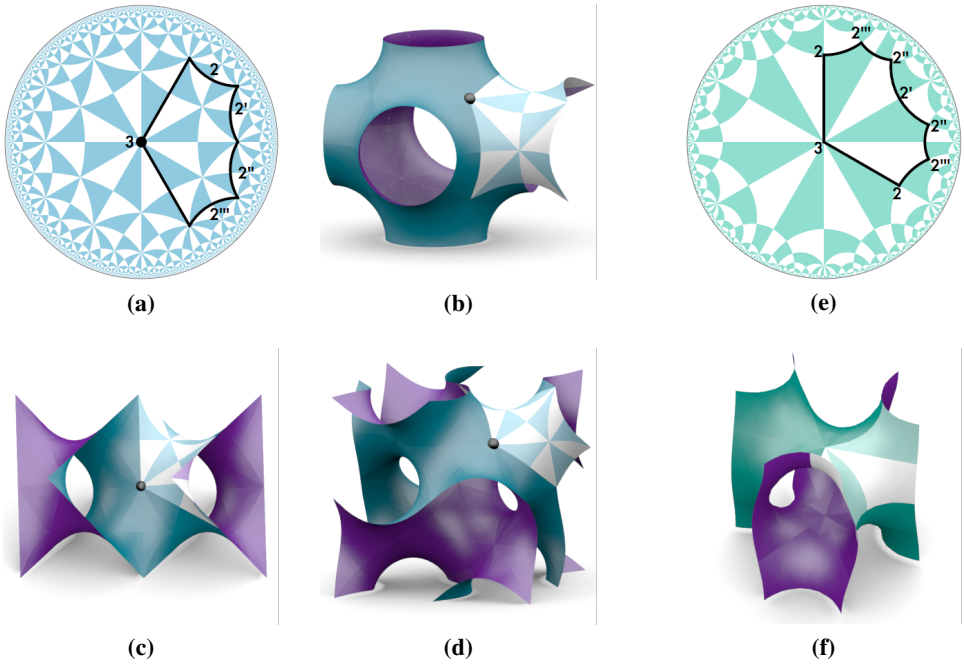

Figure 3.21: A fundamental domain outline of the 22223 symmetry group (a) embedded in the ∗246 tiling in $\mathbb{H}^2$. This region is shown as a patch of the (b) *P* surface, (c) *D* surface, and (d) *G* surface, where the back circle gives the location of the 3-fold rotation. (e) A 22223 fundamental domain shown in the ∗2226 tiling of $\mathbb{H}^2$, (f) shown as a patch of the *H* surface.

On all surfaces considered, one unit cell of the sparse nets considered in Ch. 2.4 will contain 2 vertices, each of degree-3. This implies that the quotient graph of the structure resulting from reticulation of the pattern over a minimal surface will be a θ-graph (two vertices connected by three edges). This, along with the required 3-fold symmetry of the vertex, dictates that the nets formed will be either arrays of discrete θ-graphs, or parallel

arrays of (translationally equivalent), 2-periodic **hcb** nets.

A summary of the structures that result from the reticulation of the regular ribbon tilings with a degree-3 vertex over each of the H, D, P and G surfaces is shown in Table 4.10. The structures are named so as to reflect the original tiling in $\mathbb{H}^2$ as well as the surface over which the tilings were reticulated: the structure $H_{22R}(1)$ is the reticulation of the $*2226_{22R}(1)$ tiling (from Ch. 2) over the H surface. We also show the $\mathbb{Z}\times\mathbb{Z}$ coordinates (see Ch. 2 for this construction) of the embedded edge for simplicity in our analysis of trends later in this section.

Table 3.4: Sparse degree-3 nets, with nomenclature as described previously.

Structure	Edge	Figure	Topology	Notes
H_{23R}	$\{1,0\}$	Fig. 3.22(a,b)	θ-graph	Isolated graphs
$H_{22R}(1)$	$\{1,1\}$	Fig. 3.22(c-e)	**hcb**	2D Borromean [Carl 03a]
$H_{22R}(2)$	$\{1,2\}$	Fig. 3.22(f-h)	**hcb**	$DoC = 6$ [Carl 03c], all hopf links, six edges thread each individual cycle (three from each distinct component).
$H_{22R}(5)$	$\{1,3\}$	Fig. 3.23(a-c)	θ-graph	0D to 2D catenation of θ-graphs by Hopf links
$H_{22R}(3)$	$\{3,1\}$	Fig. 3.23(d-h)	**hcb**	2D × 3D Borromean of **hcb**, no catenation or interpenetration, not Brunnian, yet still entangled, $IoS = 3$
$D_{49R}(1)$	$\{1,1\}$	Fig. 3.24(a,c,e)	**hcb**	Trivial, unentangled
$D_{49R}(2)$	$\{1,2\}$	Fig. 3.24(b,d,f)	**hcb**	4-fold interpenetration, synthesised in [Shar 00, Doma 05], $DoC = 3$
$D_{49R}(4)$	$\{1,3\}$	Fig. 3.25(a,c,e)	**hcb**	Self-catenated layers, cycles are trefoil knots
$D_{49R}(5)$	$\{1,4\}$	Fig. 3.25(b,d,f)	**hcb**	Self-catenated layers, cycles are $(4,3)$ torus knots
$P_{49R}(4)$	$\{1,3\}$	Fig. 3.26(a-c)	**hcb**	3D Borromean structure [Tong 99, Muth 02, Men 09]
$P_{49R}(5)$	$\{1,4\}$	Fig. 3.26(d-h)	**hcb**	Catenated 2-fold structure
$G^{+}_{49R}(2)$	$\{1,2\}$	Fig. 3.27(a-c)	**hcb**	3D Borromean structure [Tong 99, Muth 02, Men 09]
$G^{+}_{49R}(4)$	$\{1,3\}$	Fig. 3.27(d-g)	**hcb**	Catenated 2-fold structure
$G^{+}_{49R}(3)$	$\{3,2\}$	Fig. 3.28(a-c)	**hcb**	2 × 3D Borromean structure
$G^{-}_{49R}(3)$	$\{3,1\}$	Fig. 3.28(d-g)	**hcb**	2D to 3D catenation version of the 2D to 2D interpenetration in $H_{22R}(2)$.

The first general trend we consider is for H surface reticulations, where the tiling has symmetry $*22223$ or 22223, and the edge coordinate is given by $\{1,n\}$ (the structures H_{23R}, $H_{22R}(1)$, $H_{22R}(2)$ and $H_{22R}(5)$ are the cases of $n=0,1,2,3$ respectively). All structures are composed of multiple discrete 2-periodic layers, which fall into two genres:

1. $n=0(mod3)$: the layer consists of infinitely many catenated trivial θ-graphs, and the nature of the catenation is an $(\frac{n+2}{3},2)$ torus link. For $n=0$ (structure H_{23R}), the catenation is trivial.

2. $n=1,2(mod3)$: each layer of the structure consists of three interpenetrating components, all with the same average plane. The exception to this is the case where $n=1$ (structure $H_{22R}(1)$), which is the 2D Borromean structure and is not interpenetrating.

The 2D Borromean entanglement that arises as $H_{22R}(1)$ is initially described in [Carl 03a] and further synthesised as metal-organic chemical frameworks in [Lezn 01, Suh 03, Lian 03, Dobr 05, Lian 06, Lu 06, Zhan 07b, Zhan 07a, Li 07, Byrn 08, Men 09, Jang 09]. This structure is the entanglement of three **hcb** components where no cycles are threaded. It has the property that when one component is removed, the other two are no longer entangled. The exact reticulation has space group symmetry P312, allowing the edges to straighten away from the surface increases the symmetry to $P\bar{3}1m$.

Also constructed on the H surface, $H_{22R}(3)$ yields a structure that is the further entanglement of *2D Borromean* entangled layers. The nature in which one **hcb** component of each *2D Borromean* layer entangles with components of adjacent layers is via a *3D Borromean* entanglement (see [Carl 03c]). Equivalently, each **hcb** component within a single copy of the *3D Borromean* entanglement has two additional **hcb** components associated by a *2D Borromean* entanglement. Fig. 3.23(d-h) shows this structure. The Index-of-Separation [Carl 03c] (IoS) is 3, where an entire layer of *2D Borromean* must be removed to separate the structure in two.

A trend is also observed for D surface reticulations, where the tiling has symmetry 22223, and the edge coordinate is given by $\{1,n\}$ (the structures $D_{49R}(1)$, $D_{49R}(2)$, $D_{49R}(4)$ and $D_{49R}(5)$ are the cases of $n=1,2,3,4$ respectively). These structures are interpenetrating or self catenated disjoint layers of **hcb**. The structures cycle through three distinct genres:

1. $n=1(mod3)$: the structures consist of one connected component in each disjoint layer. This component is self catenated, where each cycle of the structure is an $(n,3)$ torus knot (when $n=1$, the cycles are trivial loops).

2. $n = 2(mod3)$: the periodic patterns have four interpenetrating components to each layer. The individual components of these layers have cycles ambient isotopic to $(n-1,3)$ torus knots, and the threading between components is by Hopf links.

3. $n = 0(mod3)$: the structure has a single component per layer. The self catenation of the cycles of these components is such that each cycle is an $(n-1,3)$ torus knots.

In the $P_{49R}(4)$ structure, the parallel **hcb** form a *3D Borromean* entangled structure: any pair of components are disjoint, but any three adjacent layers are entangled. Note that this is not Brunnian, as the removal of one component will cause the structure to separate into two parts, not separate into individual components as required by Brunnian conditions. This structure has been chemically synthesised [Tong 99, Muth 02, Men 09].

The $P_{49R}(5)$ structure is comprised of 2D **hcb** components which catenate to give a 3D structure. The IoS is 2, which indicates the structure is a 2-fold structure where the layers are catenated *i.e.* if we select every second component, the structure is still a catenated 3D object, and the $P_{49R}(5)$ structure is composed of two identical copies of this that are interpenetrating.

The general trend for structures on the P surface originating as 22223 symmetry tilings with edge coordinate of $\{1,n\}$ is similar to the trend for the same tilings on the H surface. The two sets of structures in $\mathbb{E}^3$ display a similar entanglement, but the P surface nets are a catenated 3D nets with adjacent layers being slightly offset, where the H surface nets are interpenetrating discrete layers. Another similarity between different surface reticulations is between a set of nets on the G surface and the P surface. We see that a P surface reticulation with edge coordinate $\{1,n\}$ will be ambient isotopic to a G surface reticulation with edge coordinate $\{1,n-1\}$. We can see from these structures that a broad range of interesting entanglements are possible.

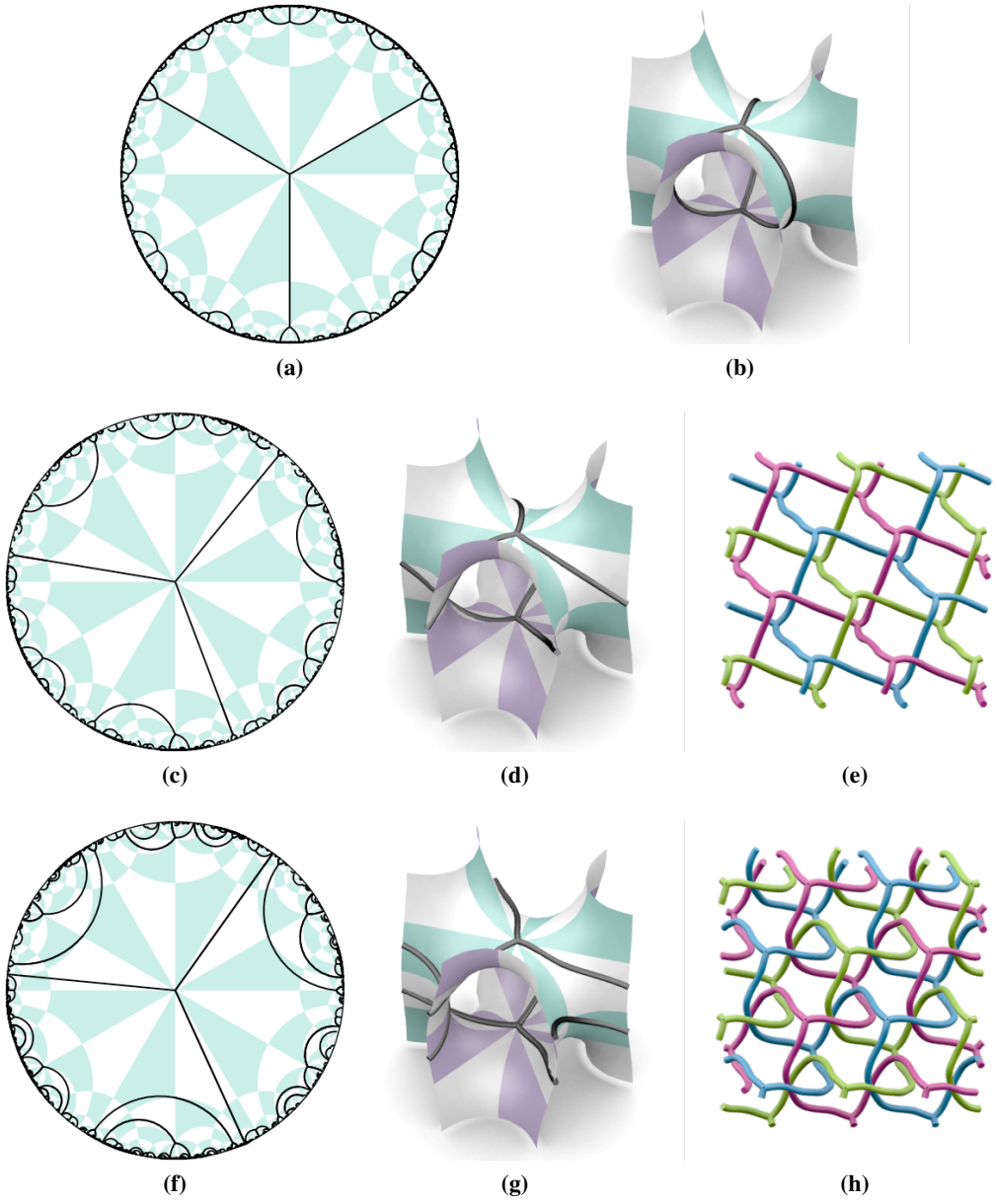

Figure 3.22: (a,b) The H_{23R} structures, shown in $\mathbb{H}^2$ and on the H surface, consists of disjoint, isolated θ-graphs. (c-e) The $H_{22R}(1)$ structure, shown in $\mathbb{H}^2$, on the H surface an in $\mathbb{E}^3$, is a $2D$ Borromean entangled structure [Carl 03a], repeated as disjoint, translated layers in $\mathbb{E}^3$. (f-h) The $H_{22R}(2)$ structure is a repeated, parallel set of interpenetrating layers each with 3 components.

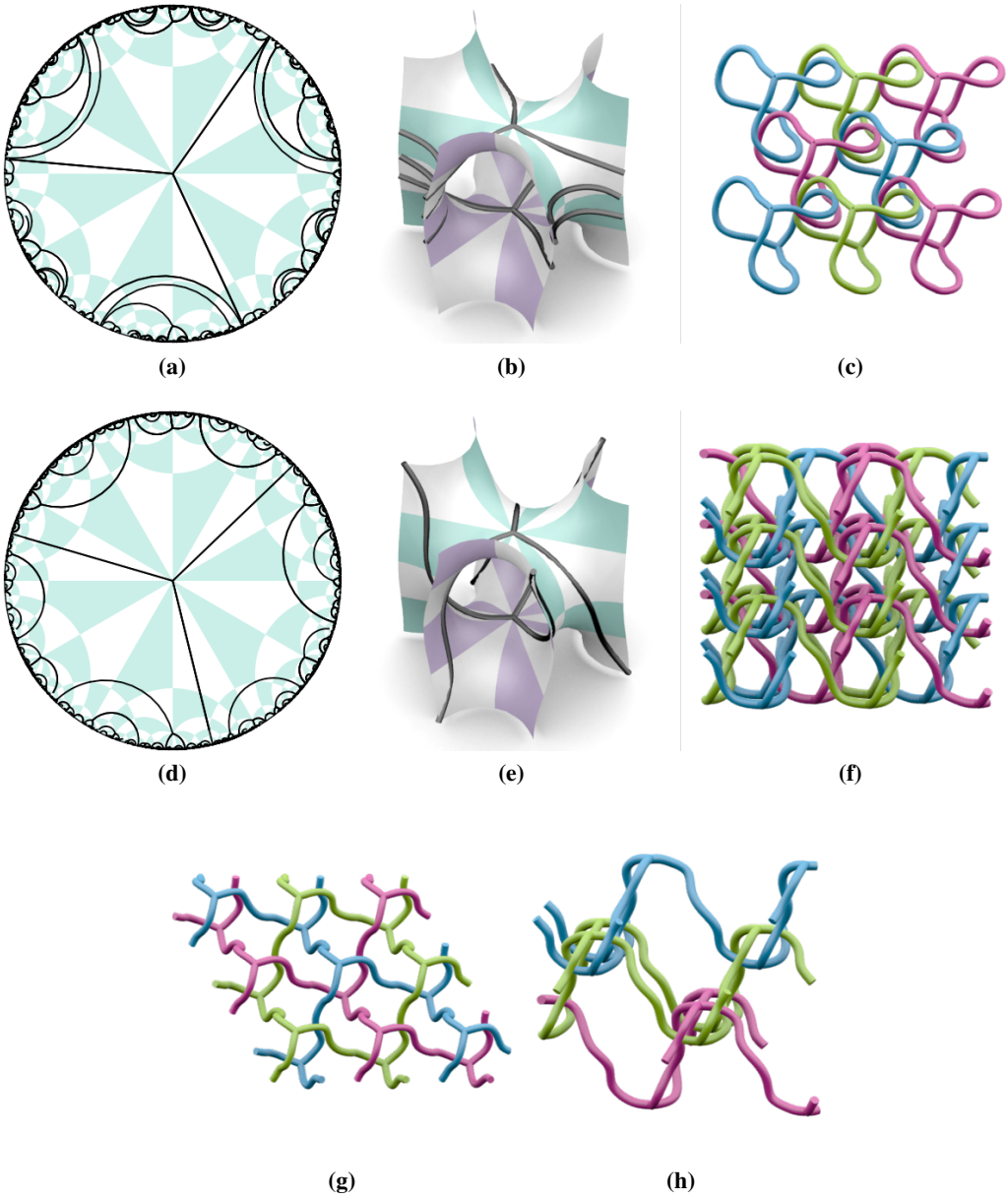

Figure 3.23: (a-c) The structure $H_{22R}(5)$, shown in $\mathbb{H}^2$, on the H surface and in $\mathbb{E}^3$, is the $0D$ to $2D$ catenation of θ-graphs by Hopf links. (d-f) The structure $H_{22R}(3)$ is a $2D \times 3D$ Borromean entanglement, which contains no catenation or interpenetration, is not Brunnian, and is still entangled. The image (g) shows one layer (with three **hcb** components) of the entanglement, which is $2D$ Borromean entangled. Image (h) shows one component from each of these 2D layers, which together give a structure which is $3D$ Borromean entangled.

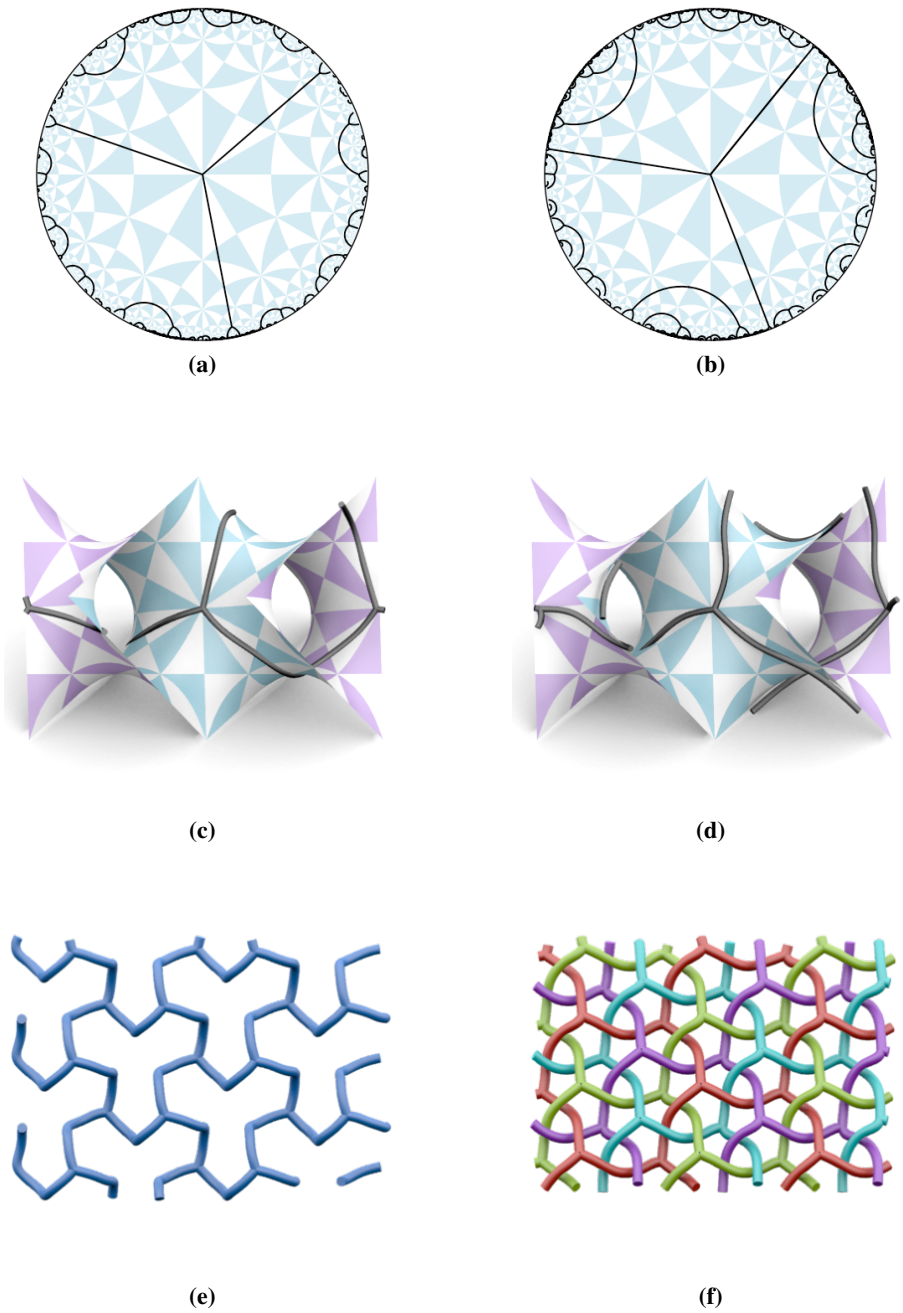

Figure 3.24: (a,c,e) The $D_{49R}(1)$ network, shown in $\mathbb{H}^2$, on the D surface and in $\mathbb{E}^3$, consists of disjoint, isolated layers of **hcb**. (b,d,f) The $D_{49R}(2)$ structure, also shown as a surface tiling, is comprised of disjoint layers with 4-fold interpenetration, observed in synthetic metal-organic frameworks [Shar 00, Doma 05].

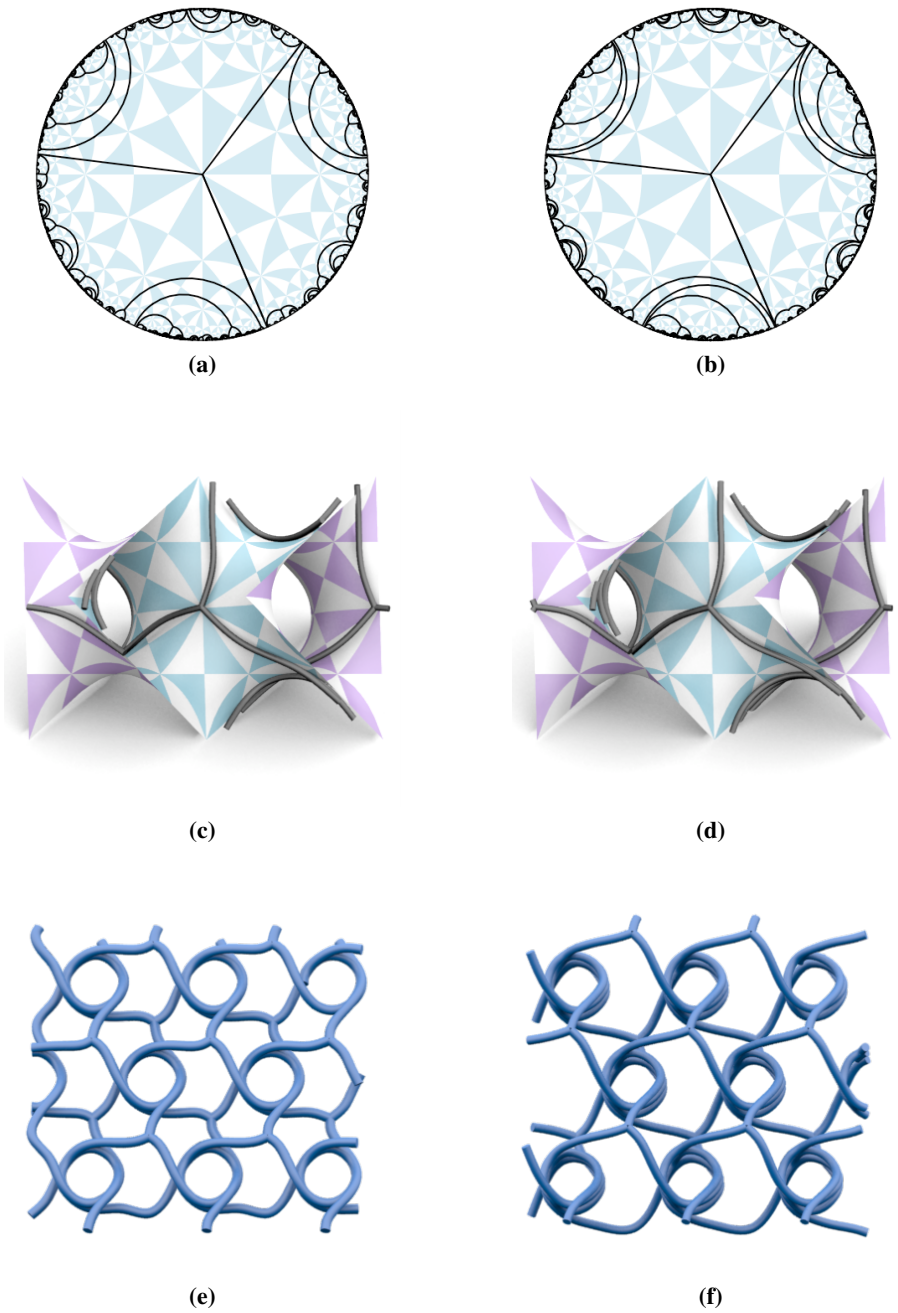

Figure 3.25: (a,c,e) $D_{49R}(4)$: this net, shown in $\mathbb{H}^2$, on the D surface and in $\mathbb{E}^3$, is comprised of disjoint, isolated layers of **hcb** that are self-catenated, and whose cycles are trefoil knots. (b,d,f) The $D_{49R}(5)$ structure is also comprised of disjoint, isolated layers of **hcb** that are self-catenated, yet here the cycles of the net are $(4,3)$ torus knots.

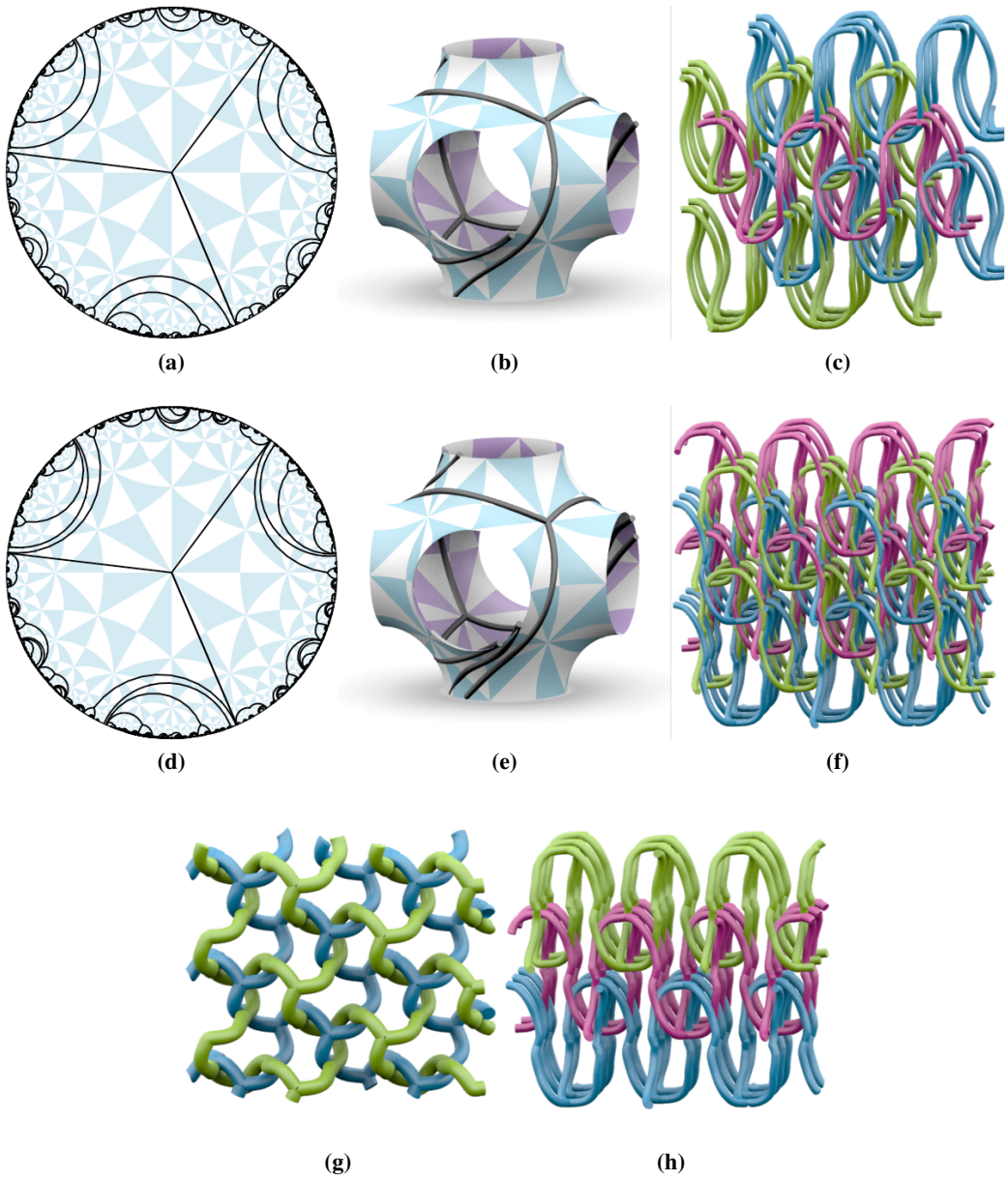

Figure 3.26: (a-c) The entangled net $P_{49R}(4)$, shown in $\mathbb{H}^2$, on one unit cell of the P surface and in $\mathbb{E}^3$, is a $3D$ Borromean entanglement of **hcb** components, as synthesised in [Tong 99, Muth 02, Men 09]. (d-h) The structure $P_{49R}(5)$ is a 2-fold catenated structure. Image (g) shows two adjacent layers of this structure are catenated and image (h) shows one constituent net, composed of every second component layer of the 2-fold structure, which is still a catenated structure.

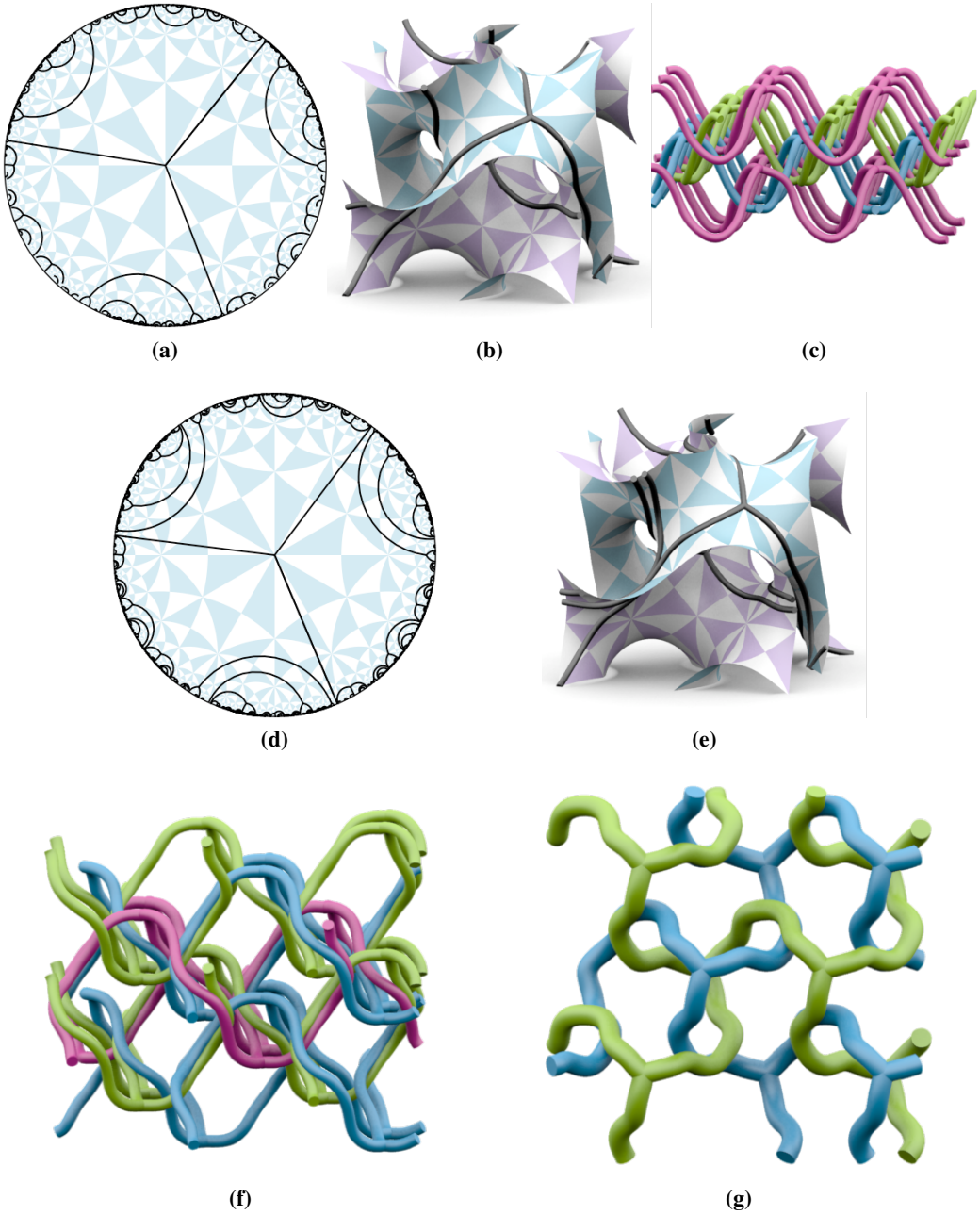

Figure 3.27: (a-c) The $G^{+}_{49R}(2)$ structure is shown in $\mathbb{H}^2$, on the G surface and in $\mathbb{E}^3$. This structure is a 3D Borromean entanglement of **hcb** components. (d-g) The $G^{+}_{49R}(4)$ structure is a 2-fold catenated structure, equivalent to the structure $P_{49R}(5)$.

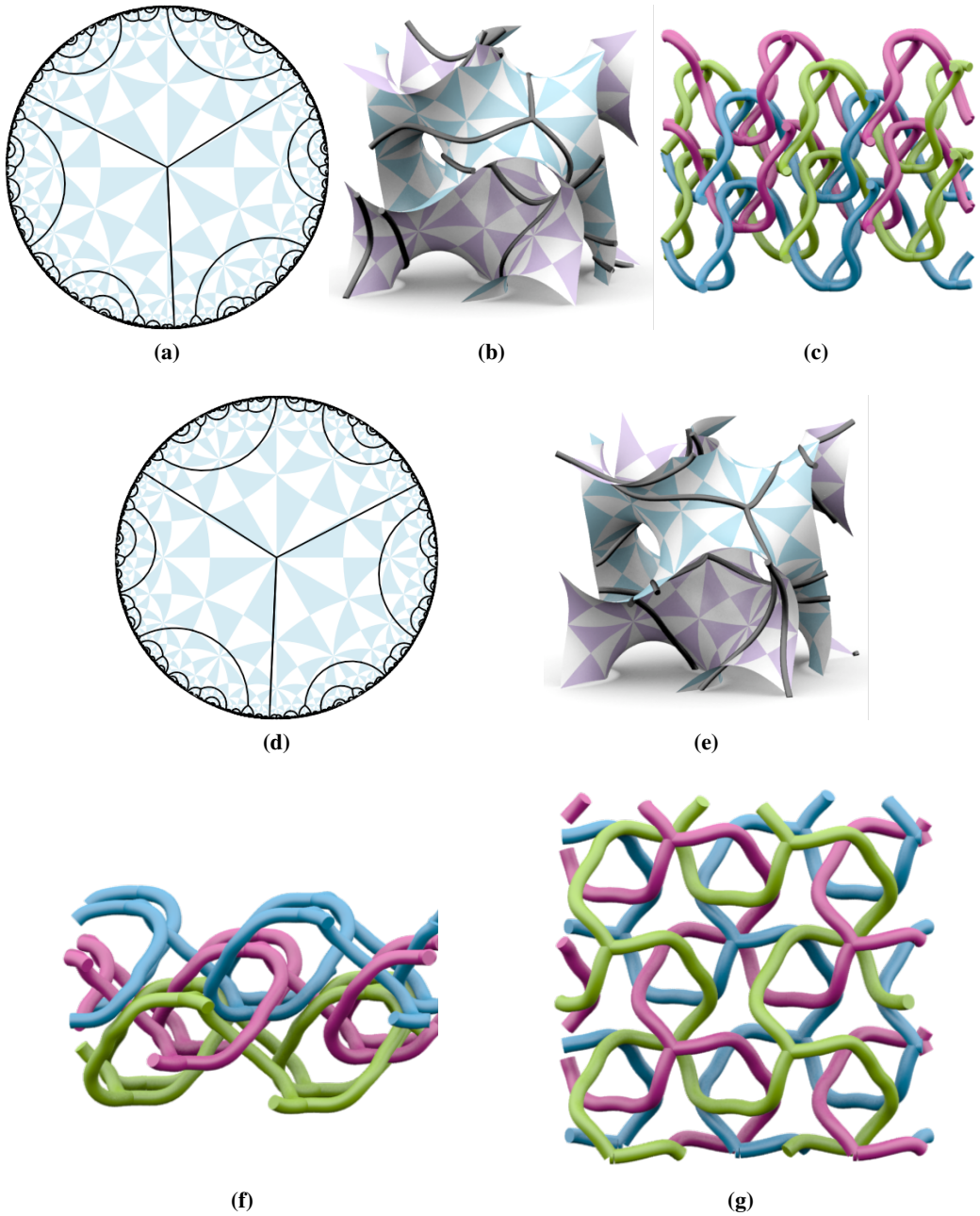

Figure 3.28: (a-c) The structure $G^{+}_{49R}(3)$, shown in $\mathbb{H}^2$, on one unit cell of the G surface and in $\mathbb{E}^3$, contains two copies of a 3D Borromean entanglement of **hcb** components. (d-g) The $G^{-}_{49R}(3)$, built by using other covering map of the G surface to the previous example, is a catenated structure. The image (g) shows that when the structure is viewed from above, the entanglement is a 2D to 3D catenation version of the 2D to 2D interpenetration of structure $H_{22R}(2)$.

3.3 Crystalline filamentous arrays

Packings of infinite 1D filaments, called filamentous arrays, occur naturally and synthetically over many different length scales: rods of strongly bonded atoms within chemical frameworks, weavings of proteins, DNA entanglements, polymer materials or textile fabrics. These filamentous arrays have a common geometric structure. Rod packings (including invariant rod packings[2]), which are a 3-periodic packings of straight, 1D rods, have been widely used in structural chemistry to describe chemical frameworks composed of rods of strongly bonded atoms [OKee 05]. The rod packings considered are composed of filaments which are straight: by generalising to packings of curvilinear filaments, we obtain broader set of structures.

The entanglement of filaments in these arrays, the way the filaments wrap and tangle around each other, is an important property: it is the entanglement alone that binds the structure, as there are no vertices to connect and stabilise. It is the entanglement that gives filamentous arrays their material properties: filaments which wind around each other are able to strengthen, pull, stabilise and push their neighbours despite not being connected. The importance of entanglement is supported by the results of mechanical testing of fibre arrays, where the way contacting fibres interact influences the properties of the soft material [Kabl 07]. We present an enumeration of entangled filament arrays with varying levels of entanglement, to bring geometric inspiration to soft fibrous materials of all length scales.

The initial catalogue of high symmetry hyperbolic free tilings shown in Ch. 2 includes a second genre of free tilings in addition to conventional tessellations, where the infinite tile has vertex-free geodesic boundaries. These tilings are complementary to the regular ribbon tilings. When these tilings are reticulated over TPMS, and the surface subsequently removed to leave only tile boundaries, we obtain a 3-periodic (crystalline) array of one-dimensional curves in $\mathbb{E}^3$ that we call crystalline filamentous arrays, or *weavings*.

To describe weavings, we define a basic structural property: each component filament is linearly approximated by the straight line which minimises the sum of the distances between points on the filament and the straight line, an average axis. It is akin to straightening a helix along its central axis. The periodicity of the filaments in these cases indicates

[2] An invariant rod packing is composed of non-intersecting rods (cylinders), which correspond to invariant line positions of the space groups: rods lie along the directions of nonintersecting symmetry axes [OKee 01]. There are exactly 14 invariant rod packings, of which 6 are cubic [OKee 05].

that this average axis will be parallel to the filaments axis of translation.

In some cases, the filaments of the weaving are unimpeded by nearby filaments during the deformation from their initial trajectory to their straight average axis, and thus on straightening of the filaments, the rod packing that results is equivalent to the weaving by ambient isotopy. The simplest weavings constructed in this chapter are related to the invariant cubic rod packings, as defined previously, already known to crystal chemists. In addition to these cubic packings, the construction technique also gives rise to weavings which are related to the remaining invariant rod packings, as well as other rod packing which are not invariant of various symmetries.

A second class includes weavings where the straightening of all filaments to their straight average axis results in a packing of intersecting rods. Weavings related to these "intersecting rod packings" form an intermediate category between those weavings related to rod packings and those that are more tangled. The third class includes weavings where the filaments are sufficiently tangled so as to impede each other from straightening to their straight average axis: the straightening of all filaments would require 'ghost' moves where the filaments pass through each other. If we allow these 'ghost' moves, and straighten the filaments in weavings such as these (not preserving equivalence by ambient isotopy), the filaments align along the rod directions of either invariant rod packings, other more general rod packings, or intersecting rod packings. We utilise this rod packing to describe the weaving, yet we note that the weaving is not actually equivalent to the rod packing by ambient isotopy: weavings such as these are referred to as a "tangled" version of a rod packing, where the term tangled denotes that the weaving is not equivalent to the rod packing by ambient isotopy, yet its filaments average axes align to form the rod packing.

We note that analysis techniques for interpenetrating nets are no longer applicable here: the structures contain an infinite number of components, the topology of each component is always a $1D$ curve, and the absence of cycles prohibits knotting and linking. To allow comparison of these filament packs, we have developed an alternative approach: the **PB-SONO** algorithm, which is introduced in Ch. 4.

Initially, we collate the rich variety of weavings that are constructed from the projection of complementary regular ribbon tilings of $\mathbb{H}^2$ to the P, D, G and H surfaces. For the first class of weavings, those which are unimpeded by nearby filaments during the deformation from their initial trajectory to their straight average axis, we give the rod packing to which it is related, which is often among the set of 14 invariant rod packings, as enumerated in [OKee 05]. For the invariant cubic rod packings, we use the names derived from

a related lattice complex of the space group on which they are constructed: Π^+, Π^*, Σ^+, Γ, Ω^+, Σ^*, where the $+$ exponent denotes one enantiomer of the packing and the $*$ exponent the inter-growth of both $+$ and $-$ enantiomers [OKee 01]. The other 8 invariant rod packings are identified by their structure number (#1-#8), as given in [OKee 05]. Where the weavings are related to other (non–invariant) rod packings, they are given a lable 'Rod (tetr.)' which reflects that they are related to a rod packing with tetragonal space group symmetry, or 'Rod (tri.)' where they have trigonal space group symmetry. Further, weavings whose filaments intersect on straightening (the second class of weavings) are referred to as simply 'Intersect'.

Weavings that belong to the third class, those whose filaments are sufficiently tangled so as to impede each other from straightening to their straight average axis, are described by the rod packing which aligns with its filaments average axes (as for the first class of weavings), which may be invariant cubic rod packing, other invariant rod packings, or other (non invariant) rod packings. The rod packing is then prefaced with the term "tangled" to indicate that it is a sufficiently tangled weaving, which is not equivalent by ambient isotopy to the rod packing specified. In a few cases, the filament trajectories of the TPMS reticulations close back on themselves to form closed loops. These cases form an interesting set of structures which are the inter-growth of closed loops, sometimes separate, sometimes entangled. These cases are referred to by the term "loops", prefaced by "Caten." (catenated) where loops thread through other loops.

Table 3.5 collates the weavings that result from the TPMS reticulation of complementary regular ribbon tilings with $*2223$ (group124), $2*23$ (group 129) and 2223 (group118) hyperbolic symmetry. These structures are named to reflect the embedded tiling name in $\mathbb{H}^2$ as well as the surface over which the tiling was reticulated. For example, the hyperbolic tiling $*246_{118C}(1)$ is the embedding of the complementary regular ribbon tiling with symmetry 2223 (group118) into the $*246$ tiling of $\mathbb{H}^2$, by the simplest embedding (embedding '(1)'). The structure $G^+_{118C}(1)$ is the reticulation of the hyperbolic tiling $*246_{118C}(1)$ over the *G* surface by one covering map. Ch. 2 details the construction and naming of hyperbolic tilings. This set of structures contains 4 of the 6 invariant cubic rod packings, as well as some tangled variants of these 4 cubic rod packings. The set also contains three intersecting rod packings.

The structures that result from the reticulation of complementary regular ribbon tilings with symmetry $*2224$ (group 123) and 2224 (group 114) over the *P*, *D* and *G* surfaces are summarised in Table 3.6. The hyperbolic free tilings from which these structures originate

Table 3.5: Weavings from $*2223$, $2*23$ and 2223 hyperbolic symmetry: nomenclature described in main text.

Structure	Packing	Structure	Packing	Structure	Packing	Structure	Packing
P_{124C}	Loops	D_{124C}	Π^*	G^+_{124C}	Helical Π^+	G^-_{124C}	Helical Π^-
P_{129C}	Helical Ω^+	D_{129C}	Loops	G^+_{129C}	Helical Σ^+	G^-_{129C}	Helical Σ^-
$P_{118C}(1)$	Intersect	$D_{118C}(1)$	Intersect	$G^+_{118C}(1)$	Intersect	$G^-_{118C}(1)$	Loops
$P_{118C}(2)$	Tangled Ω^+	$D_{118C}(2)$	Tangled Ω^+	$G^+_{118C}(2)$	Tangled $3\times\Gamma$	$G^-_{118C}(2)$	Tangled Σ^+
$P_{118C}(4)$	Caten. Loops	$D_{118C}(4)$	Π^*: woven	$G^+_{118C}(4)$	Tangled Π^+	$G^-_{118C}(4)$	Tangled Π^+
$P_{118C}(6)$	Tangled Ω^+	$D_{118C}(6)$	Tangled Ω^+	$G^+_{118C}(6)$	Tangled $3\times\Gamma$	$G^-_{118C}(6)$	Tangled Σ^+

are built in Ch. 2.3, and these structures are catalogued by the naming convention outlined above, and established in Ch. 2.3. This set of structures contains a further example of an invariant cubic rod packing, as well as 2 of the 8 other invariant rod packings. Some tetragonal (non–invariant) rod packings also arise as structures in this set.

Table 3.6: Weavings from $*2224$ and 2224 hyperbolic symmetry: nomenclature described in main text.

Structure	Packing	Structure	Packing	Structure	Packing	Structure	Packing
$P_{123C}(1)$	Loops	$D_{123C}(1)$	#2	$G^+_{123C}(1)$	#2	$G^-_{123C}(1)$	#2
$P_{123C}(2)$	#2	$D_{123C}(2)$	#6	$G^+_{123C}(2)$	Γ	$G^-_{123C}(2)$	Γ
$P_{114C}(1)$	Rod (Tetr.)	$D_{114C}(1)$	Γ	$G^+_{114C}(1)$	#2	$G^-_{114C}(1)$	#6
$P_{114C}(2)$	Intersect	$D_{114C}(2)$	#2	$G^+_{114C}(2)$	Rod (Tetr.)	$G^-_{114C}(2)$	Γ
$P_{114C}(3)$	Helical $4\times$#2	$D_{114C}(3)$	Tangled #2	$G^+_{114C}(3)$	Helical $3\times$#2	$G^-_{114C}(3)$	Tangled #2
$P_{114C}(4)$	Tangled (Tetr.)	$D_{114C}(4)$	Rod (Tetr.)	$G^+_{114C}(4)$	Intersect	$G^-_{114C}(4)$	#2
$P_{114C}(5)$	Rod (Tetr.)	$D_{114C}(5)$	Tangled Γ	$G^+_{114C}(5)$	Intersect	$G^-_{114C}(5)$	Intersect

Table 3.7 summarises the weavings that result from the reticulation of the H surface by complementary tilings of symmetry $*2226$ (group 32) and 2226 (group 31). This set of examples includes a further example of a non-cubic invariant rod packing, along with some non–invariant rod packings of trigonal symmetry.

We may also consider complementary regular ribbon tilings with $2*26$ (group 122) and 2226 (group 93) symmetry embedded in a $*246$ tiling of $\mathbb{H}^2$, enabling reticulation over the P, D and G surfaces. A summary of the filamentous arrays resulting from the

Table 3.7: Weavings from $*2226$ and 2226 hyperbolic symmetry on the H surface: nomenclature described in main text.

Structure	Packing
$H_{32C}(1)$	#3
$H_{32C}(2)$	Loops
$H_{31C}(1)$	Rod (Tri.)
$H_{31C}(2)$	Helical $3\times$#1
$H_{31C}(3)$	Tangled (Tri.)
$H_{31C}(4)$	Rod (Tri.)
$H_{31C}(5)$	Tangled #3

reticulation of these tilings over the P, D and G surfaces is provided in Table 3.8. This set of structures includes some further examples of non-cubic invariant rod packings, and some further non–invariant rod packings of trigonal symmetry.

Table 3.8: Weavings with $2*26$ and 2226 symmetry on the P, D, and G surfaces: nomenclature described in main text.

Structure	Packing	Structure	Packing	Structure	Packing	Structure	Packing
$P_{122C}(1)$	#1	$D_{122C}(1)$	Loops	$G^{+}_{122C}(1)$	#1	$G^{-}_{122C}(1)$	#1
$P_{122C}(2)$	Loops	$D_{122C}(2)$	#1	$G^{+}_{122C}(2)$	Helical $2\times$#1	$G^{-}_{122C}(2)$	Helical $2\times$#1
$P_{93C}(1)$	Π^{*}	$D_{93C}(1)$	Rod (Tri.)	$G^{+}_{93C}(1)$	#3	$G^{-}_{93C}(1)$	Rod (Tri.)
$P_{93C}(2)$	#1	$D_{93C}(2)$	Intersect	$G^{+}_{93C}(2)$	Rod (Tri.)	$G^{-}_{93C}(2)$	Rod (Tri.)

The simplest hyperbolic patterns yield a rich variety of structures in $\mathbb{E}^3$, from invariant rod packings, both cubic and non-cubic, to other non-invariant rod packings, packings with intersecting filament axes, the complex inter-growth of loops and more tangled weavings. We explore here some of the examples collated in the previous four tables.

3.3.1 Invariant rod packings: non-cubic

There are exactly 8 invariant rod packings that have non–cubic symmetry, as enumerated in [OKee 05]; four of these are composed solely of parallel rods, and the other four composed of stacked layers, where rods are parallel within a layer. Four of these rod packings arise *via* reticulations of complementary regular ribbon tilings on the P, D, G and H surfaces.

We describe these reticulations and subsequent weavings here.

The #1 rod packing [OKee 05] consists of parallel rods, whose cross section is the vertices of a $\{6,3\}$ tiling. Structures related to this rod packing (those whose filament average axes align along the rod packing) arise multiple times as reticulations of the P, D and G surfaces, namely $P_{122C}(1)$, $P_{93C}(2)$, $D_{122C}(2)$ and $G^{+}_{122C}(1)$. Fig. 3.29(a-c) shows the construction of the $G^{+}_{122C}(1)$ structure, which contains helical rods each with a chirality opposite to its neighbour. The space group of the helical array is the trigonal group $R\bar{3}c$. Other variants of this rod packing are the structures $H_{31C}(2)$ and $G^{+}_{122C}(2)$, which have triple and double helices along each rod axis respectively.

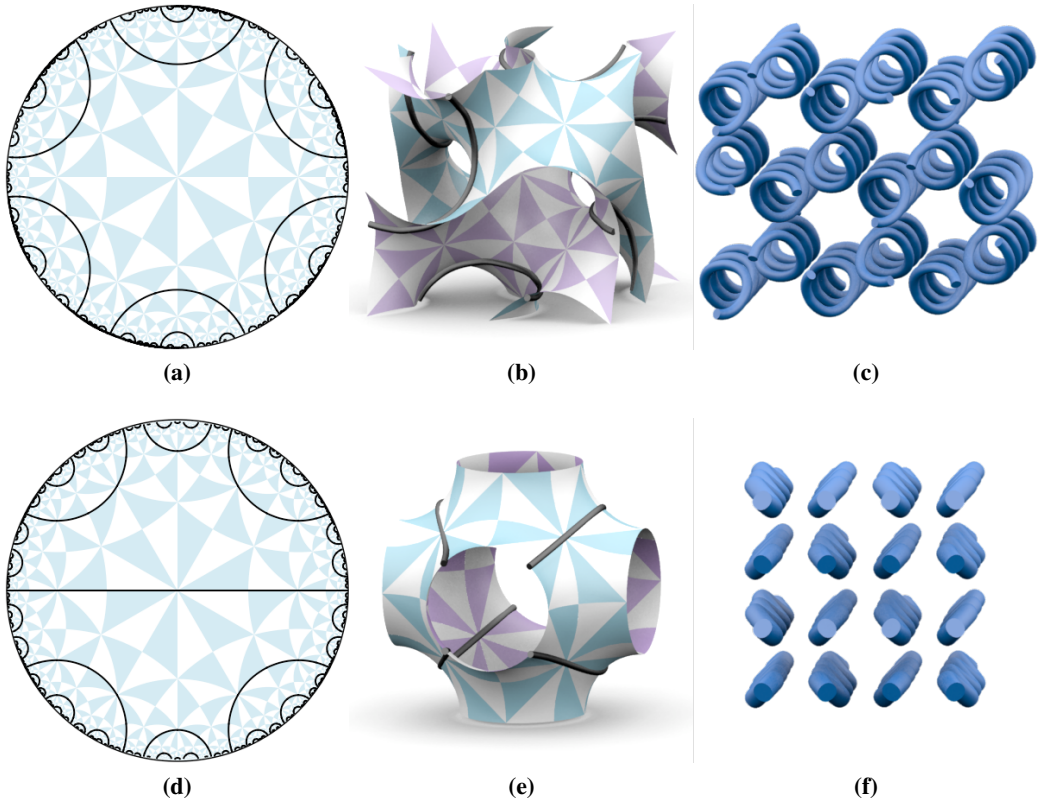

Figure 3.29: (a-c) The structure $G^{+}_{122C}(1)$, shown as a tiling of $\mathbb{H}^2$ and on the G surface, is a helical version of the #1 rod packing, where neighbouring helices have opposite handedness. (d-f) The filamentous array $P_{123C}(2)$, shown in $\mathbb{H}^2$, on the P surface and in $\mathbb{E}^3$, has undulating filaments and is related to the #2 rod packing.

Parallel rods whose cross section is the vertices of a $\{4,4\}$ tiling of $\mathbb{E}^2$ constitute the #2 rod packing [OKee 05]. Structures that are equivalent to this packing arise as tilings of the P, D and G surfaces, namely structures $P_{123C}(2)$, $D_{123C}(1)$, $D_{114C}(2)$, $G^{+}_{123C}(1)$, $G^{+}_{114C}(1)$ and $G^{-}_{114C}(4)$. Fig. 3.29(d-f) shows the construction of the structure $P_{123C}(2)$, consisting of

undulating rods, on the P surface. The space group of the array with undulating filaments is the tetragonal group $I4/mmm$. Another structure, $P_{114C}(3)$, is related to the #2 rod packing and is composed of quadruple helices along the rod axes. Similarly, the $G^{+}_{114C}(3)$ structure has triple helices along the rod axes. Further, tangled versions of the #2 rod packing arise as structures $D_{114C}(3)$ and $G^{-}_{114C}(3)$.

The #3 rod packing consists of parallel rods, whose cross section is the vertices of a trihexagonal (3.6.3.6) tiling. A structure related to this rod packing arises as a reticulation of both the G surface and H surface: these structures are $G_{93C}(1)$ and $H_{32C}(1)$, both shown in Fig. 3.30. In both structures, the reticulation has undulating filamentous components. The space group of the undulating array in both cases is the trigonal group $R\bar{3}c$. Further, a tangled version of the #3 rod packing is the $H_{31C}(5)$ structure.

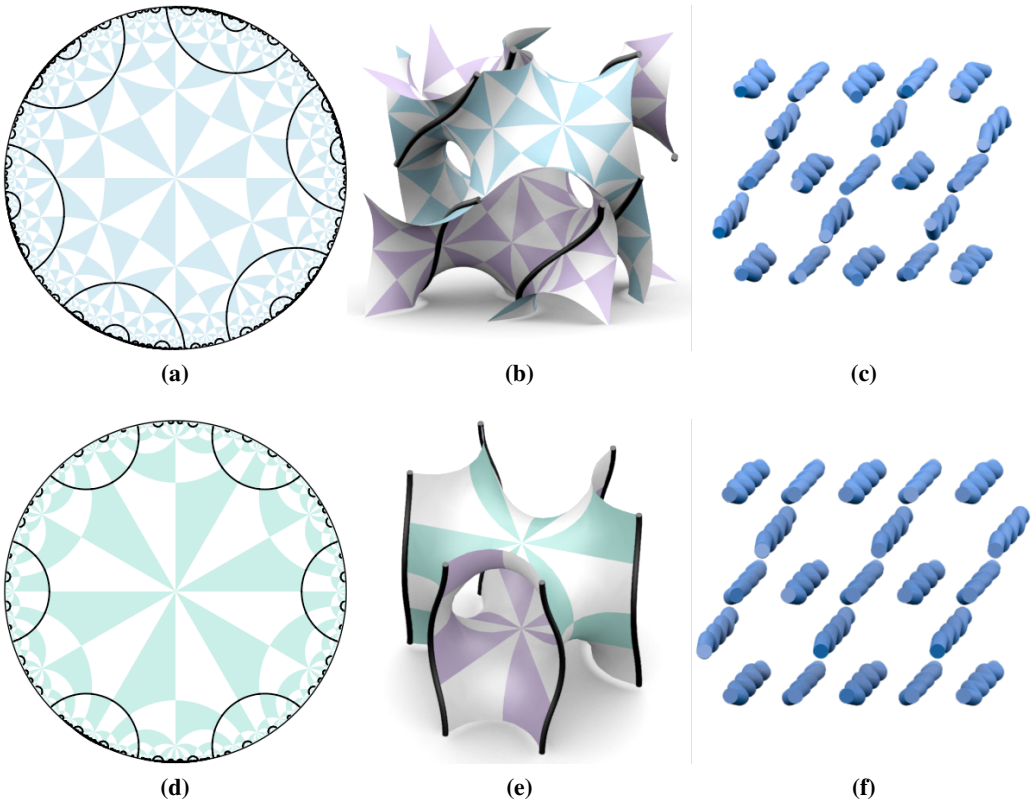

Figure 3.30: (a-c) The structure $G_{93C}(1)$, shown in $\mathbb{H}^2$, on the G surface and in $\mathbb{E}^3$, is related to the #3 rod packing, and is composed of undulating filaments. (d-f) The structure $H_{32C}(1)$, shown in $\mathbb{H}^2$, on one unit cell of the H surface and in $\mathbb{E}^3$, is also related to the #3 rod packing.

Stacked layers of parallel rods where adjacent layers are rotated through a right angle comprise the #6 rod packing. Structures related to this packing may be constructed as a tiling of the D and G surfaces, namely the structures $D_{123C}(2)$ and $G^{-}_{114C}(1)$. Fig. 3.31(a-c)

shows the construction of the $D_{123C}(2)$ structure. The space group of the array is $P4_2/mmc$, and the filaments are straight.

The #4, #5, #7 and #8 rod packings have not been constructed from complementary regular ribbon tilings of the symmetry groups considered. However a structure related to the #5 rod packing, composed of stacked layers where each subsequent layer is rotated through a right angle (at half the density of the #6 rod packing), arises as a reticulation of the D surface by a free tiling with $2*222$ symmetry (group 104), a lower order symmetry group, as shown in Fig. 3.31(d-f). The structure is composed of undulating filamentous components, and the space group of the structure is the tetragonal $I4_1/amd$. The examples considered form a very small portion of possible weavings which may be constructed by the method, so the other missing examples may arise on further enumeration of hyperbolic patterns in other symmetry groups.

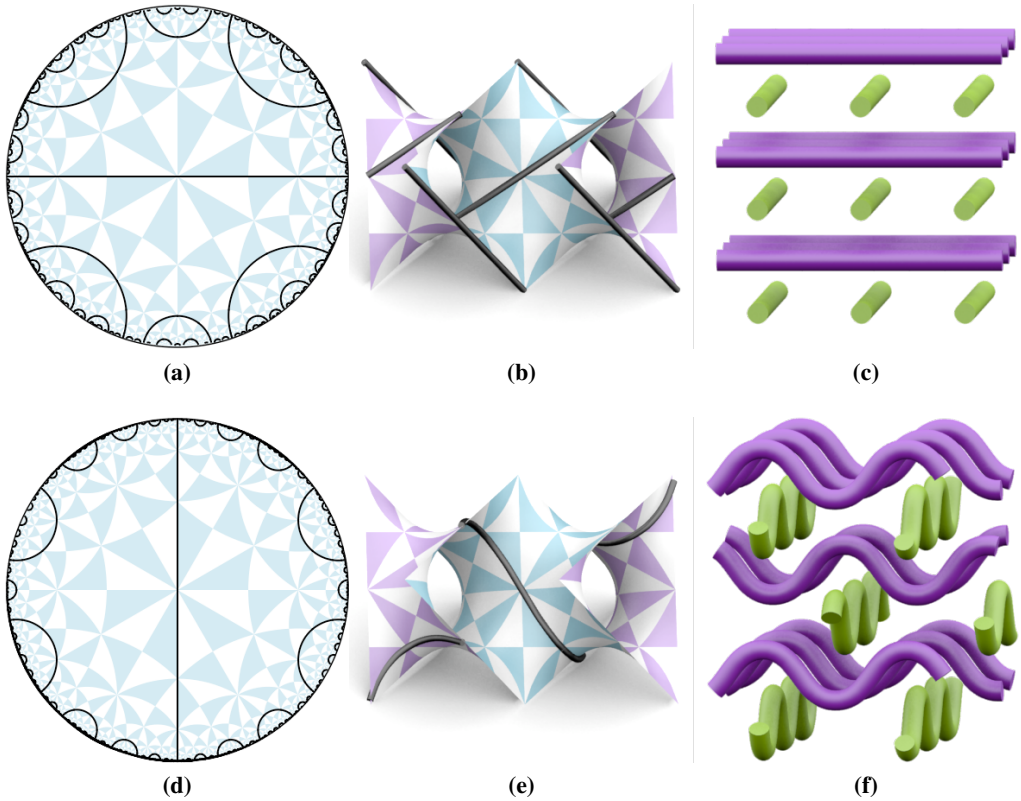

Figure 3.31: (a-c) The construction of the $D_{123C}(2)$. This structure is the #6 rod packing, consisting of straight rods in alternating layers. (d-f) The projection of a tiling with $2*222$ symmetry in $\mathbb{H}^2$, on one unit cell of the D surface, and in $\mathbb{E}^3$. This structure is an undulating version of the #5 rod packing.

3.3.2 Invariant rod packings: cubic

Exactly six invariant rod packings of cubic symmetry are enumerated in [OKee 05]. We shall see that weavings related to five of these six rod packings arise from the reticulation of TPMS by free tilings of $\mathbb{H}^2$. Further, weavings which are sufficiently tangled to preclude filament straighening, yet these invariant cubic rod packings describe their filaments average axes arise numerously: we will consider these examples in Section 3.3.6. Here we will review those weavings from the first class, who equivalent to the invariant cubic rod packings by ambient isotopy.

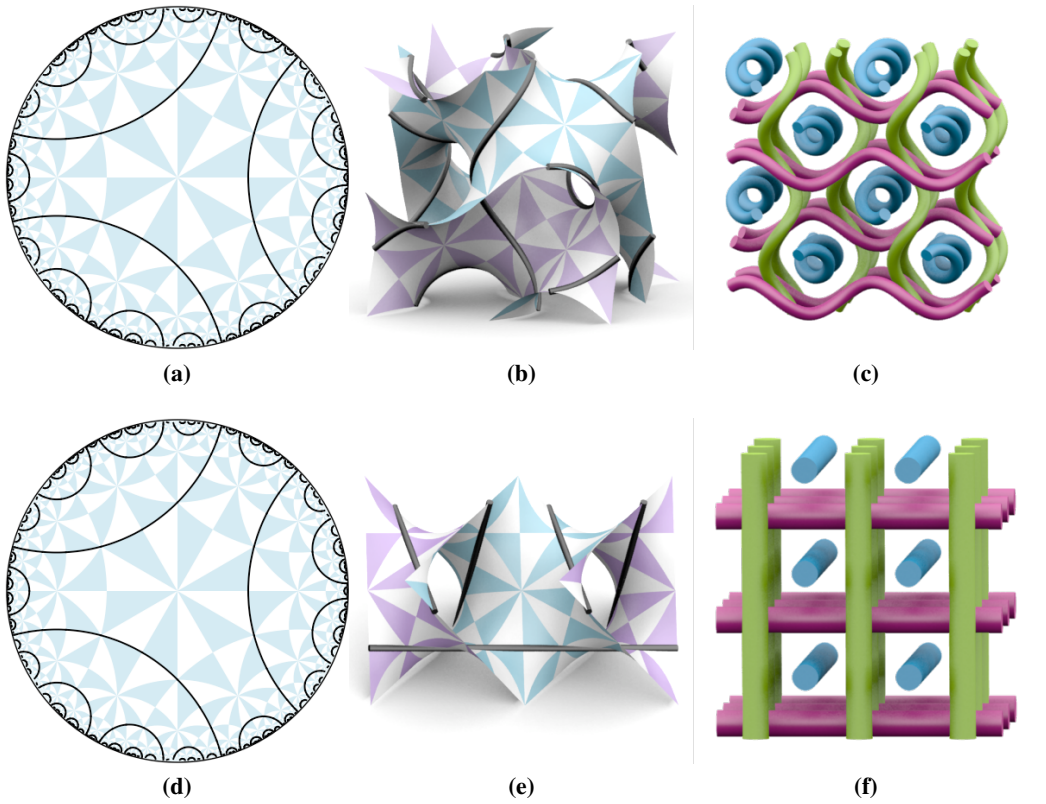

Figure 3.32: (a-c) The G^{+}_{124C} structure, shown in $\mathbb{H}^2$, on the G surface and in $\mathbb{E}^3$, is a helical version of the Π^{+} rod packing, where all helices have equivalent handedness. (d-f) The D_{124C} structure, shown in $\mathbb{H}^2$, on the D surface and in $\mathbb{E}^3$, is exactly Π^{*}.

On straightening to their average axis, the filaments of the G^{+}_{124C} weaving are arranged in the form of the Π^{+} rod packing (Fig. 3.32(a-c)). The weaving, as it sits on the G surface, is composed of perfectly helical filaments, all of equivalent chirality. Also of note is the G^{-}_{124C} weaving, which is the reticulation of the same hyperbolic tiling over the G surface by the other covering map, which gives the Π^{-} enantiomer of the chiral rod packing. Further,

all filaments in this weaving will have the opposite chirality to the enantiomeric structure. The D_{124C} structure is composed of straight rods that are arranged in a $\Pi*$ rod packing, as shown in Fig. 3.32(d-f). This rod packing is the inter-growth of both chiral enantiomers of the rod packing Π^+ and Π^-.

A helical variant of the Σ^+ rod packing arises as a reticulation of the G surface, namely G^+_{129C}, as shown in Fig. 3.33(a-c). The geometry inherited from the reticulation of the surface consists of helical filaments whose axes align along rods, where each of the helices have equivalent chirality. The G^-_{129C} weaving, obtained through the other covering map of the G surface, will be related to the Σ^- enantiomer. Further, a Γ rod packing composed of slightly undulating rods is related to the $G^+_{123C}(2)$ structure, as shown in Fig. 3.33(d-f). This Γ rod packing is also related to the $D_{114C}(1)$ structure, constructed on the D surface.

The P_{129C} structure is related to the Ω^+ rod packing. The filament geometry inherited from the surface reticulation, as seen in Fig. 3.33(g-i), is slightly helical, where the helices are all of equivalent chirality.

These structures, which are constructed from complementary regular ribbon tilings of some highest symmetry orbifolds, are related to 5 out of the 6 invariant cubic rod packings detailed in [OKee 01]. The sixth of these rod packings is the $\Sigma*$ packing, which is an interwoven variant containing a Σ^+ and a Σ^- (an enantiomeric pair). As yet, we have not been able to construct this by the TPMS reticulation method. It is probable, however, that this structure may occur at another stage of the enumeration process, likely as a free tiling on a lower symmetry orbifold within the $*246/\circ\circ\circ$ or $*2226/\circ\circ\circ$ quotient groups. In other words, these structures are a very small subset of the possible reticulations of TPMS, and hence it is likely that $\Sigma*$ will arise on further enumeration.

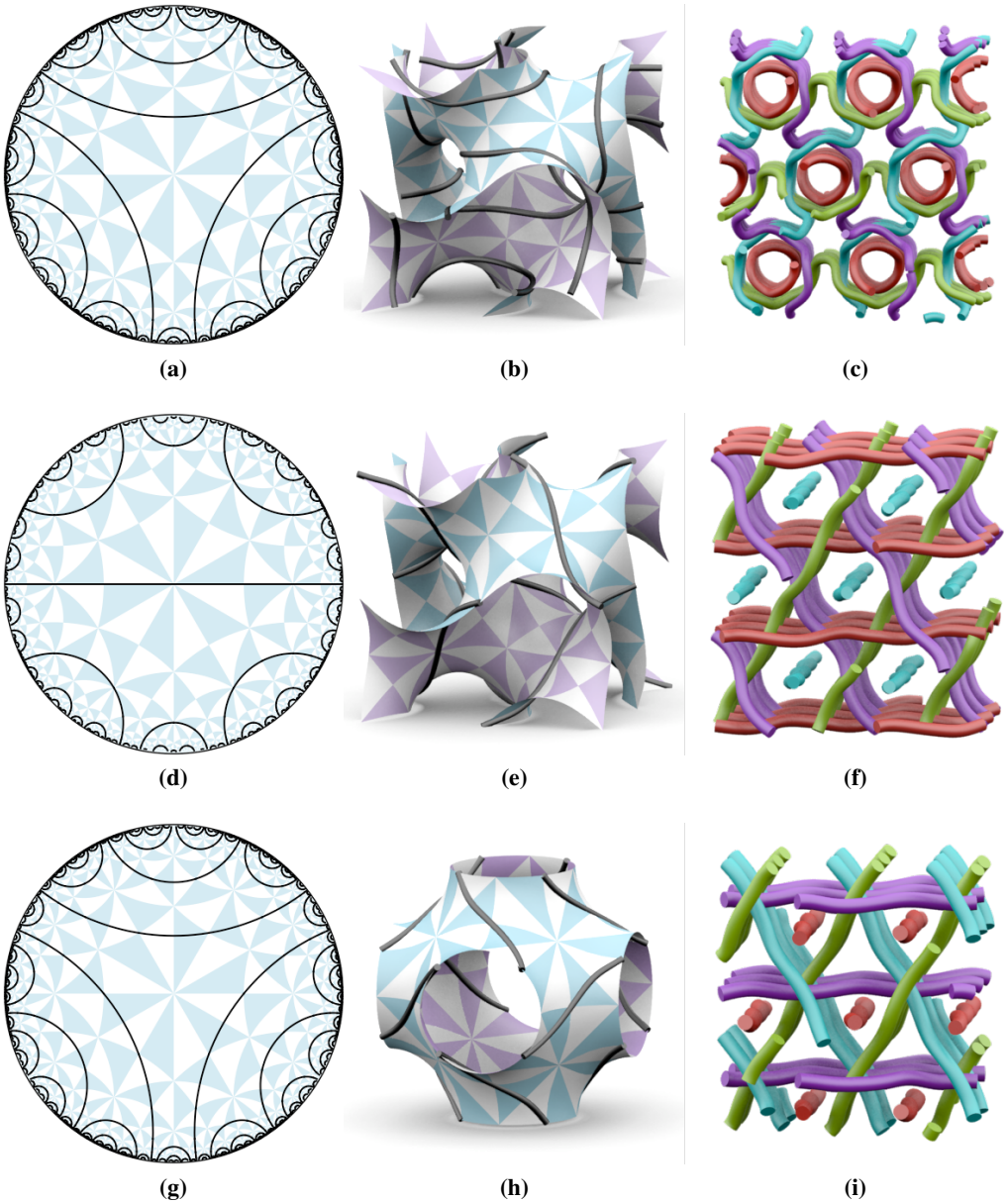

Figure 3.33: (a-c) The G^{+}_{129C} structure, shown as a tiling in $\mathbb{H}^2$, on the G surface and in $\mathbb{E}^3$, is related to the Σ^{+} rod packing. It is composed of helical filaments, with all helices of equivalent handedness. (d-f) The $G^{+}_{123C}(2)$ array, shown in $\mathbb{H}^2$, on the G surface and in $\mathbb{E}^3$, is related to the Γ rod packing, and is composed of slightly undulating rods. (g-i) The P_{129C} structure is related to the Ω^{+} rod packing. It contains slightly helical rods, all of equivalent handedness.

3.3.3 Non–invariant rod packings

Within this enumeration of structures, there are 7 structures whose filaments align the rod directions of non–invariant rod packings on straightening. These weavings have tetragonal symmetry in some cases, and trigonal symmetry in others. These rod packings have not been enumerated in [OKee 01, OKee 05], as they are not invariant rod packings: the rods do not lie along the invariant lines of the space group, they occupy other axes.

The $P_{114C}(1)$ structure is shown in Fig. 3.34(a-c). The filament geometry inherited from the surface reticulation is straight rods, where the four distinct rod positions within a unit cube cell are described by the trajectories $\{u,0,\frac{1}{2}+u\}$, $\{u,\frac{1}{2},-u\}$, $\{\frac{1}{2},u,\frac{1}{2}+u\}$ and $\{0,u,-u\}$. The structure has tetragonal symmetry $P4/nnc$. A tangled version of this weaving is also constructed via a TPMS reticulation, namely the $P_{114C}(4)$ array.

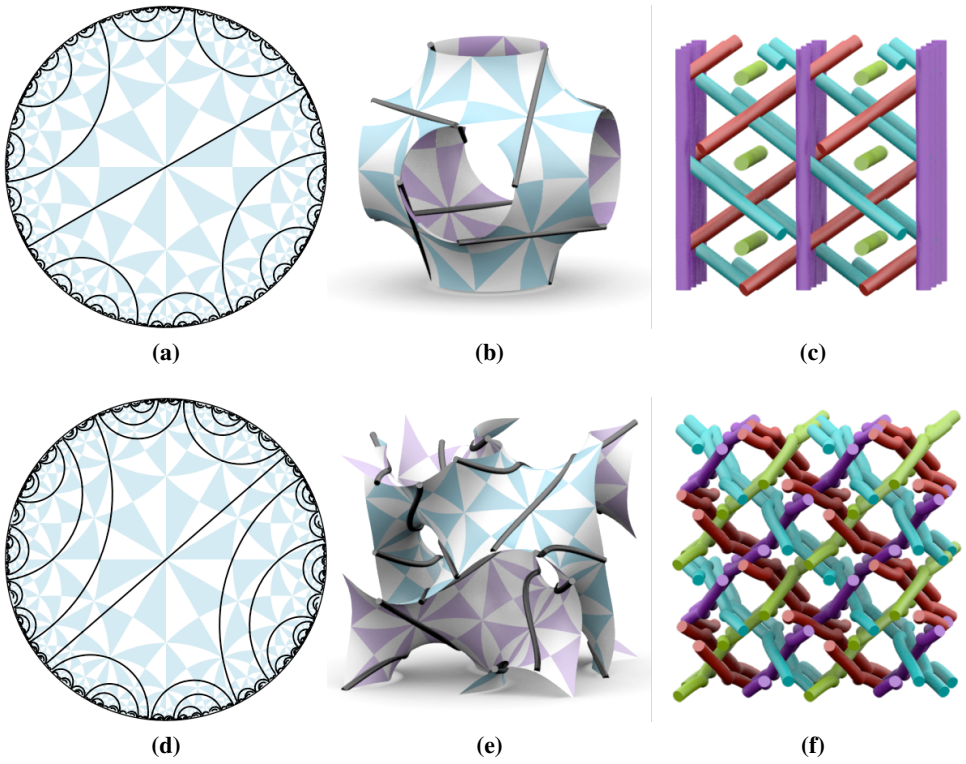

Figure 3.34: (a-c) The construction via the P surface of the $P_{114C}(1)$ structure, a tetragonal rod packing composed of straight rods. The structure is shown (a) as a tiling of $\mathbb{H}^2$, (b) on one unit cell of the P surface and (c) in $\mathbb{E}^3$. (d-f) The $G^{+}_{114C}(2)$ filamentous array is a tetragonal rod packing composed of slightly undulating filament. This structure is shown (a) in $\mathbb{H}^2$, (b) on one unit cell of the G surface and (c) in $\mathbb{E}^3$.

The $G^{+}_{114C}(2)$ weaving, shown in Fig. 3.34(d-f), has tetragonal symmetry $(I4_1/acd)$ and the filaments may be straightened to rods which maintaining ambient isotopy. The

filaments of the structure are slightly undulating, and their four distinct axes within a unit cube cell are described by the vectors $\{u,u,-3u\}$, $\{-u,u,\frac{1}{2}+3u\}$, $\{\frac{1}{2}+u,u,\frac{1}{2}+3u\}$ and $\{\frac{1}{2}-u,u,3u\}$. Another structure that is equivalent to this weaving by ambient isotopy is the $D_{114C}(4)$ structure.

The filaments of the $P_{114C}(5)$ weaving may also straighten to give a non-invariant rod packing, which is also of tetragonal symmetry ($P4/nnc$). The construction of this weaving is shown in Fig. 3.35. The weaving is composed of slightly undulating filaments, where the four distinct rod positions within a unit cube cell are described by the vectors $\{u,0,3u\}$, $\{u,\frac{1}{2},\frac{1}{2}-3u\}$, $\{0,u,\frac{1}{2}-3u\}$ and $\{\frac{1}{2},u,3u\}$.

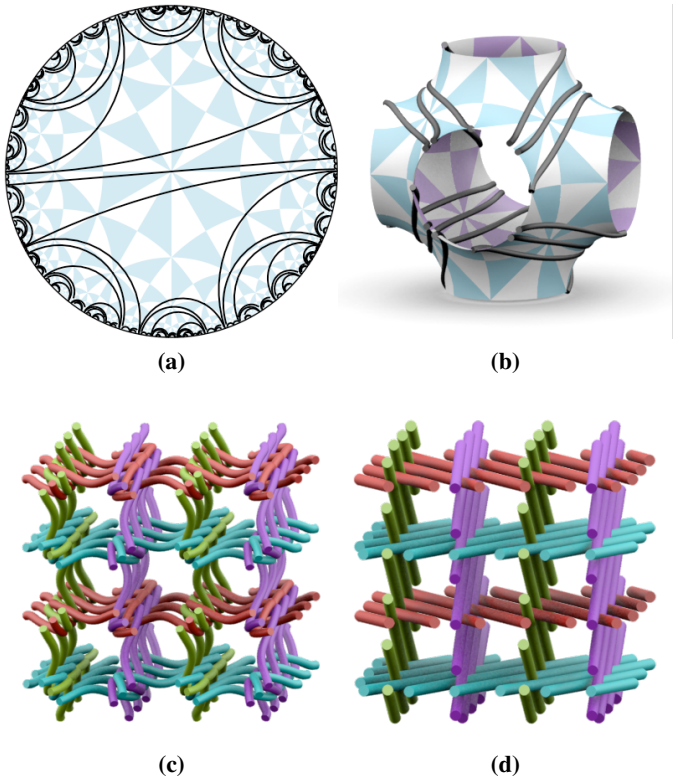

Figure 3.35: The $P_{114C}(5)$ weaving, whose filaments may straighten to give a non-invariant rod packing of tetragonal symmetry ($P4/nnc$). The weaving is composed of undulating filaments along the rod axes. The weaving is shown (a) as a free tiling of $\mathbb{H}^2$, (b) on one unit cell of the P surface, (c) in $\mathbb{E}^3$ and (d) in $\mathbb{E}^3$, where the undulating filaments have been straightened to their average axis to give rods.

The $H_{31C}(1)$ weaving, constructed on the H surface (Fig. 3.36), is a weaving whose filaments may straighten to their average axis to give a non–invariant rod packing of trigonal symmetry. The three distinct straight rod axis positions, given in crystallographic coordinates for a trigonal unit cell, are described by the vectors $\{0,u,\frac{1}{2}-u\}$, $\{\frac{1}{2}+u,u,u\}$

and $\{u, 0, -u\}$. The filaments have undulating trajectories as a reticulation on the H surface. The structure (with undulating rods) has trigonal symmetry given by the space group $P\bar{3}1c$. A tangled version of this weaving may also be constructed on the H surface, and is the $H_{31C}(3)$ structure.

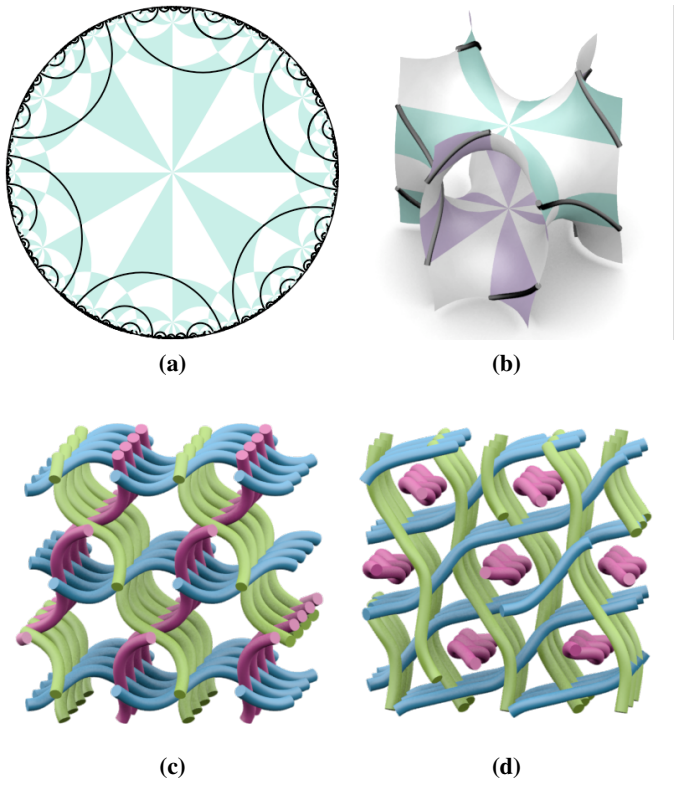

Figure 3.36: The construction of the trigonal rod packing $H_{31C}(1)$ on the H surface. The structure is shown (a) in $\mathbb{H}^2$, (b) on the H surface and (c) in $\mathbb{E}^3$. The image (d) shows a view of the rod packing along a rod axis.

Projection to the H-surface of another complementary regular ribbon tiling, and the subsequent removal of the surface in $\mathbb{E}^3$ gives the $H_{31C}(4)$ weaving, as shown in Fig. 3.37(a-c). The filaments of this weaving may pull straight to give a rod packing of trigonal symmetry. The three distinct rod positions, given in crystallographic coordinates for a trigonal unit cell, are described by the vectors $\{0, u, -3u\}$, $\{u, u, 3u\}$ and $\{u, 0, -3u\}$. The weaving has trigonal symmetry $P\bar{3}1c$.

The filaments of the weaving $G^{+}_{93C}(2)$ may also pull straight to give a rod packing with trigonal symmetry $R\bar{3}c$ (Fig. 3.37(d-f)). The three distinct rod positions, described in a cubic unit cell corresponding to the G surface cubic unit cell, are given by the vectors $\{u, \frac{1}{2}+3u, \frac{1}{2}+u\}$, $\{3u, u, \frac{1}{2}+u\}$ and $\{u, \frac{1}{2}+u, 3u\}$.

As a final example, the $G^{-}_{93C}(1)$ weaving has filament axes along a rod packing of trigonal symmetry $R\bar{3}c$. The $G^{-}_{93C}(2)$ weaving is also equivalent to this trigonal rod packing by ambient isotopy. The construction of $G^{-}_{93C}(1)$ is shown in Fig. 3.37(g-i). The alignment of the rods in a cubic unit cell, corresponding to the G surface cubic unit cell, is described by the vectors $\{-u, u, \frac{1}{2}-u\}$, $\{u, \frac{1}{2}+u, \frac{1}{2}-u\}$ and $\{\frac{1}{2}-u, u, \frac{1}{2}+u\}$. From a particular viewing direction, it appears to be a deformation of the Π^{*} invariant cubic rod packing.

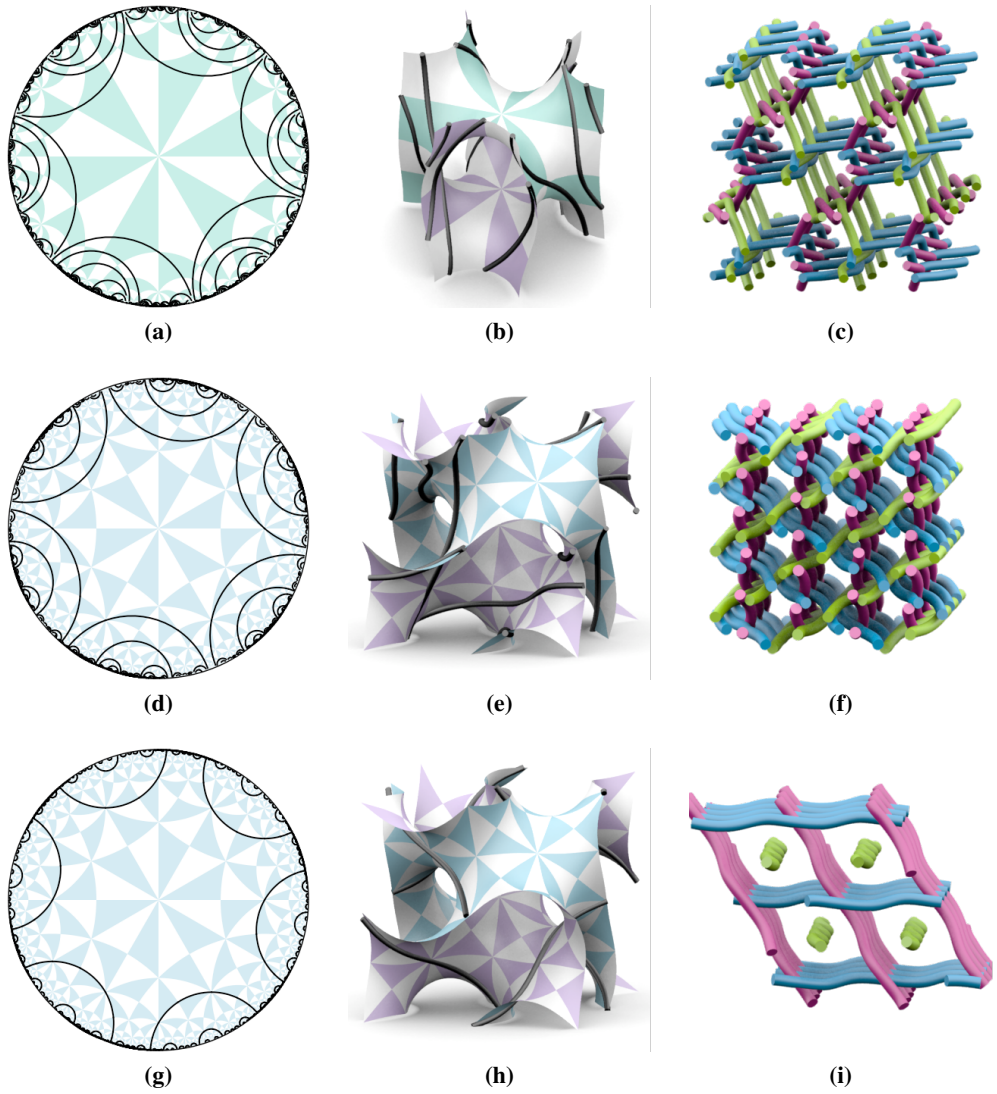

Figure 3.37: (a-c) The construction of the $H_{31C}(4)$ structure, which is related to a non–invariant rod packing of trigonal symmetry. The structure is shown in $\mathbb{H}^2$, on one unit cell of the H surface, and in $\mathbb{E}^3$. (d-f) The $G^{+}_{93C}(2)$ structure, shown in $\mathbb{H}^2$, on the G surface and in $\mathbb{E}^3$, is also related to a non–invariant trigonal rod packing. (g-i) The $G^{-}_{93C}(1)$ structure is also related to a non–invariant rod packing with trigonal symmetry.

3.3.4 Weavings with intersecting filament axes

Within our enumeration, some of the weavings have filament axes that are intersecting. Typically, this scheme of entanglement has been disallowed from enumerations of rod packings, but the extension to weavings composed of curvilinear filaments counters this. We examine some of these weavings in further detail, and describe the axes of the filaments when straightened to their average axis.

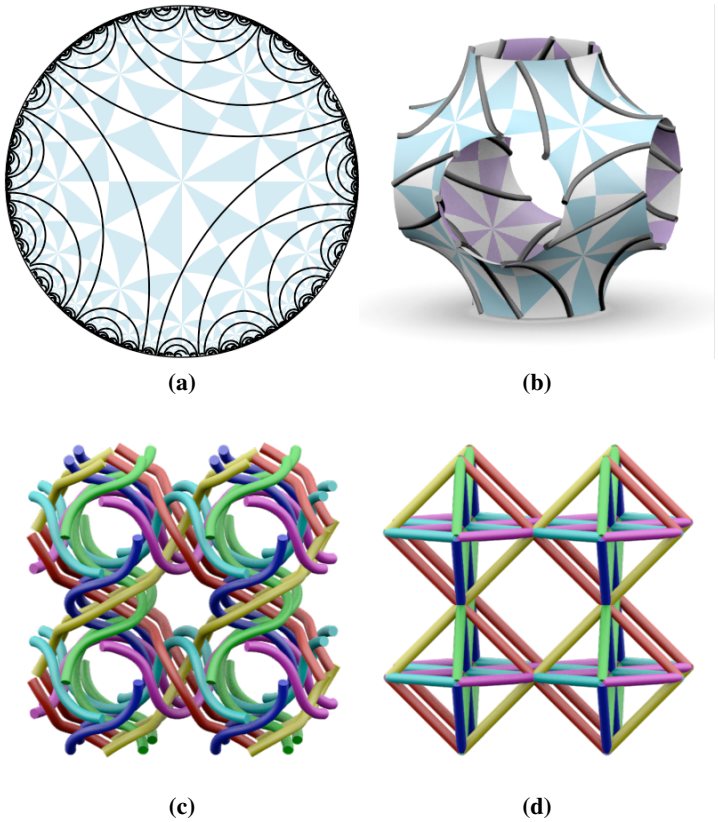

Figure 3.38: The $P_{118C}(1)$ weaving has intersecting filament axes. (a) The complementary regular ribbon tiling $*246_{118C}(1)$, shown in $\mathbb{H}^2$. (b) The tiling shown on the P surface, (c) the weaving in $\mathbb{E}^3$, and (d) The filaments pulled straight. The net which emerges when intersecting points are changed to vertices is the **reo** net.

The weaving $P_{118C}(1)$ is constructed on the P surface from a free tiling of $\mathbb{H}^2$, as shown in Fig. 3.38. On straightening the filaments of this weavings, the filament axes intersect. The six distinct average axes of the filaments, given in a cubic unit cell, are described by $\{u, \frac{1}{2} \pm u, 0\}$, $\{0, u, \frac{1}{2} \pm u\}$ and $\{u, 0, \frac{1}{2} \pm u\}$. The structure has space group $P432$ as a reticulation of the surface. The filament axes are intersecting, thus if we consider the intersection points of the straight rods to be vertices, we obtain a 3-periodic net on filament

straightening. In the case of the $P_{118C}(1)$ weaving, this net is the **reo** (or **pcu-e**) net, which has 1-transitive vertices and edges, and 2-transitive faces and tiles [OKee 08].

The weaving $D_{118C}(1)$ is constructed on the D surface from the complementary regular ribbon tiling $*246_{118C}(1)$ (Fig. 3.39). When the filaments of this weaving are pulled straight, their average axes intersect. The twelve distinct filament axes, given in a cubic unit cell, are described by $\{u,u,\frac{1}{8}\}$, $\{u,\frac{1}{2}+u,\frac{5}{8}\}$, $\{u,\frac{1}{8},u\}$, $\{u,\frac{5}{8},\frac{1}{2}+u\}$, $\{\frac{1}{8},u,u\}$, $\{\frac{5}{8},u,\frac{1}{2}+u\}$, $\{\frac{7}{8},u,-u\}$, $\{\frac{3}{8},u,\frac{1}{2}-u\}$, $\{u,\frac{7}{8},-u\}$, $\{u,\frac{3}{8},\frac{1}{2}-u\}$, $\{u,-u,\frac{7}{8}\}$ and $\{u,\frac{1}{2}-u,\frac{3}{8}\}$. The structure has space group $F4_132$ on the surface. If the intersection points of the filaments are taken as vertices, the net that defines the structure is the **crs** net (also known as **dia-e** or crystobalite), which has 1-transitive vertices and edges, and 2-transitive faces and tiles.

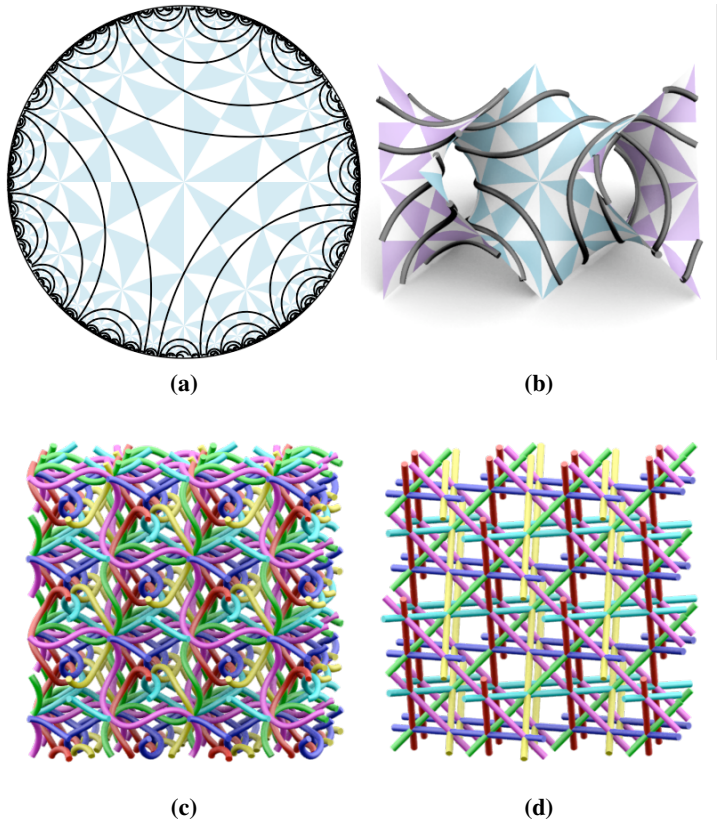

Figure 3.39: The structure $D_{118C}(1)$, shown (a) in $\mathbb{H}^2$, (b) on one unit cell of the D surface, and (c) in $\mathbb{E}^3$, is a weaving with intersecting filament axes. (d) On straightening the filaments to their average axes, they intersect. If these intersections are changed to vertices, the weaving forms a net: this net is the **crs** net.

The $G^+_{118C}(1)$ structure, as shown in Fig. 3.40, also has filament axes that are intersecting. The twelve distinct average axes of the filaments, given in a cubic unit cell, are de-

scribed by the vectors $\{u, \frac{1}{4}-u, \frac{3}{8}\}$, $\{u, \frac{1}{4}-u, \frac{7}{8}\}$, $\{\frac{3}{8}, \frac{1}{4}-u, u\}$, $\{\frac{7}{8}, \frac{1}{4}-u, u\}$, $\{u, \frac{1}{4}+u, \frac{1}{8}\}$, $\{u, \frac{1}{4}+u, \frac{5}{8}\}$,$\{u, \frac{3}{8}, \frac{1}{4}-u\}$, $\{u, \frac{7}{8}, \frac{1}{4}-u\}$, $\{\frac{1}{8}, \frac{3}{4}+u, u\}$, $\{\frac{5}{8}, \frac{3}{4}+u, u\}$, $\{u, \frac{1}{8}, \frac{3}{4}+u\}$ and $\{u, \frac{5}{8}, \frac{3}{4}+u\}$. The weaving has space group $I4_132$ on the surface. If the filaments are straightened, and the intersection points taken to be vertices, the nets that results is the chiral **nfa** net, with 1-transitive vertices, 2-transitive edges, 3-transitive faces and 2-transitive tiles.

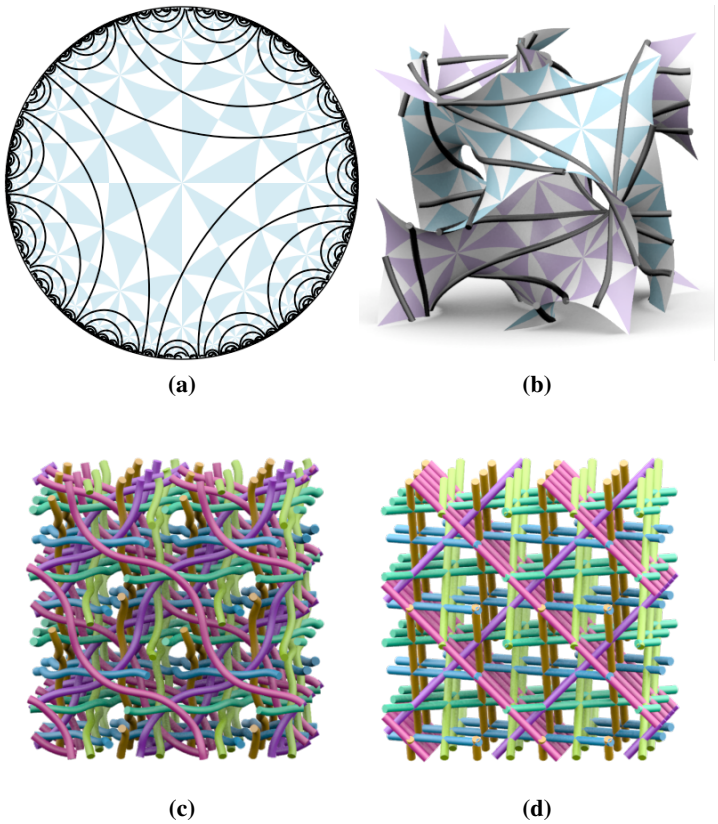

Figure 3.40: The weaving $G^{+}_{118C}(1)$, shown (a) in $\mathbb{H}^2$, (b) on one unit cell of the G surface, and (c) in $\mathbb{E}^3$. If the filaments of this weaving straightened along their average axes, they become intersecting trajectories. (d) The net that results if the intersections of the filaments are changed to be vertices of a net: this net is the chiral **nfa** net.

The $P_{114C}(2)$ weaving, as shown in Fig. 3.41, is another weaving whose filament axes are intersecting. The four distinct average axes of the filaments in this weavings, given in a cubic unit cell, are described by the vectors $\{u, u, -u\}$, $\{u, \frac{1}{2}-u, \frac{1}{2}+u\}$, $\{u, u, \frac{1}{2}+u\}$ and $\{u, \frac{1}{2}-u, -u\}$. The weaving has space group $P4/nnc$. If the intersection points of the straightened filaments are changed to vertices, the net that results is the **bcu** net (also know as *body centered cubic*), which has 1-transitive vertices, edges, faces and tiles, and thus is a regular net.

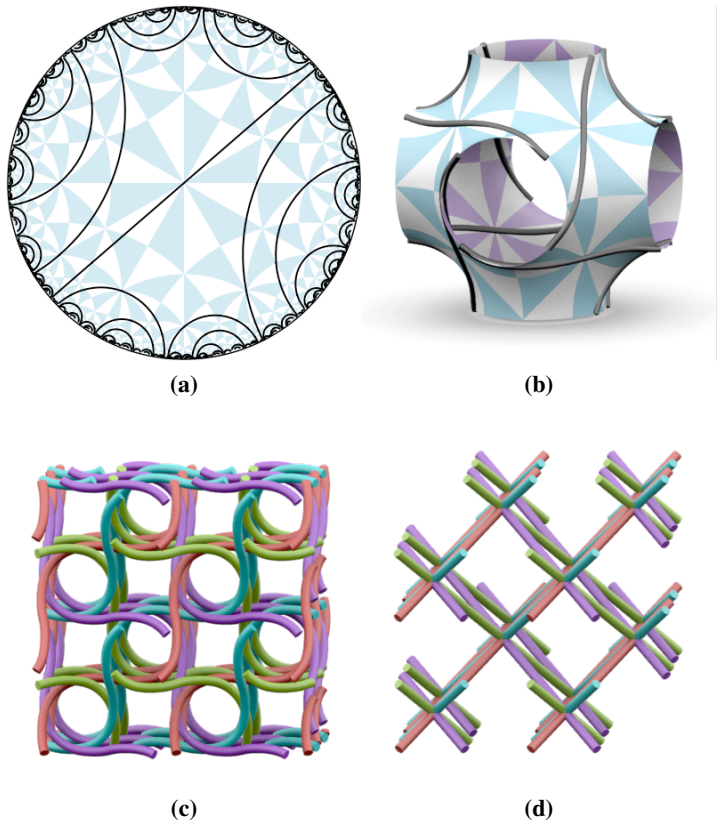

(a) **(b)** **(c)** **(d)**

Figure 3.41: The $P_{114C}(2)$ weaving, shown (a) in $\mathbb{H}^2$, (b) on one unit cell of the *P* surface, and (c) in $\mathbb{E}^3$, is another weaving whose filament axes are intersecting. (d) If the intersection points of the straightened filaments are changed to vertices, the net that results is the **bcu** net.

3.3.5 Complex inter-growth of loops

For some structures, the filament trajectories of the TPMS reticulation form closed loops in $\mathbb{E}^3$. In many cases, these loops are not threaded, and the structure is an array of disjoint loops. Fig. 3.42 shows two such examples, P_{123C} and $G^{-}_{118C}(1)$, that lie on the *P* surface and *G* surface respectively, where the two structure have a distinct geometric arrangement of the loops.

For one structure, $P_{118C}(4)$, the loops of the array are catenated (Fig. 3.42(g-k)). Each component of the structure catenates by a Hopf link with 16 of its neighbouring closed components, forming a 3D *chain-mail*. Within this structure, sheets of doubly-periodic chain-mail sit in three orthogonal planes in $\mathbb{E}^3$, all catenating. The layers have normal vector orientations of $\{1,0,0\}$, $\{0,1,0\}$ and $\{0,0,1\}$.

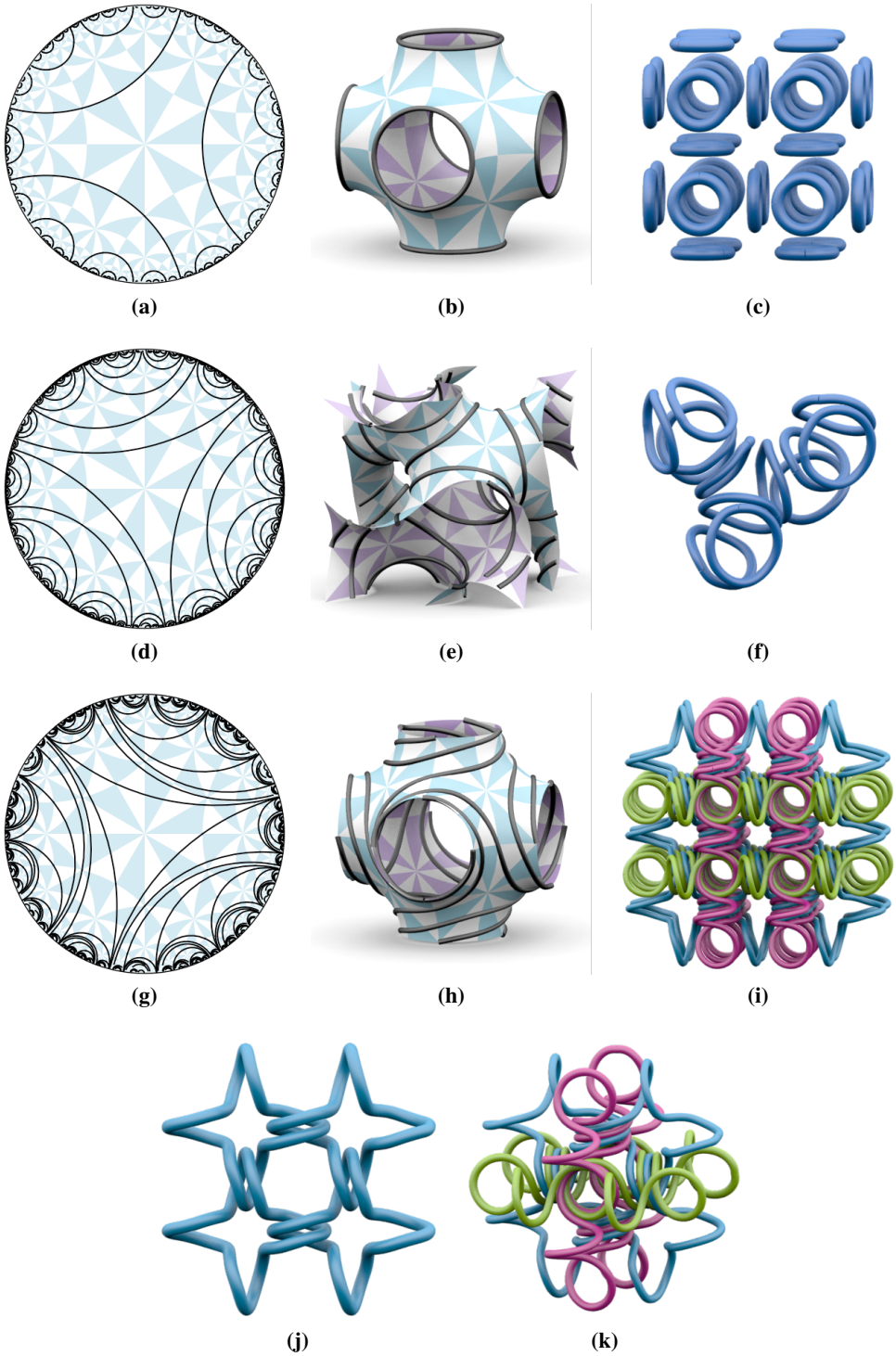

Figure 3.42: (a-c) The P_{123C} structure is an array of loops that are not threaded. (d-f) The $G^{-}_{118C}(1)$ structure, also an array of disjoint loops. (g-k) The inter-growth of closed loops: the $P_{118C}(4)$ structure. The structure is the interweaving of layers of Hopf link Chain-mail. (j) shows 4 links within a layer of the Chain-mail, highlighting the Hopf link interactions, and (e) shows the three distinct layers and how they interact.

3.3.6 More general weavings

In the third class of weavings, the filaments impede each other from straightening in unison. These are "tangled" structures. The rod axes of these arrays have been identified computationally by allowing the filaments to pass through each other and straighten to their average axes. Fig. 3.43 shows two weavings: the first is the $D_{114C}(3)$ structure, a tangled variant of the parallel square rod packing (#2 rod packing), and the second is the $H_{31C}(3)$ structure, a tangled version of the non–invariant rod packing with trigonal symmetry which arises as the $H_{31C}(1)$ weaving.

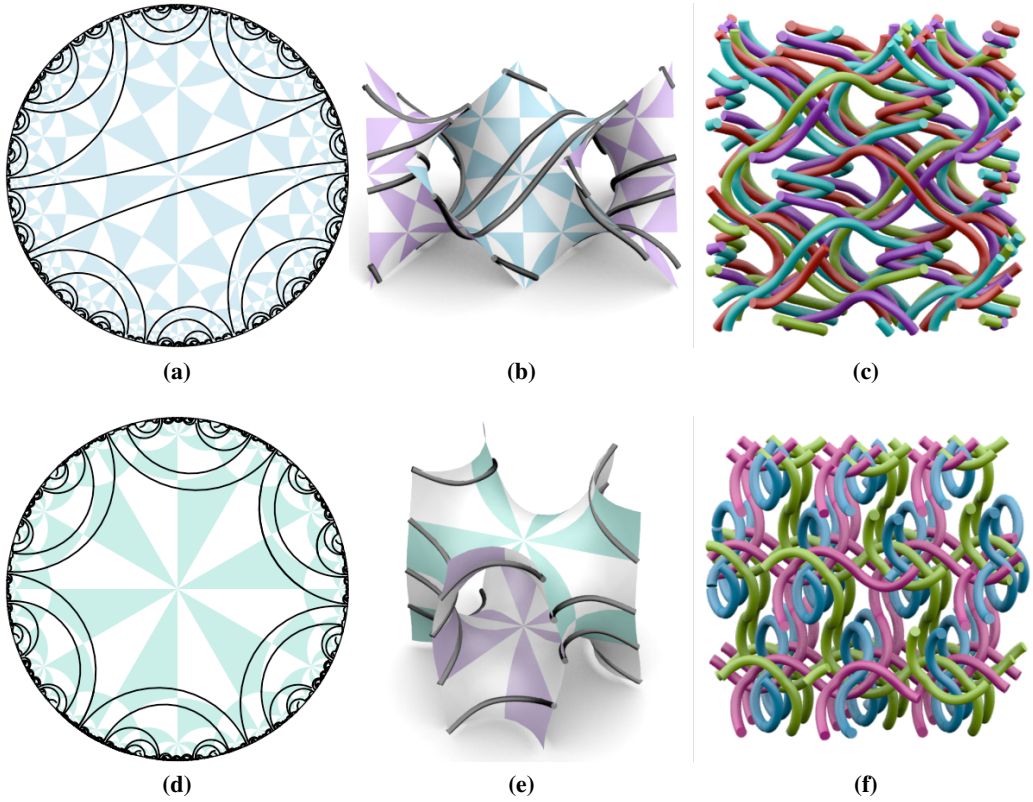

Figure 3.43: (a-c) The $D_{114C}(3)$ structure, shown in $\mathbb{H}^2$, on the D surface and in $\mathbb{E}^3$, is a tangled variant of the #2 rod packing. (d-f) The $H_{31C}(3)$ structure, also shown in $\mathbb{H}^2$, on the H surface and in $\mathbb{E}^3$, is a tangled version of the non–invariant rod packing with trigonal symmetry which arises as the $H_{31C}(1)$ weaving.

The weaving $G^{+}_{118C}(2)$ is another interesting weaving, shown in Fig. 3.44. If the filaments of the weaving are pulled straight to their average axes, disregarding changes in equivalence by ambient isotopy, the packing that results is Γ rod packing, with three filaments along each of the rods. The $G^{-}_{118C}(2)$ weaving is constructed on the G minimal surface by the same free tiling of $\mathbb{H}^2$ as the $G^{+}_{118C}(2)$ structure, yet by the other covering

map of the G surface. This structure is a tangled version of the Σ^+ rod packing, as shown in Fig. 3.45. The Σ^+ geometry of the weaving may be observed if each filament of the weaving is allowed to straighten along its axes, passing through other filaments which are obstructing the straightening.

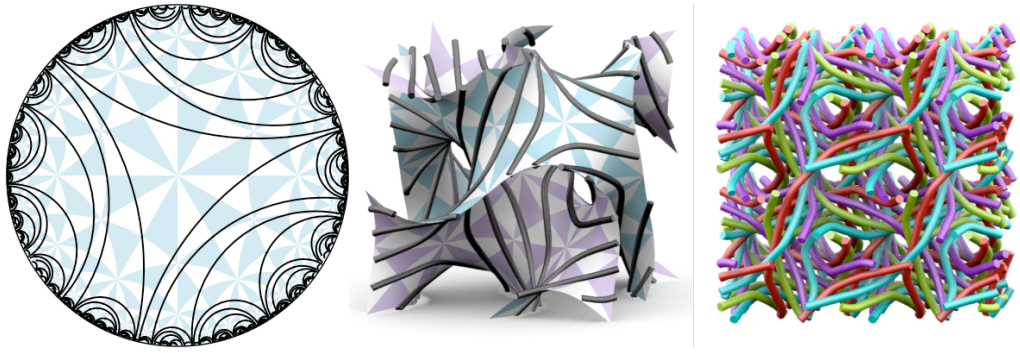

(a) **(b)** **(c)**

Figure 3.44: The $G^+_{118C}(2)$ structure is shown (a) in $\mathbb{H}^2$, (b) on one unit cell of the G surface, and (c) in $\mathbb{E}^3$. The structure is a tangled version of the Γ rod packing with 3 filaments along each rod.

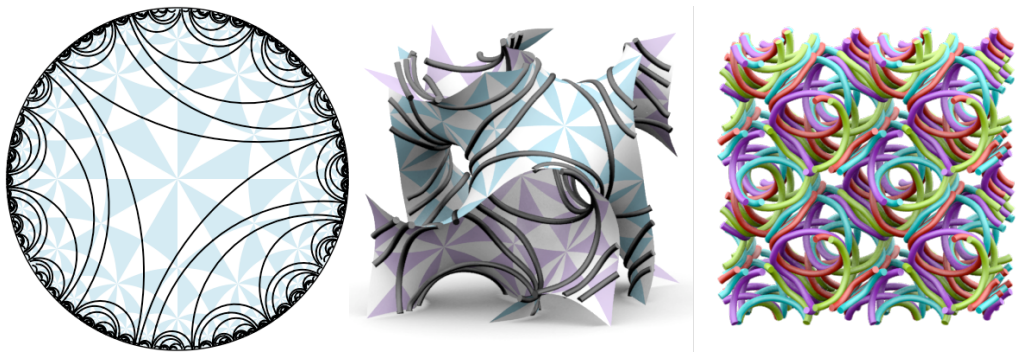

(a) **(b)** **(c)**

Figure 3.45: The $G^-_{118C}(2)$ structure is shown (a) in $\mathbb{H}^2$, (b) on one unit cell of the G surface, and (c) in $\mathbb{E}^3$. The structure is a tangled version of the Σ^+ rod packing.

It is apparent that the amount of winding of the weaving may be tuned using the obliqueness of the embedding in $\mathbb{H}^2$. A more oblique embedding of a free tiling with Stellate symmetry, signified by a higher embedding number in the weaving symbol (the '(n)' at the end of the symbol), will in general give a more woven structure in $\mathbb{E}^3$. Since the obliqueness of a free tiling embedding may have arbitrarily large in $\mathbb{H}^2$, this gives scope for the construction of weavings of arbitrary complexity.

3.3.7 Realisation of woven structures

Of the set of weavings collated in this section, some arise in the description of chemical frameworks. In particular, the invariant cubic rod packings are widely identified among chemical frameworks and synthesised as metal-organic frameworks alike. The Π^* rod packing, which may be constructed on the D surface (the D_{124C} structure) is identified as the Cr_3Si structure. Further, the Γ rod packing, which is related to the G^+_{123C} structure, is the arrangement of rods of atoms in Garnet ($Ca_3Al_2Si_3O_{12}$). Also, the Σ^+ rod packing, which is related to the G^+_{129C} weaving, details the arrangement of rod of atoms in the $SrSi_2$ structure [OKee 96].

In addition to the cubic structures, the #5 invariant non–cubic rod packing, which was constructed on the D surface has been identified as the arrangement of rod of strongly bonded atoms in the structure of the form $Hg_{3-x}MF_6$, where M may be As, Sb, Nb or Ta [OKee 96]. Many of the invariant cubic and non-cubic rod packings are also readily synthesised as metal organic frameworks: a summary of many of these examples may be found in [OKee 05]. Further, the $G^-_{93C}(1)$ weaving, shown in Fig. 3.37(d-f), has been observed as the structure of a self-assembled chemical structure in [Carl 99].

These weavings are all constructed as reticulations of TPMS, which occur on the mesoscale as membranes in biological structures [Land 95, Alms 06]. Thus a natural length scale to probe for such filamentous arrays in biological systems is the mesoscale, where the arrays may result from templating of a protein on the cubic membrane in much the same way as these weaving have come from reticulations of TPMS. We will see in Ch. 5 that one such example of a TPMS reticulation (the G^+_{129C} weaving) may be used to describe the organisation of keratin in the corneocyte of the outer layer of mammalian skin.

This chapter has shown the construction of a variety of 3-periodic structures via the reticulation of several TPMS with high symmetry free tilings of the hyperbolic plane. This construction has given a large set of examples to analyse in the next chapter, which will examine the canonical forms of these structures when ‘tightened’, and a conformation of the structure is found where the length to diameter ratio of the structure is minimised.

Chapter 4

Ideal geometry of branched and periodic structures

This chapter introduces an algorithm for the tightening of finite, periodic and branched entanglements to a canonical, least energy form. The algorithm draws inspiration from the **Shrink-On-No-Overlaps** (**SONO**) [Pier 98] algorithm for the tightening of knots and links: we call it the **Periodic-Branched Shrink-On-No-Overlaps** (**PB-SONO**). We will outline the **SONO** algorithm, and address the additional processes that are necessary to extend the algorithm to enable the tightening of both periodic and branched entanglements, encompassing finite entangled graphs, periodic entangled filaments and periodic entangled nets.

Initially, we use the new **PB-SONO** algorithm to tighten knots and examine the effectiveness of the algorithm as compared to the **SONO** algorithm: the ideal configurations and $\frac{L}{D}$ energy values can be obtained from the literature [Pier 98]. We then examine ideal conformations of finite entangled graphs, including θ-graphs consisting of two vertices connected by three edges, and entangled tetrahedron- and cube-graphs. Finally, we consider ideal conformations of periodic arrangements, including filament weavings and entangled nets with multiple components.

4.1 Ideal Knots and the SONO algorithm

An ideal knot is a minimal energy conformation of a knot. This representative of the entanglement may then be used to analyse the entanglement. Some possible energy functionals as candidates for minimisation were detailed in Ch. 1, and include the *minimum distance* energy [Simo 94], the *symmetric* energy [Buck 93, Buck 95], and the *conformal* energy [OHa 91, Dioa 98]. A simple measure of energy, which we will use in our analysis,

is the ratio of length to diameter, which we minimise to find the ideal knot conformation. This gives a quantification of the entanglement of a knot, useful in identifying entanglement that belong to distinct ambient isotopy classes. A trefoil knot for which the ratio of length to diameter has been minimised is shown in Fig. 4.1.

Figure 4.1: The ideal conformation of a trefoil knot, which minimises the ratio of length to diameter.

The main obstacle to the analysis of knots in their ideal conformations is to find the minimal energy conformation within the set of possible configurations. It is difficult to know firstly if a unique best conformation exists, and secondly if an algorithm has reached that conformation. A fruitful approach to this problem is to computationally relax any configuration to a minimal energy state, as is done by simulated annealing [Kirk 84, Laur 98], which starts by discretising the knot to a series of vertices and edges, and further defining an energy functional for the knot. To continue, a random move is applied to a vertex, the energy recalculated, and the move either accepted if the energy is lower or rejected if the energy is higher. Through the continued application of this process, an energy minimum is achieved, which is certainly a local minimum and possibly a global minimum. A similar approach is given in [Simo 94], which uses random pertubations to decrease the minimum distance energy. Another process of simulated annealing with some additional measures in place to kick out of local minima is given in [Grze 97]. An algorithm to relax the energy of a knot is given in [Kusn 97, Dioa 98]. There is no proof, however, that any of these simulated annealing algorithms find a global minimum. Further, it is not certain in many cases that a unique minimum actually exists.

The **SONO** algorithm uses a repulsion mechanism to push nearby segments of the knot away, coupled with a shrinking mechanism to tighten the knot. This algorithm is simple and efficient. This process minimises the ratio of length to radius as the energy. Mech-

anisms are in place within the algorithm to shake the knot out of local minimum energy conformations (that are not global energy minima), but a proof that these mechanisms will always ensure the global minimum is reached is still elusive. It is this **SONO** algorithm that we will extend to tighten both 3-periodic knits and nets to ideal forms by minimising the ratio of length to diameter, and we describe the details of the algorithm here.

Initially, a given configuration of the knot is discretised into a series of 'nodes' tracing around the knot trajectory, connected consecutively by 'leashes'. The radius of the knot is simulated by placing a sphere of the same radius at points along the knot trajectory, where the distance between the points (the leash length) is far smaller than the sphere radius. The algorithm shrinks the knot trajectory while maintaining this radius. When the spheres surrounding the points of the discretised knot overlap, they repel until the overlap is removed, and the shrinking proceeds, eventually giving the ideal $\frac{L}{D}$. The algorithm can be broken down into a few simple steps as follows.

Control Leashes

The 'control leashes' process ensures that the inter-node distance (length of the leashes) is kept somewhat equivalent. The leash length is initially chosen to be far smaller than the radius so as to ensure that the knot remains equivalent under ambient isotopy throughout the simulation process, and the control leashes procedure also assists in ensuring this equivalence.

In practice, this is done by testing the distance between neighbouring points at a chosen region of the knot. If it is longer (or shorter) than the required leash length, the two points are moved symmetrically towards (or away) from their centre of mass. The continued application of this process to all pairs of points along the knot controls the variation in the length of the leashes.

Find Neighbours and Remove Overlaps

This is perhaps the root of the entire algorithm, and involves identifying and removing overlaps of spheres along the knot trajectory. Initially we must identify neighbouring spheres that are allowed to overlap: those that are close along the knot trajectory. This is done by excluding an integer number of neighbouring nodes when searching for overlaps, approximated by $\left(\frac{\pi D}{2l}\right)$ rounded to the nearest integer (l is the leash length and D is the filament diameter). This corresponds to the number of neighbours with overlapping spheres

in the tightest u-turn conformation.

To identify overlapping spheres, we measure the distance between spheres along the knot. On identifying overlapping spheres (those not neighbouring in the tightest u-turn), these nodes are symmetrically moved away from their centre of mass until the new separation distance is twice the radius, plus a small value (δ). The knot conformation will approach one without overlaps on the continued application of this process to all overlapping nodes in the knot trajectory.

Tightening Process

The continued application of the procedure will result in a knot trajectory in (at least) a local minimum:

1. The (x, y, z) coordinates of the nodes of a knot are read from a file.

2. The lengths of the leashes are corrected by the 'control leashes' process.

3. Overlapping spheres around the nodes are adjusted using the Remove Overlaps procedure.

4. The knot is tightened: the (x, y, z) coordinates are multiplied by a scaling factor less than 1, while the sphere diameter is maintained.

The surface of the knot is not smooth due to the discretisation. In order to prevent the jamming of spheres along the trajectory, an additional process is implemented. This process, called the 'shift nodes' procedure, moves each node a small increment (far less than the average leash length) towards its neighbouring node. This procedure has the added bonus of smoothing the knot at the same time.

The repeated application of this algorithm tightens the knot trajectory sufficiently to an energy minima, however it requires a few additional procedures to assist in shaking the knot out of local energy minima. The simplest of these is altering the total number of nodes: either halving or doubling. As another strategy, we may increase the parameter δ, which controls how far apart the nodes are shifted in the 'remove overlaps' procedure. This temporary increase of δ helps the algorithm to jump out of local energy minima, akin to increasing the energy in a simulated annealing process.

4.2 Tightening branched and periodic entanglements

The standard **SONO** algorithm for tightening knots was insufficient to tighten finite and branched structures: it was difficult for the algorithm to minimise length around the vertices. The standard **SONO** algorithm was also insufficient to tighten periodic structures: scaling the points of the discretised knot to shrink the knot trajectory is invalid in the periodic sense, as this would only change the repeat length of the periodic boundary conditions, which we wish to remain constant.

As such, to tighten a periodic and (or) branched entanglement to a canonical form, some adaptions and an additional procedure must be added to the **SONO** algorithm. These adaptions and additions apply to both the case of branches in the entanglement and the case of periodic entanglements. This section discusses the amended algorithm, which we will call **PB-SONO**, and its implementation.

Tension

The tension process pulls consecutive points of an entangled structure towards a straight line, locally straightening each segment of the discretisation. A point of the trajectory, chosen at random, is moved toward the midpoint of its neighbours. This local straightening is applied to every point of the entanglement to give a global straightening, or tension of the structure. Where the chosen point forms part of a vertex of the entanglement, the point is moved to the barycenter of the neighbouring points along each of the edges incident at that vertex.

For the structure to maintain equivalence under ambient isotopy throughout the tension procedure, we prevent points from moving towards the ideal position if this would introduce an overlap with another sphere: where the desired position of the chosen point is within D of any other points in the entanglement (excluding neighbouring points), the point remains in its initial position. In addition to this, we limit the distance that a point may be shifted in order to ensure the preservation of equivalence under ambient isotopy: a point which is 'too far' from its desired position is shifted a small distance in the direction of the desired position.

This tension procedure somewhat fulfills the role of the control leashes procedure, so we now disregard control leashes in the implementation. To ensure that the variation of leash lengths remains small, we implement the deletion of nodes where the leashes are too short, and the insertion of nodes where the leashes are too long. A node is deleted

when the two leashes incident at that node have a combined length less than 1.2 times the average leash length. A node is inserted at the midpoint of a leash if its length is greater than 1.3 times the average leash length.

Find Neighbours and Remove Overlaps

This process remains much the same as for the standard **SONO** algorithm, but for a few small details. For knots and links, an integer number of neighbours either side of a node are disregarded as overlapping spheres. This number is selected based on a tightest u-turn that may be allowed, and is best approximated by the closest integer to $\left(\frac{\pi D}{2l}\right)$ where l is the average leash length and D is the diameter. Where the structure contains vertices, that number of neighbouring nodes is best approximated by the integer closest to

$$\left(\frac{D}{l \times sin\left(\frac{\alpha}{2}\right)}\right)$$

where α is the smallest vertex angle for which the edges incident at the vertex will be straight (edges that pull to a smaller angle in the entanglement will bulge into a curved arc). This can be seen in Fig. 4.2.

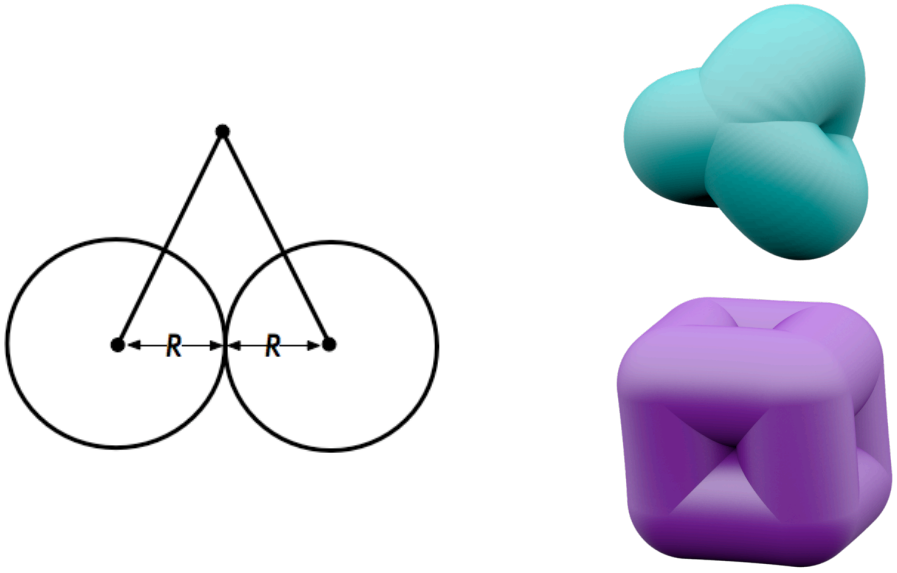

Figure 4.2: The number of skipped nodes around a vertex may be estimated for a configuration where the minimum vertex angle for which the edges are straight is given by α. For example, in the ideal unknotted θ-graph, the vertex angle wants to be 0° (the 3 edges all wish to trace directly from one vertex to the other) and hence the edges bulge to curved arcs to keep the vertex to at least a chosen α. For the ideal unknotted cube graph, α is set below 90° and the edges are straight.

To restrict the computation time when checking for overlaps, a 'binning' procedure is employed. The unit cell is divided into a series of cubic bins, where the size of the cubic bin is at least the filament diameter. All points within a bin are assigned to that bin, and a one bin thick layer of bins is created around the unit cell using periodic boundary conditions. When checking for overlapping spheres around points, one must only check in a 3x3x3 block of bins surrounding the point, minimising the number of points to check. This binning procedure is also used for checking for obstructions in the tension procedure.

In order to make the binning process run more smoothly, the periodic unit cell is justified back to 1x1x1 cube after each relaxation iteration: any points outside the unit cube (that may have moved there in one of the tightening processes) is moved to its equivalent position within the unit cube. This is a triviality, but it makes searching neighbouring bins for overlaps a simpler computation.

Tightening Process

Here is a new algorithm incorporating these new procedures, but with a somewhat equivalent core to the original **SONO** algorithm. Where the original **SONO** process follows the basic procedures of:

1. Remove overlaps
2. Shrink knot

The **PB-SONO** algorithm proceeds as follows, where there is no net change in the ratio of filament diameter to unit cell diameter:

1. Shrink filament diameter by a particular fraction ($\times f_{shrink}$)
2. Perform 'tension' process multiple times
3. Remove overlaps
4. Increase filament diameter ($\times \frac{1}{f_{shrink}}$)

For periodic entanglements, the procedure described above will, after significant repetition, converge to a specific configuration for a given filament diameter. The diameter can then be incrementally inflated, and the algorithm repeated at each increment. This is performed until the structure becomes jammed, which can be identified by the inability of

the 'remove overlaps' procedure to reach a configuration without any overlaps (the spherical nodes vibrate between each other during this process). It will be this conformation that minimises $\frac{L}{D}$.

Periodic unit cell

For periodic entanglements, this procedure is performed on a cubic unit cell, which has lattice parameters ($a = b = c = 1$; $\alpha = \beta = \gamma = \frac{\pi}{2}$), and with periodic boundary conditions. It is necessary to search for ideal conformations among many choices of lattice parameters for the unit cell, similar to deforming the unit cell. The lattice parameters that give the lowest $\frac{L}{D}$ conformation are accepted.

To emulate alteration of the lattice parameters of the unit cell within the simulation, we employ the distance metric. This uses the following formula, where the distance from point (p,q,r) to point (x,y,z), is a unit cell with lattice parameter $(a,b,c,\alpha,\beta,\gamma)$ is given by:

$$\sqrt{(p-x)^2a^2 + (q-y)^2b^2 + (r-z)^2c^2 + W}$$

where

$$W = 2ab(p-x)(q-y)cos(\gamma) + 2bc(q-y)(r-z)cos(\alpha) + 2ac(r-z)(p-x)cos(\beta)$$

In practice, a full simulation run, which begins from a small filament diameter and slowly inflates, is performed for distinct sets of lattice parameters. This must be done, rather than finding an ideal conformation then deforming the unit cell, as the radius in the deformed unit cell may need to be smaller than in the undeformed unit cell. This process of alteration of lattice parameters is very time consuming, and some intuition by the 'simulator' is usually needed for timeliness.

4.3 Results of the PB-SONO algorithm

We implement the **PB-SONO** algorithm for a variety of examples, firstly to compare with existing results in the case of finite knots, and secondly to begin to catalogue results where canonical conformations have not been enumerated previously. We begin this by implementing **PB-SONO** on a set of finite knots, then on distinct embeddings of finite graphs, including θ-graphs, tetrahedral graphs and cube graphs. We then tighten a variety of periodic entanglements of filaments and nets.

4.3.1 Knots

The **PB-SONO** algorithm tightens knots with up to 7 crossings. This process is a test for how **PB-SONO** performs in comparison to the **SONO** algorithm, as documented in [Stas 98]. These results are shown in Table 4.1.

Table 4.1: $\frac{L}{D}$ for ideal knots

	$\frac{L}{D}$ (**PB-SONO**)	$\frac{L}{D}$ (**SONO**) [Stas 98]	
0_1	3.18	3.14 (π)	Fig. 4.3(a)
3_1	16.38	16.33	Fig. 4.3(b)
4_1	21.72	20.99	Fig. 4.3(c)
5_1	23.67	23.55	Fig. 4.3(d)
5_2	25.05	24.68	Fig. 4.3(e)
6_1	28.57	28.30	Fig. 4.3(f)
6_2	29.58	28.47	Fig. 4.3(g)
6_3	29.95	28.88	Fig. 4.3(h)
7_1	30.76	30.70	Fig. 4.3(i)

Particularly for the simpler knots, we can see that the algorithm performs well in relation to the **SONO** algorithm. **PB-SONO** is slower and seems to have more difficultly in escaping from local minima, but the process of halving and subsequently doubling the number of points is enough to get comparable results. The algorithm had some trouble with the 6_2 and 6_3 knots, and the simulated $\frac{L}{D}$ values are somewhat higher than the best **SONO** result.

Fig. 4.3 shows each of the ideal conformations for these knots obtained by the **PB-SONO** algorithm. We take these results as sufficient to show the effectiveness of the **PB-SONO** algorithm, and proceed to simulate the tightening of finite entangled graphs.

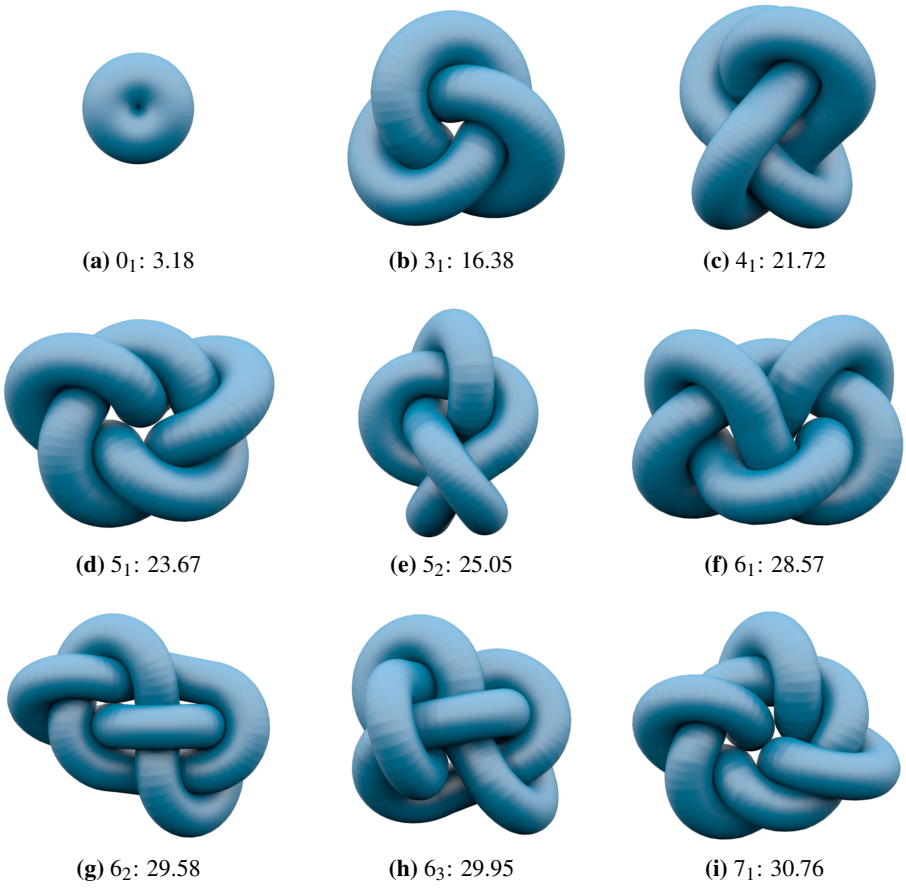

(a) 0_1: 3.18 **(b)** 3_1: 16.38 **(c)** 4_1: 21.72

(d) 5_1: 23.67 **(e)** 5_2: 25.05 **(f)** 6_1: 28.57

(g) 6_2: 29.58 **(h)** 6_3: 29.95 **(i)** 7_1: 30.76

Figure 4.3: Ideal conformations of knots up to seven crossings, as found by an implementation of the **PB-SONO** algorithm. The $\frac{L}{D}$ values for these conformations are shown under each image.

4.3.2 Finite graphs

We simulate the tightening of finite entangled graphs using the **PB-SONO** algorithm. We choose a variety of embedded (with distinct ambient isotopies) θ-graphs (two vertices connected by three edges), tetrahedral graphs and cube graphs.

θ-graphs

θ-graphs consist of two vertices connected by three edges. θ-graph embeddings that are distinct by ambient isotopy have been enumerated up to a given complexity initially by

Litherland, and more completely by Moriuchi [Mori 04]. The graph diagrams of the embeddings considered are given in Fig. 4.4, listed by the title given in the Litherland enumeration, as well as the name derived from the Moriuchi construction, which uses Conway's tangle notation [Conw 67]. We consider all embeddings up to the 6_4 embedding (Litherland enumeration), where the embeddings, 5_1 and 6_1, are "ravels" [Cast 08].

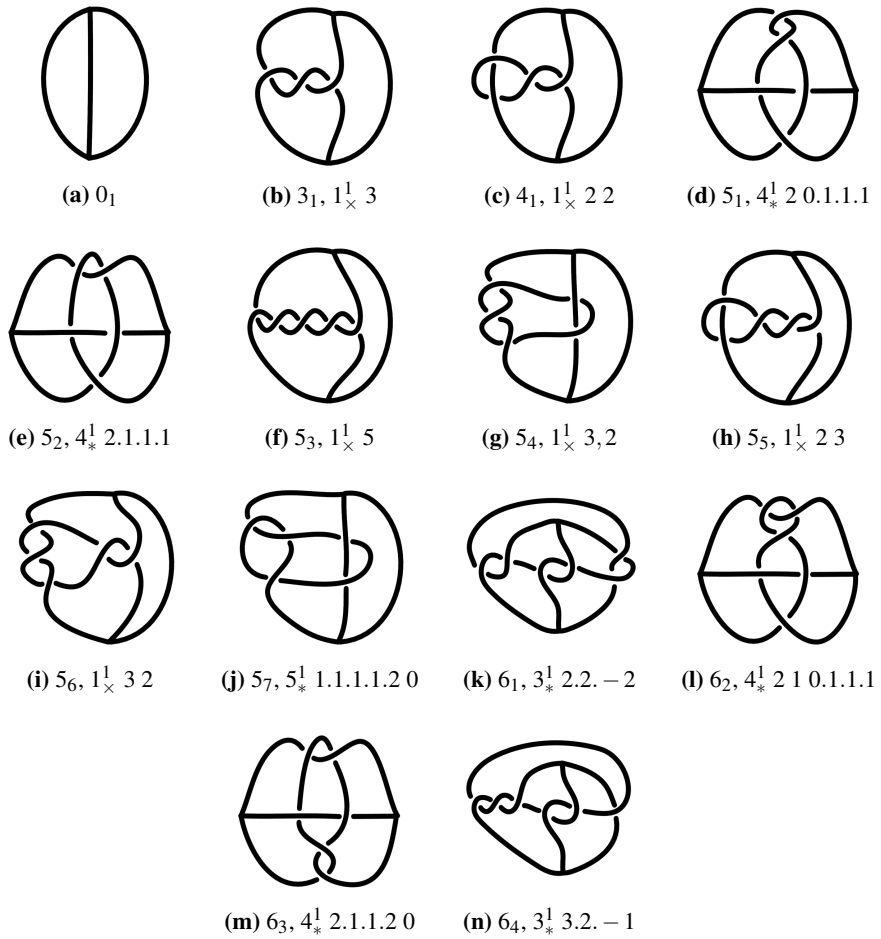

(a) 0_1 **(b)** 3_1, $1^1_\times$ 3 **(c)** 4_1, $1^1_\times$ 2 2 **(d)** 5_1, 4^1_* 2 0.1.1.1

(e) 5_2, 4^1_* 2.1.1.1 **(f)** 5_3, $1^1_\times$ 5 **(g)** 5_4, $1^1_\times$ 3,2 **(h)** 5_5, $1^1_\times$ 2 3

(i) 5_6, $1^1_\times$ 3 2 **(j)** 5_7, 5^1_* 1.1.1.1.2 0 **(k)** 6_1, 3^1_* 2.2. − 2 **(l)** 6_2, 4^1_* 2 1 0.1.1.1

(m) 6_3, 4^1_* 2.1.1.2 0 **(n)** 6_4, 3^1_* 3.2. − 1

Figure 4.4: Embedded θ-graphs up to the 6_4 embedding of the Litherland enumeration. The names shown are designated in the first case by the Litherland table, and secondly by the Moriuchi construction and enumeration [Mori 04] which uses Conway tangle notation [Conw 67].

We tightened these θ-graph embeddings algorithmically using the **PB-SONO** algorithm. The starting configurations of the embeddings were reminiscent of the planar images shown in Fig. 4.4, with only the crossings deviating from the plane. The choice of starting formation does not seem to influence the ideal forms of the graph embeddings. The $\frac{L}{D}$ measurements of the ideal conformations of these graphs are shown in Table 4.2, where they are ranked from least energy upwards.

Table 4.2: $\frac{L}{D}$ for ideal entangled θ-graphs

Litherland	Moriuchi	$\frac{L}{D}$: PB-SONO	
0_1	Trivial	5.12	Fig. 4.7(a,d)
3_1	$1^1_\times$ 3	17.44	Fig. 4.7(b,e)
4_1	$1^1_\times$ 2 2	22.77	Fig. 4.7(c,f)
5_2	4^1_* 2.1.1.1	24.42	Fig. 4.8(a,d)
5_3	$1^1_\times$ 5	24.79	Fig. 4.8(b,e)
5_1	4^1_* 2 0.1.1.1	25.08	Fig. 4.8(c,f)
5_6	$1^1_\times$ 3 2	26.17	Fig. 4.9(a,d)
5_7	5^1_* 1.1.1.1.2 0	26.30	Fig. 4.9(b,e)
5_5	$1^1_\times$ 2 3	26.52	Fig. 4.9(c,f)
5_4	$1^1_\times$ 3,2	27.98	Fig. 4.10(a,d)
6_4	3^1_* 3.2.−1	28.33	Fig. 4.10(b,e)
6_1	3^1_* 2.2.−2	29.05	Fig. 4.10(c,f)
6_2	4^1_* 2 1 0.1.1.1	30.78	Fig. 4.11(a,c)
6_3	4^1_* 2.1.1.2 0	34.15	Fig. 4.11(b,d)

Conformations of the unknotted θ-graph vary depending on the smallest vertex angle allowed. The three edges of the unknotted θ-graph would minimise their length given a vertex angle of 0°, where all three edges follow the same direct path from vertex to vertex. This choice of vertex angle, however, does not produce a stable configuration in the simulation process: the number of neighbouring points whose spheres are allowed to overlap with a chosen sphere would be infinite, as

$$\lim_{\alpha \to 0} \left(\frac{D}{l \times sin\left(\frac{\alpha}{2}\right)} \right) = \infty$$

hence all spheres in the entanglement will be allowed to overlap, and the graph will collapse to a single point. This is distinct from the case of the unknotted loop (Fig. 4.3(a)), where the neighbouring points skipped is such that each point on the loop still repels the point on the opposite side of the circle, which maintains a stable configuration.

The conformation of the trivial θ-graph where at least some spheres repel (*i.e.* the midpoints of each of the edges with each other) will consist of three semi-ellipses con-

necting the vertices: the principal diameters of the ellipses are D from vertex to vertex and $\frac{2D}{\sqrt{3}}$ in the perpendicular orientation. These three edges are not semicircles, as the distance between their midpoints must be at least D, and hence they must be distance $\frac{2D}{\sqrt{3}}$ from the central axis of the graph. This theoretical conformation, consisting of three semi-ellipses, has $\frac{L}{D} = 5.09$ and a vertex angle setting of 105°. This borderline case lies between a stable configuration and unstable configuration, and is thus difficult to achieve by simulation. An $\frac{L}{D}$ value of a stable conformation of the simulation process is 5.12, as shown in Fig. 4.5. This value is close to the ideal value, and gets as close as possible for the given simulation process.

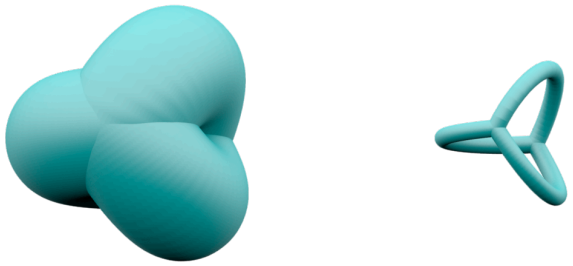

(a) **(b)**

Figure 4.5: The ideal trivial θ-graph, obtained using the **PB-SONO** algorithm. The $\frac{L}{D}$ value for this conformation is 5.12, close to the theoretical ideal value of 5.09.

The 3_1 θ-graph embedding is equivalent by ambient isotopy to a 3_1 (trefoil) knot with a connecting edge. The predicted $\frac{L}{D}$ ratio for the ideal configuration is that of the trefoil plus D units (the length of the extra edge), which translates to $\frac{L}{D} = 16.38 + 1 = 17.38$. The **PB-SONO** simulated conformation, which has $\frac{L}{D} = 17.44$, is shown in Fig. 4.6 along with an ideal trefoil trajectory. This conformation is comparable to what is expected. The $\frac{L}{D}$ value is most likely a global minimum, yet the exact conformation is not unique: the short connecting edge may be located at any contact point along the knot, which gives a set of conformations with equivalent (minimal) $\frac{L}{D}$.

Similarly, the 4_1 θ-graph embedding is equivalent by ambient isotopy to the 4_1 (figure 8) knot with an additional short connecting edge. The ideal conformation, as shown in Fig. 4.7(a,d), should have $\frac{L}{D} = 21.72 + 1 = 22.72$ (the $\frac{L}{D}$ ratio of the ideal figure 8 knot plus one), yet the simulated $\frac{L}{D}$ measure is 22.77. This seems to be within a reasonable distance to the predicted value, given the computational nature of the process. Once again, the location of the short connecting edge has some flexibility, giving an array of ideal configurations all with a minimal $\frac{L}{D}$ measure.

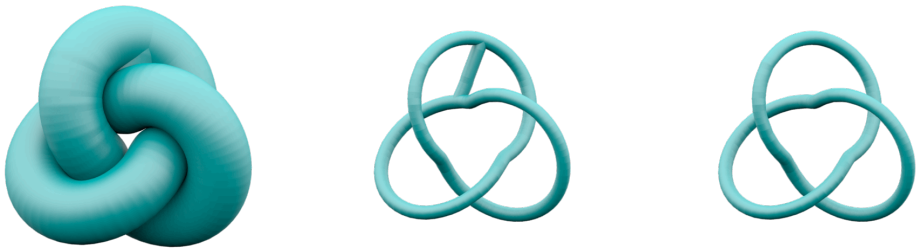

(a) θ - 3_1: 17.44 **(b)** **(c)**

Figure 4.6: (a) The ideal conformation of the 3_1 entangled θ-graph, obtained using the **PB-SONO** algorithm. The $\frac{L}{D}$ energy obtained for the given conformation is 17.44, which is comparable the energy for an ideal trefoil plus 1. (b) The radius is decreased such that the short edge may be seen. (c) The ideal trefoil knot with a decreased radius is shown for comparison.

The 5_2 θ-graph embedding has the next lowest $\frac{L}{D}$ value when tightened. This graph is equivalent under ambient isotopy to a trefoil with an additional edge, in a distinct location to the 3_1 θ-graph embedding, which was shown in Fig. 4.6. The presence of this additional edge alters the ideal conformation away from the ideal trefoil embedding, as shown in Fig. 4.8(a,d). The $\frac{L}{D}$ measurement for this conformation is 24.24. It is likely that this conformation is a unique optimum.

The ideal conformation of the 5_3 embedded θ-graph is a cinquefoil knot with an additional short connecting edge. The $\frac{L}{D}$ value obtained for the ideal conformation, shown in Fig. 4.7(c,f), is 24.79. This measure is comparable to the $\frac{L}{D}$ energy of the cinquefoil (23.67) plus one (for the edge). Slight deviations from the ideal knot trajectory (kinks) are seen at the vertices of the graph, which induce the difference in the values. These kinks are an artifact of the computational process and are not necessary to the ideal conformation of the graph embedding.

The 5_1 embedding of a θ-graph is Kinoshita's embedding, also know as a ravel [Cast 08]. It contains no knotted or linked cycles: all edges are necessary to the entanglement, as opposed to the other examples we have seen, which are equivalent to a knot with an additional edge. This specific embedding is the lowest complexity example of an entanglement of this kind. The ideal conformation has an $\frac{L}{D}$ measurement of 25.08, and the conformation, shown in Fig. 4.8(d,e), has lovely 3-fold symmetry. A few intermediate configurations are shown in Fig. 4.8(a-c), where the first image shows the starting configuration. It is clear that the symmetry of the ideal configuration emerges from the tightening algorithm regardless of the asymmetry of the starting configuration. Further, a ravelled molecule of this ambient isotopy has been recently synthesised [Li 11].

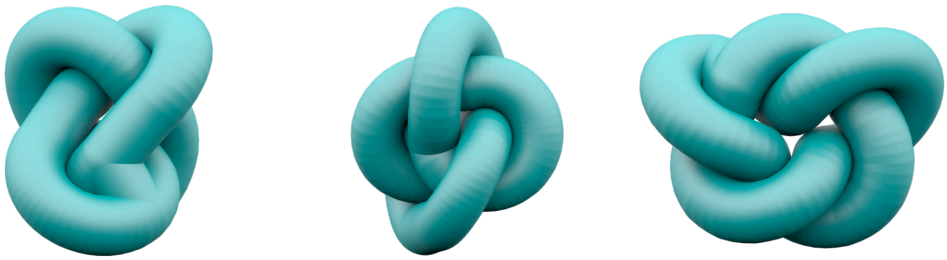

(a) θ - 4_1: 22.77 **(b)** θ - 5_2: 24.42 **(c)** θ - 5_3: 24.79

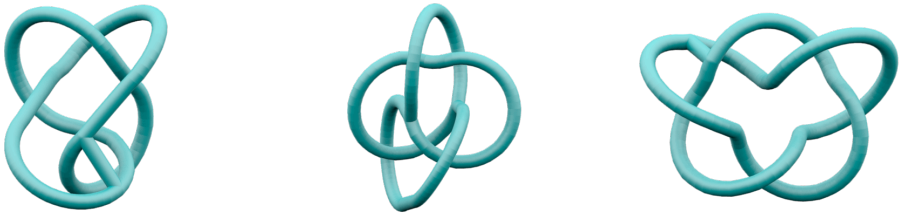

(d) θ - 4_1 **(e)** θ - 5_2 **(f)** θ - 5_3

Figure 4.7: Ideal conformations, obtained using the **PB-SONO** algorithm, of three embeddings of the θ-graph: 4_1, 5_2 and 5_3. The names shown are from the Litherland enumeration of embedded θ-graphs, and the values shown are the $\frac{L}{D}$ energy obtained for the given conformation.

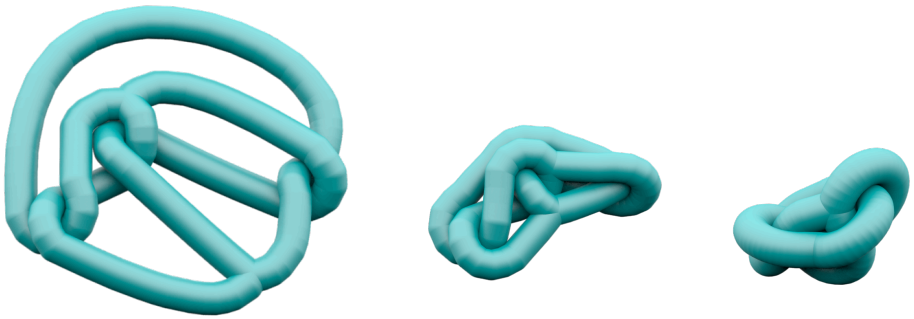

(a) **(b)** **(c)**

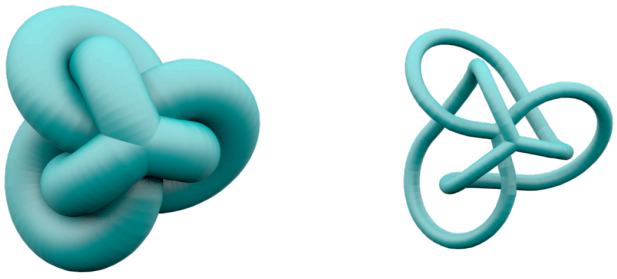

(d) θ - 5_1: 25.08 **(e)** θ - 5_1

Figure 4.8: (a-c) Three intermediate configurations in the tightening simulation of the 5_1 embedding of a θ-graph. (d,e) The ideal configuration of the 5_1 embedding of a θ-graph, which displays lovely 3-fold symmetry, an emergent trait of the graph under tightening regardless of the asymmetry of the starting configuration.

The ideal conformations of each of the 5_6, 5_7, and 5_5 θ-graph embeddings are shown in Fig. 4.9. Each of these embeddings resemble the 5_2 knot (Fig. 4.3(e)), with the addition of an edge between sections of the knot that are in contact. This additional edge may be situated in three distinct locations that produce graphs that are distinct by ambient isotopy, and these three locations are reflected in the three distinct graph embeddings. We expect the $\frac{L}{D}$ energies of these three conformations to be equivalent ($25.05 + 1$), but the values obtained are more variable (26.17, 26.30, and 26.53 respectively). This is most likely due to the simulation error involved in the implementation of the algorithm, and expect that with enough repetition of the tightening algorithm, the resulting conformations would be closer in energy. In particular, there are small kinks in the graph close to the vertices. In the 5_6 and 5_5 conformations, the location of the edge has some flexibility, and this gives a set of conformations all with a minimal energy. The 5_7 ideal embedding is unique, however, as the two segments of the knot containing the vertices are only in contact at a single point.

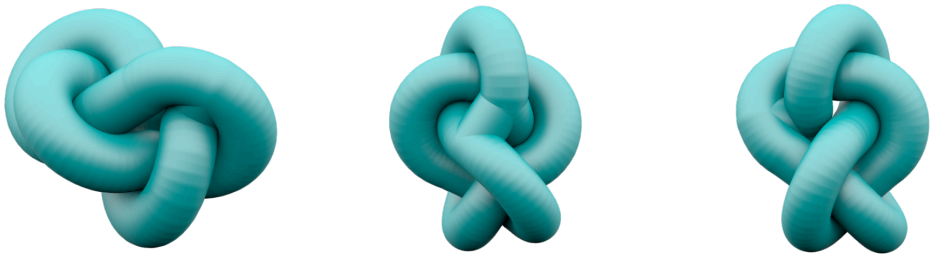

(a) θ - 5_6: 26.17 **(b)** θ - 5_7: 26.30 **(c)** θ - 5_5: 26.52

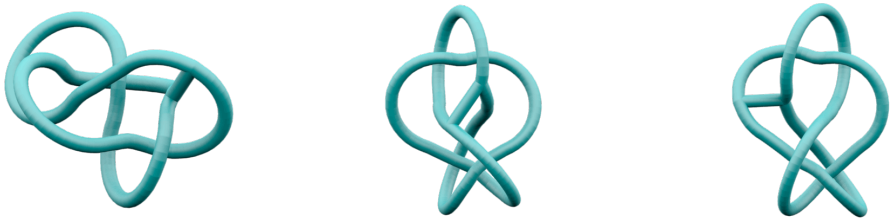

(d) θ - 5_6 **(e)** θ - 5_7 **(f)** θ - 5_5

Figure 4.9: Ideal conformations of three embeddings of the θ-graph: 5_6, 5_7, and 5_5, found by the **PB-SONO** algorithm. The $\frac{L}{D}$ measurement for each conformation is shown below each image. Each of these embeddings are equivalent to the 5_2 knot by ambient isotopy, with the addition of a short connecting edge in three distinct locations.

The 5_4 embedding of the θ-graph is equivalent by ambient isotopy to the 5_1 knot with an additional long edge. Its ideal conformation is representative of this equivalence, as shown in Fig. 4.10(a,d). The $\frac{L}{D}$ value obtained for this conformation is 27.98, indicating that the length of the additional edge wrapping around is approximately $4.3 \times D$ units.

The 6_4 embedding of the θ-graph is the least energy conformation of the embeddings with minimal crossing number of 6, among the four that we sampled. The ideal conformation of this graph embedding, as well as the ideal conformation of the 6_1 θ-graph embedding are shown in Fig. 4.10. These two configurations have $\frac{L}{D}$ values of 28.33 and 29.05 respectively. The 6_1 embedding is a ravel, as defined previously (no knotted or linked cycles) and is most likely the second least–energy ravel amongst all θ-graph embeddings.

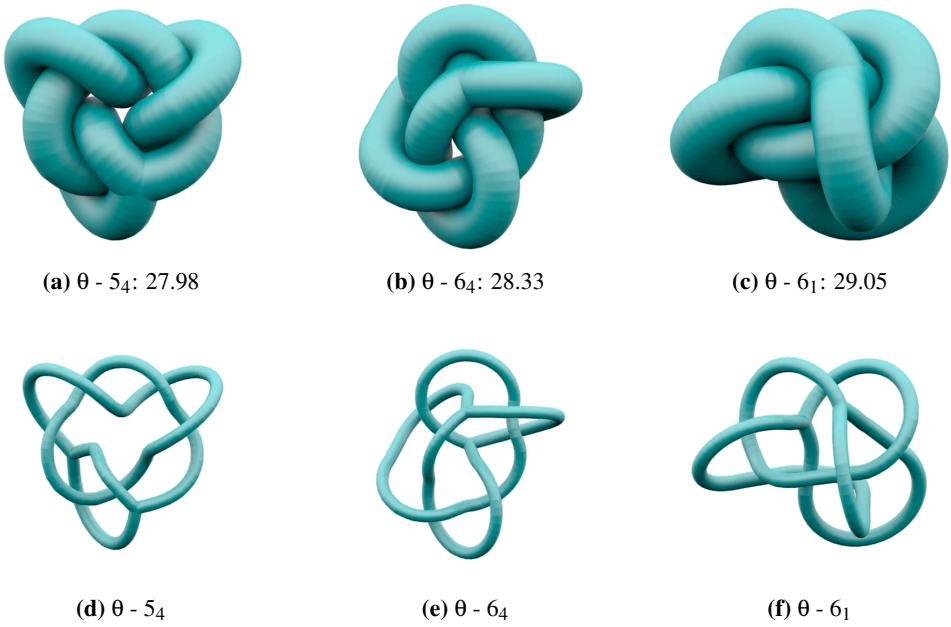

(a) θ - 5_4: 27.98 **(b)** θ - 6_4: 28.33 **(c)** θ - 6_1: 29.05

(d) θ - 5_4 **(e)** θ - 6_4 **(f)** θ - 6_1

Figure 4.10: Ideal conformations of embedded θ-graphs: 5_4, 6_4, and 6_1, obtained using the **PB-SONO** algorithm. The $\frac{L}{D}$ measurements are shown below each image.

The ideal conformations of the 6_2 and 6_3 embeddings, shown in Fig. 4.11, have the highest energies of the examples studied. The $\frac{L}{D}$ measurements are 30.78 and 34.15 respectively.

The ideal conformations of these knotted graphs give us insight into their physical presence. The quantity that we have minimised is the ratio of edge length to edge diameter, which translates to a most efficient use of material to achieve the desired entanglement. The $\frac{L}{D}$ measure of an ideal knot has a correlation with the average writhe and average crossing number of the knot [Stas 98], and this may extend to the case of knotted graphs also. These physical conformations might also give insight into how isolated entangled graphs might be arranged in chemical structures, in particular the symmetry that is induced from an energy minimisation.

Beyond considering knots and links, we have observed a second mode of entanglement

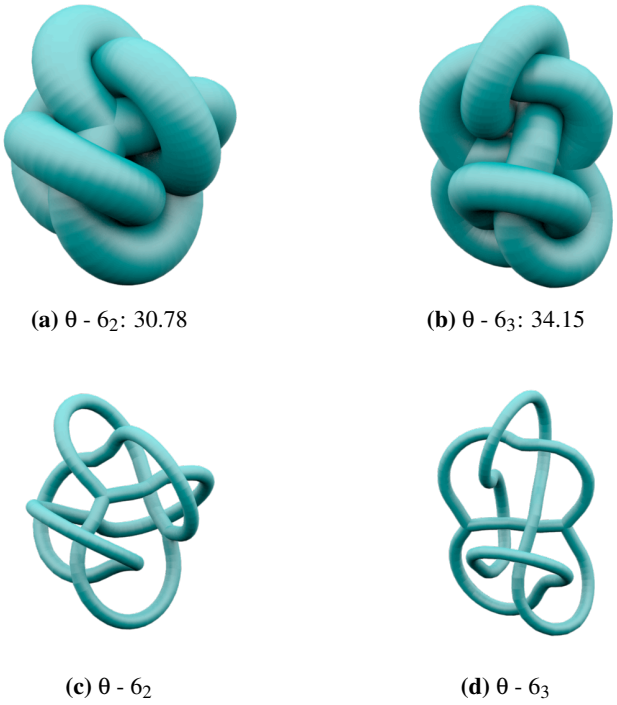

(a) θ - 6_2: 30.78 **(b)** θ - 6_3: 34.15

(c) θ - 6_2 **(d)** θ - 6_3

Figure 4.11: Ideal conformations of embedded θ-graphs: 6_2, and 6_3, obtained using the **PB-SONO** algorithm. The $\frac{L}{D}$ measurements are shown below each image.

that is unique to entangled graphs, the ravel. What about entanglement modes that are beyond θ-graph embeddings, that contain no knots, links or ravels as graph minors? This is an open question, as detailed in [Cast 11a].

Knotted Tetrahedra

A tetrahedral graph consists of four vertices each of degree three. Equivalently, it is the complete graph of degree 4 (K_4), where vertices connect to each of the other vertices by a single edge. The simplest non-trivial embeddings of a tetrahedral graph, toroidal embeddings (or isotopes [Cast 11b]), are the embeddings where the graph edges embed on the surface of a torus, yet are unable to embed on the surface of a sphere. These edges and vertices are arranged in the universal cover of the torus ($\mathbb{E}^2$, as defined at the start of Ch. 1), such that the sum Σl_i^2 over all edge lengths l_i is minimised: this is the barycentric placement of the net in $\mathbb{E}^2$ [Delg 03b]. An implicit 2D energy measure for toroidal graph embeddings is thus given by Σl_i^2 [Cast 11a, Cast 11b]. We consider the trivial tetrahedral graph plus the five least energy toroidal embeddings as candidates for tightening. These six graph embeddings are shown as planar diagrams in Fig. 4.12.

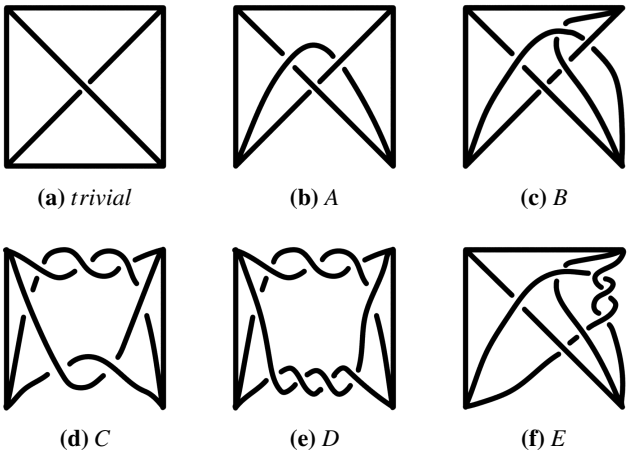

(a) *trivial* **(b)** *A* **(c)** *B*

(d) *C* **(e)** *D* **(f)** *E*

Figure 4.12: The trivial embedding plus five toroidal embeddings of the tetrahedral graph [Cast 11b], selected as candidates for the tightening algorithm **PB-SONO**.

Using the **PB-SONO** algorithm, the graphs shown in Fig. 4.12 are tightened to an ideal conformation. The $\frac{L}{D}$ measurements for the ideal conformations are shown in Table. 4.3, which relate to the conformation of the graph in $\mathbb{E}^3$. The table also shows the toroidal energy of the embedding (Energy), which relates to the embedding of the graph is the universal cover, $\mathbb{E}^2$.

Table 4.3: $\frac{L}{D}$ for ideal entangled tetrahedron graphs

Isotope	$\frac{L}{D}$ ($3D$)	Energy ($2D$)
trivial	6.61	2.35
A	18.54	3.88
B	20.09	4.55
C	25.80	4.79
E	27.42	5.75
D	33.22	5.56

An unknotted tetrahedron graph composed of straight edges would have a total length of approximately 6.93 diameters: this is achieved where the closest distance between opposite edges of the graph (those that do not share a common vertex) is D, hence the edge length must each be approximately $1.16D$. A lower total edge length is realised in a conformation where the edges curve, as shown in Fig. 4.13(a,d), which has an $\frac{L}{D}$ value of 6.61. This conformation is the ideal conformation of the trivial tetrahedron graph. We note that

the curved geometry of the edges is not an artifact of the allowed vertex angle: it is an inherent geometry of the ideal structure.

The ideal conformation of Isotope *A*, as shown in Fig. 4.13(b,e), highlights a particular knotted cycle of the embedding that is equivalent to a trefoil knot by ambient isotopy. The full graph embedding is a decoration of this trefoil cycle by two short connecting edges. As such, the expected value of $\frac{L}{D}$ for this conformation is $16.38 + 2 = 18.38$. The simulated value is 18.54, which is comparable. It seems that a small kink is present at a vertex of this configuration, which we attribute to experimental uncertainty, and this accounts for the $\frac{L}{D}$ value that is very slightly higher than expected. This kink should not be present in an ideal configuration.

Similarly, the ideal conformation of Isotope *B* has a dominant trefoil knotted cycle. In this case, however, the structure which attaches to the trefoil knot has an arrangement of vertices and edges which is distinct to Isotope *A*. The $\frac{L}{D}$ value for this conformation is 20.09 (Fig. 4.13(c,f)), which indicates that the additional structure of vertices and edges adds approximately $3.55D$ units of length to the conformation.

The *C* and *E* Isotopes of the tetrahedron graph each have the same dominant knotted cycle in their ideal conformations. In each isotope, this dominant cycle is a cinquefoil knot, as shown in Fig. 4.14. As was the case for the trefoil cycles, these two embeddings differ in the additional edges that are attached: Isotope *C* has two short connecting edges and Isotope *E* contains a more complex structure. This is reflected in the $\frac{L}{D}$ measurements, which are 25.80 for Isotope *C* (2.13 more than the cinquefoil value, which is comparable to 2) and 27.42 for Isotope *E* (3.85 more than the cinquefoil value).

The highest 3D energy embedding for these 6 simplest tetrahedral entanglements is Isotope *D*. This embedding has a dominant cycle that is a seven–crossing torus knot, reflected in the ideal conformation shown in Fig. 4.14(c,f). The ideal embedding is the ideal torus knot with the addition of two short connecting edges. This ideal geometry is reflected in the $\frac{L}{D}$ measurement, which is 33.22: 2.46 more than the value for the ideal conformation of the torus knot.

The 2D energy for these graph embeddings, calculated in the universal cover of the torus, gives an ordering of the embeddings from least to greatest energy that differs slightly from the 3D energy ranking (Table 4.3). This difference indicates that both energy measures offer alternative gauges of the complexity of embedded tetrahedron graphs.

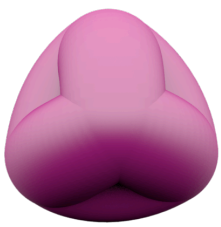

(a) Trivial: 6.61

(b) Isotope A: 18.54

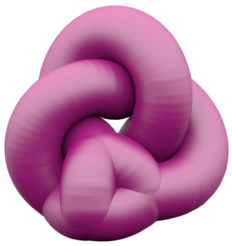

(c) Isotope B: 20.09

(d) Trivial

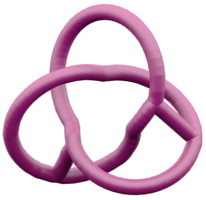

(e) Isotope A

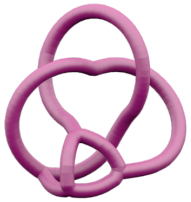

(f) Isotope B

Figure 4.13: Ideal conformations for some embedded tetrahedral graphs: trivial embedding, Isotope A, and Isotope B. These conformations were obtained using the **PB-SONO** algorithm for tightening knotted graphs. The resulting $\frac{L}{D}$ measurement is shown below each image.

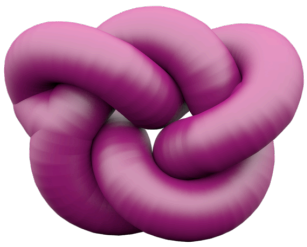

(a) Isotope C: 25.80

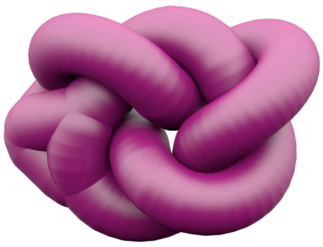

(b) Isotope E: 27.42

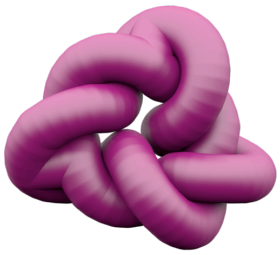

(c) Isotope D: 33.22

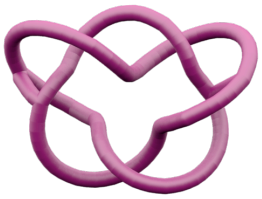

(d) Isotope C

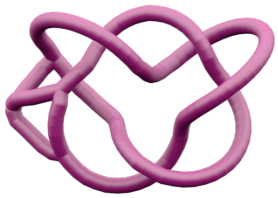

(e) Isotope E

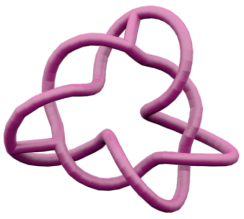

(f) Isotope D

Figure 4.14: Ideal conformations for some embedded tetrahedral graphs: Isotope C, Isotope E, and Isotope D. These conformations were obtained using the **PB-SONO** algorithm for tightening knotted graphs. The $\frac{L}{D}$ measurement of these conformation is shown below each image.

Knotted Cubes

Five simple embeddings of the cube graph, isotopes *A* through *E*, are developed in [Hyde 07]. A further five toroidal embeddings, Isotopes 1 through 5, are taken from [Cast 11b], where the least 2D energy toroidal embeddings of cube graphs have been enumerated. Each of these isotopes, along with the trivial embedding of the cube graph, are shown in Fig. 4.15.

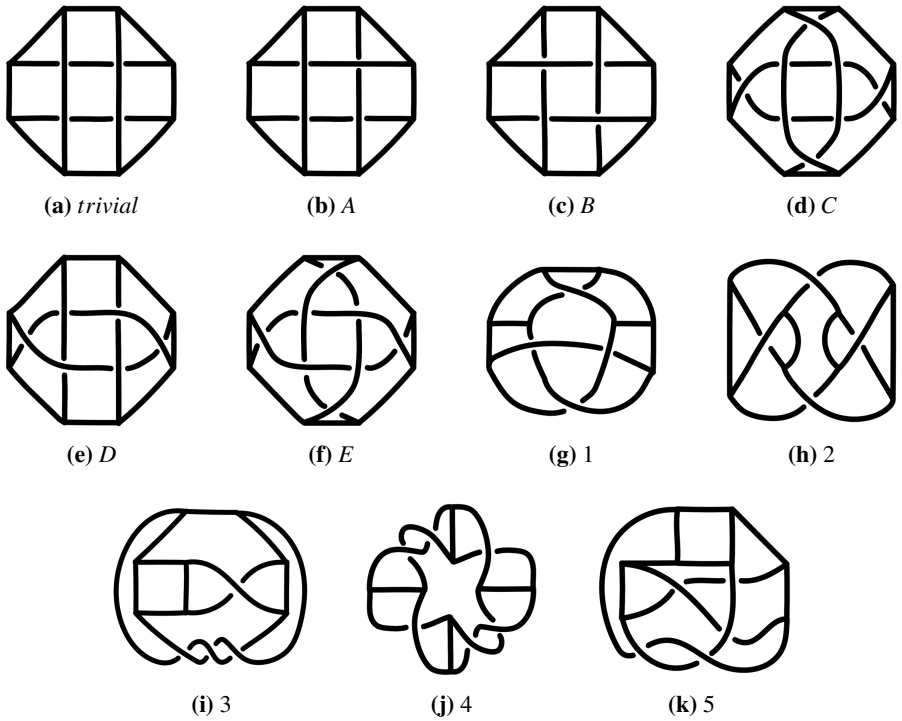

Figure 4.15: Embeddings of the cube graph, selected as candidates for the **PB-SONO** simulation. The embedding shown in (a) is the trivial embedding, the embeddings shown in (b-f) are Isotopes A through E, which are enumerated in [Hyde 07], and the embeddings shown in (g-k) are toroidal Isotopes 1 through 5, constructed in [Cast 11b].

Using the **PB-SONO** algorithm, the graphs shown in Fig. 4.15 are tightened to an ideal conformation. The resulting $\frac{L}{D}$ values for these conformations are shown in Table. 4.4. The 2D energy, as defined previously, is also shown in the table and differs from the $\frac{L}{D}$ energy of a 3-dimensional conformation.

An ideal embedding of a trivial cube graph contains straight edges, each of length *D*. This conformation has graph edges that trace along the edges of a highest symmetry cube. The simulated ideal conformation of the unknotted cube has $\frac{L}{D} = 12.04$, which is comparable to the ideal case, and displays the high symmetry of the ideal embedding, see Fig. 4.16(a,d).

Table 4.4: $\frac{L}{D}$ for ideal conformations of entangled cube graphs

Isotope	$\frac{L}{D}$: PB-SONO	Energy [Cast 11b]
trivial	12.04	0.83
A	16.97	1.33
C	21.04	1.76
1	23.77	2.82
B	24.63	2.20
D	25.21	2.31
5	26.08	3.16
3	26.31	2.98
2	28.51	2.91
4	32.08	3.14
E	34.76	3.53

The Isotope *A* cube embedding is equivalent by ambient isotopy to a Hopf link with the addition of four short edges joining the two components of the link at contacts between the components. The ideal embedding of a Hopf link, without the extra vertices and edges has $\frac{L}{D} = 2\pi$, with πD units around each of the components of the link. In the graph embedding, whose ideal form is shown in Fig. 4.16(b,e), the cycle around one component of the Hopf link consists of four edges. The minimum length for any edge in an ideal graph embedding is D, hence the cycle of a single component of the Hopf link must be at least $4D$ units, which is greater than πD. As such, the cycles must deviate significantly from their ideal trajectory. For this ideal conformation of the Isotope *A* embedding of the cube graph, $\frac{L}{D} = 16.97$.

The next most stable cube embedding via our 3D energy is Isotope *C*, which is equivalent by ambient isotopy to the 3_1 (trefoil) knot with four short connecting edges. From this geometry, we expect $\frac{L}{D} = 16.37 + 4 = 20.37$, and find that the simulated value is 21.04. We see that, compared with the Isotope *A* tetrahedron, increasing the number of additional edges seems to increase the difference in the expected and simulated values: the addition of more edges deviates the trefoil knot away from its ideal conformation. In this case, it seems that the deviation from the expected value is a feature of the ideal conformation, rather than experimental uncertainty. This ideal conformation is shown in Fig. 4.16(c,f).

Fig. 4.17 shows the next three most stable cube embedding via our 3D energy: Isotope

(a) Trivial: 12.04 **(b)** Isotope A: 16.97 **(c)** Isotope C: 21.04

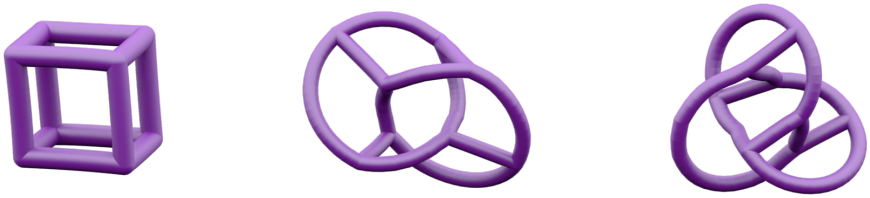

(d) Trivial **(e)** Isotope A **(f)** Isotope C

Figure 4.16: Conformations for ideal embedded cube graphs: trivial embedding, Isotope A, and Isotope C. The $\frac{L}{D}$ value is shown for each of the configurations, which are found computationally using the **PB-SONO** algorithm.

1, Isotope B and Isotope D. These three embeddings have $\frac{L}{D}$ values of 23.77, 24.63 and 25.21 respectively. For Isotope 1 there is a dominant cycle with a trefoil knot, and for Isotopes B and D, the dominant cycles form a $(4,2)$ (Whitehead) link. Isotopes B and D differ only in the formation of the additional short connecting edges attached to the $(4,2)$ link.

Fig. 4.18 includes the next three most stable cube embedding via our 3D energy: Isotope 5, Isotope 3 and Isotope 2. These three embeddings have $\frac{L}{D}$ values of 26.08, 26.31 and 28.51 respectively. Similarly, Fig. 4.19 shows the two embedded cube graphs with the highest energy from the small sample set chosen: Isotope 4 and Isotope E. These embeddings have $\frac{L}{D}$ values of 32.08 and 34.76 respectively.

Through the embedded graphs considered, we see that the 2D energy and the 3D energy of the graph embeddings differ in the relative rankings that they give. The notable embeddings that disagree are Isotope 1 and Isotope 5, which have a lower 3D energy than their high 2D energy might imply. Once again, this disagreement gives weight to both energy measures to give valid rankings of complexity.

(a) Isotope 1: 23.77 **(b)** Isotope B: 24.63 **(c)** Isotope D: 25.21

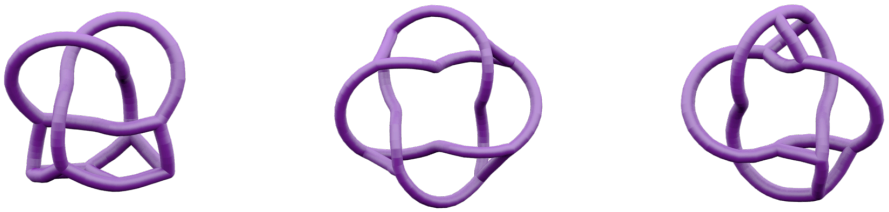

(d) Isotope 1 **(e)** Isotope B **(f)** Isotope D

Figure 4.17: Ideal conformations of embedded cube graphs: Isotope 1, Isotope *B*, and Isotope *D*.

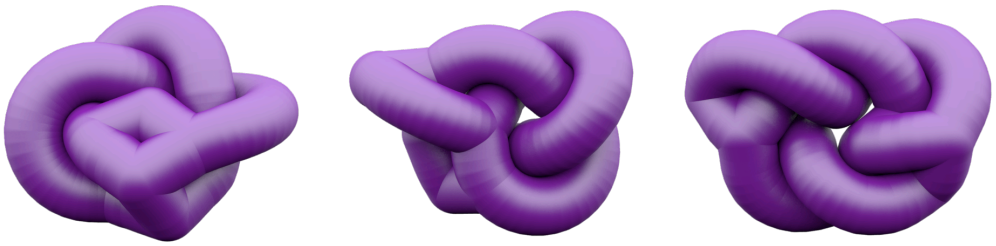

(a) Isotope 5: 26.08 **(b)** Isotope 3: 26.31 **(c)** Isotope 2: 28.51

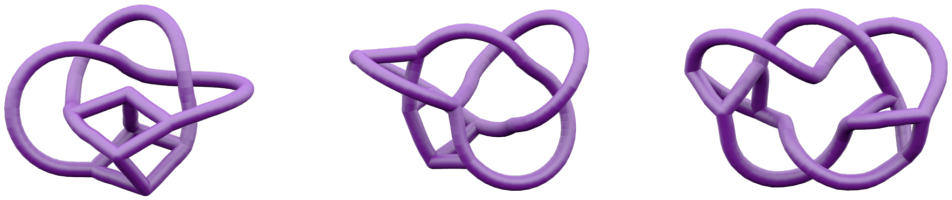

(d) Isotope 5 **(e)** Isotope 3 **(f)** Isotope 2

Figure 4.18: Ideal conformations of embedded cube graphs: Isotope 5, Isotope 3, and Isotope 2.

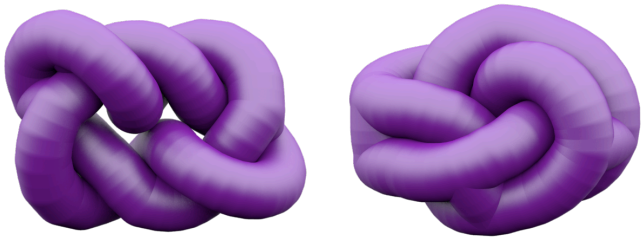

(a) Isotope 4: 32.08 **(b)** Isotope E: 34.76

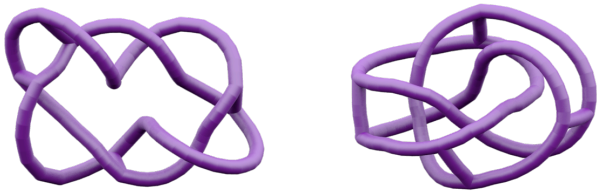

(c) Isotope 4 **(d)** Isotope E

Figure 4.19: Ideal conformations of embedded cube graphs: Isotope 4 and Isotope E.

4.3.3 Periodic entanglement of filaments

An addition to the **SONO** algorithm is the ability to tighten periodic entanglements. We consider tightening periodic arrays of filaments, which were constructed as reticulations of Triply-Periodic Minimal Surfaces (TPMS) in Ch. 3.

The ideal conformation of a periodic array is defined to be the conformation that minimises $\frac{L}{D}$ within a unit cell of the structure: $\frac{L}{D}$ is a dimensionless measure of the length per unit cell standardised by the filament diameter. The $\frac{L}{D}$ measure varies with the choice of unit cell by which to represent the periodic structure: it is invariant under scaling of the unit cell, yet the value doubles for a choice of two unit cells, halves for half a unit cell and so on. The variability of the $\frac{L}{D}$ measure makes it difficult to compare nets using this measure when testing for equivalence or comparing between nets. Despite this, the ideal conformation is well defined.

As a comparative tool between distinct entangled structures, $\frac{LD^2}{V}$ is another dimensionless measure, which gauges the packing density. This value is independent of the unit cell chosen. We note, however, that this value may not be minimised in an ideal conformation, as we will see in examples in this section.

Invariant rod packings: non–cubic

Eight distinct invariant rod packing with non-cubic symmetry are enumerated in [OKee 05]. The construction of weaving related to some of these rod packings by the reticulation of TPMS with hyperbolic free tilings, including helical and undulating filament variations, were presented in Ch. 3. The weavings constructed via the TPMS are shown in Fig. 4.20.

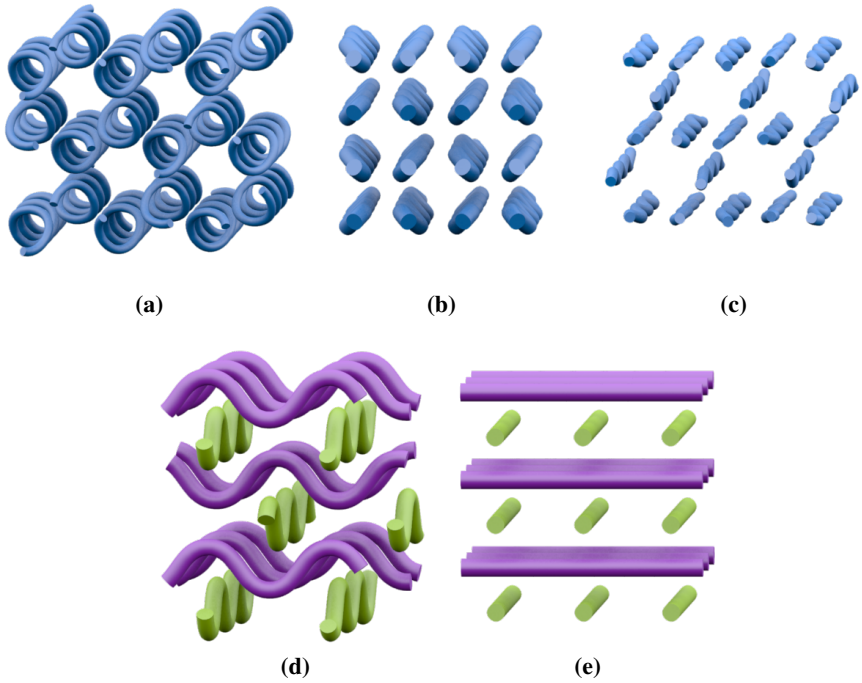

Figure 4.20: The weavings (a) $G^{+}_{122C}(1)$, (b) $P_{123C}(2)$, (c) $G_{93C}(1)$, (d) D_{104} and (e) $D_{123C}(2)$. Packings (a-c) are variants of the invariant non-cubic rod packings #1, #2 and #3, and packings (d,e) are variants of the invariant non-cubic rod packings #5 and #6.

We consider these filament packings in their ideal conformations, and describe the two measures of complexity: $\frac{L}{D}$ and $\frac{LD^2}{V}$. First, consider the invariant rod packings of non–cubic symmetry composed of only parallel rods: packings #1-#4 [OKee 05], or an equivalent filamentous variant constructed via a TPMS reticulation. On tightening, the distinct arrangements converge to a common ideal configuration, which is the #4 rod packing configuration (Fig. 4.21). The convergence of distinct parallel rod packings to a common conformation seems intuitive: there are no obstructions inhibiting the rods from compacting to the densest state. The initial unit cells for each of these packings have a differing number of rods, however these rods become symmetrically equivalent on tightening, and we simplify to a smaller unit cell containing one rod, which realises all possible symme-

tries of this packing, similar to the 'maximal symmetry' barycentric embedding of nets via found via the SyStRe algorithm [Delg]. For all choices of unit cell, the $\frac{LD^2}{V}$ value will be equivalent (1.15), however the $\frac{L}{D}$ measure will change depending on the unit cell chosen, and for the smallest unit cell which contains only one rod, $\frac{L}{D} = 1$.

Now consider the rod packings composed of stacked layers of parallel rods (#5-#8), or their filamentous variants with helical or undulating filaments. On tightening, all of these packings also converge to a common ideal conformation, equivalent to the ideal conformation of the parallel rod packings: the #4 rod packing. This result also seems intuitive, as each layer of containing rods arranged in a distinct orientation are uninhibited to rotate during the simulation to the densest conformation. The $\frac{LD^2}{V}$ and $\frac{L}{D} = 1$ values for this ideal configuration will be equivalent to the parallel rod case.

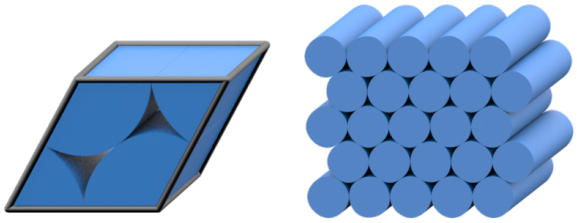

(a) **(b)**

Figure 4.21: The ideal configuration for all weavings composed of parallel rods, or alternating stacked layers of parallel rods. (a) One unit cell, which contains a single rod, has lattice parameters $(1, 1, 1, \frac{\pi}{2}, \frac{\pi}{2}, \frac{\pi}{3})$. The length of the rod is 1, the diameter is also 1, and the volume of the unit cell is $\frac{\sqrt{3}}{2}$. Thus $\frac{L}{D} = 1$ and $\frac{LD^2}{V} = 1.15$. (b) The global arrangement of the packing.

Invariant rod packings: cubic

Six invariant rod packings of cubic symmetry are enumerated in [OKee 05]. The construction of weavings related to five of these rod packings via the TPMS reticulation method, which often consist of helical or undulating filaments, was shown in Ch 3. These five weavings, which inherit the names G^{+}_{124C}, D_{124C}, G^{+}_{129C}, $G^{+}_{123C}(2)$ and P_{129C} from their construction (see § 3.3.2), are shown in Fig. 4.22.

The **PB-SONO** algorithm for tightening periodic arrays of filaments is utilised to tighten each of the filament packings shown in Fig. 4.22. Table 4.5 summarises the $\frac{L}{D}$ and $\frac{LD^2}{V}$ values for their ideal conformations, ordered by their $\frac{LD^2}{V}$ values, which is a preferred comparative tool to the $\frac{L}{D}$ measure.

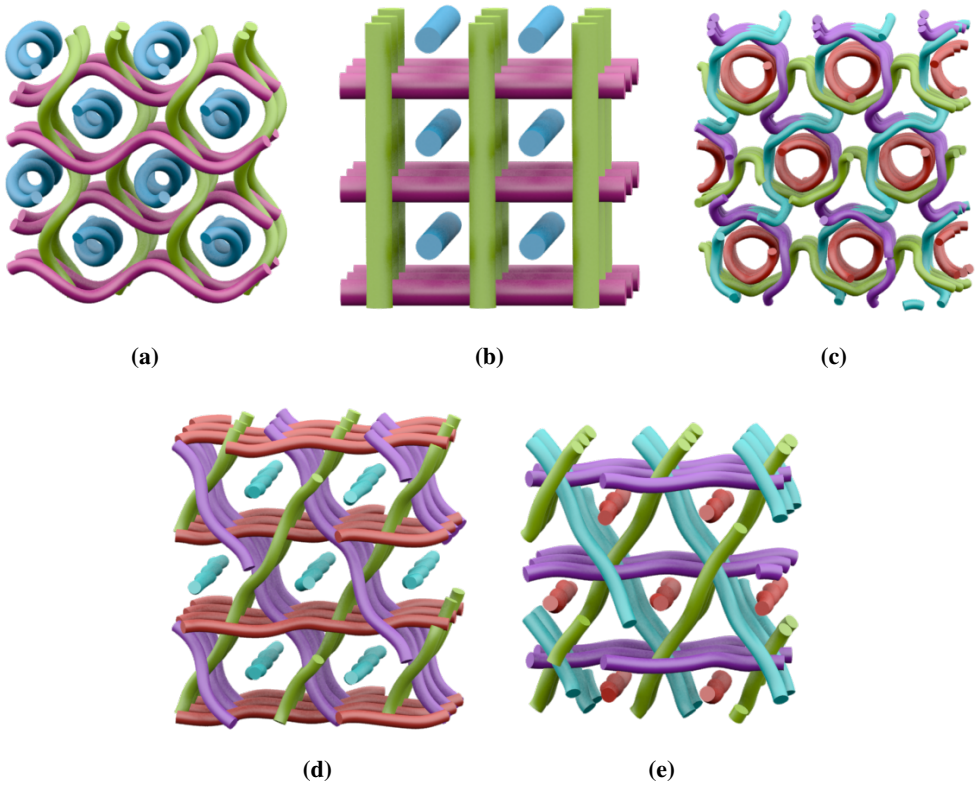

Figure 4.22: Weavings related to five invariant cubic rod packings, constructed via the TPMS reticulation method of Ch. 3: (a) G^{+}_{124C}, a helical variant of Π^{+}, (b) D_{124C}, which is exactly equivalent to Π^{*}, (c) G^{+}_{129C}, a helical version of Σ^{+}, (d) $G^{+}_{123C}(2)$, a Γ rod packing consisting of undulating filaments, (e) P_{129C}, an Ω^{+} packing with slightly helical filaments.

Table 4.5: Invariant Cubic Rod Packings: **PB-SONO**

Structure	Related rod packing	Form	$\frac{L}{D}$	$\frac{LD^2}{V}$
$G^{+}_{123C}(2)$	Γ	Straight	19.27	0.90
G^{+}_{124C}	Π^{+}	Helical	17.91	0.84
D_{124C}	Π^{*}	Straight	6.00	0.75
P_{129C}	Ω^{+}	Helical	22.78	0.57
G^{+}_{129C}	Σ^{+}	Helical	30.21	0.49

The G^{+}_{124C} structure, a helical variant of the Π^{+} rod packing, may be idealised by the **PB-SONO** algorithm (Fig. 4.23). The unique ideal conformation is composed of filaments with helical trajectories, which deviate from their straight trajectory to pack more tightly. The helical geometry of the filaments is an emergent trait of the specific entanglement, and is independent of the starting configuration. Further, the helices of the ideal structure decorate a surface parallel to the G minimal surface such that one channel is slightly deflated and the other is enlarged. The geometry that results from idealisation supports the relevance of the original TPMS geometry. The $\frac{L}{D}$ value for this conformation is 17.91 and the $\frac{LD^2}{V}$ value is 0.84.

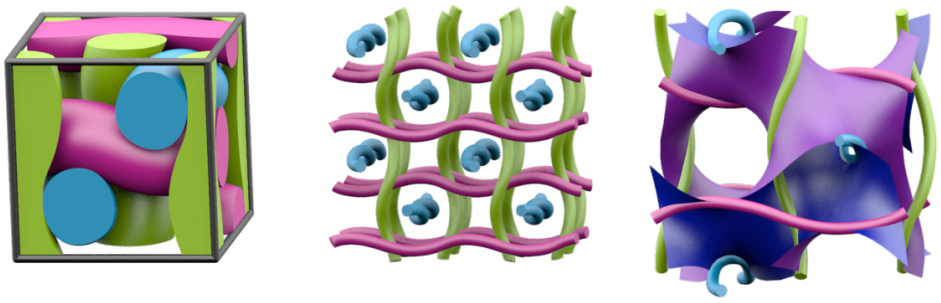

(a) **(b)** **(c)**

Figure 4.23: The ideal G^{+}_{124C} structure: a helical variant of the Π^{+} rod packing. (a) The ideal unit cell, where $\frac{L}{D} = 17.91$ and $\frac{LD^2}{V} = 0.84$. (b) The ideal structure. (c) It lies on a surface parallel to the G surface such that one channel has been deflated and the other enlarged.

The D_{124C} structure lies along the lines of the D surface, and is equivalent to the Π^{*} rod packing. The ideal configuration of this structure also consists of straight rods, as can be seen in Fig. 4.24. For this conformation, $\frac{L}{D} = 6$ and $\frac{LD^2}{V} = 0.75$.

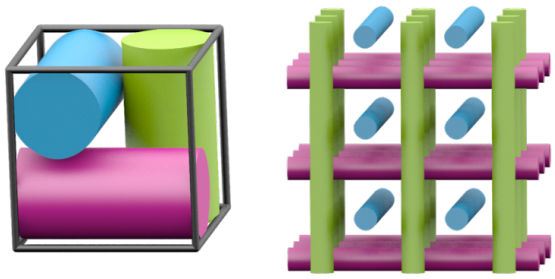

(a) **(b)**

Figure 4.24: The ideal D_{124C} structure, equivalent to the Π^{*} rod packing. (a) The unit cell, where $\frac{L}{D} = 6$ and $\frac{LD^2}{V} = 0.75$. (b) The filaments in the ideal structure are straight.

In contrast, the G^{+}_{129C} structure, which is a Σ^{+} rod packing with helical filaments, has an ideal form also composed of helical filaments along the axes of the rods (Fig. 4.25). The helical formation of the filaments is an emergent property, regardless of the starting configuration. The conformation also has the beautiful property that when the filaments are maximally inflated, they fill one channel of the G minimal surface. The $\frac{L}{D}$ value for this conformation is 30.21 and the $\frac{LD^2}{V}$ measure is 0.49, making it the least dense ideal structure of those related to the cubic rod packings.

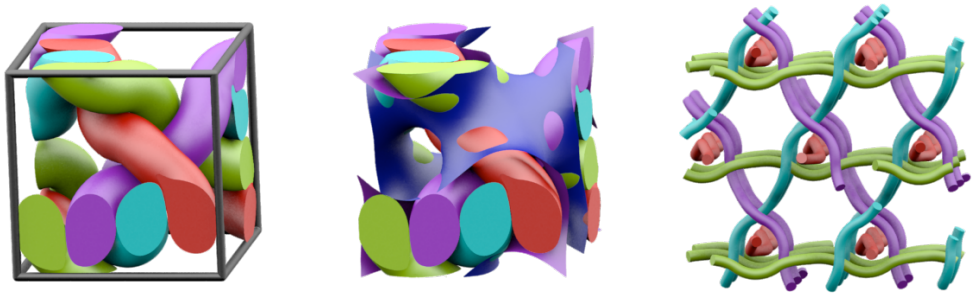

(a) **(b)** **(c)**

Figure 4.25: The ideal G^{+}_{129C} structure: a helical Σ^{+}. (a) The unit cell, where $\frac{L}{D} = 30.21$ and $\frac{LD^2}{V} = 0.49$. (b) The ideal structure fills one channel of the G minimal surface. (c) The extended ideal structure. This is the least dense ideal structure of those related to the cubic symmetry rod packings.

The $G^{+}_{123C}(2)$ structure is a Γ rod packing by undulating filaments. The ideal $G^{+}_{123C}(2)$, which minimises $\frac{L}{D}$ within one unit cell, is composed of straight rods, equivalent to the rod packing geometry (Fig. 4.26). The $\frac{L}{D}$ value for this conformation is 19.27 and the $\frac{LD^2}{V}$ measure is 0.90, making this the densest ideal structure of those related to the cubic rod packings. This is the only structure related to the cubic rod packing that does not (in an obvious way) lie on a TPMS (or slightly deformed TPMS) in its ideal form.

For all ideal structures related to the cubic rod packings (except for the ideal $G^{+}_{123C}(2)$ or Γ^{+} rod packing), any deformation of the unit cell in the simulation process both increases $\frac{L}{D}$ and decreases $\frac{LD^2}{V}$, hence the lattice parameters ($a = b = c = 1$; $\alpha = \beta = \gamma = \frac{\pi}{2}$, a primitive cubic cell) are the optimum. For the ideal $G^{+}_{123C}(2)$ structure however, an increase in the 'c' parameter gives a conformation with a higher $\frac{L}{D}$ value, and a higher $\frac{LD^2}{V}$. Hence we get a denser packing, at the expense of the L to D ratio. By definition, the primitive cubic configuration for this structure is the ideal (minimises $\frac{L}{D}$). For these other 'sub-ideal' configurations (more densely packed yet not minimising $\frac{L}{D}$), the rods are

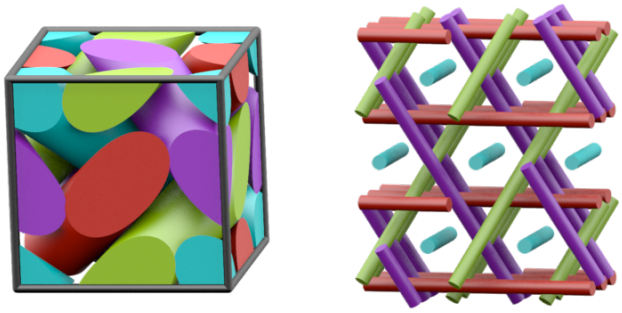

(a) **(b)**

Figure 4.26: The ideal $G^{+}_{123C}(2)$ structure, equivalent to the Γ rod packing. (a) The unit cell, where $\frac{L}{D} = 19.27$ and $\frac{LD^2}{V} = 0.90$. (b) The ideal structure has straight filaments.

undulating, where the undulations become more exaggerated with an increase of 'c'. The exact $G^{+}_{123C}(2)$ structure (as it sits on the G surface, not in an ideal form) arises among these configurations at approximately$c = 1.6$, with $\frac{L}{D} = 20.68$ and $\frac{LD^2}{V} = 0.95$.

The ideal P_{129C} structure, related to the Ω^{+} rod packing, has slightly helical filaments. The ideal geometry matches exactly to the P_{129C} geometry as constructed on the P surface, further supporting the relevance of the geometry prescribed by the TPMS reticulation method. This ideal structure is shown in Fig. 4.27. The $\frac{L}{D}$ value for this conformation is 24.06 and the $\frac{LD^2}{V}$ measure is 0.62.

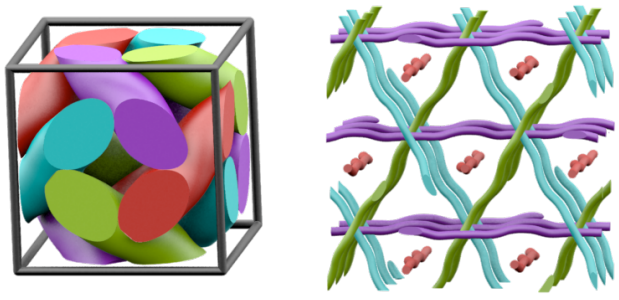

(a) **(b)**

Figure 4.27: The ideal P_{129C} structure, related to the Ω^{+} rod packing. (a) The unit cell: $\frac{L}{D} = 24.06$ and $\frac{LD^2}{V} = 0.62$. (b) Several unit cells shown with a reduced diameter to highlight the helical geometry of the rods, which match the structure as it lies on the P surface.

The $\Sigma*$ packing is a rod packing containing the interweaving of a Σ^{+} and a Σ^{-} (an enantiomeric pair). The ideal structure related to the $\Sigma*$ rod packing is exactly equivalent to the interweaving of the ideal G^{+}_{129C} and G^{-}_{129C} structures (related to the Σ^{+} and Σ^{-} pack-

ings). It is remarkable that the ideal G^{+}_{129C} structure (or equivalently the G^{-}_{129C} structure) leaves precisely the correct vacant space to intercalate the opposite enantiomer, also in its ideal form. Further, the ideal G^{+}_{129C} structure fills one channel of the G minimal surface, and the second ideal enantiomer fills the other channel.

General weavings

In Ch. 3, we constructed a variety of non-cubic, intersecting and woven rod packings via TPMS reticulations. Here we examine the ideal configurations of some of these general filament packings, beginning with some non-cubic examples.

The $P_{114C}(1)$ structure, as constructed in Ch. 3, is related to a non-invariant rod packing with tetragonal symmetry (Fig. 4.28(a)). The ideal conformation of this rod packing, that which minimises the $\frac{L}{D}$ ratio within one unit cell, sees the filaments deviate slightly from their rod axes, and become undulating trajectories. The minimum $\frac{L}{D}$ value, 15.95, occurs with lattice parameters ($a = b = 1$; $c = 0.8$; $\alpha = \beta = \gamma = \frac{\pi}{2}$). For this choice of unit cell, $\frac{LD^2}{V} = 0.7037$. This choice of unit cell does not give a densest packing ($\frac{LD^2}{V}$), as was the case for the Γ structure, and the density increases with the value of 'c' at the expense of $\frac{L}{D}$.

(a) **(b)** **(c)**

Figure 4.28: The ideal $P_{114C}(1)$ structure, which is the ideal conformation of a non-invariant rod packing of tetragonal symmetry. (a) The $P_{114C}(1)$ structure as constructed on the P surface. (b) The unit cell (dimensions $1 \times 1 \times 0.8$) of the ideal structure. (c) The ideal structure with a deflated filament diameter shows the undulating geometry of the rods.

The $G^{-}_{93C}(1)$ weaving is related to a non-invariant rod packing with trigonal symmetry, as shown in Fig. 4.29(a). When viewed along a filament axis, the packing appears to be a deformation of the Π^{*} rod packing. In the search for ideal configurations, the unit cell lattice parameters are altered so as find the least $\frac{L}{D}$ ratio within a unit cell. The ideal $G^{-}_{93C}(1)$ structure, as shown in Fig. 4.29(b,c), is precisely the Π^{*} cubic rod packing, for which $\frac{L}{D} = 6$ and $\frac{LD^2}{V} = 0.75$. Interestingly, the observation of the rod packing in the chem-

ical framework was of a weaving not in its ideal symmetry setting. This is not surprising however, given chemical bonding requirements within a chemical framework.

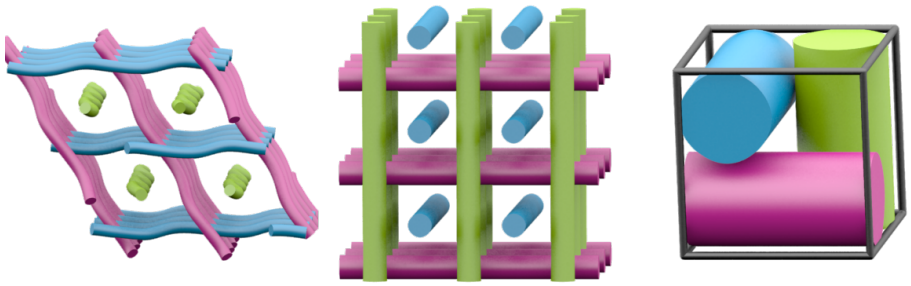

(a) (b) (c)

Figure 4.29: The ideal $G^{-}_{93C}(1)$ structure. (a) The structure as it lies on the G minimal surface has undulating rods. (b,c) The ideal structure is equivalent to the Π^{*} rod packing.

Two structures with trigonal symmetry, $H_{31C}(1)$ and $H_{31C}(3)$, are constructed on the H surface in Ch. 3. In the first structure, $H_{31C}(1)$, the filaments may straighten to rods without a change in ambient isotopy class, yet in the second structure, the filaments are sufficiently tangled to preclude this. The ideal structures in both cases, shown in Fig. 4.30, are close to the geometry inherited from the H surface. For the ideal structures $\frac{L}{D} = 12.31$ and $\frac{LD^2}{V} = 0.67$ in the first case, and $\frac{L}{D} = 25.84$ and $\frac{LD^2}{V} = 0.46$ in the second case. The shape of the unit cell in both cases remains hexagonal, with lattice parameters ($a = b = c = 1$; $\alpha = \beta = \frac{\pi}{2}; \gamma = \frac{\pi}{3}$)

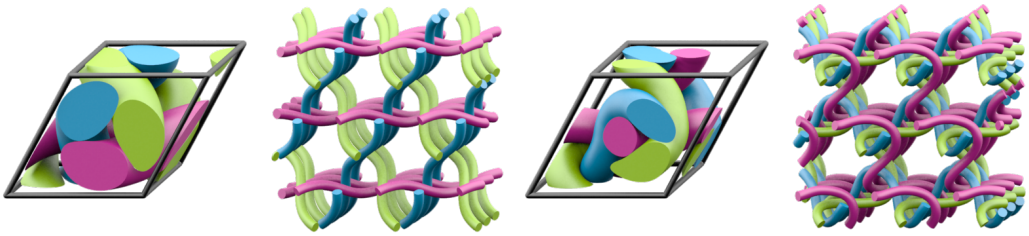

(a) (b) (c) (d)

Figure 4.30: The ideal conformations of (a,b) the $H_{31C}(1)$ structure and (c,d) the $H_{31C}(3)$ structure, shown both within one unit cell and globally with a deflated filament diameter. In each of these ideal structures, the unit cell is hexagonal.

Consider next a further class of weavings, where the filament axes are intersecting on straightening. One examples is $D_{118C}(1)$, as described in Ch. 3 and shown in Fig. 4.31. In its ideal form, $\frac{L}{D} = 145.28$ and $\frac{LD^2}{V} = 0.40$, which indicates that the structure is a very low

density material in its ideal form. The oscillating filaments of the surface reticulation are also seen in the ideal form.

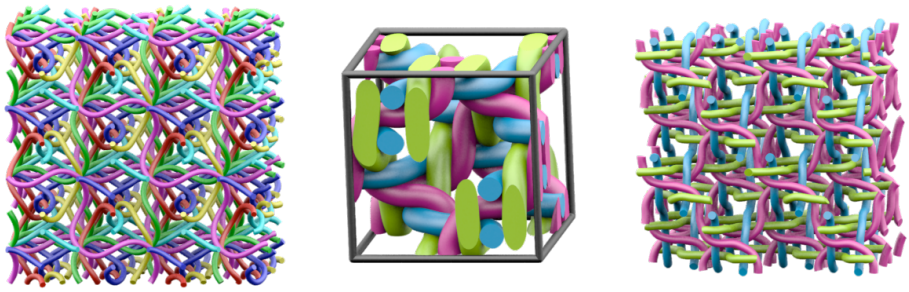

(a) **(b)** **(c)**

Figure 4.31: The $D_{118C}(1)$ structure. (a) The structure as constructed on the D surface. (b) One unit cell of the ideal configuration, where $\frac{L}{D} = 145.28$ and $\frac{LD^2}{V} = 0.40$. (c) The global ideal structure.

Another example of an intersecting rod packing is the $G^{+}_{118C}(1)$ structure, shown in Fig. 4.32(a). In its ideal configuration (Fig. 4.32(b,c)), $\frac{L}{D} = 123.84$ and $\frac{LD^2}{V} = 0.39$, where once again this gives a very low density structure. The difference between the surface reticulation and the ideal structure in this case is small, thus the ideal structure lies close to the G minimal surface.

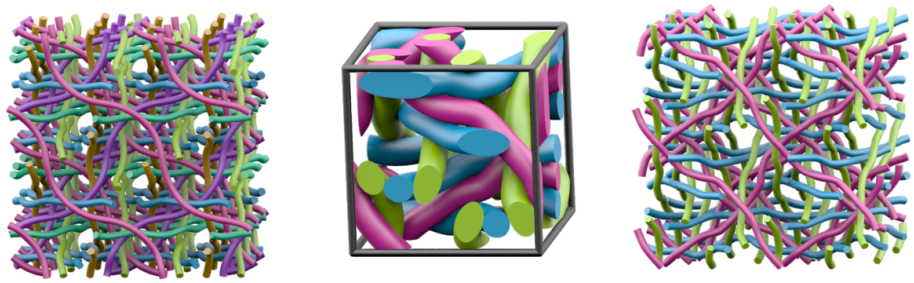

(a) **(b)** **(c)**

Figure 4.32: The $G^{+}_{118C}(1)$ structure. (a) The structure as it is constructed on the G surface. (b,c) The ideal structure, shown within one unit cell and globally with a deflated filament diameter.

A more general class of filament packings were considered in Ch. 3, where the filaments impede each other from straightening in unison *i.e.* the filaments cannot all be straightened without changing the ambient isotopy type of the weaving. This class permits the entanglement of the filaments to be as complex as desired. Fig. 4.33 shows the $G^{+}_{118C}(2)$ structure in both its standard configuration (as it lies on the G minimal surface) and in its ideal form. This structure is a tangled version of a triple Γ rod packing (a Γ

rod packing with a triple helix along each rod axis). For this ideal form, $\frac{L}{D} = 220.26$ and $\frac{LD^2}{V} = 0.51$.

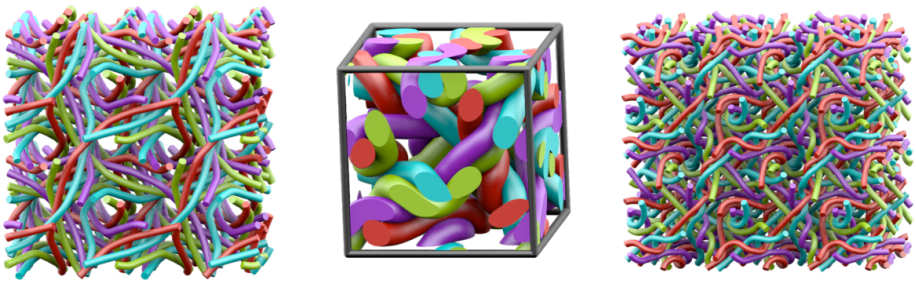

(a) **(b)** **(c)**

Figure 4.33: The $G^{+}_{118C}(2)$ structure. (a) The array as it lies on the G surface. (b,c) The ideal configuration of this weaving, shown within one unit cell and globally with a deflated filament diameter. For this configuration, $\frac{L}{D} = 220.26$ and $\frac{LD^2}{V} = 0.51$.

Fig. 4.34 shows the $G^{-}_{118C}(2)$ structure in both its surface reticulation conformation and in its ideal conformation. This structure is a tangled version of a Σ^{+} rod packing. For this ideal conformation, $\frac{L}{D} = 70.67$ and $\frac{LD^2}{V} = 0.25$, which makes this weaving the least dense (and most porous) material seen so far in this Chapter.

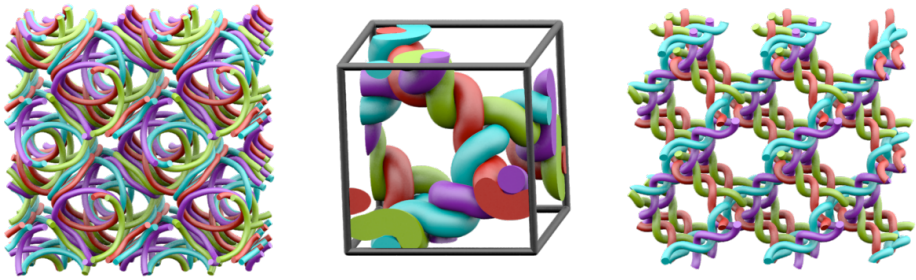

(a) **(b)** **(c)**

Figure 4.34: The $G^{-}_{118C}(2)$ structure. (a) The array as it lies on the G surface. (b,c) The ideal configuration of this weaving, shown within one unit cell and globally with a deflated filament diameter. This weaving is the least dense material of all ideal weavings studied in this chapter.

As a final example, we consider the ideal conformation of the $P_{118C}(4)$ structure, which is the inter-growth of closed loops on the P surface. As a surface reticulation, this array has very high 3D space group symmetry ($P432$). When tightened to an ideal conformation, we see that a lot of this symmetry is lost (Fig. 4.35). For this ideal configuration, $\frac{L}{D} = 85.62$ and $\frac{LD^2}{V} = 0.44$. Insight into the loss of symmetry in the idealised structure comes from

the tightening of a periodic helix composed of 4 strings: when the helix is tightened, an ideal configuration is obtained when one of the string pulls straight in the middle of the helix, and the other three wind around in a standard triple helix. We see that this behaviour occurs locally throughout the weaving, where the filament that eventually pulls straight is arbitrary. This should lead to a set of ideal configurations, all of which will have equivalent measurements, reminiscent of the ideal configurations of high complexity torus knots and links, which lose symmetry on tightening to give a non-unique tight embedding [Pier 98].

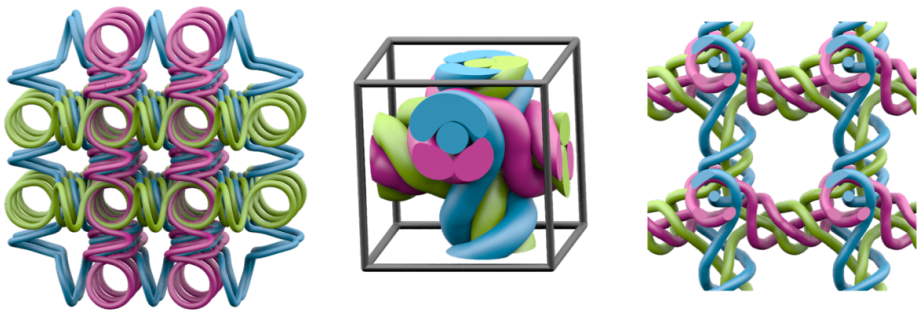

(a) **(b)** **(c)**

Figure 4.35: The $P_{118C}(4)$ structure, which is the inter-growth of closed loops in a 3-periodic chain-mail arrangement. (a) The array as it lies on the P surface, which has high 3D symmetry. (b) One unit cell of the idea conformation. (c) The extended ideal conformation: much of the symmetry that was present in the surface reticulation is lost in the ideal form, reminiscent of the loss of symmetry in high complexity torus knots and links.

In summary, the exact geometry (not just topology) inherited from the minimal surface reticulation seems to have some significance, via a number of particular cases for which the ideal geometry of the weaving is reminiscent of the TPMS reticulation geometry. We also saw that in some cases, the ideal conformation of a rod packing contained helical components rather than straight components. Note also a general trend observed is that the $\frac{L}{D}$ value gets larger as the array gets more entangled.

4.3.4 Periodic entanglement of nets

Combining the two additional capabilities of the **PB-SONO** algorithm, branches and periodicity, allows the tightening of a periodic net (as defined in Ch. 1: a simple 3-connected periodic graph). The SyStRe algorithm[Delg] performs a similar process on a set of nets known as crystallographic nets. These are nets automorphism groups are isomorphic to 3D crystallographic space groups [Klee 04].

The SyStRe algorithm gives two embeddings of the net: the first is the barycentric

placement whose form minimises the sum of the edge lengths squared, and the second is an embedding which favours uniform edge lengths, which we will refer to as the *uniform* embedding. Despite the success of the SyStRe algorithm, there are nets for which it gives no canonical form, including those with edge and vertex collisions, where multiple edges or vertices occupy the same location in the barycentric placement, and non-crystallographic nets. Additionally, the SyStRe embeddings do not consider the interpenetration of multiple net components. It is these cases, for which there is no canonical embedding, that we wish to consider in their ideal formation as found by the **PB-SONO** algorithm.

In Ch. 3, we constructed a set of nets, some with single components and some with multiple threaded components. These nets may be constructed with arbitrary complexity and with a variety of different topologies. Here we will consider the ideal conformations of some of these nets as obtained by the **PB-SONO** algorithm, to test the algorithm in relation to finding canonical forms for multiple component nets. We will consider examples from each of the topologies encountered: **srs**, **dia**, **pcu** and **hcb**.

Canonical embeddings of single component nets

Initially, we examine the tight configurations of the simplest 3-periodic nets (those that are edge-1 and vertex-1 transitive), **srs**, **dia** and **pcu**, as well as a simple 2-periodic graph, **hcb**. Further, we consider an example with an interesting SyStRe result, the ideal $(4,4,8,8)$ 2-periodic layer, as well as a net with a vertex collision in the barycentric placement, and finally a non-crystallographic net.

On tightening the **srs**, **dia** and **pcu** nets, we find that their ideal conformations are equivalent to both the barycentric embedding and the uniform embedding as given by SyStRe. These ideal conformations, which realise all possible symmetries of their graph topologies, are shown in Fig. 4.36.

The values obtained for $\frac{L}{D}$ and $\frac{LD^2}{V}$ for these ideal conformations are shown in Table. 4.6. For the values obtained, both **srs** and **pcu** have a simple cubic unit cell, and **dia** has a face centre cubic unit cell. Thus this the primitive unit cells for **srs** and **pcu** and the conventional unit cell for **dia**, note however that the $\frac{LD^2}{V}$ measure is independent of the unit cell chosen. The measurements show that the **pcu** net has the least energy (least $\frac{L}{D}$) of the three examples shown, and is also the densest arrangement (greatest $\frac{LD^2}{V}$). The **dia** net is then the second most dense, and **srs** the least dense.

Two examples of 2-periodic graphs are also tightened to an ideal conformation. The

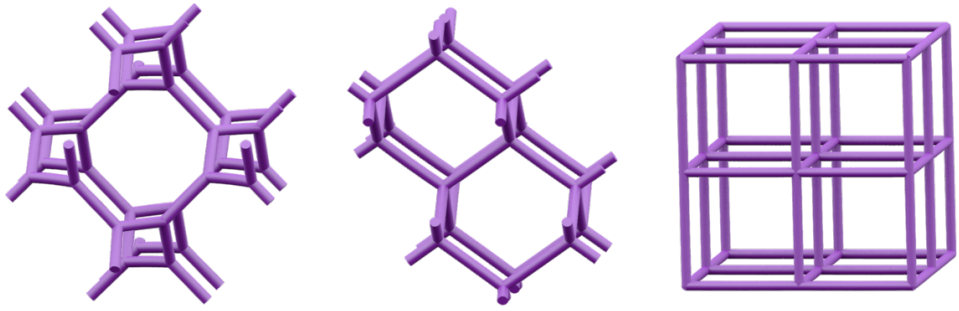

(a) **(b)** **(c)**

Figure 4.36: Ideal embeddings of the simplest 3-periodic nets: (a) **srs**, (b) **dia**, (c) **pcu**. The diameter has been decreased to show the ideal form. In all cases, the ideal configuration gives the same vertex and edge locations as for both the barycentric placement and uniform embedding given by the SyStRe algorithm.

Table 4.6: Tight 3-periodic nets

Net	$\frac{L}{D}$	$\frac{LD^2}{V}$	Lattice parameters of cell
srs	11.88	0.55	$(a=b=c=1;\ \alpha=\beta=\gamma=\frac{\pi}{2})$
dia	16.34	1.25	$(a=b=c=1;\ \alpha=\beta=\gamma=\frac{\pi}{2})$
pcu	3.00	3.00	$(a=b=c=1;\ \alpha=\beta=\gamma=\frac{\pi}{2})$

first of these is a single **hcb** net: in its ideal form, all edges are of equivalent length and $\frac{L}{D} = 2.89$, corresponding to a hexagonal 2-periodic unit cell with lattice parameters $(a=b=1;\ \gamma=\frac{\pi}{3})$. The $\frac{LD^2}{V}$ measurement is meaningless for 2-periodic structures, and thus we consider an analogous measure for a 2-periodic structure: $\frac{LD}{A}$, which measures the density of a planar projection of the structure within the area of the 2D unit cell. In its ideal configurations, the **hcb** graph has $\frac{LD}{A} = 1.20$. The ideal conformation of this net is shown in Fig. 4.37(a).

The SyStRe embedding of a net may take two forms: the barycentric embedding or the uniform embedding. For the $(4,4,8,8)$ 2-periodic graph, these two embeddings are not equivalent. On tightening by the **PB-SONO** algorithm, the ideal form is equivalent to the uniform embedding given by SyStRe, and is distinct from the barycentric embedding. This ideal configuration is shown in Fig. 4.37(b). In the ideal configuration $\frac{L}{D} = 6.05$ for lattice parameters $(a=b=1;\ \gamma=\frac{\pi}{2}$: a square unit cell), and $\frac{LD}{A} = 1.01$.

A 3-periodic net whose barycentric embedding has a vertex collision is the $2(3,5)2$ net, whose labelled quotient graph (defined in Ch. 1 [Chun 84, Eon 05]) is shown in

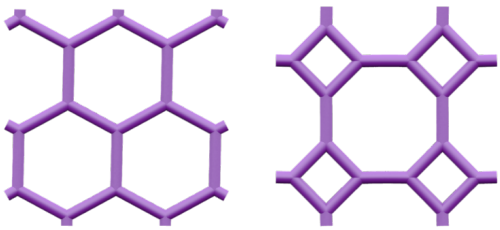

(a) (b)

Figure 4.37: Ideal embeddings of (a) **hcb**, (b) $(4,4,8,8)$. The diameter has been decreased in all cases to shown the ideal form. The configuration found by **PB-SONO** is equivalent to the uniform embedding as computed by the SyStRe algorithm.

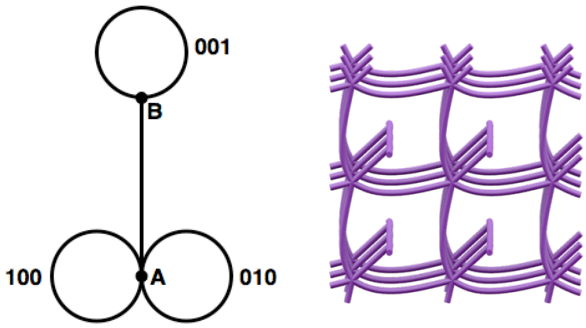

(a) (b)

Figure 4.38: (a) The labelled quotient graph of the $2(3,5)2$ net: the labels give the translations of the edges. (b) The ideal embedding for the $2(3,5)2$ net, whose vertices collide in the barycentric placement calculated by the SyStRe algorithm.

Fig. 4.38(a). It is apparent from the quotient graph that the two distinct vertices of the structure will occupy the same point in a barycentric placement. An alternative embedding for this net is given in [Eon 11], which has the vertices placed at $(0,0,0)$ and $(\frac{1}{3},0,0)$. Further, the **PB-SONO** algorithm is able to tighten nets such as this to an ideal conformation. The ideal configuration of the net, is shown in Fig. 4.38(b). This configuration has a unit cell with lattice parameters ($a = b = 1$; $c = \frac{1}{2}$; $\alpha = \beta = \gamma = \frac{\pi}{2}$), and the A and B vertices are located at $(0,0,0)$ and $(\ 0.38,\ 0.38,0)$ respectively. We see that the lower restriction on the edge length to be at least D units, discussed in the context of finite graphs earlier in this chapter, keeps the vertices from occupying the same position in the unit cell. For this ideal conformation, $\frac{L}{D} = 6.22$ and $\frac{LD^2}{V} = 1.56$. This embedding is distinct to the alternative embedding found by in [Eon 11].

The **PB-SONO** algorithm may also be used to tighten 3-periodic non-crystallographic

nets. Consider the non-crystallographic net whose quotient graph is shown in Fig. 4.39(a), this net is non-crystallographic as it may be equivalently represented by multiple quotient graphs that are not isomorphic [Eon 11]. An alternative embedding of this graph is given in [Eon 11]. The ideal configuration as found by the **PB-SONO** algorithm, shown in Fig. 4.39(b,c), is found with lattice parameters ($a = 1$; $b = c = \frac{2}{3}$; $\alpha = \beta = \gamma = \frac{\pi}{2}$), and has $\frac{L}{D} = 12.67$ and $\frac{LD^2}{V} = 1.03$. This table shows the vertex positions within the ideal unit cell, along with the vertex positions in the alternative embedding of [Eon 11]:

PB-SONO	
A	$(\frac{5}{6}, \frac{1}{2}, \frac{1}{2})$
B	$(\frac{1}{6}, \frac{1}{2}, \frac{1}{2})$
C	$(\frac{2}{3}, \frac{1}{2}, 0)$
D	$(\frac{1}{3}, \frac{1}{2}, 0)$
E	$(0, \frac{1}{2}, 0)$
F	$(0,0,0)$

[Eon 11]	
A	$(\frac{7}{8}, \frac{1}{2}, \frac{1}{2})$
B	$(\frac{1}{8}, \frac{1}{2}, \frac{1}{2})$
C	$(\frac{3}{4}, \frac{1}{2}, 0)$
D	$(\frac{1}{4}, \frac{1}{2}, 0)$
E	$(0, \frac{1}{2}, 0)$
F	$(0,0,0)$

The difference in the two embeddings (**PB-SONO** and [Eon 11]) is not large: the x coordinate of the B and D vertices (and those related by symmetry) is $\frac{1}{6}$ and $\frac{1}{3}$ for **PB-SONO** and $\frac{1}{8}$ and $\frac{1}{4}$ for [Eon 11]. If we consider the tightest embedding of the net within a different unit cell (not the ideal unit cell), namely that with lattice parameters ($a = 1$; $b = c = \frac{1}{2}$; $\alpha = \beta = \gamma = \frac{\pi}{2}$), we find that the locations of the vertices in both styles of embeddings are equivalent.

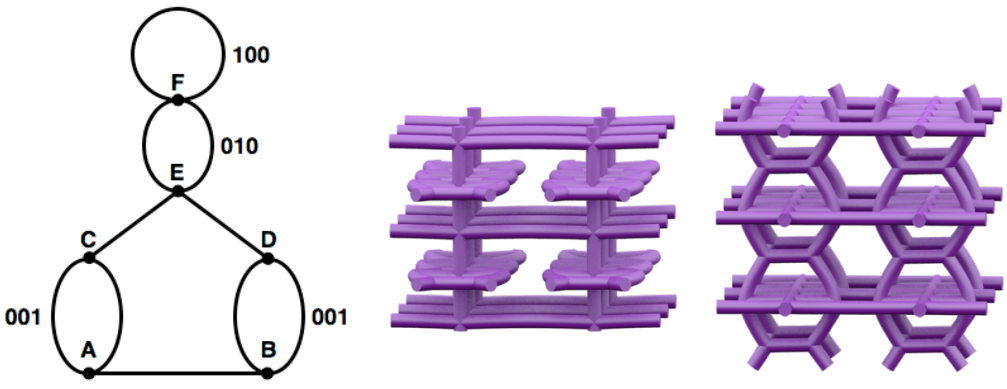

(a) **(b)** **(c)**

Figure 4.39: (a) The labelled quotient graph that represents the non-crystallographic net, where the labels specify translations. (b,c) Ideal embedding of this non-crystallographic net, as found by the **PB-SONO** algorithm, viewed down the z-axis and y-axis respectively.

Multiple srs nets

In Ch. 3, we generated a set of interpenetrating, multiple–component **srs** nets. We will explore the ideal configurations of these nets: two examples that consist of the interpenetration of two **srs** nets, the G^{+}_{124R} structure and the G^{+}_{129R} structure which are both constructed on the G surface, the D_{124R} structure which is an array of four **srs** components, and the P_{129R} structure which is composed of eight **srs** components. A summary of the $\frac{L}{D}$ and $\frac{LD^2}{V}$ measurements for these ideal configurations are shown in Table 4.7. In all cases, the ideal configuration has a cubic conventional unit cell.

Table 4.7: Ideal multi-**srs** nets

Structure	Topology	$\frac{L}{D}$	$\frac{LD^2}{V}$	Lattice parameters
G^{+}_{124R}	$2 \times$ **srs**	28.15	1.27	$(a=b=c=1; \alpha=\beta=\gamma=\frac{\pi}{2})$
G^{+}_{129R}	$2 \times$ **srs**	41.10	0.72	$(a=b=c=1; \alpha=\beta=\gamma=\frac{\pi}{2})$
D_{124R}	$4 \times$ **srs**	8.49	1.06	$(a=b=c=1; \alpha=\beta=\gamma=\frac{\pi}{2})$
P_{129R}	$8 \times$ **srs**	28.48	0.77	$(a=b=c=1; \alpha=\beta=\gamma=\frac{\pi}{2})$

The two structures G^{+}_{124R} and G^{+}_{129R} are each composed of two interpenetrating **srs** nets, where both of the components in each structure are of the equivalent chirality. The TOPOS analysis [Blat 06] of these structures in Ch. 3 indicates that these two structures are not equivalent by ambient isotopy, as they contain a distinct linking signature when analysed by cycles. On tightening, we find that the G^{+}_{124R} structure has a significantly lower $\frac{L}{D}$ energy than the G^{+}_{129R} structure: 28.1472 in the first case and 41.0965 in the second for equivalent unit cell sizes. This difference offers further support that the structures are not equivalent by ambient isotopy despite having equivalent topology, and further, the relative ranking of the two structures by $\frac{L}{D}$ energy implies that the G^{+}_{124R} structure is less entangled than the G^{+}_{129R} structure. This relative ranking is also offered by the TOPOS analysis, which identifies less links in the G^{+}_{124R} structure (18 Hopf links and one more complex link) as compared to the G^{+}_{129R} structure (23 Hopf links and 3 more complex links).

The ideal conformations for these two structures are shown in Fig. 4.40. We see that the two ideal conformations look remarkably distinct within a unit cell. In the ideal G^{+}_{124R} structure, the individual **srs** components each deviate significantly from the ideal form of a single **srs** net, and even more so in the G^{+}_{129R} structure. Interestingly, the crystallographic data from a synthesised pair of **srs** with equivalent chirality given in [Kepe 00] gives a

conformation that matches the ideal form of the G^+_{124R} structure, which suggests that these ideal conformations are relevant for chemical frameworks.

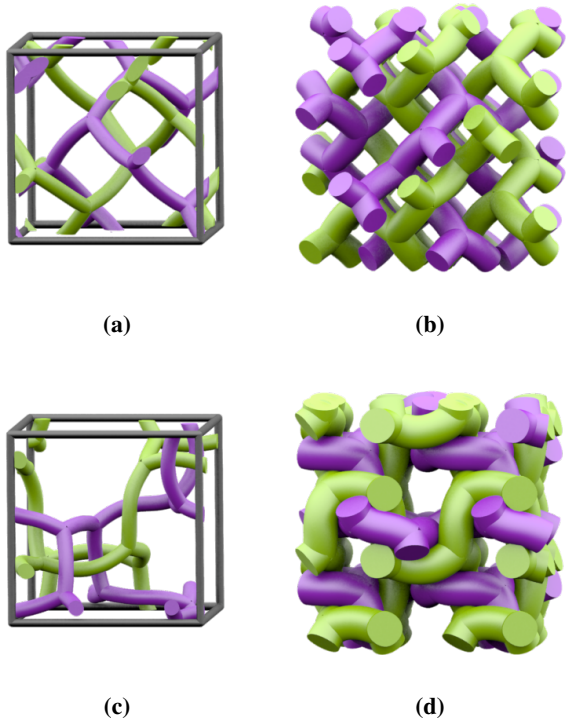

Figure 4.40: The ideal G^+_{124R} and G^+_{129R} structures, which both comprise two **srs** components of equivalent chirality. (a) One unit cell of G^+_{124R}. The ideal diameter is decreased to show the edge geometry. (b) The extended structure. (c) One unit cell of G^+_{129R}. (d) The extended structure. We can infer from the $\frac{L}{D}$ energy measurements for these ideal conformations that the G^+_{124R} is less entangled than G^+_{129R}, and the two structures are not equivalent by ambient isotopy.

We now consider the D_{124R} and P_{129R} structures, which are composed of the interpenetration of four and eight **srs** components respectively. In both cases, all **srs** components have equivalent chirality. The ideal conformations of these structures are shown in Figs. 4.41 and 4.42 respectively. The $\frac{L}{D}$ energies for the ideal conformations of these two structures are 8.49 and 28.48 respectively. The ideal unit cell of the P_{129R} structure (8 **srs**) contains exactly the vertex and edge positions of the D_{124R} structure, plus a second complete D_{124R} structure related by a $\frac{\pi}{2}$ rotation. Further, in both cases all **srs** components are in an ideal single **srs** formation. The $\frac{LD^2}{V}$ values for the two respective ideal configurations are 1.06 and 0.77, thus the 4 **srs** structure packs more densely than the 8 **srs** structure.

In both cases, all of the edges within the ideal conformation trace a straight line from vertex to vertex. This is a remarkable property for such complex interpenetrations of many components. The symmetry of the 4 **srs** structure is as found in early descriptions

of interpenetrating nets in [Well 77], as described by the space group $P4_232$. Further, this ideal configuration adds interest to such structures discussed elsewhere due to their interesting optical features, in particular the circular dichroism of the 1 **srs** and 4 **srs** structures [Saba 11].

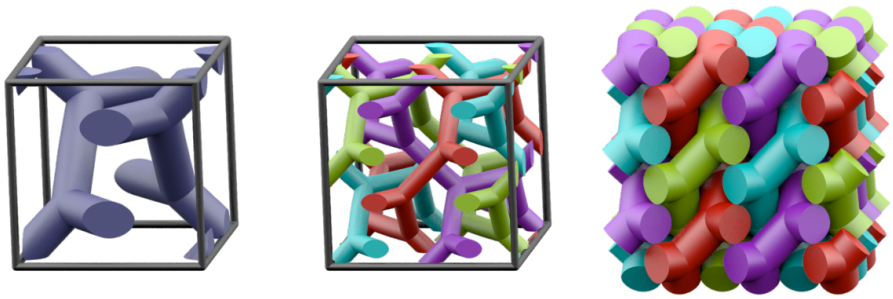

(a) **(b)** **(c)**

Figure 4.41: The ideal D_{124R}, which is composed of four **srs** components of equivalent chirality. (a) One ideal unit cell with a decreased radius to show the edge geometry. (b) A larger unit cell is shown which preserves the colouring of components: connected components map to themselves under the periodic boundary conditions. (c) The global structure, where the net edges are maximally inflated.

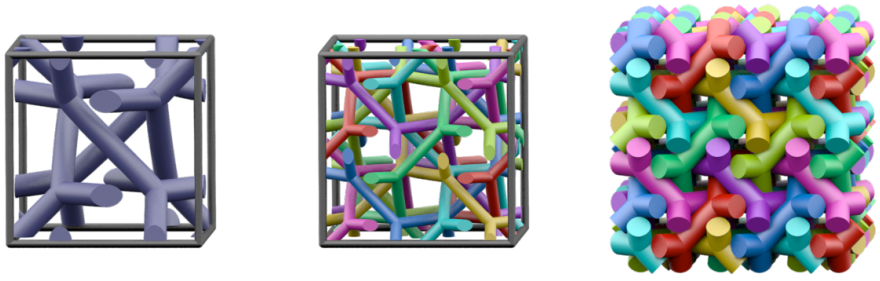

(a) **(b)** **(c)**

Figure 4.42: The ideal P_{129R} structure, which is eight **srs** components of equivalent chirality. (a) One ideal unit cell with a decreased radius. (b) A new unit cell, where connected components map to themselves under the periodic boundary conditions. (c) The full structure with the net edges maximally inflated.

Multiple dia nets

In Ch. 3, we presented a set of structures that contain multiple–components of **dia** nets that are interpenetrating. These were constructed *via* the TPMS reticulation method. We consider the tight conformation of two such cases using the **PB-SONO** algorithm, the

first is $D_{123R}(1)$ and the second is $P_{114R}(1)$. The resulting $\frac{L}{D}$ and $\frac{LD^2}{V}$ measurements for these ideal configurations are shown in Table 4.8, along with the lattice parameters of the conventional unit cell.

Table 4.8: Ideal multi-**dia** nets

Structure	Topology	$\frac{L}{D}$	$\frac{LD^2}{V}$	Lattice parameters
$D_{123R}(1)$	$2 \times$ **dia**	4.81	1.80	$(a=b=c=1; \alpha=\beta=\gamma=\frac{\pi}{2})$
$P_{114R}(1)$	$4 \times$ **dia**	18.00	1.07	$(a=b=c=1; \alpha=\beta=\gamma=\frac{\pi}{2})$

The first structure, $D_{123R}(1)$, is composed of two interpenetrating **dia** networks. The ideal configuration of this structure is shown in Fig. 4.43. The edges in this configuration are all straight, and each individual component is equivalent to an ideal embedding of a single **dia** component, where they are related by a translation. For this configuration $\frac{L}{D} = 4.81$ and $\frac{LD^2}{V} = 1.80$ for a cubic unit cell. Fig. 4.43 shows the unit cell for which these values are calculated and an additional unit cell where the translations of the periodic boundary conditions map connected components to themselves.

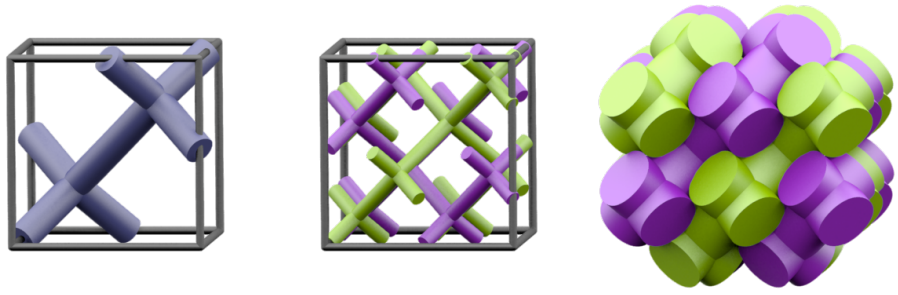

(a) **(b)** **(c)**

Figure 4.43: The ideal $D_{123R}(1)$ structure, composed of two interpenetrating **dia** networks. (a) One ideal unit cell, for which the $\frac{L}{D}$ and $\frac{LD^2}{V}$ values are calculated. (b) A larger ideal unit cell where connected (coloured) components map to themselves across the periodic boundary conditions. (c) The global structure with the radius maximally inflated.

The second structure, $P_{114R}(1)$, is composed of four interpenetrating **dia** networks. The ideal configuration of this structure is shown in Fig. 4.44. Once again, the edges in this configuration are all straight, and each individual component is equivalent to an ideal embedding of a single **dia** component, and all four components are translationally equivalent along a single translation direction. For this configuration $\frac{L}{D} = 18.00$ and

$\frac{LD^2}{V} = 1.07$ within a cubic unit cell, which gives it a higher $\frac{L}{D}$ energy and lower density than the 2 **dia** structure.

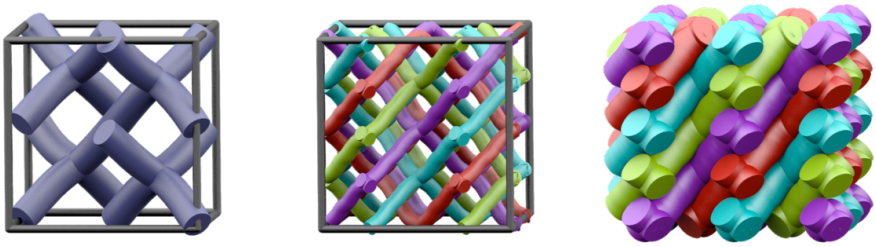

(a) **(b)** **(c)**

Figure 4.44: The ideal $P_{114R}(1)$ structure, composed of four interpenetrating **dia** networks. (a) One unit cell of the ideal structure, for which the $\frac{L}{D}$ and $\frac{LD^2}{V}$ values are calculated. (b) A larger unit cell where coloured components map to themselves across the periodic boundary conditions. (c) The full structure with the radius maximally inflated.

In both of these examples, the configuration of a component of the structure is equivalent in geometry to the ideal conformation of a single component **dia** net. From this, it may be inferred that the interpenetration of these structures is a 'least entangled' embedding of two and four components of **dia** respectively.

Multiple components of pcu

We now consider the algorithmic tightening of two examples of interpenetrating **pcu** nets, generated in Ch. 3. The resulting $\frac{L}{D}$ and $\frac{LD^2}{V}$ measurements for the ideal configurations of these two structures are shown in Table 4.9, along with the lattice parameters of the conventional unit cell.

Table 4.9: Ideal multi-**pcu** nets

Structure	Topology	$\frac{L}{D}$	$\frac{LD^2}{V}$	Lattice parameters
$P_{122R}(1)$	$2 \times$ **pcu**	12.00	1.50	$(a=b=c=1; \alpha=\beta=\gamma=\frac{\pi}{2})$
$G_{122R}(2)$	$4 \times$ **pcu**	40.46	1.09	$(a=b=c=1; \alpha=\beta=\gamma=\frac{\pi}{2})$

Fig. 4.45 shows the ideal conformation of the $P_{122R}(1)$ structure, which consists of two interpenetrating **pcu** components. The edges within the ideal conformation are straight, and each is the length of one unit cell. In total there are six distinct edges (three within

each distinct component), and the maximum possible diameter is exactly half the unit cell edge: this gives a theoretical $\frac{L}{D}$ value of 12, which is exactly replicated by the simulation. In the ideal form, each of the individual components has geometry equivalent to a single ideal **pcu** net. The $\frac{LD^2}{V}$ value for this conformation is 1.50.

The ideal conformation of the $G_{122R}(2)$ stucture, composed of four **pcu** components, is shown in Fig. 4.46. The edges within the ideal conformation deviate slightly from straight trajectories to curves: the $\frac{L}{D}$ value for a non-ideal configuration consisting of straight edges would be 48 (twelve edges each of length 1 and maximum diameter for straight edges is one quarter), yet the actual $\frac{L}{D}$ value is 40.46. This indicates a larger filament diameter and a deviation from straight edge components. This deviation to curved filaments is significant, and is not simply due to numerical uncertainty.

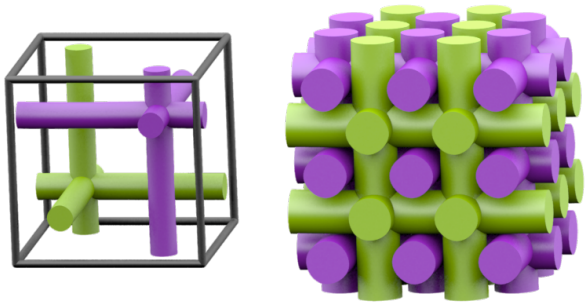

(a) **(b)**

Figure 4.45: The ideal conformation of the $P_{122R}(1)$ structure, which consists of two interpenetrating **pcu** components. (a) One ideal unit cell with a decreased radius to show the edge geometry. (b) The structure with the net edges maximally inflated.

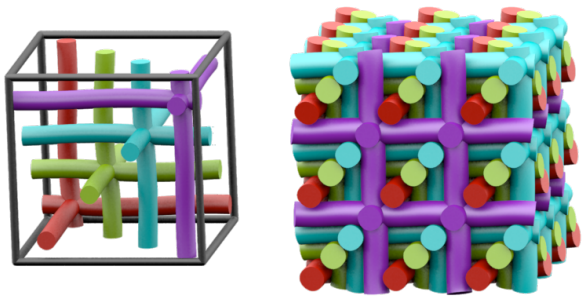

(a) **(b)**

Figure 4.46: The ideal $G_{122R}(2)$ stucture, which consists of four interpenetrating **pcu** components. (a) One ideal unit cell with a decreased radius to show the edge geometry. (b) The structure with the net edges maximally inflated. The edges of the ideal structure deviate from straight trajectories, and are significant enough to not be simply due to numerical uncertainty.

Multiple components of hcb

In Ch. 3, we constructed some 3-periodic structures that are comprised of parallel discrete 2-periodic layers of interpenetrating **hcb**. We consider the tight conformations of a single 2-periodic layer of some of these structures, found by the **PB-SONO** algorithm. The first structure, $D_{49R}(2)$, consists of four interpenetrating **hcb** layers, the second is the $H_{22R}(1)$ structure, which is equivalent to the 2D Borromean entanglement of three **hcb** layers. The third structure, $H_{22R}(2)$, is an interpenetrating set of three **hcb** layers with linked cycles, and the final structure, $H_{22R}(3)$, is a 2-periodic layer of catenated θ-graphs. The resulting $\frac{L}{D}$ measurements for the ideal configurations of these structures are shown in Table 4.10.

Table 4.10: Ideal 2-periodic multi-**hcb**

Structure	Topology	$\frac{L}{D}$	Lattice parameters
$D_{49R}(2)$	4 × **hcb**	11.06	$(a=b=1;\gamma=\frac{\pi}{3})$
$H_{22R}(1)$	3 × **hcb**: 2D Borr.	7.11	$(a=b=1;\gamma=\frac{\pi}{3})$
$H_{22R}(2)$	3 × **hcb**	14.62	$(a=b=1;\gamma=\frac{\pi}{3})$
$H_{22R}(3)$	θ-graphs: Catenated	23.05	$(a=b=1;\gamma=\frac{\pi}{3})$

Figs. 4.47 and 4.48 show the ideal conformations of these four structures. In all cases, the 3-fold symmetry inherited from the TPMS reticulation is maintained in their ideal configurations. If we consider the $\frac{L}{D}$ energy of the four structures, we see that the $H_{22R}(1)$ structure (2D borromean) has the least energy, followed by the $D_{49R}(2)$ structure (four **hcb** components). Further, the distinct 3D energies for the two 3-**hcb** patterns show their distinct ambient isotopies.

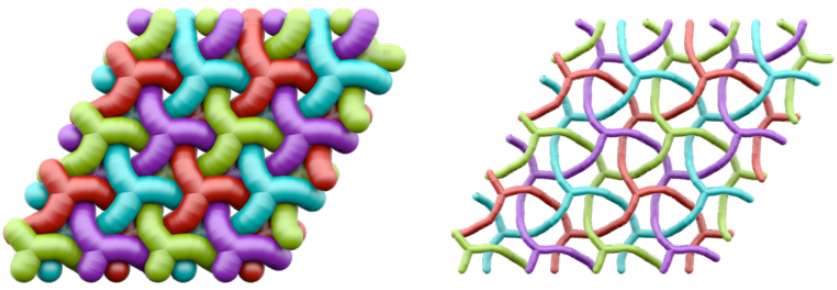

(a) **(b)**

Figure 4.47: Ideal conformation of the 2-periodic $D_{49R}(2)$ structure, which is four interpenetrating **hcb** nets. The ideal structure is shown with both a maximal and a deflated diameter.

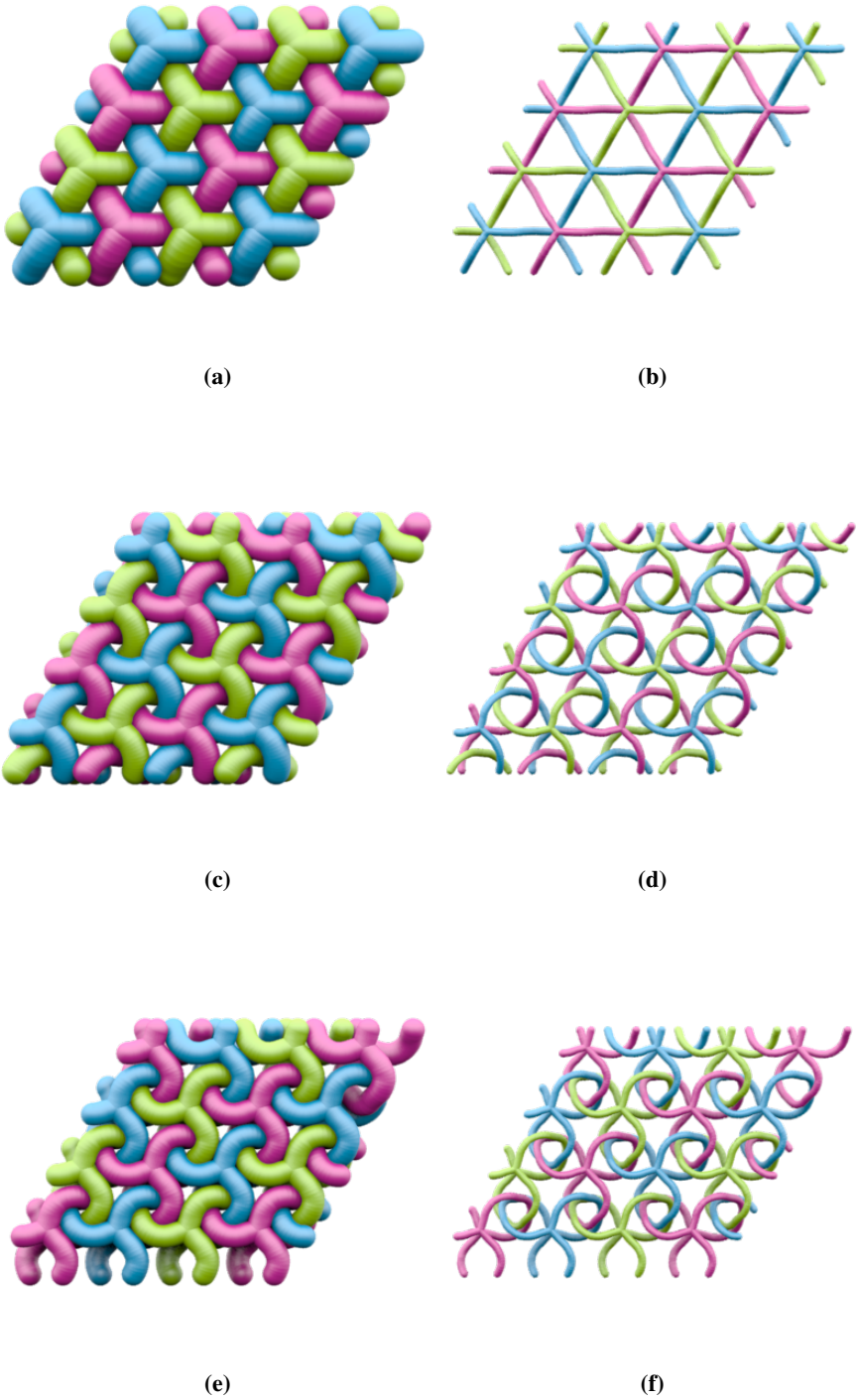

(a) **(b)**

(c) **(d)**

(e) **(f)**

Figure 4.48: Ideal conformations of three 2-periodic structures: (a,b) $H_{22R}(1)$, (c,d) $H_{22R}(2)$, (e,f) $H_{22R}(3)$, which each comprise three interpenetrating **hcb** components. Each ideal structure is shown with both a maximal and a deflated diameter.

4.4 Remarks

This chapter has described an extension to the **SONO** algorithm for tightening knots and links to the **PB-SONO** algorithm for the tightening of branched and periodic entanglements. As an initial test of the algorithm, we see that it performs comparably with the **SONO** algorithm on the tightening of knots. Further, we have presented tight embeddings of entangled θ-, tetrahedron- and cube-graphs. These tight embeddings were very accurate for the simplest entanglements (and gave results very close to as expected), yet some inexactness was present in more complex entanglements, particularly near the vertices of the graphs, where kinks are sometimes seen. These kinks, however, are only attributed to inexactness in the θ-graphs and tetrahedron-graphs cases, and are more significant and necessary in some of the embedded cube-graphs.

We have also shown tight configurations for many periodic nets. The addition of periodicity yields the uniform embedding as described by the SyStRe algorithm for those single component nets that are crystallographic and have no vertex or edge collisions. Further, the **PB-SONO** algorithm is able to tighten nets and give canonical embeddings that have vertex and edge collisions in the SyStRe embedding, as well as non-crystallographic nets. It seems to handle the interpenetration of multiple component nets in a very intuitive way. The examples shown are convincing evidence that the tight configuration found by the **PB-SONO** algorithm is a very useful tool in analysing geometry and ambient isotopy class of 3-periodic entangled nets, and is applicable to a larger class of structures than have been previously analysed. The challenge of the method is the numerical error associated with finding these ideal configurations.

When periodic packings of filaments are considered in their ideal configurations, we see the emergence of interesting filament geometries. For many of the packings considered, the straight geometry of the filaments as part of a rod packing is replaced by a helical geometry in the ideal configuration, which also retains at least all of the contacts of the rod packing. In the next chapter, we examine an interesting physical phenomenon of some tight periodic filament weavings called *Dilatancy*, which may have large ramifications in bio-inspired materials research.

Through this investigation, we see that the **PB-SONO** algorithm allows us to find canonical embeddings for a variety of new structures. These include multiple interwoven nets, nets with vertex or edge collisions, and non-crystallographic nets. Further to this, the **PB-SONO** algorithm is able to preserve the ambient isotopy of the structure, be it com-

posed of nets or filaments, through the tightening process. This is a significant result, as the previous method for finding canonical forms, the SyStRe algorithm, can only do so for some single component, crystrallographic nets. In support of the **PB-SONO** algorithm, we see the ideal form of 2 **srs** nets of equivalent chirality in a synthesised chemical framework of this topology [Kepe 00].

Chapter 5

Dilatancy of Woven Filament Arrays

We have developed a technique to generate a variety of close-packed arrays of one dimensional filaments, *via* projection of free tilings in the two-dimensional Hyperbolic plane ($\mathbb{H}^2$) into three-dimensional Euclidean space ($\mathbb{E}^3$), as decribed in Ch. 3. A rich catalogue of filament are constructed using this technique, with varying degrees of entanglement of the filaments. In Ch. 4, we have adapted algorithms developed to form canonical 'ideal' or 'tight' embeddings of knots [Katr 96, Pier 98] to arrive at canonical geometries for our weavings.

The existence of curvilinear filament geometries in tight weavings has an unexpected consequence, namely the possibility of 3D weavings that exhibit *dilatancy*, accompanied by a lowering of the fibre packing fraction and the formation of a more open weave: the volume of the weaving may be expanded while maintaining the inter-filament contacts through filament straightening. Equivalently, an internally driven straightening of the filaments within the tight configuration of a dilatant weaving will result in an expansion of the material without loss of filament contacts. We see dilatancy as an attractive material property and dilatant weaving as design target for new materials.

The free volume within a chiral, cubic and finitely dilatant weaving, the ideal conformation of the G_{129C} structure, a helical version of the Σ^+ rod packing, expands more than 5-fold on filament straightening. This remarkable three-dimensional weaving allows variation of packing density without loss of structural rigidity and is an attractive design target for materials. We propose that the ideal G_{129C} weaving is formed by keratin fibres in the outermost layer of mammalian skin, likely templated by a folded membrane.

5.1 Dilatant filament weavings

To determine if a 3-periodic weaving is dilatant, end-state configurations of the weaving under dilation must be prescribed. The initial configuration is the ideal form as determined by the **PB-SONO** algorithm described in Ch. 4; this has maximum filament diameter and a maximum number of inter-filament contacts per filament length (standardised by the filament diameter). We call the terminal configuration the *maximal* configuration, realised as follows. The unit cell is repeatedly subjected to homothetic expansion while maintaining the filament diameter, and the filaments subsequently tightened within the swollen unit cell. (This is equivalent to shrinking the filament diameter while maintaining the unit cell size and subsequently tightening the filaments.) The *maximal* configuration is reached when a further unit cell expansion results in a loss of contacts between filaments.

Closer analysis of 3D weavings reveals a rich taxonomy, amongst which we find three distinct classes. The simplest examples exhibit zero dilatancy. In these cases the ideal configuration and the maximal configuration of the weaving coincide. A second class contains weavings which dilate to accommodate a finite change in unit cell volume. When fully dilated, these finitely dilatant weavings retain all inter-fibre contacts and remain jammed. In their least dense state, finitely dilatant weavings contain rectilinear fibres and their fibre packing fraction decreases continuously during dilation, yet remains positive. The third class comprises infinitely dilatant weavings, characterised by a decrease of fibre packing fraction to zero. Since this fully dilated state is only realised for fibres of positive diameter by swelling the unit cell without limit, finite volumes of infinitely dilatant weavings will never realise this limit, since only infinitely long fibres remain jammed. We note that the hypothetical infinitely dilated configuration may consist of straight or curvilinear fibres. (In practice, infinitely dilatant weavings expand until they unjam due to loss of mutual contacts, and this end-state depends on the original fibre length.) Some examples demonstrate these various weaving classes[1].

Numerical tightening of the D_{124C} structure, equivalent to the Π^* rod packing, revealed that the ideal structure is composed of straight rods (Fig. 5.1(a)). Inflation of the unit cell while maintaining the filament diameter induces a reduction in the number of inter-fibre contacts per unit cell (Fig. 5.1(b)). Hence the tight and maximal configurations of this rod packing are equivalent, and we can infer that the weaving is not dilatant.

[1] A further class of finitely dilatant weavings can be imagined for which the maximal configuration contains curvilinear fibres. To date, however, we have failed to find an example of this class.

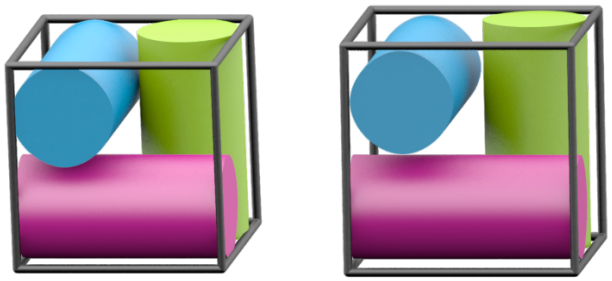

(a) **(b)**

Figure 5.1: The D_{124C} structure, equivalent to the Π^* rod packing, has zero dilatancy. (a) The ideal form of the structure within one unit cell. (b) An expansion of the unit cell immediately results in the loss of contacts between filaments.

Indeed, any weaving whose ideal configuration contains rectilinear filaments is not dilatant. However, weavings whose ideal forms display curvilinear filaments need not be dilatant. Fig. 5.2 shows the ideal $D_{114C}(3)$ structure, which is a tangled version of the #2 rod packing [OKee 05]. This structure is not dilatant, yet the ideal structure is composed of interwoven helical components. Fig. 5.2 also shows that inflation of the unit cell induces a loss of many inter-filament contacts.

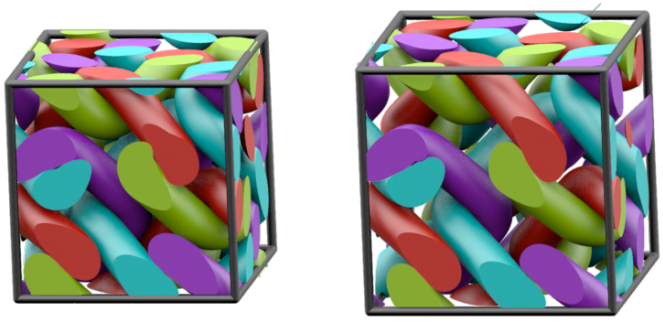

(a) **(b)**

Figure 5.2: The ideal $D_{114C}(3)$ structure, which is a tangled version of the #2 rod packing, is not dilatant. (a) The ideal unit cell, which contains curvilinear fibres. (b) A unit cell inflation induces the loss of some inter-filament contacts *i.e.* the red and blue filaments in the top right corner of the cell are not longer in contact.

Among the 3D weavings generated in Ch. 3, we have found a number of dilatant examples. Recall from the previous chapter, § 4.3.3, the ideal G_{124C} structure (helical Π^+ rod packing) is composed of helical filaments (Fig. 5.3(a)). Successive unit cell expansions

induce straightening of the helical filaments without loss of inter-filament contacts. This expansion can be continued until a final state where the filaments are completely straight and the unit cell is finite, forming the Π^+ rod packing. This is the maximal configuration (Fig. 5.3(b)). The helical filaments of the ideal Π^+ packing have length 6.466 within a $(1 \times 1 \times 1)$ unit cell, and a radius of 0.181: hence the packing fraction is 0.665. On dilation, the packing fraction decreases to 0.295 in the maximal configuration: the packing fraction is more than halved on cooperative straightening.

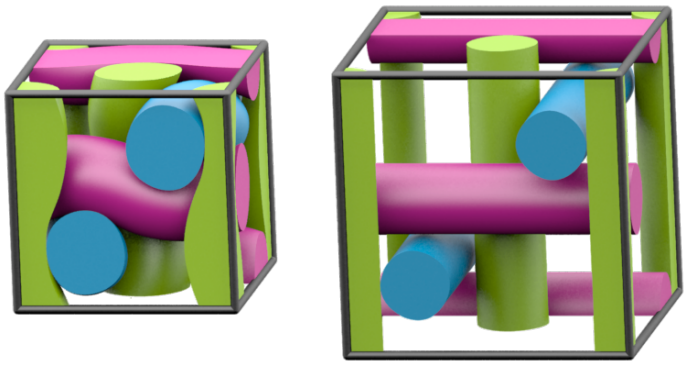

(a) **(b)**

Figure 5.3: The ideal G_{124C} structure (helical Π^+ rod packing) is finitely dilatant. (a) The ideal unit cell. (b) Consecutive unit cell expansions occur without the loss of inter-filament contacts, and the maximal configuration is the Π^+ rod packing.

A particularly large and finite dilatant behaviour is associated with the ideal form of the G_{129C} structure, which is a chiral, cubic arrangement equivalent to a helical Σ^+ rod packing. The ideal structure, shown in Fig. 5.4(a), contains helicoidal filaments that lie almost completely within one channel of the Gyroid surface, as seen in Ch. 4. The maximal configuration of the structure contains straight rods, and is precisely the Σ^+ rod packing (Fig. 5.4(b)). The helical filaments of the ideal structure have length 7.642 within a $(1 \times 1 \times 1)$ unit cell, and a radius of 0.127, and hence a packing fraction of 0.387. The packing fraction of the weaving decreases to 0.075 in the maximal configuration: a 5-fold decrease in the packing fraction. This weaving thus offers a fascinating target structure for rigid weavings capable of extreme variations in filament packing densities.

We also observe finitely dilatant behaviour in anisotropic weavings, such as the trigonal structure $H_{31C}(1)$, constructed in Ch. 3. The ideal structure has undulating filaments in a rhombohedral unit cell, as shown in Fig. 5.5(a). The maximal configuration is a trigonal rod packing of straight components, as shown in Fig. 5.5(b). In the ideal unit cell,

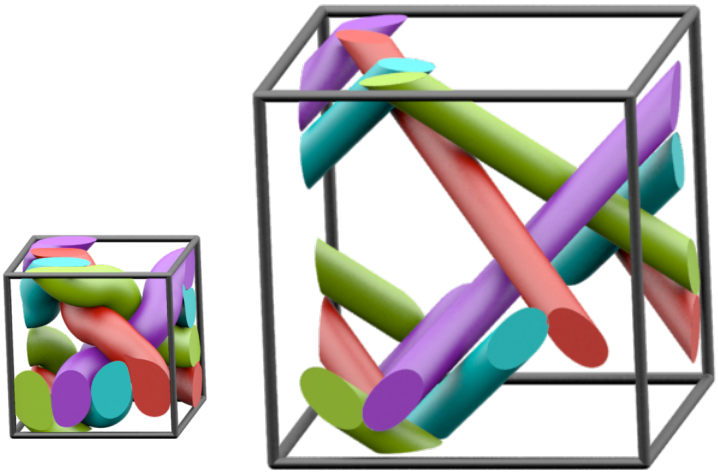

(a) **(b)**

Figure 5.4: The ideal G_{129C} structure, related to the Σ^+ rod packing, is finitely dilatant. (a) The tight unit cell. (b) The maximal state, which has no loss of inter-filament contacts, and is exactly the Σ^+ rod packing.

$L = 4.444$ and $R = 0.181$, which gives a packing fraction of 0.525 (for lattice parameters $(a = b = c = 1;\ \alpha = \beta = \frac{\pi}{2};\ \gamma = \frac{\pi}{3})$). The packing fraction of the weaving decreases to 0.204 in the maximal configuration: more than half of the ideal packing fraction.

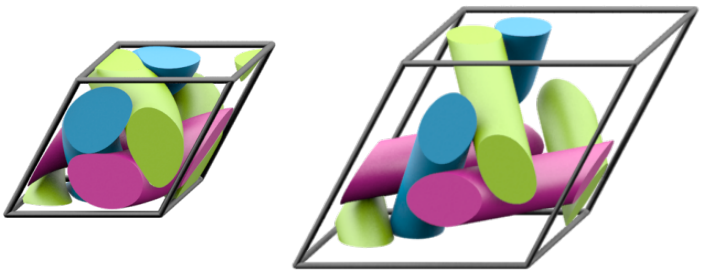

(a) **(b)**

Figure 5.5: The anisotropic trigonal structure $H_{31C}(1)$ is finitely dilatant. (a) The tight unit cell. (b) A unit cell inflation may be performed without the loss of inter-filament contacts, and the maximal configuration is composed of straight rods.

Infinitely dilatant weavings necessarily differ from those weavings that are related to crystallographic rod packings, since in the latter case the (straight) fibres are intersection-free, inducing a maximal configuration with a finite unit cell. However, weavings whose filaments intersect on straightening, as constructed in the previous chapter, § 4.3.3, are infinitely dilatant. In these cases, all inter-filament contacts remain, regardless of the increase in unit cell volume. For example, the weaving $G^{+}_{118C}(1)$, which has intersecting

filaments on straightening and whose ideal configuration is shown in Fig. 5.6(a), is infinitely dilatant. The images in Fig. 5.6(b,c) demonstrate that regardless of the amplitude of a unit cell expansion, all inter-filament contacts remain.

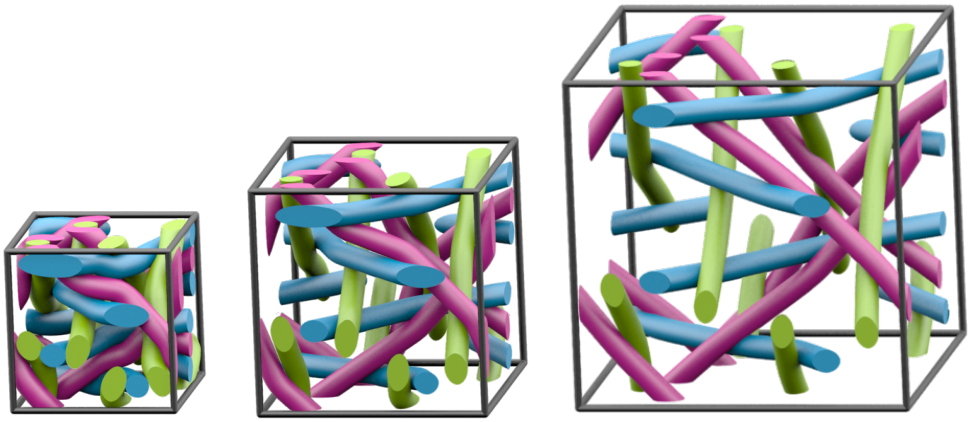

(a) **(b)** **(c)**

Figure 5.6: The ideal $G^{+}_{118C}(1)$ weaving is infinitely dilatant. (a) The ideal unit cell. (b) A small expansion sees all inter-filament contacts remain. (c) A further expansion also sees all contacts preserved. An infinite expansion see all contacts remain and the packing fraction approach zero.

Infinite dilatancy is also seen for the $D_{118C}(1)$ structure, whose ideal and expanded configurations are shown in Fig. 5.7, where all possible unit cell expansions see all inter-filament contacts preserved. It seems, within the limited catalogue of examples constructed in this thesis, that all weavings whose filaments intersect on straightening to their average axes are infinitely dilatant.

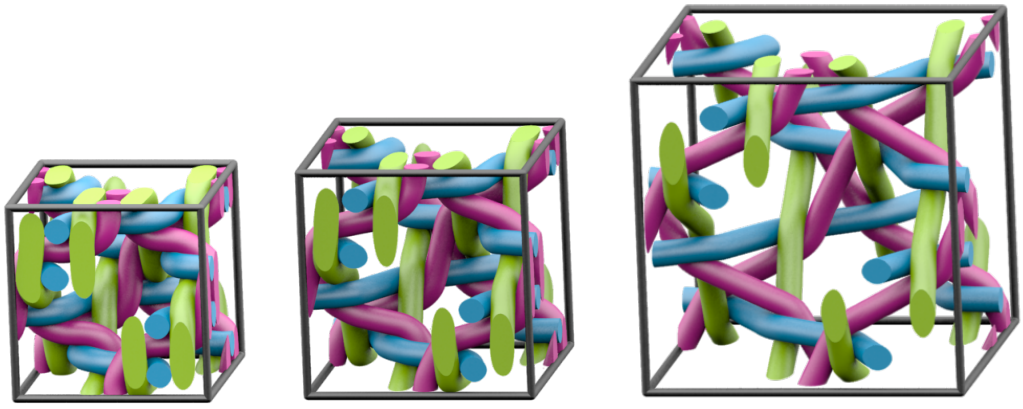

(a) **(b)** **(c)**

Figure 5.7: The $D_{118C}(1)$ structure is infinitely dilatant. (a) The ideal form within one unit cell. (b) A unit cell expansion sees the filaments remain in contact. (c) A further unit cell expansion also has all contacts preserved.

A second genre of infinitely dilatant weaving contains filaments which are sufficiently tangled to preclude rectification of the filaments without changing ambient isotopy type. For example, consider the $G^{+}_{118C}(2)$ structure, which is a tangled version of a packing which contains a triple helix each rod trajectory of the Γ. The unit cell size can be expanded without limit, without the loss of any inter-filament contacts, as illustrated in Fig. 5.8, thus this weaving is infinitely dilatant.

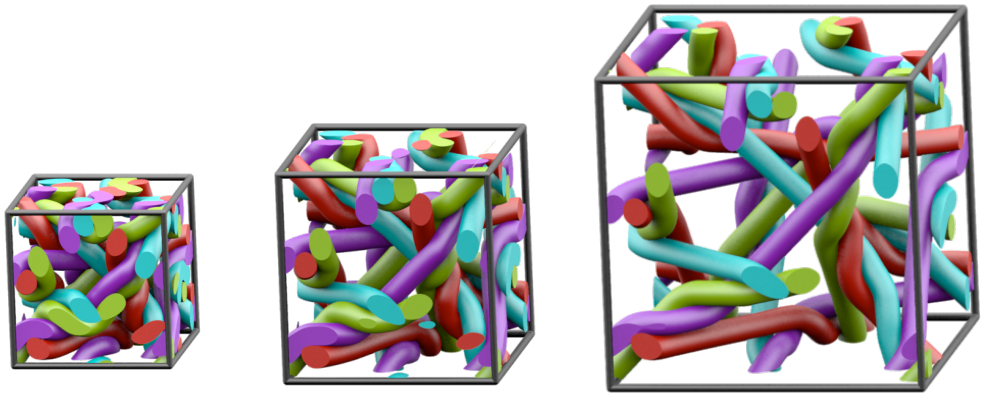

(a) **(b)** **(c)**

Figure 5.8: The ideal $G^{+}_{118C}(2)$ structure is infinitely dilatant. (a) The ideal unit cell. (b) A unit cell expansion sees the filaments remain in contact. (c) A further unit cell expansion also has all contacts preserved.

As a further example, consider the ideal $G^{-}_{118C}(2)$ structure, which is a woven variant of the Σ^{+} rod packing. We see from the consecutive unit cell expansions in Fig. 5.9 that all contacts are preserved through the expansions, and the packing is also infinitely dilatant.

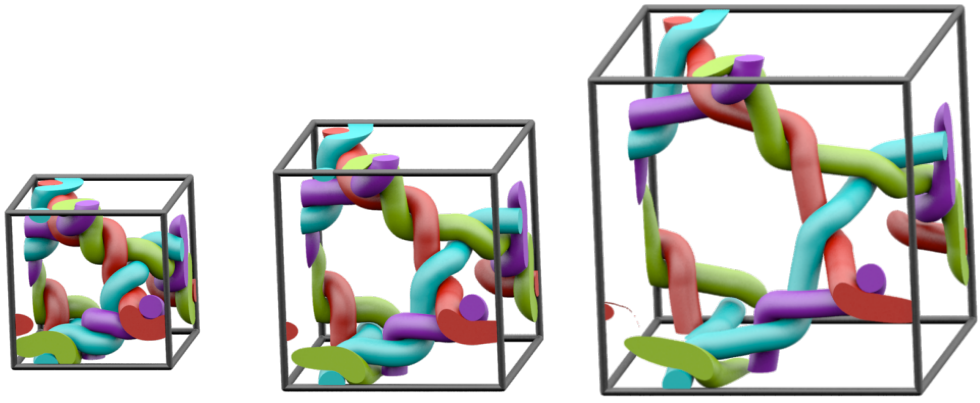

(a) **(b)** **(c)**

Figure 5.9: The ideal $G^{-}_{118C}(2)$ structure, which is a woven Σ^{+} rod packing, is infinitely dilatant. (a) The ideal unit cell. (b) A unit cell expansion sees the filaments remain in contact. (c) A further unit cell expansion also has all contacts preserved.

A formal definition of the rectification transformation for dilatant weavings runs as follows. We construct a one-parameter family of embeddings of weavings parametrised by the variable γ, which describes the fractional dilation. The initial tightest weaving is associated with $\gamma = 0$; the end-state of the dilation process, realised for the maximal configuration is realised when $\gamma = 1$. The magnitude of the dilatancy realised during the expansion process for a variety of weavings is listed in Table 5.1.

Table 5.1: Structural measurements for various structure, all normalised for unit cells of unit volume and fibres of radius R. All weavings are cubic, except $H_{31C}(1)$, which has hexagonal lattice parameters ($a = b = c = 1$; $\alpha = \beta = \frac{\pi}{2}$; $\gamma = \frac{\pi}{3}$). L is the total fibre length per unit cell; γ defines the ideal and maximal states. $f(\gamma)$ denotes the filament volume fraction. The dilatancy induced by fibre rectification is quantified by the fractional change in free and total volumes: Δ_{free} ($= \frac{V_{free}(\gamma_{max})}{V_{free}(0)}$) and Δ_{tot} ($= \frac{V_{tot}(\gamma_{max})}{V_{tot}(0)}$), where V_{free} and V_{tot} denote the free volume and the total unit cell volume respectively.

Structure	**straight?**	**class**	**cubic?**	γ	$R(\gamma)$	$L(\gamma)$	$f(\gamma)$	Δ_{free}	Δ_{tot}
$G^{+}_{123C}(2)$ (Γ)	$\surd$	non-dilatant	cubic	0	0.177	6.933	0.682	1	1
$H_{31C}(1)$	X (ideal)	dilatant (I)	trig.	0	0.181	4.444	0.525		
	$\surd$ (dilated)			1	0.115	4.243	0.204	4.330	2.581
G_{124C}	X (ideal)	”	cubic	0	0.181	6.466	0.662		
(Π^{+})	$\surd$ (dilated)			1	0.125	6	0.295	4.688	2.247
G_{129C}	X (ideal)	”	cubic	0	0.127	7.642	0.384		
(Σ^{+})	$\surd$ (dilated)			1	0.058	6.927	0.073	7.899	5.429
$G^{+}_{118C}(1)$	X (ideal)	dilatant (II)	cubic	0	0.073	18.082	0.303		
	$\surd$ (dilated)			1	0	16.965	0	∞	∞
$D_{118C}(1)$	X (ideal)	”	cubic	0	0.065	19.614	0.260		
	$\surd$ (dilated)			1	0	16.971	0	∞	∞
$G^{-}_{118C}(2)$	X (ideal)	dilatant (III)	cubic	0	0.075	10.714	0.189		
	X (dilated)			< 1	0.03	8.006	0.022	∞	∞
$G^{+}_{118C}(2)$	X (ideal)	”	cubic	0	0.066	29.074	0.398		
	X (dilated)			< 1	0.02	24.284	0.031	∞	∞

We allow only jammed configurations of the weavings during the dilation transformation, for which the number of inter-fibre contacts per unit cell is conserved. Note,

however, that if the fibre length per unit cell is reduced during dilation, the density of inter-fibre contacts per unit cell for outermost fragments of the weaving is reduced, due to this contraction. This variation leads to softening of the weaving rigidity, due to a dearth or excess of unsupported fibres in the corona. This effect is difficult to quantify, due to some flexibility in the fibre arrangement in the (unjammed) corona. A simple gauge is the number of contacts per unit length of the fibre, measured throughout the dilation process. Data are normalised against the G_{124C} weaving, that has the largest number of inter-fibre contacts per unit length of known weavings, whose number of fibre-fibre contacts is scaled to unity.

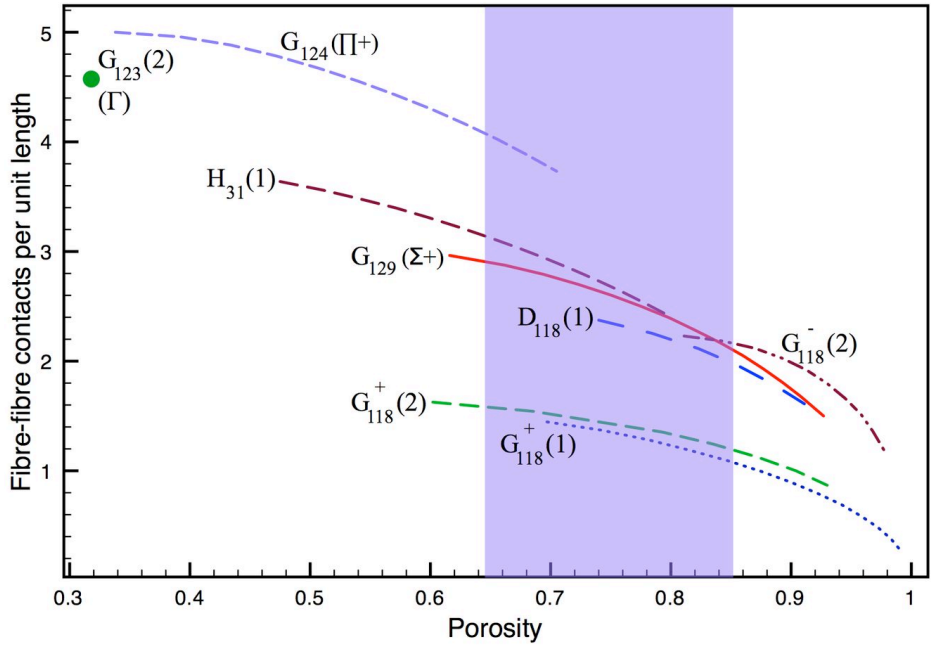

Figure 5.10: Plot of number of inter-filament contacts per unit length (for unit diameter bres) as a function of porosity for a non-dilatant weaving ($G_{123}(2)$) and some finite and infinitely dilatant examples. The shaded region indicates the range of porosities found in human corneocytes from least to most hydrated.

Dilation data for some of the 3D weavings in Table 5.1 are plotted in Fig. 5.10, which allows comparison of the rate of dilation, along with the range of porosities sustained by various weavings. These data reveal the very distinct character of various weavings. Infinitely dilatant weavings exhibit extraordinary dilation properties, however, this is achieved at the expense of significant reduction in the density of inter-fibre contacts. These cases are therefore expected to significantly soften on dilation, and finite volumes of these weavings are likely to unjam on swelling. It is also worth noting that these ex-

amples are less dense (for given porosity) than the finitely dilatant weavings, occupying a significantly larger total volume (for the same total fibre content).

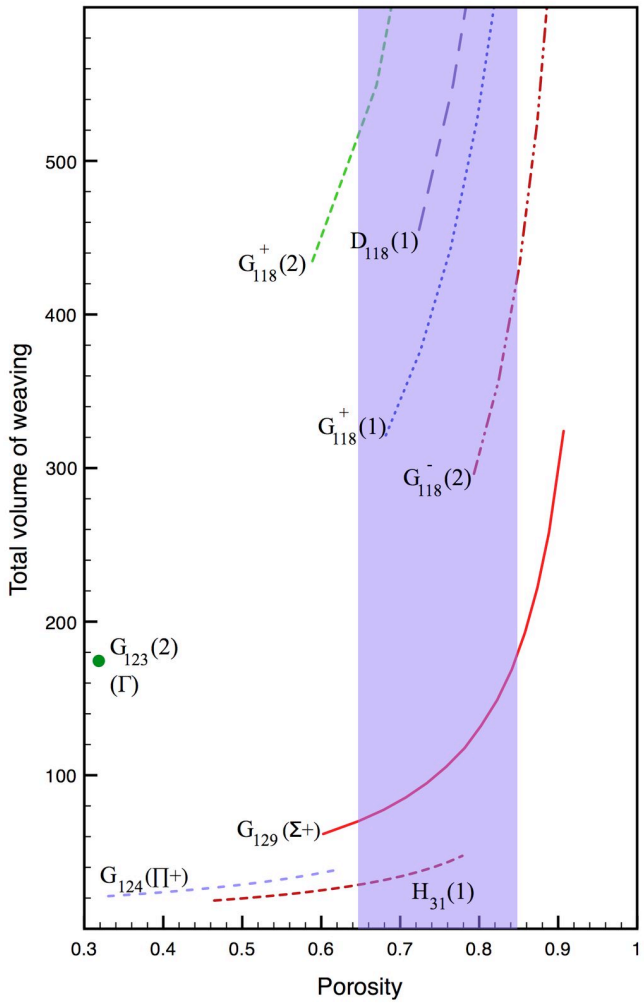

Figure 5.11: Dependence of total weaving volume per unit cell on porosity (where all bres are normalised to unit diameter) for a non-dilatant weaving ($G_{123}(2)$) and some finite and infinitely dilatant examples. The shaded region indicates the range of porosities found in human corneocytes from least to most hydrated.

Among the finitely dilatant weavings, we find significant variation in the material properties as a function of dilation. Two distinct regimes emerge, depending on the porosity of the dilated weavings. If the porosity is less than about 60%, the G_{124C} and $H_{31C}(1)$ weavings are the most compact, with the highest density of inter-fibre contacts. Above this porosity value (to ca. 93%, when the weaving is maximally dilated), dilated versions of the G_{129C} weaving affords the most compact weaving, with the highest density of inter-fibre contacts.

5.2 Keratin alignment in corneocytes

Given the remarkable combination of structural rigidity and variable porosity afforded by the G_{129C} weaving, it is worth looking for traces of the structure in natural materials. One material that necessarily combines these features is mammalian skin. Among its many functions is its homeostatic property on exposure to humidity or water: prolonged immersion in the bath will cause our skin to wrinkle due to swelling, yet this organ retains its structural integrity. The outermost "horny layer" (*stratum corneum*) of mammalian skin is composed of corneocytes, whose interior is dominated by the presence of arrays of helical keratin macrofibres [Brod 59]. On exposure to water, corneocytes can swell to many times their initial volume without significant degradation of the structural integrity of the stratum corneum [Norl 97], due to the uptake of bulk water, which occupies the fibre interstices, thereby reducing the fibre volume fraction [Norl 04]. On hydration, the corneocytes swell with little change in their total fibre content or keratin dimensions, though their helical pitch is likely to vary. In situ measurements of the hydration levels of corneocytes in human *stratum corneum* give average values varying between about 0.5 w/w [Casp 01] and 3 w/w [Bouw 03]. The stratum corneum is predominantly composed of keratin fibres, water and remnant lipids and various water-soluble substances (or 'natural moisturising factors', NMFs), including inorganics, amino acids, proteins and urea [Zhai 89]. Due to the water-binding facility of NMFs, and variation in the NMF contents and hydration within the stratum corneum, estimation of the fraction of keratin fibres within the stratum cornea is difficult to gauge precisely. Assuming densities of 1 gcm^3 for water and NMF and 1.25 gcm^3 for keratin, and a dry mass of about 80% w/w (i.e. NMFs comprise the other 20%) [Ecke 89], the hydration limits reported in [Casp 01, Bouw 03] correspond to keratin volume fractions between 15% and 35%.

The keratin fibres in the stratum corneum therefore form an array whose porosity is capable of varying between 65%-85% without loss of structural rigidity. Comparison of these data with those deduced for dilatant weavings are shown in Fig. 5.10. Evidently, the fibre weaving cannot change types during the hydration process, so a single weaving must span the complete range of porosities. Both the G_{129C} structure (Σ^+) and the $G^+_{118C}(2)$ weavings offer suitable arrangements of keratin fibres with dilatancy squarely within the estimated porosity range. The structure of the soft keratin Intermediate Filaments (IFs) that make up the fibrils as a function of hydration remains uncertain. However, dry fibrils of hard keratins are known to be helical, with pitch 470$\mathring{A}$ and diameter 74.5$\mathring{A}$ [Fras 86],

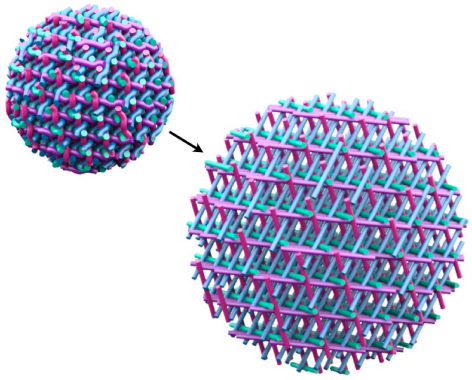

Figure 5.12: Porosity of the material increases as the filaments straighten cooperatively: A spherical section of the G_{129C} material in the tight configuration increases in porosity on straightening of the filaments. The result is the standard configuration of the Σ^+ rod packing.

giving a ratio of pitch to diameter of 6.3. Further, the structure of dry soft keratin IFs, comprising the stratum corneum, is likely to be similar [Fras 86].

The ideal $G^+_{118C}(2)$ weaving contains fibres whose geometry are complex modulated helices, with a simple axis, contrary to the structure of IFs. In contrast, the ideal G_{129C} (Σ^+) weaving is made of helical filaments (which are slightly triangular when projected along their axis, rather than the circular sections of ideal helices). Further, in their tightest configuration, corresponding to the dry state, the ratio of their pitch to fibre diameter is 6.8, close to that proposed by [Fras 86]. (Scaling the (tightest) G_{129C} weaving to give the measured pitch of 470$\mathring{A}$ implies a lattice parameter of about 550$\mathring{A}$ for the weaving.) The remarkable dilatancy of the G_{129C} weaving, which spans the measured porosity variations between dry and hydrated corneocytes, coupled with the agreement in helical dimensions in keratin IFs and the filament shape in the ideal chiral cubic weaving, suggest that keratin fibrils indeed weave within corneocytes according to the G_{129C} pattern. We suggest that the one-parameter family of 3D weavings related to the G_{129C} rod packing best describes the ideal arrangement of keratin fibres within individual corneocytes. Indeed, the G_{129C} rod packing affords a low density, rigid 3D weaving, whose economy makes it an ideal geometry for a biomaterial.

A qualitative picture of the hydration process according to this model runs as follows. Exposure to water induces the keratin fibres to unwind by sliding over each other, without compromising their structural rigidity imposed by their inter-fibre contacts. The number of point contacts per unit cell remains fixed, but they move along the fibres, thereby generating additional free volume accessible to the water. Cooperative unwinding occurs, re-

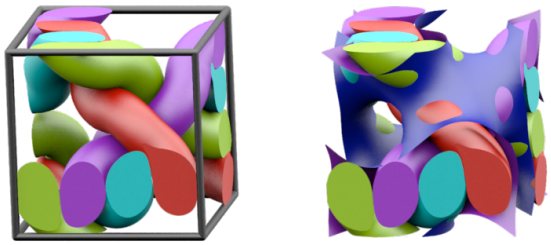

Figure 5.13: The ideal configuration of the G_{129C} structure lies to within a good approximation within a single labyrinth of the gyroid.

sulting in isotropic expansion of the corneocytes. We predict that swelling of corneocytes beyond the free volume accessible to the straightened rod packing will lead to dramatic weakening, since further swelling of the pattern can only occur by losing contacts between fibres, thereby diminishing the structural integrity of the corneocytes. Indeed, there is a limit to water uptake in skin, beyond which the stratum corneum loses its protective barrier [Will 73], (see shaded region in Figs. 5.10 and 5.11).

Evidently this Platonic idealisation of the actual process neglects a number of factors present in the stratum corneum. First, the layer is itself very anisotropic, since it is anchored to the next layer (*stratum lucidum*) on its inner side while its outer face is exposed to the atmosphere; additional structural anisotropy is caused by the pancake-shaped corneocytes. The overall expansion of the layer is therefore unlikely to be isotropic. Secondly, the inter-fibre contacts are probably extended over many atoms; nevertheless, it is likely that in the presence of water keratin fibres slide over each other readily. Finally, since the length per unit cell of fibres changes with swelling, if the total fibre length is conserved – as we expect it is – the total number of inter-fibre contacts diminishes on swelling. The combination of this effect with the changing fibre helicity is expected to induce a measurable variation in the rigidity of corneocytes with hydration, though they remain sterically jammed due to close-packing of the fibres.

It is noteworthy that the G_{129C} weaving is generated by a simple arrangement of geodesics in the gyroid TPMS, a particularly important structure, found in a variety of soft condensed materials, including membrane organelles *in vivo* [Land 95, Alms 06]. Recall also that the ideal configuration lies to within a good approximation within a single labyrinth of the gyroid (see Fig. 5.13). (Indeed, the ideal weaving is sufficiently porous to allow a second ideal weaving of the opposite hand G^{-}_{129C} to be threaded within the G^{+}_{129C}

patttern.) The relation of this weaving with the gyroid is likely more than coincidental. In pioneering structural studies of the *stratum corneum*, Norlén has noted the possible presence of lipid bilayers folded onto the gyroid surface within individual corneocytes and suggested that this geometry effectively templates an ordered arrangement of keratin fibres [Norl 04], corresponding to another weaving whose entanglements are those of the cubic Γ rod packing [OKee 05]. In contrast to the G_{129C} weaving, this pattern is achiral and relatively dense. The Γ embedding is not dilatant, hence the only route to increase the available free volume per unit cell is to lose inter-filament contacts which results in a loss of structural stability. It is noteworthy that despite his discussion of the Γ packing, Norlén suggested a chiral arrangement [Norl 04], consistent with the super-dilatant G_{129C} pattern.

Our model suggests that the corneocytes are formed *in vivo* via templating and collapse to one side of a lipid membrane folded into the gyroid, as proposed by Norlén. The expected lattice parameter for the gyroid, ca. 550$\mathring{A}$, is consistent with dimensions of cubic membranes found to date [Alms 06]. Since Nòrlen's initial proposal, chemical studies have revealed an identical mechanism for the formation of chiral inorganic networks in synthetic mesoporous materials [Ryoo 99, Tera 02]. Most recently, the presence of a chiral, cubic photonic crystal composed of chitin has been established in the wing-scales of certain species of butterflies, leading to structural colour [Mich 08, Sara 10]. Indeed, the chitin network is very similar to the geometry of the keratin fibres, though chitin forms a consolidated network (and resists swelling), in contrast to the individual keratin fibres in the stratum corneum. *Prima facie*, the structural likeness may suggest evolutionary convergence. However, it is most likely that the correspondence of morphology between mammalian skin and butterfly wings is driven by the ubiquity of the gyroid pattern in folded membranes *in vivo*, since both materials are likely templated by a lipid membrane.

Can the extraordinary material properties of mammalian skin be mimicked *in vitro*? Our understanding of the genesis of skin via lipid membrane templating suggests a route to formulate synthetic 3D filament weavings at the macromolecular scale, via templating within bicontinuous molecular mesophases. In addition, the suite of examples of 3D weavings discussed in this paper suggest that this route is a realistic one to generate weavings of various types, from dilatant examples to their conventional counterparts. Evidently, 3D weavings of one-dimensional filaments offer a wealth of distinct material responses as a function of filament geometry.

Chapter 6

Conclusion

In this thesis, we constructed novel, 3-periodic weavings and nets, then tightened them to an "ideal" shape in order to give geometric inspiration to the many disciplines of science influenced by structure. We used a set of Triply-Periodic Minimal Surfaces (TPMS) as a scaffold for their construction. These structures were engineered as tilings of the two dimensional hyperbolic plane ($\mathbb{H}^2$) to harness the simplicity of a two-dimensional surface as compared with 3D space.

To begin, we have developed a catalogue of simple, high symmetry "free" tilings of $\mathbb{H}^2$, which contains examples with both branched tile edges and infinite geodesic tile edges. Furthermore, we have embedded these tilings so as to be candidates for reticulation over the TPMS. For the Stellate orbifolds, we saw that an infinite set of embeddings are possible for a single free tiling, which leads to an infinite set of structures on each of the TPMS. As the embeddings in $\mathbb{H}^2$ become more oblique in shape, the structures that result in $\mathbb{E}^3$ become more entangled in nature.

Further, we constructed an array of 3-periodic structures relevant to the natural sciences. The nets that we constructed are, in most cases, multiple-component interpenetrating nets. Such nets arise frequently in synthetic chemical frameworks [Batt 98, OKee 00], and we generate additional, more complex examples of such nets as possible targets for synthesis. In the construction process, importance is placed on the edge geometry and ambient isotopy class of the net, not simply the topology as is the case for other enumerative techniques. Further, the 3-periodic weavings of filaments constructed in this thesis are, in the simplest cases, well recognised rod packings. Through the TPMS reticulation method, we are able to generalise the notion of a rod packing to contain curvilinear as well as rectilinear fibres, which enables the construction of a more complete taxonomy of 3-periodic weavings. A catalogue of 3-periodic entanglements of infinite filaments is certainly missing from the current literature, and these new structures may provide insight

into weavings of polymers, proteins and DNA.

This thesis has described an extension of the **SONO** algorithm for tightening knots and links: the **PB-SONO** algorithm tightens branched and periodic entanglements. We saw that it performs comparably with the **SONO** algorithm for the tightening of knots. Further, we tightened entangled θ-, tetrahedron- and cube- graphs, which were very accurate for the simplest entanglements (and gave results close to as expected).

We saw "tight" configurations for many periodic nets. The addition of periodicity yielded the uniform embedding as described by the SyStRe algorithm for single component nets. Further, the **PB-SONO** algorithm was able to find a canonical form for nets that have vertex and edge collisions in the SyStRe embedding, as well as a canonical form for non-crystallographic nets. The algorithm handles the interpenetration of multiple component nets in a very intuitive way. The examples shown are convincing evidence that the tight configuration found by the **PB-SONO** algorithm is a very useful tool in analysing geometry and ambient isotopy class of 3-periodic entangled nets, and is applicable to a larger class of structures than have been previously analysed. Evidence of the relevance of the ideal embeddings of nets comes from the ideal structure of two interpenetrating **srs** nets of equivalent chirality, which has equivalent geometry to that given by the crystallographic data for a synthesised framework containing these components. Thus the ideal embedding somehow replicates the conditions within this real chemical framework. The challenge of this method, however, is the numerical error associated with finding these ideal configurations.

An interesting consequence of the idealisation of rod packings to optimal configurations is the geometry of the filaments is helical. Often the geometry prescribed by the idealisation is equivalent to the geometry as the weavings sits on the TPMS, which gives encouragement to the reticulation method of obtaining filament geometry. The helical geometry of some some rod packings in their ideal configurations leads to the exotic physical property of dilatancy.

The consequences of dilatant weavings are immense. These structures are attractive design targets for new synthetic materials, stemming from the potent increases in the free volume of the material on straightening of the filaments, while maintaining structural stability of the material. As a bio-material, this beautiful property in the ideal G_{129C} weaving gives an explanation for the keratin organisation in the corneocytes of the stratum corneum layer of the skin. The dilatancy of the keratin matrix allows us to explain the remarkable structural rigidity of the skin during the uptake of water and subsequent swelling of the

skin. The ramifications of understanding the keratin organisation are immense: the barrier properties of the skin are important in many areas of the medical and therapeutic sciences, and are strongly related to the structural form of the layers within skin.

The scope for further enumeration of more structures of this kind is large. The free tilings of $\mathbb{H}^2$ that have been considered here are a tiny set of the possible tilings of this kind. Firstly, the tiling considered were all of very high symmetry, thus there is scope to extend to lower symmetry groups of $\mathbb{H}^2$. Further, one may consider more oblique embeddings of the free tilings when embedding to be commensurate with the TPMS. We may also generalise further to tilings commensurate with other TPMS of higher genus and also to free tilings which contain both branched boundary components and infinite geodesic boundary components, which will give packings of nets and filaments in unison of the TPMS. In considering only the simplest free tilings on the simplest TPMS, we were able to identify a wealth of interesting structure, and we predict that many more interesting structures will come from further enumeration. We saw that the ideal conformation of a structure often relates to a TPMS reticulation, which gives further encouragement of what we might find on further enumeration of reticulations of these surfaces.

An obvious application of this work is in new materials made from long tangled filaments. For such materials, the dilatancy property discussed may have significant influence in material functionality. Further to this, knowledge of these structures may assist in identifying them in naturally occurring settings, particularly in biological systems. Furthermore, we consider the interesting photonic crystal property of the chitin network in butterfly wings, which is chiral and fills one channel of the gyroid, as described in [Saba 11]. Perhaps a similar effect is present in the chiral keratin arrangement in the skin, which also fills one channel of the gyroid minimal surface. Given a suitable length scale, it may give a partial reflection of the ultra violet spectrum of light, and further act as a natural sunscreen? We saw that many of the 3-periodic weavings displayed both chiral and dilatant properties, which may lead to materials with an interesting fusion of optical and material properties.

Bibliography

[Alms 06] Z. A. Almsherqi, S. D. Kohlwein, and Y. Deng. "Cubic membranes: a legend beyond the flatland of cell membrane organization". *J Cell Biol*, Vol. 173, pp. 839–844, 2006.

[Bage 64] F. Bagemihl. "Analytic continuation and the schwarz reflection principle". *Proc Natl Acad Sci U S A*, Vol. 51, pp. 378–380, 1964.

[Batt 98] S. R. Batten and R. Robson. "Interpenetrating nets: ordered, periodic entanglement". *Angew Chem Int Ed*, Vol. 37, pp. 1460–1494, 1998.

[Bear 95] A. F. Beardon. *The geometry of discrete groups*. Springer-Verlag New York Inc., 1995.

[Blat 06] V. A. Blatov. "Multipurpose crystallochemical analysis with the program package TOPOS". *IUCr CompComm Newsl*, Vol. 7, pp. 4–38, 2006.

[Bouw 03] J. A. Bouwstra, A. de Graaff, G. S. Gooris, J. Nijsse, J. W. Wiechers, and A. C. van Aelst. "Water distribution and related morphology in human stratum corneum at different hydration levels". *J Invest Dermatol*, Vol. 120, pp. 750–758, 2003.

[Brod 59] I. Brody. "The keratinization of epidermal cells of normal guinea pig skin as revealed by electron microscopy". *J Ultrastruc Res*, Vol. 2, pp. 482–511, 1959.

[Buck] G. Buck and J. Simon. "The unified theory of filament entanglement". http://www.gregorybuck.com/pages/pdfs.html.

[Buck 07] G. R. Buck and J. K. Simon. "Total curvature and packing of knots". *Topol Appl*, Vol. 154, pp. 192 – 204, 2007.

[Buck 08] G. Buck, R. G. Scharein, J. Schnick, and J. Simon. "Accessibility and occlusion of biopolymers, ray tracing of radiating tubes, and the temperature of a tangle". *Phys Rev E*, Vol. 77, p. 011803, 2008.

[Buck 93] G. Buck and J. Orloff. "Computing canonical conformations for knots". *Topol Appl*, Vol. 51, pp. 247–253, 1993.

[Buck 95] G. Buck and J. Orloff. "A simple energy function for knots". *Topol Appl*, Vol. 61, pp. 205–214, 1995.

[Buck 98] G. Buck. "Four-thirds power law for knots and links". *Nature*, Vol. 392, pp. 238 – 239, 1998.

[Byrn 08] P. Byrne, G. O. Lloyd, N. Clarke, and J. W. Steed. "A "compartmental" borromean weave coordination polymer exhibiting saturated hydrogen bonding to anions and water cluster inclusion". *Angew Chem*, Vol. 47(31), pp. 5761–5764, 2008.

[Carl 03a] L. Carlucci, G. Ciani, and D. M. Proserpio. "Borromean links and other non-conventional links in polycatenated coordination polymers: re-examination of some puzzling networks". *CrystEngComm*, Vol. 5(47), pp. 269–279, 2003.

[Carl 03b] L. Carlucci, G. Ciani, D. M. Proserpio, and S. Rizzato. "New architectures from the self-assembly of MIISO4 salts with bis(4-pyridyl) ligands. The first case of polycatenation involving three distinct sets of 2D polymeric (4,4)-layers parallel to a common axis". *CrystEngComm*, Vol. 5, pp. 190–199, 2003.

[Carl 03c] L. Carlucci, G. Ciani, and D. M. Proserpio. "Polycatenation, polythreading and polyknotting in coordination network chemistry". *Coord Chem Rev*, Vol. 246, pp. 247 – 289, 2003.

[Carl 99] L. Carlucci, G. Ciani, P. Macchi, D. M. Proserpio, and S. Rizzato. "Complex interwoven polymeric frames from the self-assembly of silver(I) cations and sebaconitrile". *Chem Eur J*, Vol. 5(1), pp. 237–243, 1999.

[Casp 01] P. J. Caspers, G. W. Lucassen, E. A. Carter, H. A. Bruining, and G. J. Puppels. "In vivo confocal raman microspectroscopy of the skin: noninvasive determination of molecular concentration profiles". *J Invest Dermatol*, Vol. 116, pp. 434–442, 2001.

[Cast 08] T. Castle, M. E. Evans, and S. T. Hyde. "Ravels: knot-free but not free. Novel entanglements of graphs in 3-space". *New J Chem*, Vol. 32, pp. 1484–1492, 2008.

[Cast 11a] T. Castle, M. E. Evans, and S. T. Hyde. "Entanglement of embedded graphs". *Prog Theor Phys Supp*, 2011. In press, available at http://people.physics.anu.edu.au/~sth110/Kyoto_tangle_submit_red.pdf.

[Cast 11b] T. Castle, V. Robins, and S. T. Hyde. "Toroidal entangled polyhedral graphs: Tetrahedra, octahedra and cubes". 2011. In preparation.

[Char 85] J. Charvolin. "Crystals of interfaces: the cubic phases of amphiphile/water systems". *J. Phys. Paris*, Vol. 46(C3), pp. 173–190, 1985.

[Chen 01] B. Chen, M. Eddaoudi, S. Hyde, M. O'Keeffe, and O. M. Yaghi. "Interwoven metal-organic framework on a periodic minimal surface with extra-large pores". *Science*, Vol. 291, pp. 1021 – 994, 2001.

[Chun 84] S. J. Chung, T. H. Hahn, and W. E. Klee. "Nomenclature and generation of three-periodic nets: the vector method". *Acta Cryst*, Vol. A40, pp. 42 – 50, 1984.

[Conw 02] J. H. Conway and D. H. Huson. "The orbifold notation for two-dimensional groups". *Struct Chem*, Vol. 13, pp. 247 – 257, August 2002.

[Conw 08] J. H. Conway, H. Burgiel, and C. Goodman-Strauss. "Generalized schläfli symbols". In: *The symmetries of things*, Chap. 20, pp. 269–282, A K Peters Ltd., 2008.

[Conw 67] J. H. Conway. "An enumeration of knots and links, and some of their algebraic properties". In: J. Leech, Ed., *Computation Problems in Abstract Algebra*, pp. 329 – 358, Pergamon Press, Oxford, England, 1967.

[Conw 92] J. Conway. *Groups, combinatorics and geometry*. *London Mathematical Society Lecture Note Series 165*, Cambridge University Press: Cambridge, 1992.

[Coxe 47a] H. S. M. Coxeter. *Non-euclidean geometry*. University of Toronto Press, Toronto, 1947.

[Coxe 47b] H. S. M. Coxeter. *Regular polytopes*. Methuen and Co., 1947.

[Coxe 72] H. S. M. Coxeter and W. O. J. Moser. *Generators and relations for discrete groups*. Springer-Verlag, Berlin, 1972.

[Crom 04] P. Cromwell. *Knots and links*. Cambridge University Press, 2004.

[Delg] O. Delgado-Freidrichs. "Generation, Analysis and Visualization of Reticular Ornaments using GAVROG". available at http://www.gavrog.com.

[Delg 02] O. Delgado-Friedrichs, M. OKeeffe, and O. M. Yaghi. "Three-periodic nets and tilings: regular and quasiregular nets". *Acta Cryst*, Vol. A59, pp. 22–27, 2002.

[Delg 03a] O. Delgado-Friedrichs. "Data structures and algorithms for tilings I". *Theor Comput Sci*, Vol. 303, pp. 431 – 445, 2003.

[Delg 03b] O. Delgado-Friedrichs and M. O'Keeffe. "Identification of and symmetry computation for crystal nets". *Acta Cryst*, Vol. A59, pp. 351 – 361, 2003.

[Dier 92] U. Dierkes, S. Hildebrandt, and F. Sauvigny. *Minimal surfaces*. Vol. 339 of *A series of Comprehensive Studies in Mathematics*, Springer-Verlag, 1992.

[Dioa 98] Y. Dioa, C. Ernst, and E. J. V. Rensburg. "Knots with minimal energies". In: A. Stasiak, V. Katritch, and L. H. Kauffman, Eds., *Ideal Knots*, pp. 52 – 69, World Scientific, 1998.

[Dobr 05] L. Dobrzanska, H. G. Raubenheimer, and L. J. Barbour. "Borromean sheets assembled by self-supporting argentophilic interactions". *Chem Commun*, p. 5050, 2005.

[Doma 05] K. V. Domasevitch, I. Boldog, E. B. Rusanov, J. Hunger, S. Blaurock, M. Schröder, and J. Sieler. "Helical bipyrazole networks conditioned by hydrothermal crystallization". *Z Anorg Allg Chem*, Vol. 631, pp. 1095–1100, 2005.

[Dres 87] A. W. M. Dress. "Presentations of discrete groups, acting on simply connected manifolds, in terms of parametrized systems of Coxeter matrices - a systematic approach". *Adv Math*, Vol. 63, pp. 196 – 212, 1987.

[Ecke 89] R. Eckert. "Structure, function and differentiation of the keratinocyte". *Physiol Rev*, Vol. 69, pp. 1316–1345, 1989.

[Eon 05] J.-G. Eon. "Graph-theoretical characterization of periodicity in crystallographic nets and other infinite graphs". *Acta Cryst*, Vol. A61, pp. 501–511, 2005.

[Eon 11] J.-G. Eon. "Euclidian embeddings of periodic nets: definition of a topologically induced complete set of geometric descriptors for crystal structures". *Acta Cryst*, Vol. A67, pp. 68–86, 2011.

[Fogd 92] A. Fogden and S. T. Hyde. "Parametrisation of triply periodic minimal surfaces. 2. Regular class solutions". *Acta Cryst*, Vol. A48, pp. 575 – 591, 1992.

[Fran 99] G. K. Francis and J. R. Weeks. "Conway's ZIP proof". *Am Math Mon*, Vol. 106, No. 5, pp. 393–399, 1999.

[Fras 86] R. D. Fraser, T. P. MacRae, D. A. Parry, and E. Suzuki. "Intermediate filaments in alpha-keratins". *Proc Natl Acad Sci U S A*, Vol. 83, pp. 1179–1183, 1986.

[Gros 92] J. L. Gross and T. W. Tucker. *Topological graph theory*. Dover Publications, 1992.

[Grze 97] R. P. Grzeszczuk, M. Huang, and L. H. Kauffman. "Physically-based stochastic simplication of mathematical knots". *IEEE T Vis Comput Gr*, Vol. 3(3), pp. 262–272, 1997.

[Hilb 52] D. Hilbert and S. Cohn-Vossen. *Geometry and the imagination*. Chelsea Publishing Group, 1952.

[Huso 93] D. H. Huson. "The generation and classification of tile-k-transitive tilings on the Euclidean plane, sphere, and hyperbolic plane.". *Geometriae Dedicata*, Vol. 47, pp. 295 – 310, 1993.

[Hyde 00a] S. T. Hyde and C. Oguey. "From 2D hyperbolic forests to 3D Euclidean entangled thickets". *Eur Phys J B*, Vol. 16 (2000), pp. 613 – 630, 2000.

[Hyde 00b] S. T. Hyde and S. J. Ramsden. "Chemical frameworks and hyperbolic tilings". In: P. Hansen, P. Fowler, and M. Zheng, Eds., *Discrete Mathematical Chemistry*, pp. 203 – 224, American Mathematical Society, 2000.

[Hyde 00c] S. T. Hyde and S. J. Ramsden. "Polycontinuous morphologies and interwoven helical networks". *Europhys Lett*, Vol. 50, pp. 135 – 141, 2000.

[Hyde 03a] S. T. Hyde, A. K. Larsson, T. D. Matteo, S. J. Ramsden, and V. Robins. "Meditation on an Engraving of Fricke and Klein (The Modular Group and Geometrical Chemistry)". *Aust J Chem.*, Vol. 56, pp. 981 – 1000, 2003.

[Hyde 03b] S. T. Hyde, S. Ramsden, T. D. Matteo, and J. J. Longdell. "Ab-initio construction of some crystalline 3D Euclidean networks". *Solid State Sci*, Vol. 5 (2003), pp. 35 – 45, 2003.

[Hyde 03c] S. T. Hyde and S. J. Ramsden. "Some novel three-dimensional euclidean crystalline networks derived from two-dimensional hyperbolic tilings". *Eur Phys J B*, Vol. 31, pp. 273 – 284, 2003.

[Hyde 06] S. T. Hyde, O. D. Friedrichs, S. J. Ramsden, and V. Robins. "Towards enumeration of crystalline frameworks: the 2D hyperbolic approach". *Solid State Sci*, Vol. 8, pp. 740 – 752, 2006.

[Hyde 07] S. T. Hyde and G. Schröder-Turk. "Tangled (up in) cubes". *Acta Cryst*, Vol. A63, pp. 186–197, 2007.

[Hyde 10] S. T. Hyde, V. Robins, and S. J. Ramsden. "Epinet". http://epinet.anu.edu.au, 2010.

[Hyde 11] S. T. Hyde, S. J. Ramsden, and V. Robins. "A topological approach to two-dimensional crystallography: orbifolds". *in preparation*, 2011.

[Hyde 84] S. T. Hyde and S. Andersson. "A systematic net description of saddle polyhedra and periodic minimal surfaces". *Z Kristallogr*, Vol. 168, pp. 221 – 254, 1984.

[Hyde 91] S. T. Hyde. "Hyperbolic surfaces in the solid-state and the structure of ZSM-5 zeolites". *Acta Chem Scand*, Vol. 45, pp. 860 – 863, 1991.

[Hyde 93] S. T. Hyde. "Crystalline frameworks as hyperbolic films". In: J. Boland and J. D. FitzGerald, Eds., *Defects and processes in the solid state: Geoscience applications*, Elsevier, Amsterdam, 1993.

[Hyde 97] S. T. Hyde, S. Andersson, K. Larsson, Z. Blum, T. Landh, S. Lidin, and B. W. Ninham. *The language of shape: the role of curvature in condensed matter: physics, chemistry and biology*. Elsevier Science B.V., 1997.

[Hyde 99] S. T. Hyde and S. J. Ramsden. "Crystals. Two-dimensional non-euclidean geometry and topology". In: D. Bonchev and D. Rouvray, Eds., *Chemical Topology: Applications and Techniques*, pp. 35 – 174, Gordon and Breach Science Publishers, N.Y., 1999.

[Jang 09] J.-J. Jang, L. Li, T. Yang, D.-B. Kuang, W. Wang, and C.-Y. Su. "Self-assembly of 2D borromean networks through hydrogen-bonding recognition". *Chem Commun*, pp. 2387–2389, 2009.

[Kabl 07] A. Kabla and L. Mahadevan. "Nonlinear mechanics of soft fibre networks". *J. R. Soc. Interface*, Vol. 4(12), pp. 99–106, 2007.

[Katr 96] V. Katritch, J. Bednar, D. Michoud, R. G. Scharein, J. Dubochet, and A. Stasiak. "Geometry and physics of knots". *Nature*, Vol. 384, pp. 142–145, 1996.

[Kepe 00] C. J. Kepert, T. J. Prior, and M. J. Rosseinsky. "A versatile family of interconvertible microporous chiral molecular frameworks: the first example of ligand control of network chirality". *J Am Chem Soc*, Vol. 122, pp. 5158–5168, 2000.

[Kepe 98] C. J. Kepert and M. J. Rosseinsky. "A porous chiral framework of coordinated 1,3,5–benzenetricarboxylate: quadruple interpenetration of the (10,3)-a network". *Chem Commun*, pp. 31–32, 1998.

[Kirk 84] S. Kirkpatrick, C. D. Gelatt, and M. P. Vecchi. "Optimization by simulated annealing". *Science*, Vol. 220, pp. 671–680, 1984.

[Klee 04] W. Klee. "Crystallographic nets and their quotient graphs". *Cryst Res Technol*, Vol. 39, pp. 959–968, 2004.

[Koch 99] E. Koch and W. Fischer. "Sphere packings and packings of ellipsoids". In: *International Tables for Crystallography, Vol. C (Second revised edition)*, pp. 738 – 743, Kluwer Academic Publishers, 1999.

[Kusn 97] R. B. Kusner and J. M. Sullivan. *Geometric Topology*. AMS/International Press, Cambridge, MA, 1997.

[Land 95] T. Landh. "From entangled membranes to eclectic morphologies – cubic membranes as subcellular space Organisers". *FEBS Lett*, Vol. 369(1), pp. 13–17, 1995.

[Laur 98] B. Laurie. "Annealing ideal knots and links: methods and pitfalls". In: A. Stasiak, V. Katritch, and L. H. Kauffman, Eds., *Ideal Knots*, pp. 42 – 51, World Scientific, 1998.

[Lezn 01] D. B. Leznoff, B.-Y. Xue, R. J. Batchelor, F. W. B. Einstein, and B. O. Patrick. "Gold/gold interactions as crystal engineering design elements in heterobimetallic coordination polymers". *Inorg Chem*, Vol. 40(23), p. 60266034, 2001.

[Li 07] J. Li, L. Song, and S. Du. "A novel borromean (6, 3) net assembled by nest-shaped clusters WOS3Cu3 as knots". *Inorg Chem Commun*, Vol. 10(3), pp. 358–361, 2007.

[Li 11] F. Li, J. K. Clegg, L. F. Lindoy, R. B. Macquart, and G. V. Meehan. "Metallosupramolecular Self-Assembly of a Universal 3-Ravel". *Nat Commun*, 2011. In press.

[Lian 03] R. Liantonio, P. Metrangolo, T. Pilati, and G. Resnati. "Fluorous interpenetrated layers in a three-component crystal matrix". *Cryst Growth Des*, Vol. 3(3), p. 355361, 2003.

[Lian 06] R. Liantonio, P. Metrangolo, F. Meyer, T. Pilati, W. Navarrini, and G. Resnati. "Metric engineering of supramolecular Borromean rings". *Chem Commun*, p. 1819, 2006.

[Lord 06] E. A. Lord, A. L. Mackay, and S. Ranganthan. *New geometries for new materials*. Cambridge University Press, 2006.

[Lu 06] X.-Q. Lu, M. Pan, J.-R. He, Y.-P. Cai, B.-S. Kang, and C.-Y. Su. "Three-fold parallel interlocking of 2-D brick-wall networks showing ladder-like unsymmetrical borromean links". *CrystEngComm*, Vol. 8(8), p. 827, 2006.

[Mari 00] A. Maritan, C. Micheletti, A. Trovato, and J. Banavar. "Optimal shapes of compact strings". *Nature*, Vol. 406, pp. 287 – 288, 2000.

[Men 09] Y.-B. Men, J. Sun, Z.-T. Huang, and Q.-Y. Zheng. "Rational construction of 2D and 3D borromean arrayed organic crystals by hydrogen-bond-directed self-assembly". *Angew Chem*, Vol. 48(16), pp. 2873–2876, 2009.

[Mich 08] K. Michielsen and D. G. Stavenga. "Gyroid cuticular structures in butterfly wing scales: biological photonic crystals". *J. R. Soc. Interface*, Vol. 5, pp. 85–94, 2008.

[Moln 02] E. Molnar. "On triply periodic minimal balance surfaces". *Struct Chem*, Vol. 13, pp. 267–275, 2002.

[Mori 04] H. Moriuchi. "An enumeration of theta-curves with up to seven crossings, Proceedings of the East Asian School of Knots, Links and Related Topics". 2004. Available at knot.kaist.ac.kr/2004/proceedings.php.

[Muth 02] S. Muthu, J. H. K. Yip, and J. J. Vittal. "Coordination networks of Ag(I) and N,N- bis(3-pyridinecarboxamide)-1,6-hexane: structures and anion exchange". *J Chem Soc, Dalton Trans*, p. 4561, 2002.

[Norl 04] L. Norlén and A. Al-Amoudi. "Stratum corneum keratin structure, function, and formation: the cubic rod-packing and membrane Templating Model". *J Invest Dermatol*, Vol. 123, pp. 715–732, 2004.

[Norl 97] L. Norlén, A. Emilson, and B. Forslind. "Stratum corneum swelling. Biophysical and computer assisted quantitative assessments". *Arch Dermatol Res*, Vol. 289, pp. 506–513, 1997.

[OKee 00] M. O'Keeffe, M. Eddaoudi, H. Li, T. Reineke, and O. M. Yaghi. "Frameworks for extended solids: geometry design principles". *J Solid State Chem*, Vol. 152, pp. 3–20, 2000.

[OKee 01] M. O'Keeffe, J. Plevert, Y. Teshima, Y. Watanabe, and T. Ogama. "The invariant cubic rod (cylinder) packings: symmetries and coordinates". *Acta Cryst*, Vol. A57, pp. 110–111, 2001.

[OKee 05] M. O'Keeffe. "Rod packings and metal-organic frameworks constructed from rod-shaped secondary building units". *J Amer Chem Soc*, Vol. 127(5), pp. 1504–1518, 2005.

[OKee 08] M. O'Keeffe, M. A. Peskov, S. J. Ramsden, and O. Yaghi. "The reticular chemistry structure resource (RCSR) database of, and symbols for, crystal Nets". *Accts Chem Res*, Vol. 41, pp. 1782–1789, 2008.

[OKee 96] M. O'Keeffe and B. G. Hyde. *Crystal structures I. Patterns and symmetry*. Mineralogical Society of America, 1996.

[Olse 10] K. Olsen and J. Bohr. "The generic geometry of helices and their close-packed structure". *Theor Chem Acc*, Vol. 125, pp. 207 – 215, 2010.

[OHa 91] J. OHara. "Energy of a knot". *Topology*, Vol. 30(2), pp. 241–247, 1991.

[Pier 98] P. Pieranski. "In search of ideal knots". In: A. Stasiak, V. Katritch, and L. H. Kauffman, Eds., *Ideal Knots*, pp. 20 – 41, World Scientific, 1998.

[Przy 01] S. Przybyl and P. Pieranski. "Helical close packing of ideal ropes". *Eur Phys J E*, Vol. 4(4), pp. 445 – 449, 2001.

[Rams 09] S. J. Ramsden, V. Robins, and S. T. Hyde. "Three-dimensional euclidean nets from two-dimensional hyperbolic tilings: kaleidoscopic examples". *Acta Cryst*, Vol. A65, pp. 81–108, 2009.

[Robi 04a] V. Robins, S. J. Ramsden, and S. T. Hyde. "2D hyperbolic groups induce three-periodic euclidean reticulations". *Eur Phys J B*, Vol. 39, pp. 365 – 375, 2004.

[Robi 04b] V. Robins, S. J. Ramsden, and S. T. Hyde. "Symmetry groups and reticulations of the hexagonal H surface". *Physica A*, Vol. 339, pp. 173–180, 2004.

[Robi 05] V. Robins, S. J. Ramsden, and S. T. Hyde. "A note on the two symmetry-preserving covering maps of the gyroid minimal surface". *Eur Phys J B*, Vol. 48, pp. 107–111, 2005.

[Ryoo 99] R. Ryoo, S. H. Joo, and S. Jun. "Synthesis of highly ordered carbon molecular sieves via template–mediated structural transformation". *J Phys Chem B*, Vol. 103, p. 7743, 1999.

[Saba 11] M. Saba, M. Thiel, M. D. Turner, S. Hyde, M. Gu, K. Grosse-Brauckmann, D. N. Neshev, K. Mecke, and G. E. Schröder-Turk. "Circular dichroism in biological photonic crystals and cubic chiral nets". *Phys Rev Lett*, 2011. in press.

[Sado 89] J. F. Sadoc and J. Charvolin. "Infinite periodic minimal surfaces and their crystallography in the hyperbolic plane". *Acta Cryst*, Vol. A45, pp. 10 – 20, 1989.

[Sado 90] J. F. Sadoc. *Geometry in condensed matter physics*. Vol. 9 of *Directions in condensed matter physics*, World Scientific, 1990.

[Sara 10] V. Saranathan, C. O. Osuji, S. G. J. Mochrie, H. Noh, S. Narayanan, A. Sandy, E. R. Dufresne, and R. O. Prum. "Structure, function, and self-assembly of single network gyroid ($I4_132$) photonic crystals in butterfly wing scales". *Proc Natl Acad Sci U S A*, Vol. 107(26), pp. 11676–11681, 2010.

[Scha 98] R. G. Scharein. *Interactive topological drawing*. PhD thesis, Department of Computer Science, The University of British Columbia, 1998.

[Scho 70] A. H. Schoen. "Infinite periodic minimal surfaces without self-intersections". *NASA Technical Note*, Vol. TN D-5541, 1970.

[Shar 00] C. V. K. Sharma, R. J. Diaz, A. J. Hessheimer, and A. Clearfield. "Double stranded chains and interwoven structures: the role of conformational isomerism in coordination polymers". *Cryst Eng*, Vol. 3(3), pp. 201–208, 2000.

[Simo 09] J. Simon. "Long tangled filaments". In: D. Buck and E. Flapan, Eds., *Applications of knot theory*, pp. 155 – 181, American Mathematical Society, 2009.

[Simo 94] J. K. Simon. "Energy functions for polygonal knots". *J Knot Theor Ramif*, Vol. 3(3), pp. 299–320, 1994.

[Spiv 79] M. Spivak. *A comprehensive introduction to differential geometry*. Vol. 5, Publish or Perish Inc., 1979.

[Stas 98] A. Stasiak, J. Dubochet, V. Katritch, and P. Pieranski. "Ideal knots and their relation to the physics of real knots". In: A. Stasiak, V. Katritch, and L. H. Kauffman, Eds., *Ideal Knots*, pp. 1 – 19, World Scientific, 1998.

[Stil 87] J. Stillwell. *Geometry of surfaces*. Springer-Verlag, 1987.

[Suh 03] M. P. Suh, H. J. Choi, S. M. So, and B. M. Kim. "A new metal-organic open framework consisting of threefold parallel interwoven (6,3) nets". *Inorg Chem*, Vol. 42(3), p. 676678, 2003.

[Tera 02] O. Terasaki, Z. Liu, T. Ohsuna, H. J. Shin, and R. Ryoo. "Electron microscopy study of novel Pt nanowires synthesized in the spaces of silica mesoporous materials". *Microsc Microanal*, Vol. 8, pp. 35–39, 2002.

[Thur 80] W. Thurston. *The geometry and topology of three-manifolds*. Princeton University: Princeton, New Jersey, 1980.

[Tong 99] M.-L. Tong, X.-M. Chen, B.-H. Ye, and L.-N. Ji. "Self-assembled three-dimensional coordination polymers with unusual ligand-unsupported Ag-Ag bonds: syntheses, structures, and luminescent properties". *Angew Chem*, Vol. 38(15), pp. 2237–2240, 1999.

[Well 77] A. E. Wells. *Three-dimensional nets and polyhedra*. *Wiley monographs in crystallography*, Wiley-Interscience, 1977.

[Will 73] I. Willis. "The effects of prolonged water exposure on human skin". *J Invest Dermatol*, Vol. 60, pp. 166 – 171, 1973.

[Zhai 89] H. Zhai, H. I. Maibach, and K.-P. Wilhelm, Eds. *Dermatotoxicology*. Informa Healthcare, seventh Ed., 1989.

[Zhan 07a] X.-L. Zhang, C.-P. Guo, Q.-Y. Yang, T.-B. Lu, Y.-X. Tong, and C.-Y. Su. "Discrete chiral single-crystal microtubes assembled with honeycomb coordination networks showing structural diversity and borromean topology in one single crystal". *Chem Mater*, Vol. 19, p. 4630, 2007.

[Zhan 07b] X.-L. Zhang, C.-P. Guo, Q.-Y. Yang, W. Wang, W.-S. Liu, B.-S. Kang, and C.-Y. Su. "Formation of two (6,3) networks showing structural diversity, borromean topology and conformational chirality in the same crystal". *Chem Commun*, p. 42424244, 2007.

Appendix A

Commensurate orbifold subgroups

Table A.1: Subgroups of $*246$ commensurate with the P, D and G minimal surfaces [Robi 04a].

Group #	Orbifold	Index	Maximal subgroups
131	$*246$	1	130, 129, 128, 127, 126 125, 124, 123, 122
130	246	2	120, 118, 116, 114, 93
129	$2*23$	2	121, 119, 118, 113, 99
128	$4*3$	2	121, 117, 116, 110, 98
127	$*266$	2	120, 119, 117, 104, 96
126	$6*2$	2	121, 120, 115, 100, 94
125	$*344$	2	119, 116, 115, 107, 95
124	$*2223$	2	118, 117, 115, 102, 97
123	$*2224$	3	114, 113, 112, 111, 110, 109, 108, 107, 106, 105, 104, 103, 102, 101, 100
122	$2*26$	4	99, 98, 97, 96, 95, 94, 93, 89
121	$23\times$	4	92, 53, 52
120	266	4	92, 54, 50
119	$*2323$	4	92, 81, 48
118	2223	4	92, 49, 77
117	$2*33$	4	92, 65, 47
116	344	4	92, 86, 51
115	$3*22$	4	92, 55, 46
114	2224	6	87, 86, 78, 77, 76, 61, 54
113	$2*22$	6	81, 80, 79, 77, 75, 56, 53
112	$**2$	6	85, 82, 80, 73, 72, 70, 61
111	$22*2$	6	85, 79, 76, 68, 67, 66, 58
110	$24*$	6	86, 85, 84, 65, 62, 59, 53
109	$24*$	6	87, 84, 74, 73, 71, 58, 56
108	$2*44$	6	84, 82, 78, 75, 69, 66, 64
107	$*2244$	6	86, 81, 74, 70, 68, 64, 55

Table A.1: Subgroups of $*246$ commensurate with the P, D and G minimal surfaces [Robi 04a].

Group #	Orbifold	Index	Maximal subgroups
106	$4*22$	6	79, 78, 74, 72, 63, 62, 57
105	$**2$	6	69, 68, 63, 61, 60, 59, 56
104	$2*222$	6	83, 82, 81, 65, 63, 58, 54
103	$*2244$	6	87, 83, 80, 67, 64, 62, 60
102	$*22222$	6	77, 73, 66, 65, 60, 57, 55
101	$*22222$	6	91, 90, 89, 88, 83, 76, 75, 71, 70, 59, 57
100	$2*222$	6	72, 71, 69, 67, 55, 54, 53
99	$22*3$	8	52, 49, 48, 42
98	$*3\times$	8	52, 51, 47, 40
97	$22*3$	8	49, 47, 46, 37
96	$*2626$	8	50, 48, 47, 36
95	$*3\times$	8	51, 48, 46, 45
94	$26\times$	8	52, 50, 46, 15
93	2226	8	51, 50, 49, 44
92	2323	8	14, 13
91	$*22*$	12	43, 42, 40, 39, 38, 34, 30
90	$2*2222$	12	44, 39, 36, 35, 34, 33, 23
89	$22*22$	12	45, 44, 42, 40, 37, 36, 15
88	$2**$	12	45, 43, 38, 37, 35, 33, 31
87	2244	12	27, 18, 17
86	2244	12	21, 17, 14
85	$2\times\times$	12	29, 21, 19
84	$44\times$	12	32, 19, 17
83	$*222222$	12	38, 36, 28, 27, 20
82	$*22\times$	12	28, 24, 19
81	$22*22$	12	28, 26, 14
80	$*2*2$	12	29, 28, 18
79	$222\times$	12	29, 26, 16
78	2244	12	24, 17, 16
77	22222	12	18, 16, 14
76	22222	12	44, 43, 27, 21, 16
75	$22*22$	12	42, 35, 32, 28, 16
74	$44*$	12	26, 22, 17
73	$2**$	12	22, 19, 18
72	$2*\times$	12	41, 31, 29, 24, 22
71	$222*$	12	32, 31, 30, 27, 23, 22, 15
70	$**22$	12	45, 39, 28, 22, 21
69	$*22\times$	12	41, 32, 30, 25, 24
68	$*2*2$	12	26, 25, 21
67	$22*22$	12	41, 29, 27, 25, 23
66	$22*22$	12	25, 19, 16
65	$222*$	12	20, 19, 14

Table A.1: Subgroups of $*246$ commensurate with the P, D and G minimal surfaces [Robi 04a].

Group #	Orbifold	Index	Maximal subgroups
64	$*4444$	12	28, 25, 17
63	$2*\times$	12	26, 24, 20
62	$44*$	12	29, 20 17
61	$\circ 2$	12	24, 21, 18
60	$**22$	12	25, 20, 18
59	$2**$	12	40, 33, 32, 21, 20
58	$222\times$	12	27, 26, 19
57	$2*2222$	12	37, 34, 22, 20, 16
56	$2\times\times$	12	32, 26, 18
55	$*222222$	12	25, 22, 14
54	22222	12	27, 24, 14
53	$222\times$	12	32, 29, 14
52	$3\times\times$	16	13, 4
51	$\circ 3$	16	13, 12
50	2266	16	13, 2
49	22223	16	13, 11
48	$*3*3$	16	13, 10
47	$*3*3$	16	13, 9
46	$3\times\times$	16	13, 3
45	$*\times\times$	24	12, 10, 3
44	222222	24	12, 11, 2
43	$\circ 22$	24	12, 11, 8
42	$22*\times$	24	11, 10, 4
41	$*\times\times$	24	8, 6, 5
40	$*\times\times$	24	12, 9, 4
39	$**\times$	24	12, 10, 6
38	$***$	24	10, 9, 8
37	$22*\times$	24	11, 9, 3
36	$22*2222$	24	10, 9, 2
35	$22*\times$	24	11, 10, 5
34	$*2222\times$	24	11, 9, 6
33	$**\times$	24	12, 9, 5
32	$22\times\times$	24	7, 5, 4
31	$\times\times\times$	24	8, 5, 3
30	$\circ*$	24	8, 6, 4
29	$22\times\times$	24	7, 5
28	$*22*22$	24	10, 7
27	222222	24	8, 7, 2
26	$22\times\times$	24	7
25	$*22*22$	24	7, 6
24	$\circ 22$	24	8, 7
23	$2222*$	24	6, 5, 2

Table A.1: Subgroups of $*246$ commensurate with the P, D and G minimal surfaces [Robi 04a].

Group #	Orbifold	Index	Maximal subgroups
22	$22**$	24	7, 6, 3
21	$\circ 22$	24	12, 7
20	$22**$	24	9, 7
19	$22\times\times$	24	7
18	$\circ 22$	24	7
17	4444	24	7
16	222222	24	11, 7
15	$2222\times$	24	4, 3, 2
14	222222	24	7
13	$\circ 33$	32	1
12	$\circ\circ$	48	1
11	$\circ 2222$	48	1
10	$****$	48	1
9	$****$	48	1
8	$\circ\circ$	48	1
7	$\circ 2222$	48	1
6	$\circ**$	48	1
5	$\times\times\times\times$	48	1
4	$\times\times\times\times$	48	1
3	$\times\times\times\times$	48	1
2	22222222	48	1
1	$\circ\circ\circ$	96	

Table A.2: Subgroups of $*2226$ commensurate with the H minimal surface [Robi 04b].

Group #	Orbifold	Index
32	$*2226$	1
31	2226	2
30	$26*$	2
29	$22*3$	2
28	$*3*$	2
27	$*3*$	2
26	$*22223$	2
25	$*2266$	2
24	$2*2222$	3
23	2626	4
22	22223	4
21	$3\times\times$	4
20	$\circ 3$	4
19	$*33*$	4
18	$3**$	4
17	$*3*3$	4
16	$22*\times$	6
15	222222	6
14	$*2222\times$	6
13	$**\times$	6
12	$**\times$	6
11	$22*2222$	6
10	$2222*$	6
9	$\circ 33$	8
8	$**\times\times$	12
7	$\circ 2222$	12
6	$\circ\circ$	12
5	$**\times\times$	12
4	$\times\times\times\times$	12
3	$\circ**$	12
2	22222222	12
1	$\circ\circ\circ$	24